Two-dimensional materials:

from hybrid magnetic multilayers to superconducting single layers

Instituto de Ciencia Molecular

Universidad de Valencia

...

Memoria presentada por Efrén Navarro Moratalla para aspirar al grado de Doctor en Nanociencia y Nanoteconología (programa ref. 3045)

...

Dirigida por el Dr Eugenio Coronado Miralles y el Dr Carlos Martí Gastaldo

D. Eugenio Coronado Miralles, catedrático del Departamento de Química Inorgánica de la Universidad de Valencia y D. Carlos Martí Gastaldo, doctor por la misma Universidad y actualmente investigador del 'Department of Chemistry' de la 'University of Liverpool',

CERTIFICAN:

Que la memoria presentada por el D. Efrén Navarro Moratalla con título "*Two-dimensional materials: from hybrid magnetic multilayers to superconducting single layers*" corresponde a su Tesis Doctoral y ha sido realizada bajo su dirección en el Instituto de Ciencia Molecular, autorizando mediante este escrito la presentación de la misma para optar al grado de Doctor.

En Paterna, a 25 de abril de 2013.

Dr. Eugenio Coronado Miralles

Dr. Carlos Martí Gastaldo

Efrén Navarro Moratalla

Agradecimientos

Es mucha la gente que de un modo u otro se encuentra reflejada en este proyecto. Para empezar quería agradecerle a Eugenio el gran apoyo que me ha brindado durante todo este tiempo. Sin duda hay muchas formas de abordar la ciencia, pero la tuya, tanto lo bueno como lo menos bueno, dejará huella en mi de por vida. En este mismo párrafo inicial también tiene cabida uno de los químicos más comprometidos y dedicados que he conocido, y ese eres tú, Carlos. Gracias a ti también por todo lo que me transmitiste y por lo que me sigues transmitiendo tanto a nivel personal como profesional. No tiene precio.

Gracias también a mis almas gemelas aquí en el laboratorio: Julia y Concha. Cada uno vemos las cosas de un modo distinto pero al final entre todos salimos adelante. Os quiero mucho chicas. Salva, lamento que tuvieras que tomar esta decisión, pero esto lo empezamos juntos y juntos lo terminaremos. Gracias por estar ahí.

Le he reservado un lugar especial dentro de esta sección a Elena, sin la cual mucho de lo mejor de esta tesis no lo podría haber escrito. Ha sido una excelente compañera de fatigas y de sobresaltos pero también de grandes alegrías y mejores invenciones. Gracias por el positivismo y por enseñarme que detrás de un punto y aparte siempre viene algo, aunque no lo parezca.

También me gustaría dedicarle unas de líneas a todas las personas que han estado a mi lado, científica y personalmente, compartiendo incontables horas de trabajo. Gracias José por tu eterna disponibilidad para todo lo que no sea el volei. Ánimo porque al final las cosas caen por su propio peso. Angelito, hace tiempo que no disfruto de tu presencia, te echo mucho de menos. Y Chema, gracias por las medidas y por un sentido del humor que siempre agradezco. Gracias Gloria y espero que te vaya muy bien con todos tus proyectos vitales. Y gracias también a Eva ¿Quien te pedirá que le limpies sustratos cuando ya no esté aquí? Mis chapuzas no serían nada sin la diligente asistencia de Jorge, gracias muchacho. Los que siempre han estado ahí para casi cualquier cosa sois vosotros: Maritere, Pilar, Enrique y Toni. Gracias por hacer del SCSIE un lugar mejor. A Saïd le debo, a parte de unas fotos de difracción que quitan la respiración, un gran apoyo en todo momento y algún que otro momento de congelación. Alicia, gracias por

velar siempre por mi, algún día correremos un maratón juntos. ¿Y qué decir del maestro de maestros: Marcelo Arias? Sin tu dedicación y amor por lo que haces yo ni sabría lo que sé y desde luego mi ciencia seria mucho peor. Es una pena que la labor de un buen artesano este tan mal valorada. También he de agradecer el trabajo de Salomé con los análisis elementales y a los servicios técnicos de la Universidad de Vigo y de la Universidad de Alicante por los análisis de XPS.

Y un rinconcito para los que estuvieron al principio pero ya no han visto el final de mi proyecto: Nora, Murad. Y a los que se fueron y ya están de vuelta: Sergio, aun nos queda mucho por re(correr) como en los viejos tiempos; y María, no sabes lo que me alegra verte feliz. Te lo mereces.

Hace muy poco que llegó la nueva generación con empuje e ilusión. Os ha tocado empezar en un momento delicado pero tenéis todo el apoyo de gente entregada por la ciencia. Remember Víctor, you'll never walk alone!

Gracias al resto de la UIMM y en particular a los Ramones, a los forofos del balonpié, y a los del padel, a Mauri, a Alex Gaita por ser tan auténtico, a Alicia por su dedicación y ayuda incondicional, a Yan por cuidarme tanto, y a Juanpi por esas pesquisas filosóficas de ultima hora de la tarde (noche).

Al equipo de administración más resuelto del mundo entero, también me encuentro en deuda con vosotros, Marian, Paco, Estela y María Jesús. Así no cuesta hacer papeles. Y no me olvido de Manuel, eficiente a todos los niveles. 'Templao', nunca ha llegado a cuajar una salidita al monte. Gracias también a Alex Gómez por esos frecuentes paquetes y por mantener el consumo de gas a raya.

Debo agradecer esta tesis también a todas las personas con las que he tenido el placer de colaborar todos estos años. Gracias al equipo de la Autónoma: a Hermann por no darse nunca por vencido a pesar de lo raros que somos los químicos y a José Augusto, a Gabino, a Guillermo y a Jorge. También he de agradecer a José Luis Vicent sus consejos en el crecimiento de cristales. Aún guardo como oro en paño tu manuscrito con la receta. Agradezco mucho toda la dedicación y amabilidad del grupo de Fernando en Zaragoza. Se nota que amas lo que haces. También le agradezco mucho a João el gran trabajo realizado con el Mössbauer y el gran trato que siempre me ha dedicado. Muito obrigado por tudo! Asimismo quería expresar mi gratitud a Angel Rubio y a Pierluigi por el fantástico

trato que siempre me prestan y por la multitud de nuevos proyectos conjuntos que sin duda traerán mucho éxito en un futuro no muy lejano. Finalmente, quería también mencionar mi corta pero intensa estancia en Delft. Agradezco mucho la acogida que me diste y admiro mucho tu entusiasmo por la ciencia, Andrés. De ti y de toda la gente con la que he trabajado me he traído a casa mucho más que solo resultados de laboratorio.

Y llega el turno de los sufridores, de los que sin comerlo ni beberlo se han tenido que conformar con verme poco y a veces mal. Gracias a mis a amigos de toda la vida por seguir a mi lado: Isa, Keles, Dani y Javi. Gracias a Luis por todos los planes que algún día cumpliremos. A Alfredo y a Alicia, que envidia me dais allí tan lejos. Gracias Nacho por ser el más cumplidor. Y sobre todo gracias a Choche por inspirarme en tantas cosas. Eres referente. Und auch meine Freunde von Deutschland un Österreich, vielen Dank Euch beiden: Johannes Ahrens und Johannes Karu (immer da für mich).

Para María no tengo palabras que puedan describir lo mucho que le agradezco todos estos años. Ha sido una historia increíble y lo mejor aún está por llegar.

Por ultimo, quería agradecer a mi familia por su incesante apoyo, a mi hermana Carla, a mi espléndida abuela Carmen y mi padres Maite y Adolfo. Esta tesis tiene un poco de cada uno de vosotros y por eso mismo estoy tan orgulloso de ella.

To my beloved dwellers of this world...

Abstract

The project herein described has been motivated by the interest on magnetic multifunctional materials based on layered architectures. Though the list of hybrid layered materials is long and despite the fact that most of the components used in this investigation are based on well-known precursors, this dissertation illustrates how there are still vast domains in this field that remain unexplored.

The first part of the thesis deals with hybrid magnetic multilayers made out of cyanide based networks and layered double hydroxide solid-state hosts. Though both components have been exhaustively studied in the past, this work describes the unprecedented *in situ* confined growth of a cyanide network within the basal galleries of LDHs. The growth of the cyanide-based magnets within a diamagnetic LDH allows for the confirmation that the confining effect provokes a down-shift of the critical temperature in comparison with the 3-D analogue. Following, the same strategy was employed to attempt the growth of bimetallic cyanides within magnetic LDHs as the host architecture. Yet, in this case the divalent metal acts as a scavenging agent, drawing the precursor hexcyanometalate out of the LDH galleries. The system so obtained may be better described as a nanoparticle/nanolayer composite combining the magnetic properties of the pristine LDH and Cr-Ni Prussian blue analogue (PBA).

The second part explores the chemistry and physics of layered transition metal dichalcogenides (TMDCs). Chapter 2 provides with an in-depth insight into the experimental detail of the synthesis of neutral TMDCs as polycrystalline and single crystalline materials. The intercalation reaction with simple alkali metals is then looked into in preparation for the following chapters where Na-intercalates are used as precursors of multifunctional hybrid materials.

In this line, Chapter 3 is devoted to the synthesis of a mixed solid-state/molecule based material that combines superconductivity with single-molecule magnetism (SMM). This is achieved by delaminating pristine Na_xTaS_2 in solution to form stable nanosheet sols that could be conveniently re-stacked together in the presence of Mn_4 cationic SMMs. An in-depth analysis performed by SQUID magnetometry permits identifying a transition to the superconducting state at around 4 K and Arrhenius type relaxation of the out of phase component of the

AC susceptibility coming from the inserted molecules.

In addition, Chapter 4 demonstrates the general applicability of the delamination/flocculation technique with TMDCs by the isolation of a further hybrid material this time combining spin crossover (SCO) mono-nuclear complexes with the intrinsic superconducting properties of the TaS_2 layers. On the basis of magnetic measurements and Mössbauer spectroscopy, it is confirmed that the low temperature transition to the Meissner state gives way to a gradual spin equilibrium up to 400 K.

The final part of the work is motivated by the vast experience acquired in the exfoliation of TMDCs. In this context research was devoted to the isolation of single or few layer TaS_2 flakes. Since the exfoliation techniques in solution afford generally defective layers with small surface areas, the field of the all-dry exfoliation methods is explored. A variation of the micro-mechanical method is developed allowing to deposit atomically thin patches of TaS_2 in a variety of substrates. The deposition of such specimens on a Si/SiO_2 surface opens the door for the fabrication of single-flake devices and for the first time, superconductivity is observed in an exfoliated atomically thin layer. The final chapter shows how these TaS_2 layered may be chemically modified to construct Ta_2O_5/TaS_2 bi-dimensional patterns via atomic force microscopy-local oxidation nanolithography (AFM-LON).

The work described in this dissertation has given rise to the following publications:

"Hybrid magnetic superconductors formed by TaS_2 layers and spin crossover complexes." E. Coronado, M. Giménez-Marqués, C. Martí-Gastaldo, G. Mínguez-Espallargas, E. Navarro-Moratalla, J. C. Waerenborgh. *Submitted.*

"Scanning tunneling measurements of layers of superconducting 2H-$TaSe_2$: Evidence for a zero-bias anomaly in single layers." J. A. Galvis, P. Rodière, I. Guillamón, M. R. Osorio, J. G. Rodrigo, L. Cario, E. Navarro-Moratalla, E. Coronado, S. Vieira, H. Suderow. Physical Review B, 87 (9), 094502 (2013).

"Fast and reliable identification of atomically thin layers of $TaSe_2$ crystals." A. Castellanos-Gomez, E. Navarro-Moratalla, G. Mokry, J. Quereda, E. Pinilla-Cienfuegos, N. Agraït, H. S. J. van der Zant, E. Coronado, G. A. Steele, G. Rubio-Bollinger. Nano Research, 6 (3), 191 - 199 (2013).

"Chiral charge order in the superconductor 2H-TaS_2." I. Guillamon, H. Suderow, J.G. Rodrigo, S. Vieira, P. Rodière, L. Cario, E. Navarro-Moratalla, C. Martí-Gastaldo, E. Coronado. New Journal of Physics, 13, 103020 - 103029 (2011).

"Hybrid Magnetic/Superconducting Materials Obtained by Insertion of a Single-Molecule into TaS_2 Layers." E. Coronado, C. Martí-Gastaldo, E. Navarro-Moratalla, E. Burzurí, A. Camón, F. Luis. Advanced Materials, 23, 5021 - 5026 (2011).

"Coexistence of superconductivity and magnetism by chemical design." E. Coronado, C. Martí-Gastaldo, E. Navarro-Moratalla, A. Ribera, S. J. Blundell, P. J. Baker. Nature Chemistry, 2, 1031 - 1036 (2010).

"Confined Growth of Cyanide-Based Magnets in Two Dimensions." E. Coronado, C. Martí-Gastaldo, E. Navarro-Moratalla, A. Ribera. Inorganic Chemistry, 49, 1313 - 1315 (2010).

Patent: P201300252, "Método y sistema de exfoliación micromecánica por vía seca de materiales laminares bidimensionales." *Pending*.

2DN	Bi-dimensional nano-sheet
a_s	shearing acceleration
AEC	anionic exchange capacity
AES	Auger electron spectroscopy
AFM	atomic force microscopy
AFM-LON	atomic force microscopy-local oxdiation nanolithography
aka.	also known as
ARPES	angle-resolved photoemission spectroscopy
ARR	ammonia releasing agent
B	magnetic induction (flux)
BS	basal spacing
ca.	counter alia
CDW	charge density wave
conc.	concentrated
CT-AFM	conducting-tip atomic force microscopy
CVT	chemical vapour transport
DLS	dyanimc light scattering
DVT	direct vapour transport
EPMA	electron-probe microanalysis
et al.	et alii (and others)
EtOH	ethanol
FEG	field emission gun
gof	goodness of fit
LS	low spin
LON	local oxidation nanolithography
hcp	hexagonal close packing
hBN	hexagonal boron nitride
H	magnetic field strength
HMT	hexamethylenetetramine
HR-TEM	high-resolution transmission electron microscopy
HS	high spin
HT	hydrothermal
ID	inner diameter
IC	incommensurate
ICP-OES	induction coupled plasama optical emission spectroscopy
iPrOH	iso-propanol
IS	isomer shift (Mössbauer)
LDH	layered double hydroxide
min	minutes
n	refraction index
NA	numerical aperture
NC	nearly commensurate
O_h	octahedral (ligand field)
OD	outer diameter
pdmH	pyridine-2,6-dimethanol
PL	photoluminescence
PLD	periodic lattice distortions
PTFE	poly(1,1,2,2-tetrafluoroethylene) (teflon)
px	pixel
QS	quadrupole splitting (Mössbauer)
RMS	root mean squared (roughness)

r	reflection
r. t.	room temperature
rpm	revolution per minute
SC	superconductivity/superconductor
SAED	selected-area electron diffraction
SEM	scanning electron spectroscopy
SET	single electron transistor
SMM	single molecule magnet
STM	scanning tunnelling microscope
T	temperature
t	time; transmission
T_c	Curie critical temperature (ferromagnetism)
t_r	reaction time
TEM	transmission electron microscopy
TG	thermogravimetry
TM	transition metal
TMDC	transition metal dichalcogenide
UHV	ultra high vacuum
v_s	shearing speed
XPS	X-Ray photoelectron spectroscopy
XRPD	X-Ray powder diffraction

Contents

0

Solid-state chemistry and hybrid multifunctionality

A few introductory words

intercalate
[in- **tur** -k *uh* -leyt]

1. to interpolate; interpose
2. to insert (an extra day, month etc.) in the calendar

ORIGIN: 1605-15; <L *intercalātus* ptp. of *intercalāre* to inset a day or month into the calendar, equiv. to *inter-* inter + *calā-* (s. of *calāre* to proclaim) + *-tus* ptp. suffix.

"Intercalation chemistry is the soft chemistry route [...] working at the borderlines of solution chemistry, solid-state chemistry, and colloid chemistry. It is ideally suited to the fabrication of organic/inorganic multilayer assemblies. The constrained space in the interlayer galleries, with its peculiar electrostatic conditions and with the template effects of the intracrystalline boundaries, forms a "reaction vessel" of its own, giving insight into the weak interactions responsible for supramolecular organization."

Anton Lerf, 2000

Materials science, considered as one of the most antique forms of engineering and applied science, has lately emerged as a very powerful area of research in chemistry and physics.[1] It has therefore brought together scientists and engineers over the past few decades with the shared interest of designing new materials for a wide variety of applications.

In this context, modern researchers reinforce multidisciplinary lines of investigation where new multifunctional materials with interesting property combinations are eagerly sought for. These are materials that combine several physical properties of interest such as ferromagnetism, conductivity,

1 Callister, Jr., William D. *Materials Science and Engineering - An Introduction*, John Wiley and Sons, **2000**.

superconductivity, optical activity or non-linear optics. It is here where the design and synthetic power of chemists nicely blends with the in-depth theoretical and experimental property study which physicists perform so fervently.

Molecular chemistry has turned out to be particularly significant in the field, providing an interesting versatility to traditional materials science. This chemical approach allows for a careful design of the material, starting with the election of appropriate molecular building blocks, and then, introducing the chance to favour a specific supramolecular interaction between the different building units that will bestow targeted properties to the final substance. The combination of different starting units has not only permitted the coexistence or synergy of different properties in a single material, but it has also launched the capacity to generate molecular heterostructures in a homogeneous material. In this way, it has yielded the so called multifunctional hybrid materials.[2] They combine different physical properties in novel hybrid organic-inorganic matrices. Within these multifunctional materials, special efforts have been dedicated to the development of structures of relevance in magnetism, which is the main focus of this project.[3, 4, 5]

A slight variation of the same approach consists in blending soluble molecular building blocks with traditional insoluble inorganic materials. The combination of molecular and solid-state *synthons* has motivated the design of unprecedented hybrid multifunctional materials based in the self-assembly of a polymeric molecule-based structure within a traditional solid inorganic host. This gives rise to co-operativity in the all-new molecule-based part in contrast with the properties of the parent molecular fragments. The resulting structures combine the robustness of traditional inorganic frameworks with the flexibility and variety

2 a) Sato, O.; Iyoda, T.; Fujishima, A.; Hashimoto, K. *Science* **1996,** *272,* 704. (b) Coronado, E.; Giménez-López, M. C.; Korzeniak, T.; Levchenko, G.; Romero, F. M.; Segura, A.; García-Baonza, V.; Cezar, J. C.; de Groot, F. M. F.; Milner, A.; Paz-Pasternak, M. *J. Am. Chem. Soc.* **2008,** *130,* 15519. (c) Inoue, K.; Kikuchi, K.; Ohba, M.; Ökawa, H. *Angew. Chem. Int. Ed.* **2003,** *42 (39),* 4810–4813. (d) Train, C.; Gheorghe, R.; Krstic, V.; Chamoreau, L.-M.; Ovanesyan, N.; Rikken, G.; Gruselle, M.; Verdaguer, M. *Nat. Mat.* **2008,** *7,* 729–734. (e) Cui, H.; Wang, Z.; Takahashi, K.; Okano, Y.; Kobayashi, H.; Kobayashi, A. *J. Am. Chem. Soc.* **2006,** *128,* 15074–15075. (f) Rogez, G.; Viart, N.; Drillon, M. *Angew. Chem. Int. Ed.* **2010,** *49,* 1921–1923. (g) Clemente-León, M.; Coronado, E.; Martí-Gastaldo, C.; Romero, F. *Chem. Soc. Rev.* **2011,** *40,* 473–497. (h) Coronado, E.; Mínguez Espallargas, G. *Chem. Soc. Rev.* **2013,** *42,* 1525.

3 a) Coronado, E.; Galan-Mascaros, J. R.; Gomez-Garcia, C. J.; Laukhin, V. *Nature* **2000,** *408 (6811),* 447–449. (b) Coronado, E.; Galán-Mascarós, J. R. *J. Mater. Chem.* **2005,** *15,* 66.

4 Coronado, E.; Day, P. *Chem. Rev.* **2004,** *104 (11),* 5419–5448.

5 Coronado, E.; Gómez-García, C. J.; Nuez, A.; Romero, F. M.; Waerenborgh, J. C. *Chem. Mater.* **2006,** *18,* 2670.

of properties of molecular architectures. This very last twist in intercalation chemistry has been little explored so far. However, seminal works reported by our research team have clearly demonstrated the technique's potential for the facile combination of two functional subnetworks in a single phase.[6] Thus a big avenue of hybrid materials synthesized by this technique is expected to come in the following times.

At the same time, the last word in traditional intercalation chemistry has not yet been said.[7] In the more classical approach, a discrete guest species is dispersed within the host structure in such a way that both preserve the identity of the precursor materials. Even though the intercalation reaction has caught the eye of materials researchers for more than two generations, the possibilities of intermixing a host structure and a guest entity are so vast that only a minute part of the combinations have been tried out. Recently, much effort has been devoted to the controlled organization and confinement at the nano-scale of functional molecules within the voids provided by a solid-state framework.[8] In particular, interest has been drawn towards the incorporation of optical and magnetic properties within traditional mesoporous media.[9] The integration of novel functionalities in hybrid organic/inorganic materials is still a very active area of research with a flowering future.

Surprisingly, most of the research in the field of multifunctional hybrids has been focused in the use of three-dimensional host structures. Yet, layered solid-state structures offer unmatched possibilities in that which respects their processability and their chemical versatility. As a matter of fact, intercalation can

---

6 Coronado, E.; Martí-Gastaldo, C.; Navarro-Moratalla, E.; Ribera, A.; Galán-Mascarós, J. *J. Mater.. Chem.* **2010,** *20,* 9476–9483.

7 *Intercalation reaction* (also contains definition of *insertion reaction*): reaction, generally reversible, that involves the penetration of a host material by guest species without causing a major structural modification of the host. Intercalation can refer to the insertion of a guest species into a one-, two- or three-dimensional host structure. The guest species is not distributed randomly but occupies positions predetermined by the structure of the host material. Examples of intercalation reactions are the insertion of lithium into layered TiS_2 [Li_xTiS_2 ($0 \leq x \leq 1$)] and of potassium into the layers of graphite (C_8K).
From: *IUPAC. Compendium of Chemical Terminology, 2nd ed. (the "Gold Book").* Compiled by A. D. McNaught and A. Wilkinson. Blackwell Scientific Publications, Oxford, **1997**.

8 a) Popović, Z.; Busby, M.; Huber, S.; Calzaferri, G.; De Cola, L. *Angew. Chem. Int. Ed.* **2007,** *46,* 8898–8902. (b) Strassert, C. A.; Otter, M.; Albuquerque, R. Q.; Höne, A.; Vida, Y.; Maier, B.; De Cola, L. *Angew. Chem. Int. Ed.* **2009,** *48,* 7928–7931.

9 Clemente-León, M.; Coronado, E.; Forment-Aliaga, A.; Amorós, P.; Ramírez-Castellanos, J.; González-Calbet, J. M. *J. Mater.Chem.* **2003,** *13,* 3089–3095.

literally speaking only occur in a layer-like material. This is the only family of materials where an entity may be strictly interposed between layers. Linguistic matters left aside, it may be argued that layered materials are among the most convenient hosts to perform intercalation chemistry. Since the first time that the word intercalation was used to describe the potassium uptake by graphite,[10, 11] much knowledge has been accumulated concerning the intercalation of guest species in layered materials.[12, 13] Traditionally, intercalation has been performed by direct diffusion, this is, by allowing a guest entity to slowly permeate the host material driven by a direct concentration gradient. Alternatively, this may be done by pulling the host structure apart and segregating the individual layers in stable colloids to later on re-stack or flocculate them together again in the presence of the guest species. The preparation of colloids from layered materials is a well-established discipline owing to the ancient technological relevance of clays.[14] However, the more recent development of such exfoliation/flocculation techniques for a wide range of long-forgotten layered materials has boosted the design and synthesis of new multifunctional combinations of layered materials that could not be accessed by the direct intercalation approach. Layered double hydroxides (LDHs), layered metal oxides and transition metal dichalcogenides (TMDCs) are just a few protagonists of the *renaissance* of the layered materials that has just begun.

But that which has undoubtedly pushed layered materials back in the spotlight is the very recent discovery of graphene back in year 2004. An entirely new field regarding the study of solid-state bi-dimensional systems made out of atomically thin flakes has emerged since that date. Nobel prize laureates Geim and Novoselov continue nowadays to explore the possibilities that graphene offers

10 Schleedeand, A.; Wellmann, M. *Z. Phys. Chem. B* **1932,** *18,* 1

11 Fredenhagenand, K.; Cadenbach, G. *Z. Anorg. Allg. Chem.* **1926,** *158,* 249.

12 a) McDonnell, F. R. M.; Pink, R. C.; Ubbelohde, A. R. *J. Chem. Soc.* **1951,** 191. (b) Rüdorff, W. *Angew. Chem.* **1959,** *71,* 487.

13 Lerf, A. *Handbook of Nanostructured Materials and Nanotechnology* **2000,** *5,* 1–166.

14 van Olphen, H. *Clay Colloid Chemistry. For Clay Technologists, Geologists, and Soil Scientists.* Wiley, New York, **1977**.

in both the most fundamental but also applied sense.[15, 16] The availability of new mechanical deposition techniques and novel characterization technologies foresee the discovery of new dimensionality-related phenomena and the application of one carbon atom thick crystals in a wide range of devices too. However, the low throughput of the mechanical exfoliation of graphite yields only enough graphene for fundamental research and prototypic testing. This brings us back to the already mentioned liquid exfoliation methodologies as a convenient approach to scale up the production of graphene. In this context, graphene science feeds back on the great knowledge accumulated over time concerning the colloidal chemistry of other layered materials. Thus, layered compounds and hybrid composites of graphene are nowadays a key area of modern materials science.[17]

The work herein described imbibes from the long history of intercalation in layered materials and has also been inspired by the just starting *layered materials' rush*. It attempts to explore the new horizons of the of the soft chemistry approach to novel multifunctionality on the one hand and the fundamental physics that lie beneath solid-sate bi-dimensional systems on the other. May the research here described persuade the reader in digging deeper in such a fascinating and fruitful world as is the bi-dimensional universe of layered materials.

---

15 a) Gorbachev, R. V.; Geim, A.K.; Katsnelson, M. I.; Novoselov, K. S.; Tudorovskiy, T.; Grigorieva, I. V.; MacDonald; A. H., Morozov, S. V.; Watanabe, K.; Taniguchi, T.; Ponomarenko, L. A. *Nat. Phys.* **2012,** *8 (12),* 896–901. (b) Haigh, S. J.; Gholinia, A.; Jalil, R.; Romani, S.; Britnell, L.; Elias, D.C.; Novoselov, K.S.; Ponomarenko, L. A.; Geim, A.K.; Gorbachev, R. *Nat. Mat.* **2012,** *11 (9),* 764–767. (c) Mayorov, A. S.; Elias, D. C.; Mukhin, I. S.; Morozov, S. V.; Ponomarenko, L. A.; Novoselov, K. S.; Geim, A. K.; Gorbachev, R. V. *Nano Lett.* **2012,** *12 (9),* 4629–4634.

16 a) Grigorenko, A. N.; Polini, M.; Novoselov, K. S. *Nat. Phot.* **2012,** *6 (11),* 749-758. (b) Georgiou, T.; Jalil, R.; Belle, B. D.; Britnell, L.; Gorbachev, R. V.; Morozov, S. V.; Kim, Y.-J.; Gholinia, A.; Haigh, S. J.; Makarovsky, O.; Eaves, L.; Ponomarenko, L. A.; Geim, A. K.; Novoselov, K. S.; Mishchenko, A. *Nat. Nanotech.* **2012,** *8,* 100–103. (c) Kravets, V. G.; Schedin, F.; Jalil, R.; Britnell, L.; Gorbachev, R. V.; Ansell, D.; Thackray, B.; Novoselov, K. S.; Geim, A. K.; Kabashin, A. V.; Grigorenko, A. N. *Nat. Mat.* **2013,** *12,* 304–309. (d) Novoselov, K. S., Fal'Ko, V. I., Colombo, L., Gellert, P. R., Schwab, M. G., Kim, K. *Nature* **2012,** *490 (7419),* 192–200.

17 Huang, X.; Qi, X.; Boey, F.; Zhang, H. *Chem. Soc. Rev.* **2012,** *41,* 666.

1

LDH-based materials

1 Introduction

Hybrid structures based on both solid-state and molecule-based building blocks offered us a manifold of possibilities awaiting to be exploited. Within this context, a big family of materials arises from the use of layered double hydroxides (LDHs) as inorganic host structures. The layered structure of these anionic clay hosts together with the ability to highly tune their intra-layer chemical hydroxide composition makes them especially convenient for the chemical design of new hybrids. These are materials where one can finely tailor the magnetic properties of the hydroxide layer for combination with the properties of a hypothetical molecule-based counterpart structure. It is a versatile approach that has already been reported as a strategy for the insertion of magnetic complexes into layered double hydroxide systems.[1]

1 Layered Double Hydroxides

By the term layered double hydroxide (LDH) — also referred to as hydrotalcite-like compounds or anionic clays —[2] we describe a particular class of laminate compounds represented by the general formula $[M^{II}_{3-x}M^{III}_{x}(OH)_6]^{x+}(A^{m-})_{x/m} \bullet nH_2O$, where M^{II} and M^{III} stand for metallic cations and A for interlayer anions of charge -*m*. This means that structurally they are constituted by positively charged metal hydroxide sheets that pillar one on top of the other and that are electrostatically balanced by anions located in the interlayer interstitial space. This makes it an unusual class of solid-state chemistry materials, nowadays dominated by a big number of families of compounds with negatively charged layers (*i.e.* kaolinite and other clays).

To fully understand the structure of these compounds, one should recall the structural morphology of brucite, $Mg(OH)_2$, where octahedra of Mg^{2+} (6-fold

1 Coronado, E.; Galán-Mascarós, J.; Martí-Gastaldo, C.; Ribera, A. *Chem. Mater.* **2006,** *18,* 6112–6114.

2 Hydrotalcite: discovered in Sweden around 1842, it is a hydroxycarbonate of magnesium and aluminum of general formula $Mg_6Al_2(CO_3)(OH)16{\cdot}4(H_2O)$. It occurs in nature in foliated, contorted plates and/or fibrous masses and that can be easily crushed into white powder in the same manner one can do with talc, to which it owes its name ("hydro" after its high water content and "talcite" for its softness).

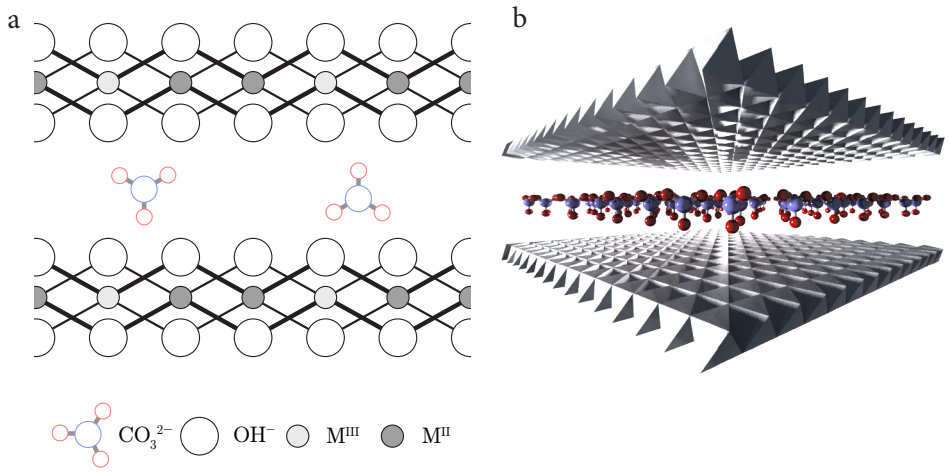

Figure 1.1 Schematic (**a**) and 3-D (**b**) representation of a LDH-CO_3.

coordinated to OH^- ions) share edges to form stacked infinite layers held together by hydrogen bonds. Hydrotalcite structure arises upon partial substitution of these Mg^{2+} ions by a similar radius trivalent (or tetravalent, *ie.* Ta^{IV}) metal ion to generate positive charges within the hydroxide sheet. This net positive charge needs to be compensated by anions that place themselves randomly between brucite-like lamellae, where water may also be found. These interlayer entities are free to move along the inter-sheet free space by breaking and reconstituting the hydrogen bonds that bind them to the brucite layer hydroxides (see Figure 1.1).

Having considered the structural details of LDH materials, one may appreciate how their features, and consequently properties- amongst which lie the magnetic ones, of particular interest for the subject matter of this project- are mainly determined by the compositional and stacking nature of the brucite-like sheets and by the position and nature of the anions and water molecules in the interlayer region.

Concerning their chemical composition one finds that a big range of divalent and trivalent cations are susceptible of substituting Mg in brucite, giving rise to a big family of anionic clays. Most commonly M^{II} and M^{III} may be Ca^{2+}, Mg^{2+}, Mn^{2+}, Fe^{2+}, Co^{2+}, Ni^{2+}, Cu^{2+} or Zn^{2+} and Fe^{3+}, Al^{3+}, Cr^{3+}, Co^{3+}, Ni^{3+}, Mn^{3+}or V^{3+}, respectively, with values of x namely in the range $0.1 \leq x \leq 1.0$. In relation to

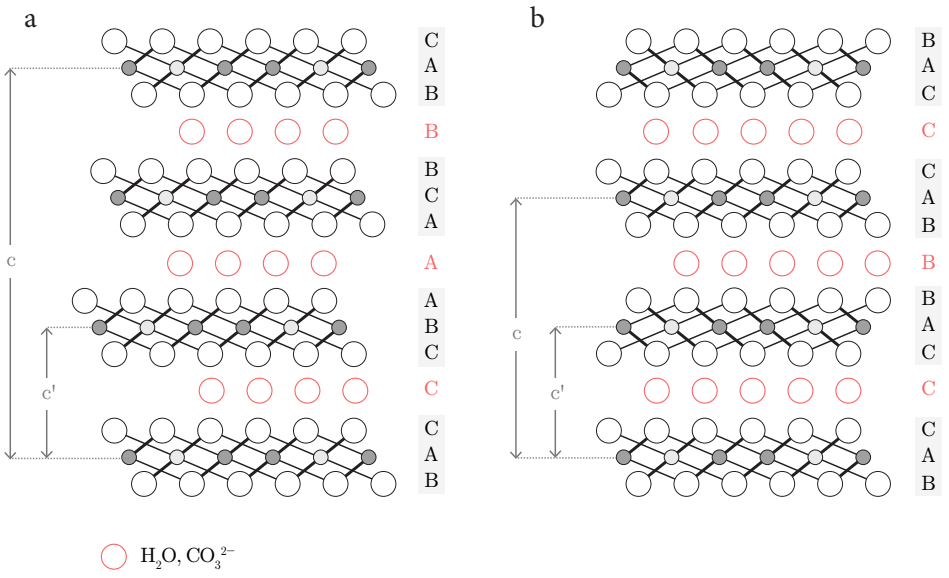

Figure 1.2 Possible brucite-like layer stacks: hydrotalcite stack (**a**) and sjögrenite stack (**b**).

the anionic counter ions, LDHs may be formed with a wide variety of them, for instance: halides, CO_3^{2-} or NO_3^-, always in such a stoichiometrical ratio that all the positive hydroxide layer charge is counterbalanced.

Regarding the layer stacking, brucite-like sheets can pillar one on top of the other with two different symmetries: rombohedral or hexagonal. Calling BAC the OH-M-OH brucite layer projection down the three-fold axis of the OH groups, the stack may have a rombohedral sequence BC-CA-AB-BC including three sheets in the unit cell, or alternatively BC-CB-BC with this with two sheets in the unit cell for the hexagonal symmetry lattice (see Figure 1.2). Pristine hydrotalcite crystallizes in the rombohedral 3*R* symmetry with unit cell parameters of a and $c = 3c'$ (c' being the thickness of one brucite-like sheet and one interlayer space *aka.* basal spacing BS, as shown in Figure 1.2a).

LDHs, as such or used as oxides after calcination, have found many practical applications in a variety of different technological, industrial and scientific fields.[3] Not only are they of great relevance for the chemical community, as intrinsic

3 Cavani, F.; Trifirò, F.; Vaccari, A. *Catalysis Today* **1991,** *11,* 173–301.

heterogeneous catalysts (hydrogenation, polymerization and petrol cracking processes) or catalyst support (Ziegler-Natta, CeO_2), but they also excel as outstanding materials for industrial, adsorbent or medical applications.[3, 4]

LDH materials are therefore very relevant in the field of catalysis, with direct industrial implications. Also important in this industrial sense is their great potential as adsorbents. Of great environmental impact are their applications as chlorine ions exchagers and for the purification of water containing waste anions (organic and inorganic). Even more, LDHs have been studied as potential iodide scavengers in an attempt to improve long-lived radionuclide getters used in nuclear fuel disposal, being its major drawback the easy replacement of iodide by carbonate ions.[5]

Equally interesting are the properties that come up from the use of LDHs as oxides following calcination processes. Some of the more interesting ones include: high surface area, basic properties, very small and controlled oxide crystal sizes, thermal stability and the so called 'memory effect', by which mild calcination-formed oxides may be reconstructed under certain conditions to give the original LDH on being treated with water solutions containing various anions.[3]

2 The ion exchange process

Since Bish and Brindley's first discovery of the ion exchange process in the late 70s, LDHs have been well known for their anion exchange properties.

Bish and Brindley noticed that if takovite was treated with dilute aqueous HCl its basic hydrotalcite-like morphology was not altered at all, but a new layered double hydroxide structure was formed instead.[6] The new compound maintained the hydroxide layer composition and structure, thus could only be distinguished from the original by looking at the crystallographic unit cell value of *c*'. IR spectroscopy revealed how indeed there had been an exchange of CO_3^{2-}

4 a) Li, B.; He, J.; Evans, D. G.; Duan, X. *Appl. Clay Sci.* **2004,** *27,* 199–207. (b) Li, B.; He, J.; Evans, D. G.; Duan, X. *Int. J. Pharm.* **2004,** *287,* 89–95. (c) Xu, Z. P.; Lu, G. Q. M. *Pure App. Chem.* **2006,** *78,* 1771–1779.

5 Kaufhold, S.; Pohlmann-Lortz, M.; Dohrmann, R.; Nüesch, R. *App. Clay Sci.* **2007,** *35,* 39–46.

6 *Takovite*: Ni-Al hydrotalcite-like mineral of general formula: $Ni_6Al_2(OH)_{16}(CO_3,OH)\cdot 4(H_2O)$.

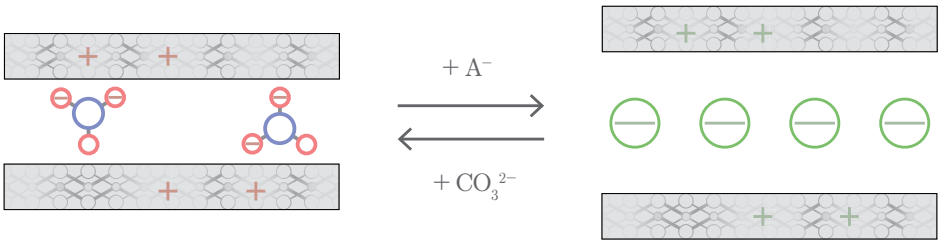

Figure 1.3 Ion exchange process in a LDH

by Cl^- ions.[7] Following, a reasonable amount of research has been devoted to the intercalation of molecular compounds interwoven with the layers of metal hydroxide.[8]

Along these lines, anions located in the interlayer regions can generally be easily replaced in hydrotalcite-like compounds allowing for the incorporation of a wide variety of diverse negatively charged species. The general conditions and procedures were optimised by Bish and involved treating the carbonate-containing LDH with a diluted aqueous solution of a mineral acid at room temperature for variable but generally long reaction times (several days).[9] Carefully controlling the exchange conditions, one may succeed in replacing simple inorganic anions of synthetic starting material LDHs (very frequently CO_3^{2-}) by other simple inorganic ions (Cl^-, NO_3^-, SO_4^{2-}, by use of the corresponding acids). The exchange technique is therefore the standard method to synthesize LDHs containing anions other than carbonate, since if no extra care is taken, the general availability of this anion in air-exposed aqueous media and its high affinity for LDH compounds directs most syntheses towards the carbonate clay product.

A simplified scheme of the, at least in principle, reversible process can be viewed in Figure 1.3, where other important aspects to note are that the intercalate stoichiometry depends on the charge ratio of the exchanged species and also that

7 Bish, D.L.; Brindley, G.W. *Am. Miner.* **1977.** *62 (5-6),* 458-464.

8 a) Rives, V. *Layered Double Hydroxides: Present and Future*; , Ed. Nova Science Publishers: New York, **2001**. (b) Leroux, F., Besse, J.P. in: Wypych, F. M.; Satynarayana, K. G., *Clay Surfaces: Fundamentals and Applications*; Ed. Elsevier: London, **2004**, 459-495.

9 Bish, D.L. *Bull. Min.* **1980,** *103 (2),* 170–175.

the basal spacing may be dramatically altered by the ion replacement, expanding or contracting the lattice cell.

In this way, Bish and Brindley lead the way to a new big field in solid-state chemistry that focuses on the intercalation of different guests between LDH host sheets. These simple inorganic counterions may now be replaced by direct treatment solutions of more complex inorganic or organic anions (e.g. carboxylates) or even polymeric anionic biomolecules such as DNA. Several remarkable breakthroughs in the field are worth mentioning, like for instance the first report of an attempt to exchange LDH hydrotalcite-like compounds containing polyoxometalate anions via the terephthalate-pillared clay and later exchange with the polyanion under mild aqueous acid conditions.[10]

A more in depth study of the exchange with different more complex molecules has even revealed certain shape selectivity in the process of intercalation of LDHs. This could be concluded after discovering the selective exchange of certain position isomers, fact which launches the potential of LDHs in its use as isomeric mixture resolver.[11]

The result of this intense research on anionic clay intercalation compounds has produced a big variety of LDH derivatives for advanced applications.[4] Drug molecule LDH intercalates allow for a better-controlled drug release and a reduction in the frequency of dose intake. Other intercalates for instance are of interest in agrochemistry, used as agrochemicals support and delivery, or as scavenging agents to remove pollutants from water to reduce the eutrophication impact of agrochemicals in the environment.[12]

Once obtained, new ion-exchanged synthetic LDHs are also very easily identified and characterised by X-Ray powder diffraction (XRPD) analysis. Diffractograms show peaks that are characteristic of the inter-layer ordering and of the distance between layers, providing a clear idea of the exchange process and the resulting material.

10 a) Drerdzon, M.A. in *Proc. Symp.* on *New Catalytic Materials and Techniques*, ACS Meeting, Div. of Petroleum Chem., Miami (USA) **1989.** *34 (3),* 511. (b) Drerdzon, M.A. *Inorg. Chem.***1988**, *27*, 4628

11 *For instance:* (a) Ragavan, A.; Khan, A. I.; O'Hare, D. *J. Mater. Chem.* **2006,** *16 (6),* 602–608. (b) Williams, G. R.; Dunbar, T. G.; Beer, A. J.; Fogg, A. M.; O'Hare, D. *J. Mater. Chem.* **2006,** *16 (13),* 1231–1237.

12 *Example:* Ragavan, A.; Khan, A.; O'Hare, D. *J. Mater. Chem.* **2006,** *16 (42),* 4155-4159.

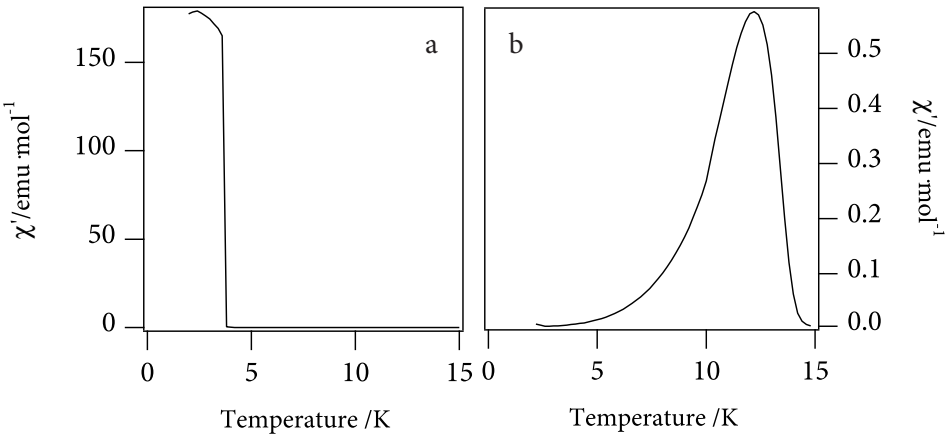

Figure 1.4 AC magnetic susceptibility showing the ferromagnetic behaviour of NiAl-NO_3 (**a**) and the ferrimagnetic properties of NiFe-NO_3 (**b**).

3 LDHs as magnetic hosts

At this stage, much has already been said about the interesting properties and general applications of LDH compounds, and yet, we are still missing a few words on one of their most charming — at least in the context of this investigation — property: their magnetic behaviour. An immediate consequence of their chemical versatility is that, though original Mg-Al hydrotalcite was a diamagnetic material, substitution of the diamagnetic metals by other paramagnetic ones produces a series of compounds with amazingly diverse magnetic behaviours.[13] Magnetic exchange interactions (J) and critical temperatures (T_C for ferromagnets and T_N for antiferromagnets) of the anionic clays are therefore subtle to tune via the electronic nature of the metals used. Ferromagnetic (CoAl and NiAl for instance) and ferrimagnetic (as in NiFe or NiCr) spontaneous magnetization below a certain temperature are some of the consequences of the inclusion of paramagnetic atoms in the hydrotalcite-like compounds. This may be appreciated by looking at the thermal variation of the AC susceptibility as shown in Figure 1.4.

13 a) Laget, V.; Hornick, C.; Rabu, P.; Drillon, M.; Ziessel, R. *Coord. Chem. Rev.* **1998,** *178-180,* 1533-1553. (b) Coronado, E.; Galán-Mascarós, J. R.; Martí-Gastaldo, C.; Ribera, A.; Palacios, E.; Castro, M.; Burriel, R. *Inorg. Chem.* **2008,** *47,* 9103-9110. (c) Almansa, J. J.; Coronado, E; Martí-Gastaldo, C.; Ribera, A. *Eur. J. Inorg. Chem.* **2008,** *36,* 5642-5648.

At this stage, one may appreciate how the combination of exceptional intercalation capabilities and diverse magnetic properties results in an extraordinary host material, ideal for nesting other interesting anionic substructures in novel multifunctional materials.

In addition, one may appreciate how the combination of exceptional intercalation capabilities and diverse magnetic properties results in an extraordinary host material, ideal for nesting other interesting anionic substructures in novel multifunctional materials.

4 *In situ* polymer growth at LDHs

The intercalation chemistry of discrete species in LDHs has been intensively studied (view previous section 2 on ion exchange). However, though less explored, another very interesting category of hybrid structures with potential applications arises from the *in situ* construction of interlayer molecule-based networks.

In this context, the polymerization of organic polymers within the basal spacing of LDHs and hydrocalumites have drawn much attention in the past.[14, 15] This line of investigation has also provided interesting examples of hybrid LDH-conducting polymer heterostructures.[16] In these studies the LDH material acts as a solid state support for the organization of the polymeric material and at the same time it plays an electrochemically active role in the interaction with other electrolytes.[17]

Still, *in situ* polymerization within LDHs has completely neglected the use of coordination polymers. So, in spite of the great chemical and physical versatility of other metal-organic frameworks, their combination with LDHs has been omitted. A possible explanation could be the strict restriction imposed by the solid state

14 In allusion to the composition, hydrocalumites contain water, Ca and Al as in the following general formula: $Ca_8Al_4(OH)_{12}(Cl, CO_3, OH)_{2-x}{\cdot}4H_2O$

15 a) Mostafa Moujahid, E.; Besse, J.-P.; Leroux, F. *J. Mater. Chem* **2002,** *12,* 3324–3330. (b) Mostafa Moujahid, E.; Besse, J.-P.; Leroux, F. *J. Mater. Chem.* **2003,** *13,* 258–264. (c) Vieille, L.; Taviot-Guého, C.; Besse, J.-P.; Leroux, F. *Chem. Mater.* **2003,** *15,* 4369–4376. (d) Vaysse, C.; Guerlou-Demourgues, L.; Duguet, E.; Delmas, C. *Inorg. Chem.* **2003,** *42,* 4559–4567. (c) Martínez-Gallegos, S.; Herrero, M.; Rives, V. *J. Appl. Polym. Sci.* **2008,** *109,* 1388–1394.

16 Challier, T.; Slade, R. C. T. *J. Mater. Chem* **1994,** *4,* 367.

17 Doménech, A.; Coronado, E.; Lardiés, N.; Martí-Gastaldo, C. M.; Doménech-Carbó, M. T.; Ribera, A. *J. Electroanal. Chem.* **2008,** *624,* 275–286.

host. Indeed the charge density per surface area unit for a desired polymer must be close to that of LDH hydroxide layer in order for *in situ* polymerization to proceed.[18] Still, an adequate choice within the vast family of coordination polymers should provide with interesting hybrid phases.

18 Leroux, F.; Taviot-Guého, C. *J. Mater. Chem.* **2005,** *15,* 3628.

2 Confinement of cyanide networks in two dimensions

Previous works reported by Coronado *et al.* show a first attempt to obtain magnetic multilayers by the polymerisation of a layered bimetallic oxalate 2-D network in the basal spacing of an LDHs.[19] However, although the study provides good proof of the capability of LDHs to act as robust hosts upon insertion of polymeric structures, the intercalation of an extended coordination network could not be attained. In this line, there was experimental evidence of the presence of mere oligomeric species with different bridging modes in the inter-lamellar region. The extended coordination structure polymerisation is desirable if one aims at preparing a molecule-based magnet inserted into the solid-sate clay host.

1 Chemical design

A detailed study of the surface density charge in the host and guest layered structures reveals a possible hindrance in the synthesis of the extended oxalate network due to a charge mismatching. The whole stability of the system relies in effect in this electrostatic equilibrium of opposite sign charges of both subsystems: the solid-state host and the molecule-based guest.

Figure 2.1 shows fragments of the projections of both sub-lattices along their respective crystallographic *c*-axis. On the left one finds an accurate representation of a bimetallic (transition metals A and B) 2-D oxalate of general formula $[A^{II}B^{III}(C_2O_4)_3]^-$. The LDH projection is depicted on the right and corresponds to the unit formula: $[C^{II}{}_2D^{III}{}_1(OH)_6]^+$. Taking these structural and chemical parameters into consideration and, if one were to imagine an ideal material constituted by bimetallic 2-D oxalate anionic layers interwoven between LDH cationic sheets, the charge surface (δ) matching calculus reflects a poor equivalence. Thus, oligomers develop at best and the formation of an extended oxalate-supported network exhibiting spontaneous magnetization was never achieved.

19 Coronado, E.; Martí-Gastaldo, C.; Navarro-Moratalla, E.; Ribera, A.; Galán-Mascarós, J. *J. Mater.. Chem.* **2010,** *20,* 9476–9483.

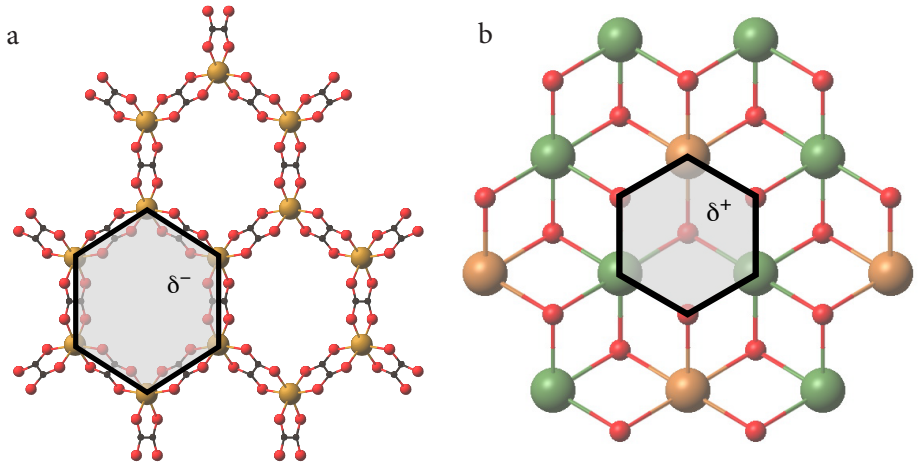

Figure 2.1 2-D bimetallic oxalate (**a**) and LDH (**b**) network surface charge density. Here: $\pm q$ is the net units of charge in shaded areas; P is the regular hexagon perimeter; A_p is the hexagonal apothem; S_{hex} (surface area of an elongated hexagon) $= 2 \times S_{triangle} + S_{rectangle}$.

However, if one considers the charge per unit surface area in the case of a $[M^{II}M^{III}(CN)_6]^-$ bimetallic cyanide extended network should it be confined to two dimensions, one may appreciate how the charge matching drastically improves (see Figure 2.2). In this way, one could imagine the possibility to form this ideal two-dimensional substructure to try and combine both networks in the same material, to produce a balanced hybrid with precisely charge matched sub-lattices. Furthermore, not only will the bimetallic cyanide network allow us to better fit the LDH surface-charge, but it will also allow us to introduce a magnetically active and tuneable guest that will add up to the final multifunctionality of the material. This could, in principle, give rise to a hybrid material whose magnetic properties could be very finely controlled, separately tayloring both the solid-state and the molecular-based components.

This project will focus in the careful design of new LDH-bimetallic cyanide multifunctional hybrids, their synthesis and the final characterization of their

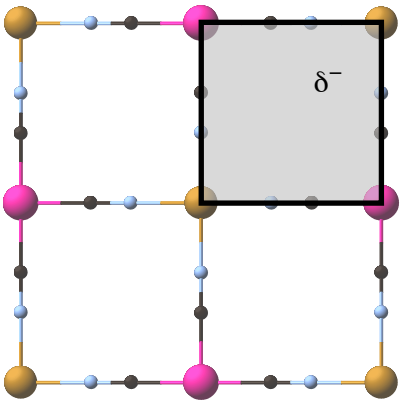

$$\delta^{-} = \frac{-q}{S_{sq}} = -0.024\ \text{Å}^{-2}$$

Figure 2.2 PB Surface charge density. Where: $\pm q$ is the net units of charge in shaded area; S_{sq} is the surface area of shaded square.

physical properties and their response to different stimuli, specially focusing on the magnetic phenomena.[20]

In this context, the proposed system is expected to excel as tunable multifunctional material in so far its magnetic properties should be sensitive to changes in both the nature of the LDH and also the coordination polymer. From a synthetic point of view, this could be an excellent opportunity to attempt the confinement of a Prussian-blue-type structure in a real two-dimensional space and so attempt to produce an authentic 2-D cyanide-bridge bimetallic metal network. On that note, the magnetic study of such a layered cyanide and the comparison with the 3-D lattice would allow for the direct observation of the effect of dimensionality in the spontaneous magnetization of the system.

In addition, the use of a magnetic LDH would allow to combine the intrinsic magnetic properties of both sub-lattices and also to look into the interaction between the clay and the coordination-polymer layers. At a theoretical level, data coming from such a multi-layer magnetic system could provide useful information about the mutual influence of the magnetic properties at the two different moieties,

20 Coronado, E.; Martí-Gastaldo, C.; Navarro-Moratalla, E.; Ribera, A. *Inorg. Chem.* **2010,** *49,* 1313–1315.

providing with information about how the ordering of one sub-lattice could alter the properties of the other layer type by dipolar interactions.

2 About the molecule-based guest

Prussian blue is a clear example of how an anciently known compound can still be subject of investigation in cutting-edge research lines long after its first discovery, already about 300 years ago.[21] Only in the mid 60s could the structure of this bimetallic cyanide network be elucidated by joint analysis of the results of X-Ray powder diffraction, IR, UV-Vis and Mössbauer spectroscopy experiments.[22] Extreme insolubility and facile metal impurity occlusion meant severe hindrance for the structural determination of this iron cyanide compound.

Nowadays we can undoubtedly state that original Prussian blue synthesized by direct precipitation from aqueous potassium ferrocyanide and ferric salt solutions- is described by the general formula $Fe^{III}_4[Fe^{II}(CN)_6]_3\Diamond_1 \bullet 14H_2O$ ($\Diamond$ symbolizes $[Fe^{II}(CN)_6]$ vacancies necessary to maintain a 4 : 3 stoichiometry) and crystallizes in a face-centered-cubic lattice alike the one shown in Figure 2.3. Taking a closer look at the 3-D model shown, one may also notice the very large interstitial sites present in the lattice.[23] These are very characteristic of PB cubic structures and should be void in pristine ideal PB.

It is also worth writing a brief note on the synthesis of PB. There are two, in principle non-equivalent, ways of producing the final metal cyanide-bridged network: causing the precipitation of Prussian blue by addition of a ferric (Fe^{3+}) salt to a ferrocyanide solution or inversely, by pouring a ferrous (Fe^{2+}) salt over a solution of an alkali metal hexacyanoferrite to obtain what traditionally was called Turnbull's blue.[24] For a long time it was believed that both species were different. Later crystallographic and Mössbauer studies have nonetheless confirmed that both compounds are identical ferric ferrocyanide and that either

21 Prussian blue was one of the first synthetic pigments discovered accidentally in Berlin in 1704.

22 *Mösbauer:* Fluck, E.; Kerler, W.; Neuwirth, W. *Angew. Chem. Int. Ed.* **1963.** *2,* 277. *XRPD:* Keggin, J. F.; Miles, F. D. *Nature* **1936.** *137,* 577. (b) *IR:* Emschwiller, G. *Compt. Rend.* **1954.** *238,* 1414. (c) *UV-Vis:* Robin, M. B. *Inorg. Chem.* **1962.** *1,* 337. (d) Duncan, J. F.; Wigley, P. W. R. *J. Chem. Soc.* **1963.** *1020–1025.*

23 Weiser, H. B.; Milligan, W. O.; Bates, J. B. *J. Phys. Chem.* **1942.** *46,* 99–111

24 Izatt, R. M.; Watt , G. D.; Bartholomew, C. H.; Christensen, J. J. *Inorg. Chem.* **1970,** *9 (9),* 2019–2021.

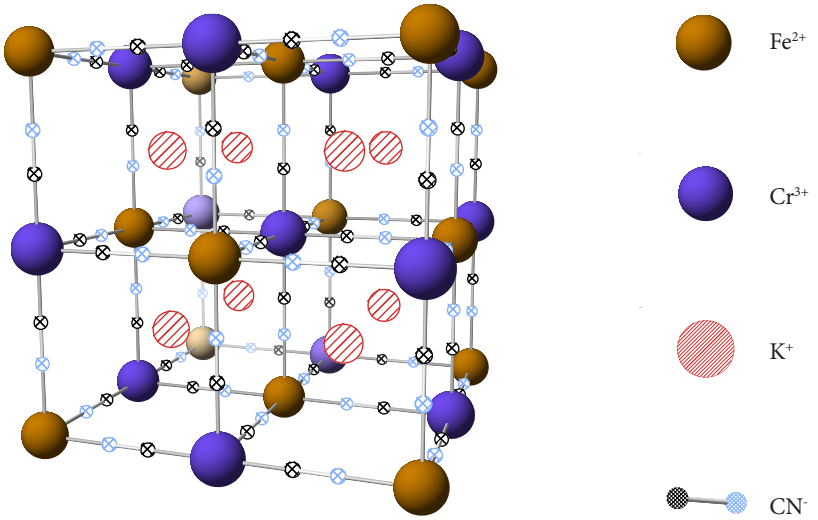

Figure 2.3 Representation of the unit cell of the Fe^{II}-Cr^{III} PBA: $KCr^{III}[Fe^{II}(CN)_6]\cdot 4H_2O$

synthetic pathway is suitable for the synthesis of a unique cyanide-metal network. An internal redox reaction promotes spontaneous electron transfer from cation to anion in Turnbull's blue and this can be directly monitored through Mössbauer spectroscopy. In this way, one may confirm how the oxidation state of the iron ions at the two different cyanide sites is the same in the differently synthesized compounds.[25]

Now if one substitutes the iron starting materials by alternative cation cyanides and salts, a large family of face-centered cubic cyanide bridged systems may be obtained. This is what is known as the family of Prussian Blue Analogues (PBA). In general, combining a metal A salt with a C salt of B hexacyanide will produce a network of general formula: $C_nA_p[B(CN)_6]_q \bullet xH_2O$, where $[B(CN)_6]$ occupies the vertices and centers of the faces, A stands at the octahedral sites and C is generally a monovalent cation that may occupy some of the mentioned interstitial tetrahedral moieties in the cyanide lattice. An example of a common PBA crystal structure can be viewed in Figure 2.3.

25 Cosgrove, J. G.; Collins, R. L.; Murty, D. S. *J. Am. Chem. Soc.* **1973.** *95 (4),* 1083–1086.

2.1 Interest in molecular magnetism

The big relevance of magnetic properties in materials science has already been introduced throughout the previous sections. Moreover, the important role of molecular chemistry in the field of magnetism has also been discussed. These areas have consequently inspired one of the main aims of this thesis as is the design of hybrid materials with interesting magnetic functionality.

Molecular magnetism has revolutionised traditional investigation in magnetism by enhancing its intrinsic multidisciplinary nature.[26] Modern magnetism conceives new molecular systems from the initial designing stages and spans all the way through the synthesis and applications.

Thus PBAs arise amongst the most exciting and versatile molecule-based magnetic systems. The list of interesting properties that PBAs offer the scientists is vast: low temperature magnetic bulk ordering phenomena, solid-state redox activity, photomagnetism, electrochromism, pressure and photo-isomerism, etc.[27] Together with their chemical diversity, simplicity of the starting molecular entities and synthetical possibilities, PBAs are excellent candidates for the hybrid materials here described.

2.2 An all-new chemistry for a structural challenge

A crucial implication that may be extracted from the atomic structure presented is the fact that these cyanide coordination polymers always grow as three-dimensional bulk materials. Many research has been devoted to the controlled dimensionality reduction of such systems. Several strategies have been therefore employed, namely the use of capping ligands, or on the growth of monolayers onto substrates by means of the LB technique.[28]

---

26 Kahn O. *Molecular Magnetism*, VCH, New York, **1993**.

27 *For a review on metal-cyanide networks see for instance:* (a) Shriver, D. F. *Struct. Bond.* **1966**. *1*, 32. (b) Dunbar, K. R.; Heintz, R. A. *Prog. Inorg. Chem.* **1997,** *45,* 283. (c) de Tacconi, N. R.; Rajeshwar, K.; Lezna, R. O. *Chem. Mater.* **2003,** *15,* 3046–3062. (d) Herrera, J. M.; Bachschmidt, A.; Villain, F.; Bleuzen, A.; Marvaud, V.; Wernsdorfer, W.; Verdaguer, M. *Philos. T. Roy. Soc. A* **2008,** *366,* 127–138.

28 a) Lescouëzec, R.; Toma, L.; Vaissermann, J.; Verdaguer, M.; Delgado, F. S.; Ruiz-Pérez C., Lloret, F.; Julve, M. *Coord. Chem. Rev.* **2005,** *249,* 2691-2729. (b) Culp, J. T.; Park, J.-H.; Frye, F.; Huh, Y.-D.; Meisel, M. W.; Talham, D. R. *Coord. Chem. Rev.* **2005,** *249,* 2642-2648.

Our approach constitutes the first direct strategy employed for the growth control of a bimetallic cyanide.[29] LDHs offer the synthetic chemist an all-new (bi) dimension where traditional chemical reactions may be tried out. Its basal spacing conforms a nano-reactor where one may perform coordination chemistry under molecule-scale bi-dimensional confinement. In this line, the synthetic strategy presented in this chapter tried to mimic the traditional precipitation method of PBAs but this time using the LDH basal space as a two-dimensional reactor that should trap the precursor metallic complex confining their growth in two dimensions.

3 General synthetic approach

The preparation of the hybrid bimetallic cyanide-LDH materials was inspired both by the precipitation reaction of PBAs (*vide supra*) and by the general ion exchange process (recall section 2 of Chapter 1, page 14). The first step was the formation of the pristine LDH material from simple inorganic salts in a basic medium (*vide infra* section 4.1). Following, the trivalent metal hexacyanometallate was inserted in the galleries of the LDH host by simple ion exchange in the presence of high $[M^{III}(CN)_6]^{3-}$ concentrations. This yielded the solid-state precursor of the final coordination polymer (section 4.2). To finish off, the polymerization of the bimetallic cyanide network in between LDH layers was attempted by soaking the precursor material in divalent metal aqueous concentrated solutions (section 5).

The aim was to optimize a robust synthetic methodology that could permit the combination of different LDH systems with a wide variety of different bimetallic cyanide networks. Although the general procedure used for the synthesis of each particular hybrid was consistent, no universal reagent mixture ratio was found to be appropriate in all cases. The synthetic conditions therefore needed to be optimized in each specific situation and are carefully detailed in the experimental section at the end of the chapter.

In general, the synthetic route involved the use of well-established solid-state chemistry techniques blended with air-sensitive methodologies that allowed for improved phase purity of the obtained compounds.

29 Due to the distinct chemical and structural nature in comparison with 3-D PBAs, the term bimetallic cyanide will be used from now on to refer to the cyanide-based part of the hybrid materials proposed

Following, an exhaustive view of the synthetic process is provided and the properties of the resulting materials are introduced. The discussion will be divided in two sections: the synthesis and magnetic properties all the precursor materials (pristine LDHs and hexacyanometalate intercalates) on the one hand; and the synthesis and magnetic properties of the final hybrid magnetic multilayers on the other. The quality of the synthesized materials was evaluated on the basis of a variety of analytical techniques such as: X-Ray powder diffraction (XRPD) to check crystallinity; electron-probe microanalysis (EPMA) used for chemical characterization in terms of metallic ratio estimation; Fourier-transform infrared spectroscopy (FT-IR) for anion detection; or thermogravimetric analysis (TG) for water content estimation. The discussion of the properties will be based on the full magnetic characterization of the synthesized materials establishing clear relationships with the proposed structures.

4 Precursor materials

4.1 Starting LDHs

The direct synthesis of simple inorganic anion LDHs has been extensively studied in the past, yet it continues to be revisited by solid-state chemists in an attempt to improve the control over the characteristics of the final materials. The phase and chemical purity, the crystal morphology, the degree of crystallinity and the crystallyte size are, among others, crucial parameters that may be tightly controlled at present.[30]

Good-quality pure LDHs have been traditionally prepared by *co-precipitation* methods from metal salt aqueous solutions via addition of NaOH (titration increasing pH method or co-precipitation at constant pH either at low or high supersaturation).[31] Yet, there are other alternative methods such as the *homogeneous precipitation*. In the latter, LDHs are prepared by the hydrothermal reaction of metal salts with organic precursors.[32] However, even though all the methods available could be suitable for the synthesis of any anionic LDH clay, the

30 Okamoto, K.; Iyi, N.; Sasaki, T. *Appl. Clay Sci.* **2007,** *37,* 23–31.

31 (a) Miyata, S.; Kumura, T. *Chem. Lett.* **1973,** *2,* 843–848. (b) Miyata, S.; *Clay. Clay. Miner.* **1975,** *23 (5),* 369-370. (c) Reichle, W. T. *Solid State Ionics* **1986,** *22 (1),* 135–141.

32 For a comprehensive review on different synthesis methods see reference 8.

synthetic methodology employed has a big influence in the properties of the final material. Along these lines, co-precipitation LDHs are usually obtained in the gel form and are then aged to improve crystallinity, but even so, crystal sizes hardly ever exceed 1 μm (hundreds of nanometers in general). The large surface area showed by these materials make them excellent candidates in catalysis. On the other hand, crystals yielded by homogeneous precipitation methods tend to show bigger more uniform morphologies and better-defined hexagonal shapes. The latter method includes the use of ammonia-realeasing reagents (ARRs, generally urea or hexamethylenetetramine, HMT) that increase the pH upon being hydrolised at high temperatures, provoking the metal hydroxide precipitation.

In our case, the preference, once synthesizing starting material LDHs, was to obtain good phase purity and crystallinity with an homogeneous morphology and crystallite size. To obtain an exceptionally crystalline starting material was a major priority taking into account that several reaction steps generally meant crystallite erosion and a loss of crystallinity.

To obtain improved ion exchange capabilities being another of our main concerns, our starting LDHs had to incorporate an easily replaceable anion between the layers. In this way, a particularly suitable type of anionic clay was the nitrate-LDH system. NO_3^- entity is a low charge density and easily exchangeable ion as opposed to CO_3^{2-} of much higher affinity towards LDH inter-laminar space.

It has already been commented how one of the main advantages of using LDHs comes from the possibility of tuning the magnetic properties of the layers by simply modifying the metallic composition. In this way two types of starting LDHs were synthesized according to their magnetic behaviour: diamagnetic nitrate LDHs (MgAl-NO_3, ZnAl-NO_3) and magnetic nitrate LDHs (CoAl-NO_3).[33]

Two sets of different common LDHs were chosen as starting *diamagnetic systems*: ZnAl-NO_3 (**1**) and MgAl-NO_3 (**4**). Whilst the co-precipitation method,[34] at constant pH, directly afforded a good crystalline nitrate clay in the first case, one of the best established and controlled synthesis described for the latter involved

33 Note the general abridged nomenclature employed composed by the divalent metal followed by the trivalent metal and finally the anionic inter-layer species: $M^{II}M^{III}$-A

34 The synthesis was adapted from the original method reported by Miyata: Miyata, S. *Clay. Clay. Miner.* **1980,** *28,* 50–56.

the homogeneous precipitation method followed by ion exchange reaction (CO_3^{2-} by NO_3^-).[30]

SEM imaging techniques allowed for the comparison of the morphology of the crystallites that conformed the powder samples. Figure 2.4a and b show very similar particle size for both samples, though higher homogeneity in the case of MgAl LDH. Crystallinity depicted by XRPD (see Figure 2.4c) was equally high in both materials and the patterns could be successfully indexed according to the so mentioned 3R symmetry (recall Figure 1.2 on page 13). EPMA estimations approximately fitted the ideal $2M^{2+}$: $1M'^{3+}$ ratio (see Table 2.1). Finally, FT-IR spectrometry provided with the final confirmation of phase purity of the samples due to the big sensitivity of the technique to anions such as CO_3^{2-} and NO_3^-. Their ν_3 stretching modes show up in the low wavelength region (centred at ~ 1350 and ~ 1380 cm^{-1} respectively). In our particular case, a single well-defined sharp peak at 1380 cm^{-1} is indicative of pure nitrate phase as can be appreciated for compound **1** in Figure 2.4d.

Compound	Alias	M^{II} / Al
1	ZnAl-NO_3^-	1.84
4	MgAl-NO_3^-	1.53
5	CoAl-NO_3^-	1.32

Table 2.1 Metallic ratios of precursor LDH NO_3^- materials calculated from SEM EPMA data.

The extension of this work to magnetic LDHs is trivial, thanks to the fact that most synthetic LDHs of paramagnetic metallic composition combine first row transition metals with Al. This family of magnetic LDHs are described by the following general formula: $[TM_{3-x}Al_x(OH)_6]^{x+}(A^{m-})_{x/m} \bullet nH_2O$, where TM stands for the paramagnetic transition metal. Taking our diamagnetic LDHs as a starting reference, it is only a question of formally substituting diamagnetic Mg or Zn by a different transition metal. This implies chemical substitutions of similar atomic radii metals to which lattice parameters are almost insensitive.

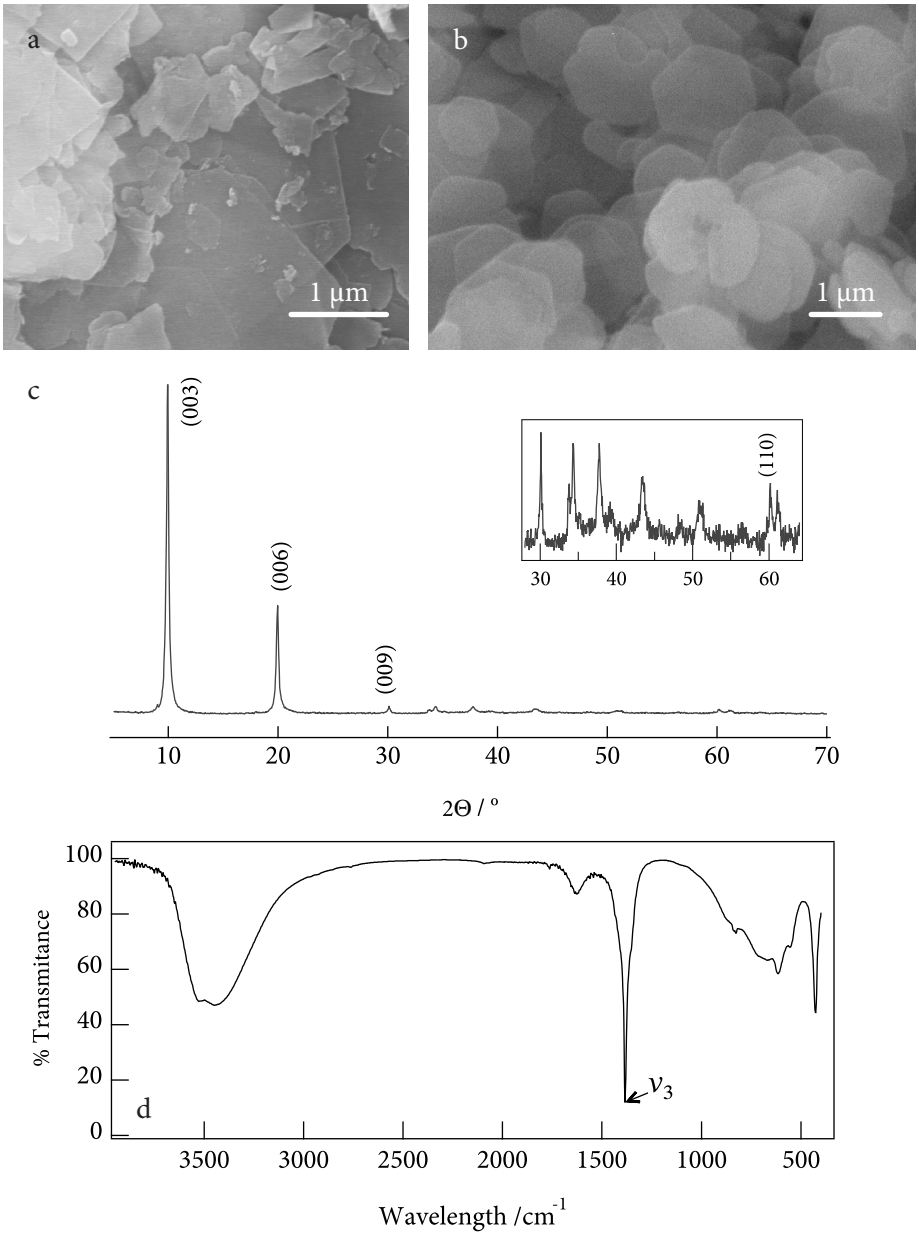

Figure 2.4 Selected characterisation of diamagnetic LDHs: SEM imaging of the crystallite morphology of **1** by co-precipitation (**a**) and **4** by homogeneous precipitation (**b**); XRPD pattern of **1** showing main out-of-plane (00*l*) and in-plane (110) reflections according to the 3R symmetry (**c**); FT-IR spectrum of **1** highlighting most prominent vibration mode of the NO_3^- anion (1384.6 cm^{-1}).

The preparation of magnetic LDHs has been studied in the past.[35] In particular, CoAl-NO_3 (**5**) was the material of choice as a *magnetic hosts*. This system was relatively easy to obtain via homogeneous precipitation synthesis of the carbonate hydrotalcite and subsequent carbonate-nitrate simple ion exchange. CoAl-NO_3 is also structurally and compositionally very similar to the ZnAl-NO_3 clay previously described. Yet, oppositely to the diamagnetic system, CoAl-NO_3 presents a low temperature magnetic ferromagnetic ordering. Also, given the fact that it is composed by a single type of magnetic metal (Co^{2+}), it is conceptually easier to understand than for other higher critical temperature (T_C) magnetic LDHs, which behave as glassy magnets and exhibit exchange interaction competitions arising from the presence of different paramagnetic ions. The latter is the case of, for instance, FeNi or CrNi LDHs.[36]

In the CoAl system, preliminary tests demonstrated that the homogenous precipitation synthetic strategy allowed for the recovery of more crystalline and homogeneous samples. A wide range of different conditions (temperature, reaction times, ARRs) were consequently tested within the context of homogeneous precipitation. The resulting materials were analysed in search of the most crystalline and pure LDH phase. The experiments clearly showed that homogeneous precipitation with urea at high temperatures (140-190 ºC) during 1 or 2 days afforded the best materials in terms of crystallinity, platelet size homogeneity and LDH phase purity. However, the hydrothermal synthesis of the CoAl system resulted in the carbonate LDH **3** being recovered, thus the nitrate clay CoAl-NO_3 (**5**) was obtained after a final anion exchange step.

SEM images of the products obtained after both synthetic steps are shown in Figure 2.5a and b. As may be appreciated, very homogeneous disc-like micrometric crystals of **5** were attained via the hydrothermal synthetic approach.

The XRPD patterns of both **3** and **5** showed sharp and well defined peaks indicative of a high crystallinity (see Figure 2.5c). Taking a more careful look at the most prominent peaks, one may relate the changes observed in the

35 *For example:* Ma, R.; Takada, K.; Fukuda, K.; Iyi, N.; Bando, Y.; Sasaki, T. *Angew. Chem. Int. Ed.* **2008,** *47,* 86–89

36 (a) Pérez-Ramírez, J.; Ribera, A.; Kapteijn, F.; Coronado, E.; Gómez-García, C. *J. Mater. Chem.* **2002,** *12,* 2370–2375 (b) Almansa, J.; Coronado, E.; Martí-Gastaldo, C.; Ribera, A. *Eur. J. Inorg. Chem.* **2008,** *5642–5648.*

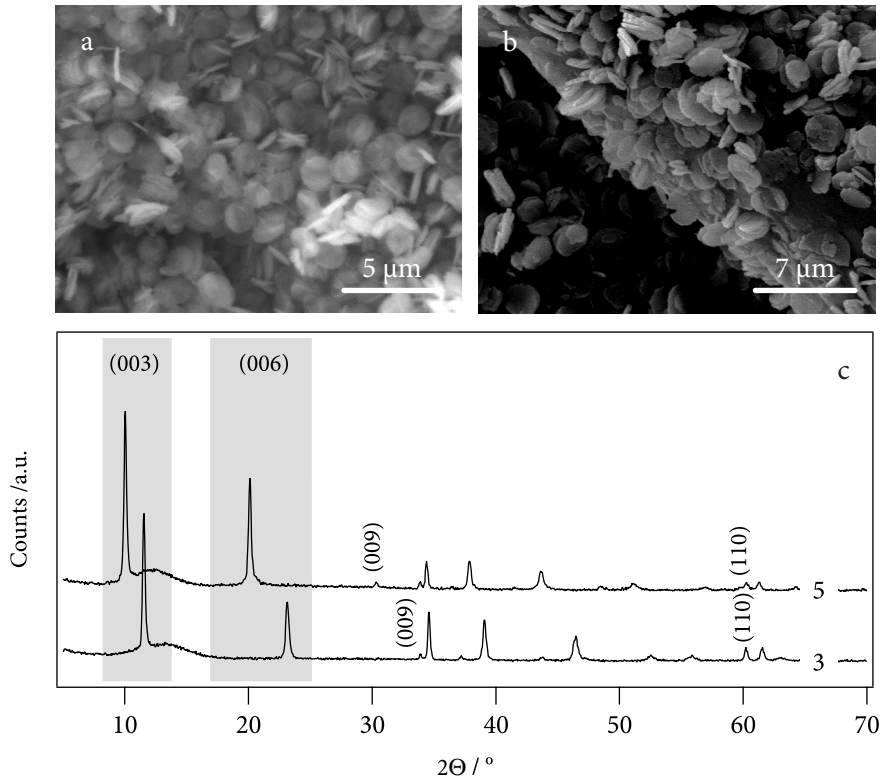

Figure 2.5 Two-step synthesis of CoAl-NO_3 LDH as seen by different techniques: SEM images of **3** (**a**) and same LDH after anion exchange in diluted HNO_3 **5** (**b**); XRPD patterns (**c**) of compounds **3** (*bottom*) and **5** (*top*).

diffraction patterns with the carbonate-nitrate ion exchange process. Knowing that the LDH compounds dealt with are all analogous sheet stacks crystallizing in the rombohedral 3R symmetry, an adequate indexation of the powder pattern provides very useful structural information. One of the principal features observed in these diffraction patterns is the very intense and sharp low-angle diffraction peaks assigned to (00*l*) basal reflections. Besides, the other key feature is the broad peak around $2\Theta = 60^{o}$ that may be associated to the in-plane reflection (110) with respect to the rombohedral crystallographic axes. Coming back to our specific CoAl case study, a $\Delta 2\Theta \sim 1.5^{o}$ general negative shift of the (003) reflection peak is observed upon exchanging the CO_3^{2-} anions with NO_3^{-} ones. This change is also inevitably manifested in the (006) and (009) related reflections. The situation

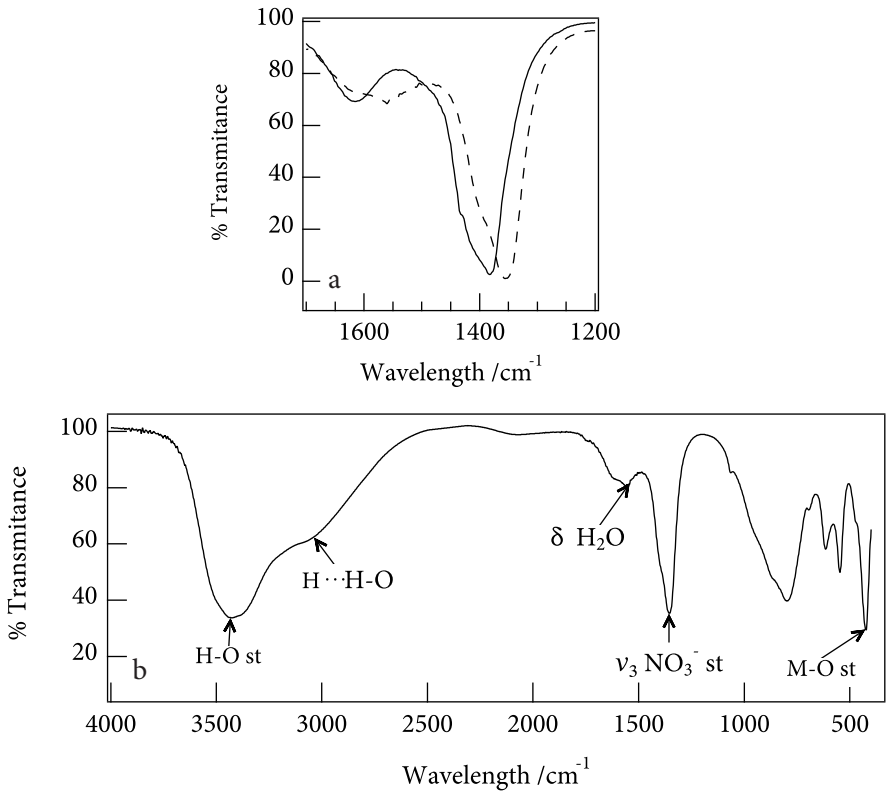

Figure 2.6 a. NO_3^--CO_3^{2-} anion exchange as seen by the FT-IR ν_3 stretching peak shift of **5** (*continuous*) with respect to **3** (*dashed*). **b**. Generic FT-IR spectrum of an LDH-NO_3 showing main vibration mode features.

clearly demonstrates the simple uniaxial increase of the basal spacing (BS) on substituting the more densely charged CO_3^{2-} by the NO_3^- anion. And on the contrary, the 60º doublet remains unaffected, evidencing that the hydroxide in-plane structure remains untouched. These observations are all in good agreement with other very exhaustive peak indexations of carbonate analogous CoAl-LDH systems previously reported.[37]

Lastly, while describing the FT-IR spectra of **5** it is interesting to go over the rest of the main general features of LDH vibration modes (see Figure 2.6).

37 *For instance:* (a) Liu, Z.; Ma, R.; Osada, M.; Iyi, N.; Ebina, Y.; Takada, K.; Sasaki, T. *J. Am. Chem. Soc.* **2006,** *128,* 4872-4880. (b) Pagano, M. A.; Forano, C.; Besse J. P. *J. Mater. Chem.* **2003,** *13,* 1988–1993.

This will come in handy once characterising the more complex hybrids, allowing direct identification of the vibrational features that belong to each constituent and allowing for the recognition of peak shifts and their chemical implications. Apart from the anion stretching peaks already discussed (~1380 cm^{-1} is ν_3 antisymmetric stretching for nitrate, ~1350 cm^{-1} for carbonate) there are other characteristic bands worthwhile describing: the absorption at 3500 - 3600 cm^{-1} is attributed to the H-bonding stretching vibrations of the OH; a shoulder present at around 3000 cm^{-1} has been attributed to hydrogen bonding between H_2O and the interlayer anions;[38] a medium intensity H_2O bending vibration broad band can normally be observed at around 1620 cm^{-1}; the 600 - 1000 cm^{-1} broad band region involves anion bending modes and oxygen-cation hydroxide layer vibration;[39] and finally, another sharp and intense peak at around 420 cm^{-1} is also assigned to a metal-oxygen vibration.

Sample	Water content		*Empirical formula*
	Wt. loss / %	n H_2O	
1	17.6	3.17	$Zn_{1.94}Al_{1.06}(OH)_6(NO_3)_{1.06}\bullet 3.17(H_2O)$
5	14.6	4.24	$Co_{1.71}Al_{1.29}(OH)_6(NO_3)_{1.29}\bullet 4.24(H_2O)$

Table 2.2 Water content calculated from TG data and empirical formulas of precursor NO_3^- LDHs.

On the basis of the information provided by the different techniques, empirical formulae of both the diamagnetic and the magnetic precursor materials could be estimated. This was done taking the metallic ratio resulting from EPMA microanalysis and normalizing to fit the general formula: $[M^{II}_{2-x}M^{III}_{x}(OH)_6]^{x+}$. Next, one checks by FT-IR spectroscopy the anionic species present – when dealing with nitrates and carbonates the ν_3 stretching mode is easiest to identify – and its coefficient is calculated to match the charge of the cationic counterpart. To complete the empirical formula, the sample weight loss up until 250 ºC measured by TG techniques indicates the hydration water molecules per unit formula. Results for LDHs **1** and **5** are shown in Table 2.2.

38 a) Miyata S. *Clay. Clay Min.* **1975,** *23,* 369. (b) Bish, D.L.; Brindley, G.W. *Amer. Min.* **1977,** *62,* 458.

39 (a) Hernandez-Moreno, M.J.H.; Ulibarri, M.A.; Rendon, J.L.; Sema, C. *J. Phys. Chem. Min.,* **1985,** *2,* 34. (b) Serna, C.J. ; Rendon J.L.; Iglesias, J.E. *Clay. Clay Min.* **1982,** *30,* 180.

The magnetic properties of these materials have already been reviewed in the introductory chapter and will therefore not be presented in this section. For further reference please go back to section 3 in Chapter 1 (page 17).

4.2 Hexacyanometallate intercalates

a. Synthesis

The insertion of hexacyanometallates in LDH hosts has already been studied in depth in the past.[40] The isolation of these inetercalates is achieved by a simple direct ion exchange. The chemical equilibrium shown in Equation 2.1 describes the process.

$$[M^{II}_2 M'^{III}(OH)_6](NO_3)\cdot nH_2O + \frac{1}{3}K_3[M'^{III}(CN)_6] \xrightarrow{H_2O,\,Ar} [M^{II}_2 M'^{III}(OH)_6][M'^{III}(CN)_6]_{\frac{1}{3}}\cdot mH_2O + KNO_3$$

Equation 2.1 Hexacyanometallate intercalate generic synthesis

Among the well-known hexacyanometallate complexes, a classical species was selected: the Cr(III) complexes. Iron and chromium hexacyanometallates have provided good LDH intercalation case studies in the past.[41] In addition, the combination of $[Cr(CN)_6]^-$ with a wide range of different divalent cations has afforded some of the most interesting and renowned cyanide-bridged networks in the literature, such as original high T_C Ni-Cr PBA.[42]

In this way, the hexacyanometallate-LDH materials were synthesized by stirring samples of the nitrate LDHs (**1** and **5**) in concentrated solutions of chromimum(III) hexacyanometallate potassium salts. Special care was taken in maintaining a CO_2-free atmosphere to avoid phase contamination by carbonate intercalation. This limitation also meant that the work-up of reaction crudes had to be performed inside a specially conditioned CO_2-free N_2 filled glove box. It is worthwhile emphasizing the importance of thoroughly washing these materials to remove excess adsorbed metal complex. The drying of these intermediate

40 *For instance*: Holgado, M.; Rives, V.; Sanromán, M.; Malet, P. *Solid State Ionics* **1996,** *92,* 273–283.

41 Crespo, I.; Barriga, C.; Rives, V.; Ulibarri, M. *Solid State Ionics* **1997,** *101-103,* 729–735.

42 Gadet, V.; Mallah, T.; Castro, I.; Verdaguer, M.; Veillet, P. *J. Am. Chem. Soc.,* **1992,** *114 (23),* 9213-9214.

compounds was also critical and had to be done *in vacuo* over NaOH pellets again to prevent CO_2 absorption.

The result in all cases was the quantitative recovery of a fine powder where the success of the exchange process could be evidenced by a subtle though clear colour change: the ZnAl system starts off as a white powder and ends as a yellowish solid (**6**); CoAl LDH is pale pink and turns ochre after intercalation (**7**).

The chemical composition and the phase purity of the final intercalation compounds were checked by EPMA, XRPD and FT-IR spectroscopy. The first technique provided us with estimations of the chemical composition in terms of the heavier element ratios (view Table 2.3). This data allows for the calculation of what is known as the anionic exchange capacity (AEC) of our LDH host. AEC measures the maximum intercalated amount of the new anion compared to the theoretical quantitative ion replacement and was found to be very high in all our precursor LDH intercalates and in good agreement with electroneutrality ($3[M^{II}_2Al_1(OH)_6]^+ : 1[Cr^{III}(CN)_6]^{3-}$). The values depicted a fovourable ion exchange reaction that starts off with an easily replaceable nitrate anion and exchanges it by a threefold charged hexacyanometallate expected to have a greater affinity towards the host.

Compound	Zn/Al	Co/Al	Cr/Al	AEC / %
6	1.99	-	0.24	73
7	-	1.57	0.20	60

Table 2.3 Metallic molar ratios calculated from SEM EPMA data.

XRPD patterns obtained for the hexacyanometallate intercalates **6** and **7** presented the expected profile characteristic of a layered LDH. Low-angle characteristic sharp diffraction basal reflection peaks may be indexed as (00l) reflections assuming a 3R symmetry (review Chapter 1). The negative peak shift in contrast to the (00*l*) positions of pristine nitrate LDHs reflects a drastic interlamellar space expansion, as is expected judging the size of the hexacyanometallates compared to that of nitrate anion in good agreement

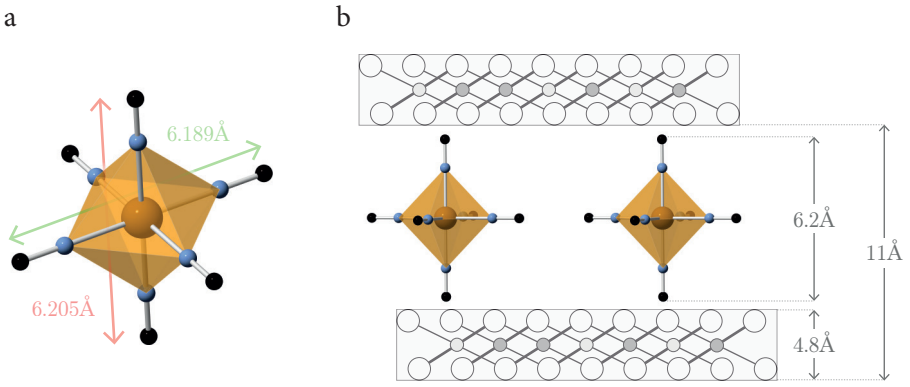

Figure 2.7 Cartoon representation of the chromium hexacyanometallate species dimensions (**a**) and its insertion between LDH planes (**b**).

with the dimensions of the anion (see Figure 2.7). Basal spacing increases from BS = 8.79 Å for the NO_3 LDHs to around 11 Å for the intercalated compounds. These values are in excellent agreement to those previously reported by Rives *et al.* for the intercalation of hexacyanometallates.[41] Finally, the typical in-plane broad peak found at around 2Θ = 60º can be ascribed to the (110) reflection, in the exact same position as for the original LDHs. Unit cell parameters derived from peak positions are shown in Table 2.4.

Conpund	(hkl) 2θ / º				Cell parameters / Å			
	(003)	(006)	(009)	(110)	$d_{(110)}$	*a*	*c*	BS
6	8.11	16.12	24.20	60.25	1.54	3.08	32.93	10.98
7	7.91	15.76	23.73	60.21	1.54	3.08	33.67	11.23

Table 2.4 Structural data extracted from XRPD patterns of LDH-hecyanochromate materials. $d_{(110)}$ refers to the real space dimension corresponding to the (110) in-plane reflection and is half the a crystallographic axis length. BS = *c*/3 in the case of the 3R crystal systems.

Of great importance is to note that cell parameter *a* is very sensitive to any chemical change affecting the LDH layers. The extremely homogeneous values

observed in the table and the precise coincidence with the original LDH values are indicative of the presence of unspoiled LDH sheets. It is also worth commenting on the great homogeneity of the powder patterns of all synthesized precursors despite variations in the metal and LDH nature. Only minor differences could be observed in the crystallinity of the different materials. In this line, the CoAl system was found to be slightly more degraded (< signal-to-background ratio) during the hexacyanometallate intercalation process than its ZnAl analogue systems. The XRPD patterns of the precursor materials will be plotted later on to allow for a direct comparison with the final hybrid multilayer system (*vide infra* section 5 on page 44).

FT-IR spectra were obtained for both hexacyanometallate intercalates prepared as KBr diluted pellets (view Figure 2.8) provided with useful analytical and structural information. On the one hand, they allowed a quick identification of the anionic species present in our compounds, namely nitrate, carbonate and hexacyanometallate ions. By this means slight carbonate impurities ($\nu_3 \sim 1350\ cm^{-1}$) are unveiled for some intercalates, in agreement with works presented by Rives *et al.*[39] This is consistent with the XRPD observations and the AEC deviations from quantitative exchanges. However, it is important to stress that diffraction patterns did not show any evidence of carbonate-containing LDH phase, concluding that carbonate is simply adsorbed on the external surface of the crystallites or in a non-ordered manner in the inter-lamellar space. Now looking at the cyano triple bond stretching region (2000 - 2200 cm^{-1}) one may quickly note the presence of our cyano complexes (2050 - 2100 cm^{-1}). On the other hand, peak shifts or fine structure alterations compared to pure LDH or metal salts spectra is indicative of chemical modifications due to host-guest interactions. In this way one may appreciate how the LDH band structure remained unchanged in comparison to that of the original nitrate clay: all spectra show a very broad band between 3600 - 3300 cm^{-1} due to the stretching ν_{OH} mode of hydroxyl brucite-like layer groups, a bending δ_{H_2O} medium-intensity peak at 1620 cm^{-1} and lattice vibration bands below 1000 cm^{-1}. Cyanide stretching mode ν[C-N] peaks for both precursors presented only very slight shifts with respect to the potassium hexacyanochromate(III) salt: 2129 cm^{-1}.[43] However, they exhibited a remarkable CN peak splitting. In this way

43 Kettle, S. F. A.; Aschero, G. L.; Diana, E.; Rossetti, R.; Stanghellini, P. L. *Inorg. Chem.* **2006,** *45 (13),* 4928-4937.

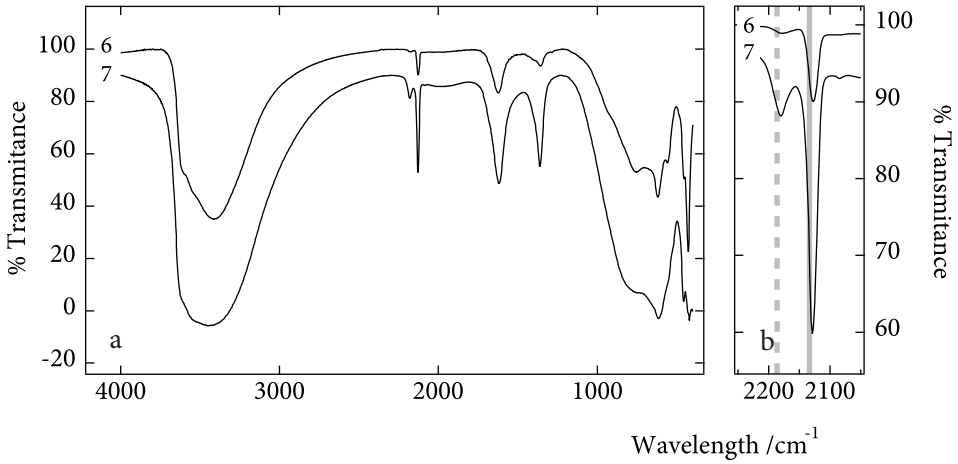

Figure 2.8 IR spectra of LDH-$[Cr^{III}(CN)_6]$ intercalates: ZnAl-$Cr(CN)_6$ (**6**) and CoAl-$Cr(CN)_6$ (**7**). The spectrum of compound **7** has been offset by -10% for clarity. (**b**) show the $\nu_{C\text{-}N}$ region of the full-range spectra at (**a**). Positions of the $\nu_{C\text{-}N}{}^{1}$ and the $\nu_{C\text{-}N}{}^{2}$ have been highlighted with a continuous and a dashed line respectively.

a ~ 50 cm^{-1} gap doublet was accounted for both **6** and **7** (view Table 2.5). This could indicate host-guest chemical interactions and a preferential orientation of the metallic complex in the LDH interlamellar space leading to the differentiation of the initially octahedral-symmetry and undistinguishable cyanide ligands.[44] The LDH host created an anisotropic moiety so that the brucite-like layers interact preferentially (via hydrogen bonding for instance) with some of the cyanide groups that surround the Cr^{3+} ion. This suggests some kind of differentiation of the cyanide ligands in two groups: apical and equatorial ones, where apical ones are expected to be closer to the hydroxide sheet and equatorial ones further away (review Figure 2.7). This hypothetical model is in good agreement with the basal spacing calculated from XRPD with the O_h C_4 axis perpendicular to the basal planes. In fact, this orientation was preferred in search of systems that could restrict the growth dimensionality of our cyanide based polymers. Furthermore, it is also coherent at a qualitative level with the difference in peak intensity between both vibration modes given the ratio 2 apical CN^- : 4 ecuatorial CN^-.

44 Carpani, I.; Berrettoni, M.; Giorgetti, M.; Tonelli, D. *J. Phys. Chem. B* **2006,** *110,* 7265-7269.

In that which concerns the thermal decomposition of hexacyanometallate LDH intercalates, a detailed study has previously been reported by Frost *et al.*[45] TG profiles were very similar for precursors **6** and **7** and are very well described following Frost's detailed conclusions. In the low temperature region, up to around 220 - 260ºC, DTA curves show two main broad exothermic bands (centred at around 50ºC and 200ºC) that correspond to the thermal desorption of surface and intercalated water molecules. Note that whilst for **6** the main water loss band is the one corresponding to the intercalated water molecules, in compound **7** the water molecules appear to be much more superficial as suggested by the stronger band at approximately 50ºC. Overall, the adsorbed water loss until ~ 270 ºC accounted for roughly 20% of the sample weight. Following, the CN^- units are lost in two steps at around 260ºC (some dehydroxilation also takes part at this stage) and 400°C, being the latter the dominant feature of the DTA curve. Finally, according to that reported by Frost *et al.*, the constitutional water loss is completed in four main distinct steps evolving water vapour at 303, 352, 404 and 409°C. However, the prominence of other major weight loss processes together with the big peak overlap completely masks these hydrotalcite dehydroxilation features in our curves. TG/DTA curves obtained for a selection of precursors **6** and **7** in air in the 25-800ºC range are represented in Figure 2.9.

Compound	Vibration modes / cm^{-1}		
	$\nu_{C\text{-}N}{}^{1}$	$\nu_{C\text{-}N}{}^{2}$	$\Delta\nu_{C\text{-}N}$
6	2127.7	2177.2	49.8
7	2129.1	2180.0	50.9

Table 2.5 $\nu_{C\text{-}N}$ IR stretching modes in LDH-hexacyanometallate precursor intercalates.

Bringing the chemical composition EPMA data and the qualitative identification of species via IR together with TG data one may estimate the empirical formula of the precursor compounds **6** and **7**. This was done as previously described for pure LDHs. From EPMA metallic ratios, a normalization

45 Frost R. L.; Musumeci, A. W.; Theo Kloprogge, J.; Weier, M. L.; Adebajo, M. O.; Martens W. *J. Therm. Anal. Cal.* **2006,** *86 (1),* 205–209.

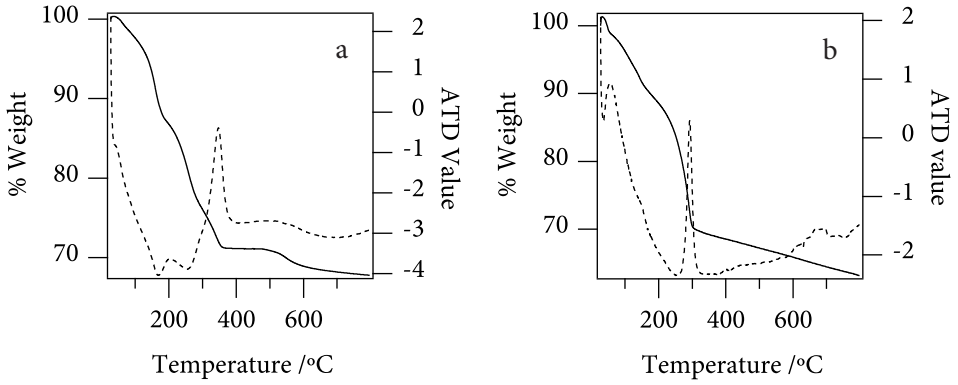

Figure 2.9 TG (*continuous*) and DTA (*dashed*) curves of LDH-hexacyanocrhomate precursor intercalates **6** (**a**) and **7** (**b**) in the 25 - 800 ºC range and in an air.

is performed to fit the LDH part: $[M^{II}_{3-3x}M'^{III}_{3x}(OH)_6]^{3x+}$. The hexacyanochromate empirical coefficient is calculated proportionally, taking the EPMA ratio of the intercalated metal with respect to one of the LDH metals. Next, the excess charge is compensated until electroneutrality by the introduction of a non-stoichiometric quantity of anions according the species identified by FT-IR. Finally to complete the empirical formula, the sample weight loss up until ~ 250 ºC extracted from TG data indicates the hydration water molecules per unit formula. The resulting empirical formulas are listed in Table 2.6.

Compound	Water content		*Empirical formula*
	Wt. loss / %	n H_2O	
6	19.4	3.4	$[Zn_{1.99}Al_{1.01}(OH)_6][Cr(CN)_6]_{0.24}(CO_3)_{0.15}\bullet 3.4(H_2O)$
7	15.9	3.2	$[Co_{1.83}Al_{1.16}(OH)_6][Cr(CN)_6]_{0.23}(CO_3)_{0.23}\bullet 3.2(H_2O)$

Table 2.6 Empirical formulas estimated for LDH-hexcyanochromate precursor materials **6** and **7**.

In general, the estimated empirical formulas were in accordance with that expected for a pure LHD-hexacyanometallate intercalate, though intercalation of variable ratios of atmospheric CO_2 adsorbed carbonate was unavoidable.

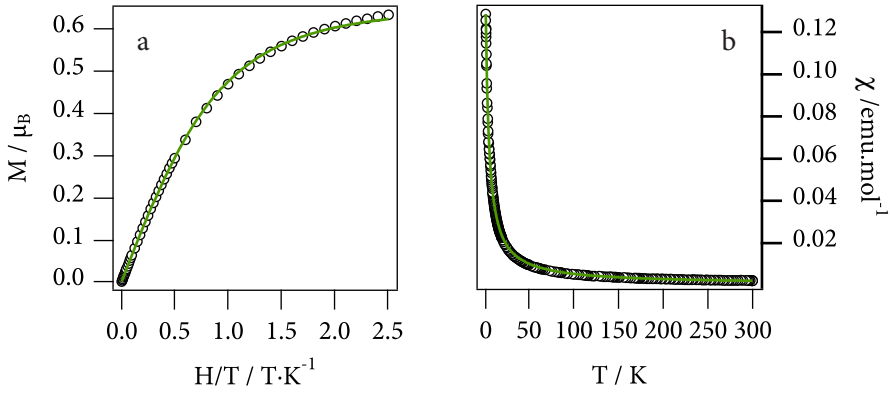

Figure 2.10 a. Thermal dependence of the magnetic susceptibility of **6** in the 2-300 K interval. The line shows the fit to the Curie-Weiss law (Curie constant: C = 0.50 ± 0.002 emu·K·mol^{-1}, Weiss constant: θ = -1.88 ± 0.02 K).**b**. Field dependence of the isothermal magnetization of **6** measured at 2 K. Red line shows the fit of the experimental data to the Brillouin function with S = 1.5 (g = 1.792 ± 0.002).

b. Magnetic properties

The magnetic measurements of compound **6** were in good agreement with those expected for discrete isolated hexacyanochromate complexes diluted in the diamagnetic ZnAl LDH matrix. The material exhibited paramagnetic behaviour as confirmed by the isothermal field dependence of the magnetization (M), which could be perfectly fitted according to a Brillouin function with S = ³⁄₂ (being S the effective spin value; see green line in Figure 2.10a). The estimated g = 1.8 value, slightly deviates from that expected for an isotropic Cr^{3+} ion, probably as a result of the presence of dipolar interactions in the LDH interlayer space. The thermal variation of the DC susceptibility (χ) is also consistent with the paramagnetism observed in the magnetization curve following an exponential regime in the whole temperature range. The profile defined by the experimental data could be fitted to the Curie-Weiss law as shown in Figure 2.10b with a Curie constant, C = 0.50 emu·mol^{-1}, in excellent agreement with the value calculated for the chromium content derived from the metallic analysis, 0.45 emu·mol^{-1}.

In the same line, an analogous behaviour could be observed for compound **7** in the high temperature regime. In this way the experimental data in the

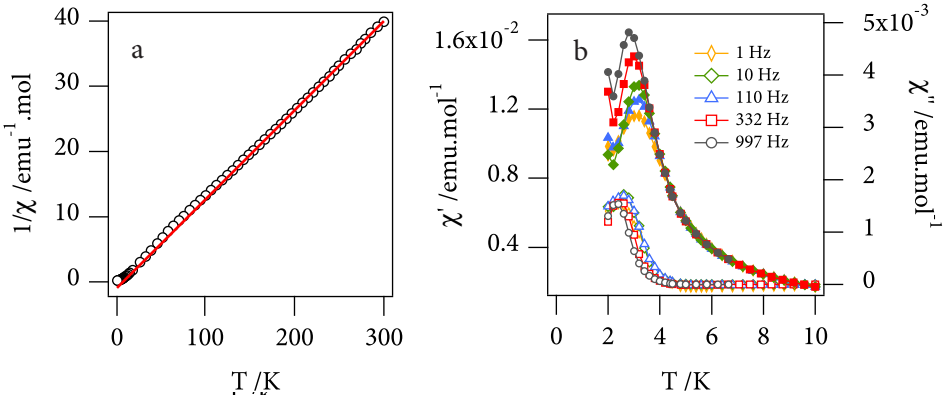

Figure 2.11 a. Thermal dependence of the inverse of the magnetic susceptibility of **7** in the 2 - 300 K interval. The line shows the fit to the Curie-Weiss law (C = 7.28 emu·K·mol^{-1}, θ = 8.68 K, R^2 = 0.9998).**b**. Thermal variation of the AC susceptibility of **7** at different frecuencies.

150 - 300 K range was well described by the Curie-Weiss law as illustrated by the high-temperature fit of the inverse of χ (see Figure 2.11a). The value of C = 7.28 emu·K·mol^{-1} is only slightly smaller than the expected spin-only value of 7.73 emu·K·mol^{-1} for the combination of octahedral Co^{2+}, d^7 (μ_{eff} = 3.87 μ_B, S = ⅔) and octahedral Cr^{3+}, d^7 (μ_{eff} = 3.87 μ_B, *S* = ⅔) in the stoiochimetric ratio calculated from EPMA, indicating that a small orbital contribution in line with the values reported in the literature for other CoAl systems.[36] Additionally, this time the material exhibited spontaneous magnetization below 5 K too. The long range ordering phenomenon was reflected by the low temperature deviation of 1/χ and more clearly by the thermal variation of the AC susceptibility. In this way, the onset temperature of the out-of-phase component of the AC susceptibility (χ") permitted estimating a T_C value of around 4.5 K in good accordance with that previously reported for pristine CoAl LDH systems.[36]

5 Hybrid LDH-bimetallic cyanide materials

The final step in order to assemble the bimetallic cyanide network in between the LDH planes was to expose the precursor material previously described to a freshly-prepared concentrated aqueous solution of a divalent metal salt ($M^{II}A_2$, where M^{II} is the divalent metal and A the counteranion, see Equation 2.2). The

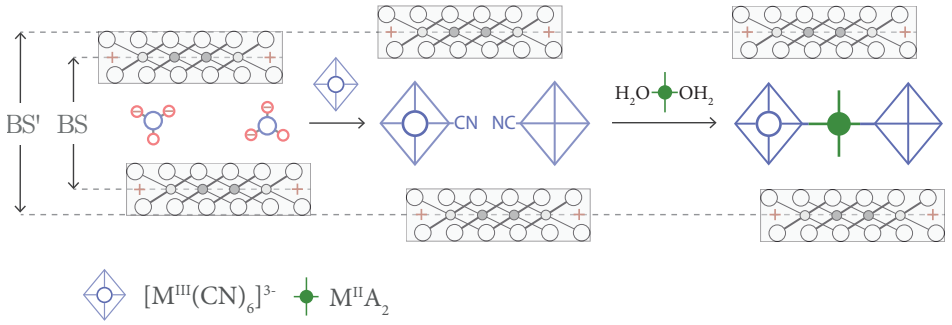

Figure 2.12 Schematic representation of the two-step synthetic process starting with the NO_3^--$[M^{III}(CN)_6]^-$ and culminating with the linkage of the hexacyanometallate units by the divalent metal. The gallery height expansion (BS to BS') is highlighted by the dashed lines (*not to scale*).

divalent metal was expected to diffuse into the LDH galleries and react with the hexcyanometallate entities, linking them together in an extended coordination polymer as illustrate by the scheme in Figure 2.12.

$$[[M^{II}{}_2M'^{III}(OH)_6][M''^{III}(CN)_6]_{\frac{1}{m}} \cdot nH_2O + \frac{1}{m}M''^{II}A_2 \xrightarrow{H_2O,Ar} [M^{II}{}_2M'^{III}(OH)_6][M''^{II}M''^{III}(CN)_6]_{\frac{1}{m}}A_2 \cdot kH_2O$$

Equation 2.2 Generic polymerization reaction of a bimetallic cyanide within an LDH host.

The synthetic aspects of the polymerisation reaction were initially explored with a diamagnetic LDH. This would provide with useful experience for the optimization of the reaction conditions. In addition, it would allow for the study of the magnetism inherent to the bimetallic cyanide multilayer system. Upon completing the magnetic study with the ZnAl system (**6**), the analogous reaction was tested starting from the magnetic-host precursor **7**.

As a general synthetic remark it is important to re-emphasize the importance of keeping a CO_2-free atmosphere whenever the LDH materials were being handled in suspension in order to avoid the contamination of samples with the LDH-CO_3 phase. In this way, the general manipulation of the reaction media was done inside a glove box. Once dry, CO_2 diffusion into the layered material was considered negligible.

a

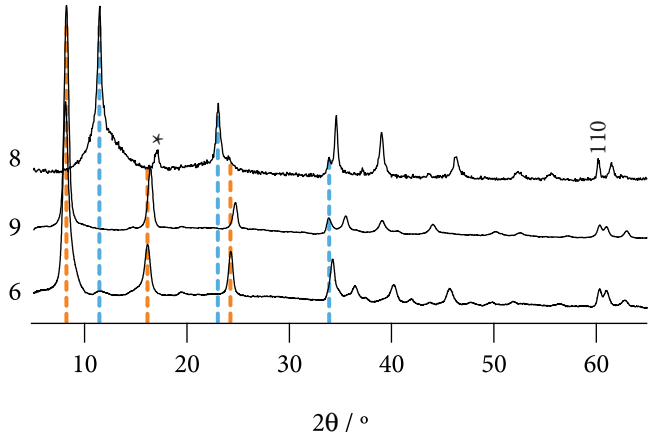

b

Compound	(*hkl*) 2θ / °				Cell parameters / Å		
	(003)	(006)	(009)	(110)	*a*	*c*	BS
8	11.55	23.25	33.90	60.30	3.06	23.25	7.75
9	8.03	15.90	23.87	60.33	3.10	33.30	11.10

Figure 2.13 XRPD studies of hybrid LDH-bimetallic cyanide samples synthesize form chloride (**8**) and nitrate (**9**) Ni salts. **a**. Spectra highlighting the two types of (00*l*) refelction families: expanded (*orange*) and contracted (*blue*). The pattern of precursor material **6** has also been included for reference. The asterisk marks an non-indexable peak most probably due to a 3-D PBA impurity. **b**. Table listing the crystallographic unit cell parameters extracted from the patterns at (**a**) assuming rombohedral 3R symmetry.

5.1 Synthesis and magnetism of a 2-D cyanide network

As stated earlier, the polymerisation of the Cr^{3+}-Ni^{2+} cyanide within the ZnAl host would provide with the best possible scenario to study the magnetism of the hypothetical 2-D ferromagnetic multilayer.

Firstly, the optimisation of the reaction conditions was addressed. In this way, standard ion exchange conditions such as the ones employed for the synthesis of compound **6** were initially tested: room temperature stirring of a suspension of

precursor material **6** in a concentrated (~ 2×10^{-2} M) aqueous solution of $NiCl_2$ for 48 hrs. The preliminary tests revealed almost no Ni intake. However, the use of a more concentrated divalent metal solution (~ 0.2 M) in swelling solvent mixtures at the same temperature and during the same reaction time sufficed to even exceed the expected $1Cr^{3+}$: 1 Ni^{2+} ratio as seen by SEM-EPMA: Ni/Cr = 1.67.[46] The slurry was then filtered off, thoroughly washed with degassed milli-Q water and dried *in vacuo* to recover a greenish powder (**8**).

Even more surprisingly, structural data of **8** extracted from XRPD experiments depicted a smaller gallery height (BS ~ 7.8 Å) in comparison with the precursor material. This BS value was totally unexpected and far too narrow for the bimetallic cyanide network to fit. Oppositely, if the same procedure was carried out but employing the nitrate Ni salt ($Ni(NO_3)_2{\cdot}6H_2O$) instead of the chloride one a totally different compound **9**, from a structural point of view, was obtained. Indeed a value of BS = 11.1 Å could now be estimated from the position of the (00*l*) out-of-plane Bragg peaks. Figure 2.13 shows a comparison of the XRPD data obtained for precursor material **6** and hybrid samples of **8** and **9**. In addition, the Ni/Cr = 1.15 ratio calculated from EPMA spectra for **9** this time suggested the formation of the 1 : 1 coordination polymer. This was indicative of the formation of the cyanide-linked Cr^{3+}-CN-Ni^{2+} network in good agreement with that expected for the ideal value of the Ni/Cr = 1 coordination polymer. Thus the anion appears to play an active role in the polymerisation reaction, yet the actual mechanism in which it is involved remains unclear. It is suggested that the Cl^- anion could have an effect in the coordination sphere of the divalent metal given its greater coordination in comparison to the NO_3^- molecule.

In this context, XPS experiments were conducted in order to ascertain if the coordination environments of the Ni centres in samples **8** and **9** were distinguishable. Unfortunately, no apparent differences could be detected probably due to lack of sensitivity to the coordination sphere of the 2p and 3p electronic levels probed by the technique . Further experiments still need to be performed in order to unearth the role of the anion.

---

46 Swelling agent: fluid used to swell a gel, network or solid. (From *IUPAC. Compendium of Chemical Terminology, 2nd ed. (the "Gold Book")*. Compiled by A. D. McNaught and A. Wilkinson. Blackwell Scientific Publications, Oxford, **1997**)

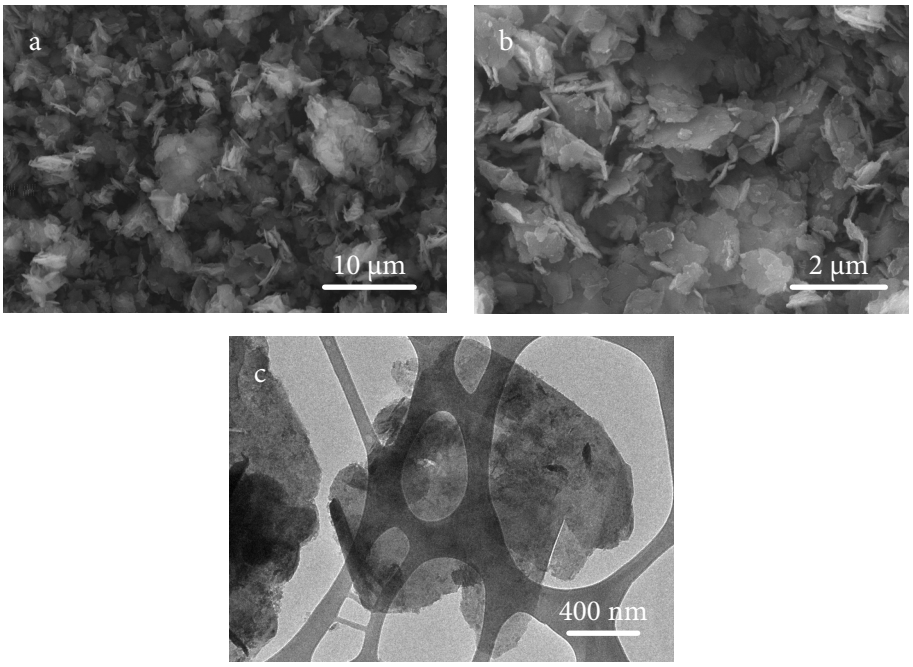

Figure 2.14 Electron microscopy images of compound **9**: different magnification SEM images of the crystallites (**a** and **b**); HR-TEM image of a high aspect ratio crystallite (**c**).

Meanwhile, the Ni^{2+} nitrate salt proved as an adequate starting material for controlling the growth of the bimetallic cyanide in between LDH layers. A closer inspection at the powder samples of **9** via SEM permitted to observe how they were very homogeneous and composed exclusively of approximately hexagonal crystallites, discarding the formation of any co-precipitated contaminant phase, namely the bulk Ni-Cr 3-D PBA (see Figure 2.14a and b). Furthermore, samples prepared by drop-casting a suspension of compound **9** in ethanol on a C coated Cu grid were analysed under the high-resolution transmission electron microscopy (HR-TEM). The images obtained from this technique further confirmed the only presence of high-aspect ratio platelets with characteristic LDH morphologies thus reinforcing the hypothesis of the isolation of a pure hybrid phase. An representative example of the crystallites found in samples of compound **9** as seen by HR-TEM is shown in Figure 2.14c.

Additional chemical characterization techniques provided with extra information regarding the exact composition of hybrid compound **9**. For instance, FT-IR experiments were conducted in an attempt to check the presence of residual nitrate and carbonate anions and monitor the nature of the intercalated moieties. In fact, the presence of NO_3^- anions is remarkable (strong band at 1384.7 cm^{-1}), the latter representing the main source of contamination in the synthetic route. Furthermore, it was observed how the stretching mode ν[C-N] peaks remained almost unaltered with respect to the precursor material **6**: $\nu_{C\text{-}N}{}^{1}$ = 2168.4 cm^{-1}, $\nu_{C\text{-}N}{}^{1}$ = 2126.3 cm^{-1}, $\Delta\nu_{C\text{-}N}$ = 42.1 cm^{-1}. The peaks coming from the LDH host were also coincident to those observed for the precursor LDH materials. Finally, TG data permitted estimating a 15.3% of water content per unit formula. The combination of these findings permitted estimating the following empirical fomrula: $[Zn_{1.95}Al_{1.05}(OH)_6][(Cr(CN)_6)_{0.27}Ni_{0.31}](NO_3)_{0.86}\bullet 2.78(H_2O)$.

Once the phase purity was confirmed, the magnetic properties measured for compound **9** could be entirely attributed to the bi-dimensional cyanide-based magnetic lattice. For this purpose, the thermal variation of the magnetic susceptibility of **9** was recorded in the 2 - 300 K range under an external applied field of 1000 G. Figure 2.15a shows how upon cooling, the χT product remains almost constant from its room temperature value of 0.85 emu·K·mol^{-1} (expected value: 0.82 emu·K·mol^{-1}) down to 100 K. Then, it starts to increase abruptly, confirming the presence of ferromagnetic Cr^{3+}-Ni^{2+} coupling through the cyanide bridge, as expected from the strict orthogonality between the magnetic orbitals t_{2g} and e_g in the cyanide square lattice. The positive value of θ = 71.4 K extracted from fitting the inverse of the magnetic susceptibility in the high temperature region to the Curie-Weiss law additionally supports this point (see Figure 2.15b). The isothermal field dependence of the magnetization measured at 2 K shows the typical profile for a soft ferromagnet (view Figure 2.15d and e), with a fast increase of the magnetization up to 0.15 T. Saturation is only reached at higher fields with a maximum value of M_S =1.1 μ_B at 5 T in accordance to the expected value M_S =1.3 μ_B. A small coercive field of 0.14 kG could also be estimated from hysteresis loops measured at 2 K.

The presence of long-range magnetic ordering in 9 was confirmed by dynamic magnetic measurements, explored in the 1 - 10000 Hz interval with an external

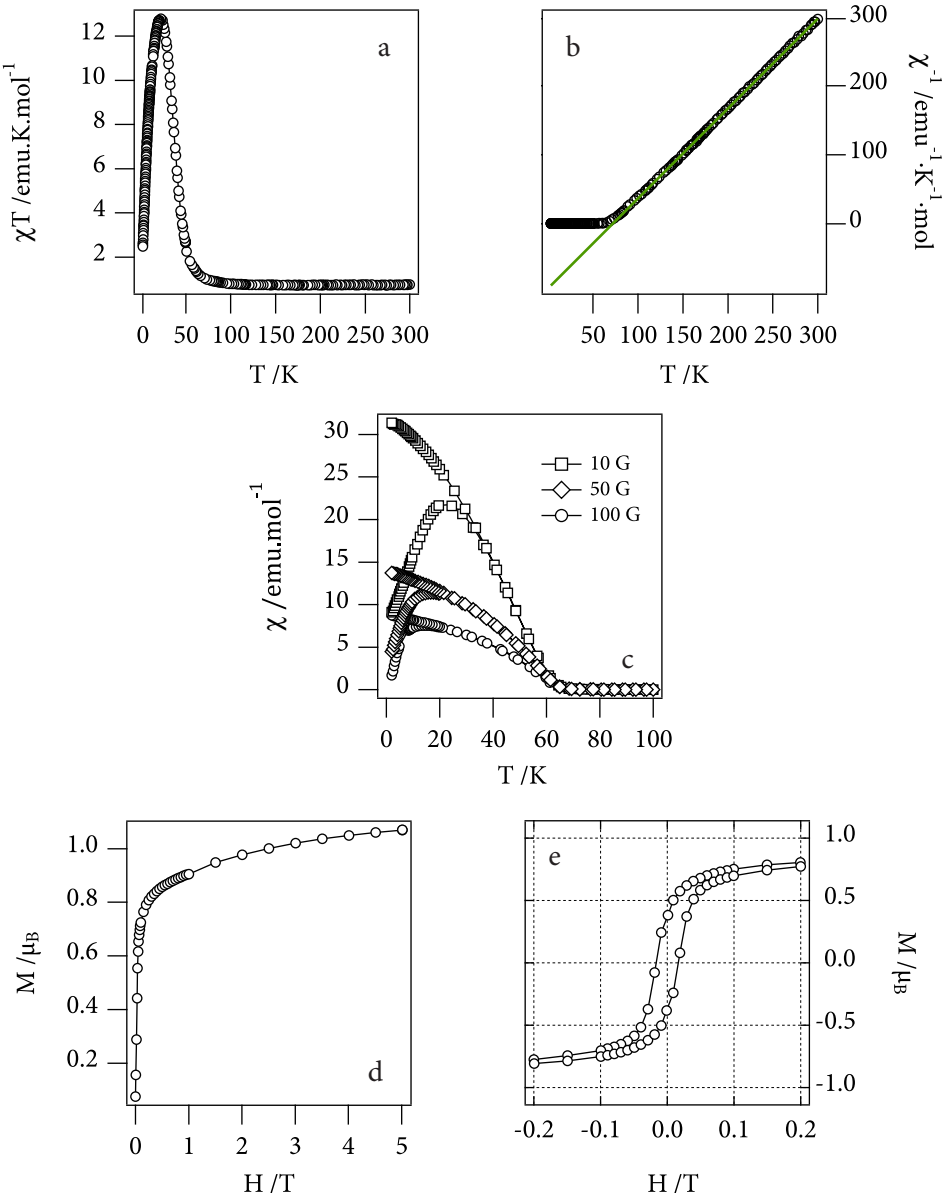

Figure 2.15 DC magnetic characterization of **9**. **a**. Thermal variation of the χT product in the 2 - 300 K range under an external applied field of 1000 G. **b**. Thermal variation of the inverse of the molar magnetic susceptibility. The line shows the fit to the Curie-Weiss law (C = 0.77 emu·K·mol^{-1}; θ = 71.4 K). **c**. Field-cooled zero-field-cooled plots under varying external applied fields. **d**. Isothermal field dependence of the magnetization measured at 2 K. **e**. Low-field region of the hysteresis loop of **9** measured at 2 K.

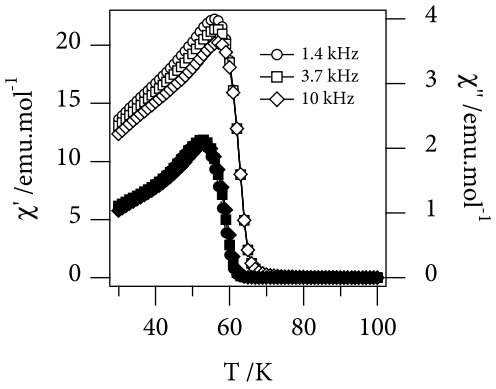

Figure 2.16 Thermal variation of the AC susceptibility under an external applied field of 3.95 G. The hollow markers represent the in-phase component and the filled ones the out-of-phase one. The line are just a guide to the eye.

applied field of 3.95 G. Both, the in-phase (χ') and out-of-phase (χ") components of the AC susceptibility define a peak below 70 K (see Figure 2.16). Minor frequency-dependence of the maxima position is observed for χ". This feature is probably related to the dynamics of the domain walls in the ordered ferromagnetic state, as previously observed for other bimetallic cyanide-bridged bi-dimensional ferromagnets.[47] Attending to the onset temperature of χ", this is approximately 65 K. This value agrees with the divergence point of the field-cooled and the zero-field-cooled thermal variation of the susceptibility shown in Figure 2.15c. The estimated T_C is approximately four-sixths of that reported for the classical 3-D Ni^{II}-Cr^{III} PBA (T_C = 90 K).[42] Given that in a general approximation, T_C is proportional to the number of effective magnetic neighbours (*N*),[48] this decrease seems to indicate that whilst in the 3-D PBA case each Cr centre is surrounded by six Ni atoms (*N* = 6), only four effective magnetic interactions are present in **9** (*N* = 4). This is the final proof that the LDH host has played an effective templating role in **9**, making the $[Cr(CN)_6]^{3-}$ and Ni^{2+} centres to interconnect in the two dimensions.

47 Coronado, E.; Gómez-García, C. J.; Nuez, A.; Romero, F. M.; Waerenborgh, J. C. *Chem. Mater.* **2006,** *18,* 2670-2681.

48 a) Verdaguer, M.; Bleuzen, A.; Marvaud, V.; Vaissermann, J.; Seuleiman, M.; Desplanches, C.; Scuiller, A.; Train, C.; Garde, R.; Gelly, G.; Lomenech, C.; Rosenman, I.; Veillet, P.; Cartier, C.; Villain, F. *Coord.. Chem. Rev.* **1999,** *190,* 1023-1047. (b) Néel, L. *Ann. Phys. Paris,* **1948,** *3,* 137-198.

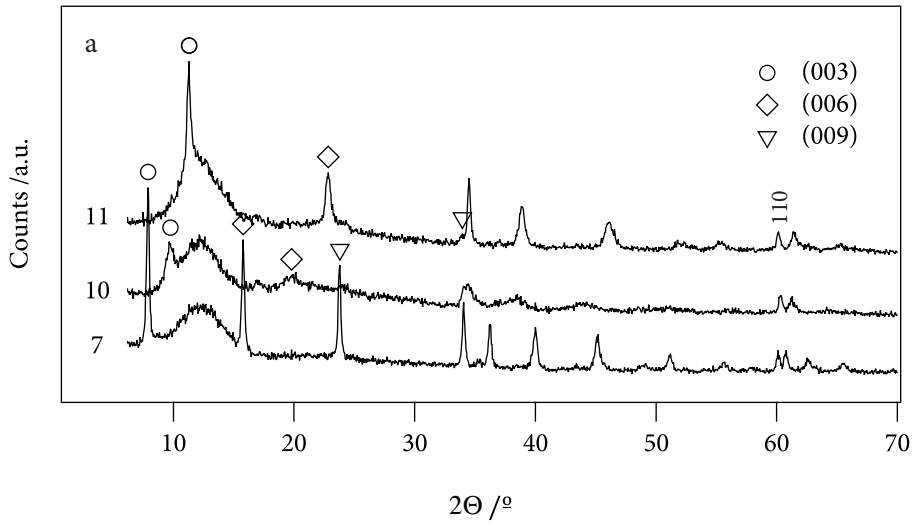

b

Compound	(*hkl*) 2θ / º				Cell parameters / Å		
	(003)	(006)	(009)	(110)	*a*	*c*	BS
7	7.90	15.80	23.80	60.15	1.54	33.62	11.21
10	9.75	19.80	-	60.35	1.53	29.25	9.75
11	11.30	22.85	33.95	60.10	1.54	23.53	7.84

Figure 2.17 a. XRPD patterns of precursor compound **7** and hybrid samples **10** and **11**. The (00*l*) have been taged with different markers: circles for (003), rhombi for (006) and triangles for (009). **b**. Crystallographic unit cell parameters extracted from the patterns at (**a**).

5.2 Towards magnetic multilayers

Preliminary tests were conducted in order to try to reproduce the growth of a bi-dimensional bimetallic cyanide network but within the CoAl magnetic LDH host. In this line, precursor material **7** was reacted with concentrated aqueous solutions of $Ni(NO_3)_2 \cdot 6H_2O$ following the procedure optimised for the polymerisation inside the ZnAl analogue. In this way compound **10** was isolated and analysed.

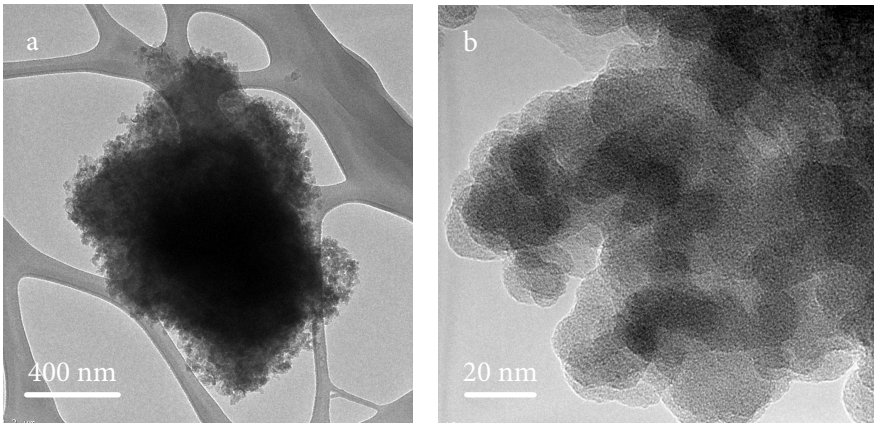

Figure 2.18 HR-TEM images of selected particles of **10** on a C-coated Cu grid. The sample was prepared by dispersing the powder in EtOH via ultrasound treatment and by casting a drop on the grid.

EPMA data of **10** depicted a quantitative Ni uptake in so far a metallic ratio value of Cr/Ni = 1.15 could be estimated. Unfortunately, the XRPD pattern of the hybrid sample (see Figure 2.17) portrayed an anomalous gallery height and very poor crystallinity. In this case, a value of BS = 9.75 Å could be calculated from the position of the (00*l*) reflections. This was indicative of the collapse of the original structure pillared by the hexacyanochromate units. As a matter of fact the gallery height was surprisingly similar to that of pristine CoAl-NO_3 LDH.[3] FT-IR studies exhibit a very intense $\nu_3[NO_3]$ = 1384.7 cm^{-1} peak, revealing the presence of vast amounts of such anion. Finally, HR-TEM studies confirmed that the morphology of the particles in powder samples of **10** was not made of homogenous platelets as in **9**. Instead, the exhaustive exploration of the crystallites in **10** revealed the presence of high-aspect ratio flakes covered in a high density of spherical particles. Figure 2.18 shows an example of these composite particles. Therefore, there are strong evidences of the collapse of the LDH like structure and the co-precipitation of 3-D PBA nano-particles along with the LDH layers. In this line, previous studies have already reported the acceleration of the exfoliation and subsequent nanocomposite formation of an LDH host upon the interlamellar polymerisation of an organic extended structure.[15c, 49] Unfortunately, the weakness

49 Lee, W. D.; Im, S. S. *J. Polym. Sci. Part B: Polym. Phys.* **2007,** *45,* 28.

of the diffraction signal impeded confirming the presence of the PBA crystalline phase.

The segregation of the LDH and the PBA components is confirmed by carrying out a simple ion exchange in a concentrated NaCl aqueous solution. In this way, crystallinity is recovered in a layered structure with the characteristic BS of a Cl^- LDH (reported BS values for Cl^- LDHs are approximately 7.86 Å).[3] Figure 2.17a illustrates the whole process as seen by XRPD, demonstrating how the divalent metal had scavenged the hexacyanochromate out of the CoAl host, the latter behaving like a completely independent LDH system.

In any case, the magnetic properties of the composite material were probed by measuring the thermal variation of the susceptibility in 2 - 300 K range under an external applied field of 1000 G (see Figure 2.19a). The thermal dependence of the molar χT product was analogous to that of compound **10**, remaining almost constant from its room temperature value of 7.19 emu·K·mol^{-1} (expected value: 7.93 emu·mol^{-1}) down to 100 K and then abruptly increasing probably due to the spontaneous magnetization of the Ni-Cr PBA part of the material up to a value of approximately 112 emu·K·mol^{-1}. However, the big increase in χT completely obscures the magnetic ordering of the LDH component in the DC measurements. On the other hand, the spontaneous magnetization of the CoAl counterpart is reflected in the thermal dependence of the AC susceptibility shown in Figure 2.19b. In this way, a T_C of approximately 4.7 K could be estimated from the turning point described by the curve at the lower temperature range. No regarding the PBA component, a T_C of around 58 K could be inferred from the onset of the out-of-phase component of the AC susceptibilty. This ties in correctly with the structural data, indicating the presence of nanoparticles of another well-known PBA system $Ni_3[Cr(CN)_6]_2 \cdot 9H_2O$ as is suggested by its comparable T_C = 60 K.[50, 51] Finally, a hysteresis loop characteristic of a soft magnet with an effective small coercive field of just 20 G could be observed at 10 K. However, the coercivity

50 a) Entley, W. R.; Treadway, C. R.; Girolami, G. S. *Mol. Cryst. Liq. Crys. A* **1995,** *273,* 153–166. (b) Ruiz, E.; Rodríguez-Fortea, A.; Alvarez, S.; Verdaguer, M. *Chem. Eur. J.* **2005,** *11,* 2135–2144.

51 It is important to emphasize that this PBA is different from the $A[NiCr(CN)_6]$ (A = alkali metal ion, namely Cs^+ with $T_C \sim 90$ K) , both regarding the stoichiometry and the atomic structure. In this case, the coordination polymer exhibits a Ni: Cr ratio of 3 : 2 ratio and the structure displays vacant $[Cr(CN)_6]^{3-}$ positions in the cubic lattice avoiding the occlusion of alkali cations in the structure. The presence of the latter in compound 9 was discarded by the observation of a remarkably different stoichiometry and the homogeneity in the crystallite morphologies as seen by SEM and HR-TEM.

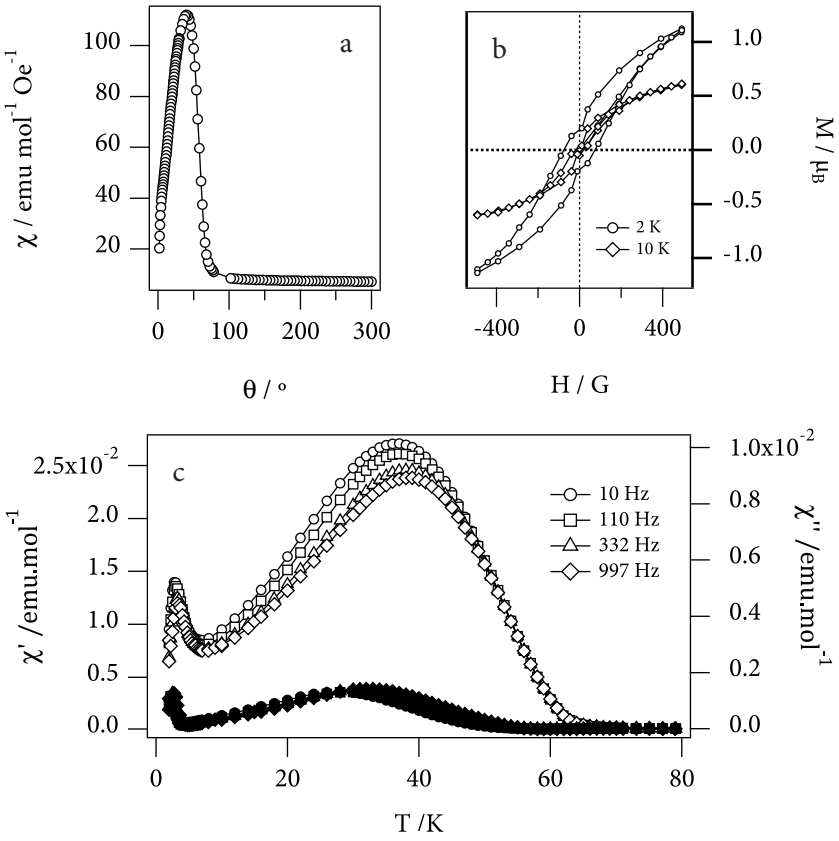

Figure 2.19 a. Thermal variation of the χT product of **10** in the 2 - 300 K range under an external applied field of 1000 G. **b**. Low-field region of the hysteresis loop of **10** measured at 2 K (black) and 10 K (red). **c**. Thermal variation of the AC susceptibility under an external applied field of 3.95 G. The hollow markers represent the in-phase component and the filled ones the out-of-phase one. The line are just a guide to the eye.

seemed to be enhanced by the magnetization of the LDH component since on cooling from 10 to 2 K the coercive field had risen to around 100 G. Still, more experiment need to be conducted to verify that the effect is due to the interaction between components and not just a mere temperature effect.

Despite the fact that the current conditions lead to the collapse of the layered structure, it has been demonstrated by the diamagnetic case study that the growth of the Cr-Ni cyanide may be indeed restricted by the host LDH. The case here

described constitutes the first attempt to isolate a magnetic multilayer and further efforts will be devoted to modify the reaction conditions to try and adapt the reaction to the idiosyncrasy of the CoAl system.

6 Conclusions

The design and synthesis of layered magnetic structures from the perspective of the hybrid solid-state/molecule-based approach is investigated in this chapter.

In particular, the use cationic LDH hosts as templating agents in the formation of anionic 2-D cyanide-based multilayers is addressed. In this context, proof is provided of the viability of a bimetallic cyanide molecular ferromagnet to be grown by the directed assembly of its molecular components in the confined interlamellar space offered by the LDH. This prevented the formation of the thermodynamically favoured 3-D system. However, the starting materials (the anion effect) and the synthetic conditions needed to be finely adjusted in order to avoid the unruly precipitation of the 3-D PBA.

The isolation of a magnetic multilayer made out of Cr-Ni cyanide sheets interleaved with LDH layers constitutes the first example of intercalation of a molecule-based magnet into a solid-state host. It is worthwhile mentioning that so far the methods employed for reducing the dimensionality of bimetallic cyanides were based on the use of capping ligands, or on the growth of monolayers onto substrates by means of the LB technique.[28] In comparison with these methods, the approach herein described is solely based in inorganic building-blocks. Thus, it provides an efficient way to design more complex inorganic/inorganic magnetic hybrids in which the physical properties of the molecule-based magnets, including the photomagnetism exhibited by the PBAs, are expected to be combined, or even coupled to those introduced by the employment of magnetic LDHs.

Unfortunately, preliminary attempts to synthesize a magnetic multilayer with two different magnetic sub-lattices have proved unfruitful. However, the work here presented is just the beginning and further investigations will allow for an improved control of the technique. As a matter of fact, some attention has already been drawn on the topic as illustrated by very similar studies recently reported.[52]

52 Layrac, G.; Tichit, D.; Larionova, J.; Guari, Y.; Guérin, C. *J. Phys. Chem. C* **2011,** *115,* 3263–3271.

7 Experimental procedures and recipes

Synthesis of starting LDHs

Synthesis of ZnAl-NO_3 LDH [1]: A constant pH co-precipitation method was herein employed, only very slightly modifying the method previously reported by Miyata.[34] It consists in a preparation of the double hydroxide by reaction of its respective nitrate salts in a 2 : 1 molar ratio. The whole reaction was carried in an excess of nitrate, so that the nitrate was the only anion present at the interlaminar space. Two solutions: a) 1 M solution of Zn^{2+} and Al^{3+} and b) 1M solution of NaOH and $NaNO_3$ were added dropwise at a controlled rate while the mixture was mechanically stirred at room temperature, keeping a constant pH of 8. Once the mixing process was finished, the resulting slurry was kept 1 hr more at room temperature and later on heated at 80 ºC at atmospheric pressure and with continuous stirring. The white gel was aged over 5 days at that temperature whilst stirring. Finally it was filtered, washed thoroughly with distilled decarbonated water to attain nitrate excess elimination, and vacuum-dried at room temperature. The process yielded white fine powder **1**.

IR (KBr pellet) ν/cm^{-1}: 3530.1 (br, st); 3447.7 (br, st); 1627.0 (br); 1383.9 (sh, st); 832.4 (w); 665.6 (br, m); 613.8 (m); 555.3 (w); 426.4 (sh, m).

Metallic ratio estimated from EPMA (calculated for $H_6N_1O_9Zn_2Al_1$): Found Zn/Al = 1.84 (2.00).

Water content (TG): 17.6%

Empirical Formula: $[Zn_{1.94}Al_{1.06}(OH)_6](NO_3)_{1.06}\bullet 3.2(H_2O)$; FW = 380.24

Synthesis of MgAl-CO_3 LDH [2]: For the synthesis of this particular LDH one of the procedures developed by Okamoto *et al.* turned out to produce adequate crystal sizes.[53] Typically, 413 mg of $Al(NO_3)_3{\cdot}9H_2O$ (1.1 mmol) and 563mg of $Mg(NO_3)_2{\cdot}6H_2O$ (2.2 mmol) were dissolved in 22 mL of milli-Q. 358 mg of urea (6 mmol) were then added to the solution and the mixture was sealed inside a 40 mL Teflon acid digestion vessel and kept inside an oven or 24 hrs at 138ºC.

53 Okamoto, K.; Iyi, N.; Sasaki, T. *Appl.Clay Sci.* **2007,** *37,* 23–31.

Switching off the electrical oven the vessel was left to cool down (cooling rate: ~0.6 °/min) and its content filtered *in vacuo* under a CO_2-free atmosphere and washed with 1L of degassed milli-Q water. A small volume of methanol was added to favour drying the sample. Overnight drying *in vacuo* over P_2O_5 and NaOH pellets yielded a white fine powdery solid **2**.

IR (KBr pellet) ν/cm^{-1}: 3451.5 (br, st); 1621.8 (br); 1353.4 (sh, st); 1062.0 (w); 947.6 (w); 781.2 (st); 685.3 (m); 552.1 (m); 448.6 (sh, st).

Metallic ratio estimated from EPMA (calculated for $C_1H_{12}O_{15}Mg_4Al_2$): Found Mg/Al = 1.64 (2.00).

Water content (TG): 9.6%

Empirical Formula: $[Zn_{1.86}Al_{1.14}(OH)_6](CO_3)_{0.57}\bullet 1.1(H_2O)$; FW = 232.47

Synthesis of CoAl-CO_3 LDH [3]: Exactly the same procedure as for **2** was followed for the synthesis of the Co-Al LDH. 413 mg of $Al(NO_3)_3{\cdot}9H_2O$ (1.1 mmol) and 640 mg of $Mg(NO_3)_2{\cdot}6H_2O$ (2.2mmol) were dissolved in 22mL of milli-Q. 358 mg of urea (6 mmol) were then added to the solution and the mixture was sealed inside a 40 mL Teflon acid digestion vessel and kept inside an oven or 24 hrs at 138 °C.The method afforded a pastel-pink silky solid **3**.

IR (KBr pellet) ν/cm^{-1}: 3423.3 (br, st); 1620.0 (br); 1355.6 (st); 1062.0 (w); 798.5 (st); 690.1 (w); 614.1 (m); 546.9 (m); 422.2 (sh, st).

Metallic ratio estimated from EPMA (calculated for $C_1H_{12}O_{15}Co_4Al_2$): Found Co/Al = 1.53 (2.00).

Water content (TG): 14.5%

Empirical Formula: $[Zn_{1.81}Al_{1.19}(OH)_6](CO_3)_{0.59}\bullet 2.2(H_2O)$; FW = 316.63

Synthesis of nitrate LDHs via ion exchange methods

Synthesis of MgAl-NO_3 LDH [4]: A suspension of 250mg of **2** (0.1 mmol) in 250 mL of the solution 1M $NaNO_3$ and 10 mM HNO_3 was stirred for 1 or 2 days

under argon atmosphere, then filtered off, washed and dried as described in the previous procedure. This produced a white fine powder **4**.

IR (KBr pellet) ν/cm^{-1}: 3546.0 (br, st); 3447.3 (br, st); 1627.0 (br); 1383.9 (st); 1067.1 (w); 832.4 (w); 680.0 (m); 546.3 (w); 446.8 (sh, st).

Metallic ratio estimated from EPMA (calculated for $H_6N_1O_9Mg_2Al_1$): Found Mg/Al = 1.52 (2.00).

Water content (TG): 9.6%

Empirical Formula: $[Mg_{1.81}Al_{1.19}(OH)_6](NO_3)_{1.19}\bullet 1.34(H_2O)$; FW = 275.97

Synthesis of CoAl-NO_3 LDH [5]: Typically 250 mg of **3** (0.79 mmol) were weighed and placed inside a round-bottomed flask. The CO_2 inside was thoroughly removed using a continuous Ar flow through the system for at least 20 minutes. Separately, 250 mL of a solution 1 M $NaNO_3$ (21.25 g, 0.25 mol) and 10 mM HNO_3 (227 mg of HNO_3 70% conc., 2.5mmol) in degassed milli-Q water was prepared under inert atmosphere. The solution was added over the pink solid and left to stir briskly during 4 days under Ar pressure. Resulting suspension was filtered off under a CO_2-free atmosphere and washed with 1 L of degassed milli-Q water and a few drops of methanol. Drying was performed *in vacuo* over P2O5 and NaOH pellets yielding a pastel-pink glistening solid **5**.

IR (KBr pellet) ν/cm^{-1}: 3518.5 (br, st); 3420.6 (br, st); 2422.7 (w); 2394.1 (w); 1764.8 (w); 1617.7 (br); 1560.4 (w); 1381.9 (st); 1066.3 (w); 825.0 (m); 731.0 (br); 666.0 (br); 612.5 (st); 474.3 (m); 422.1 (sh, st).

Metallic ratio estimated from EPMA (calculated for $H_6N_1O_9Co_2Al_1$): Found Co/Al = 1.32 (2.00).

Water content (TG): 14.6%

Empirical Formula: $[Co_{1.71}Al_{1.29}(OH)_6](NO_3)_{1.29}\bullet 2.2(H_2O)$; FW = 598.90

Synthesis of LDH-hexacyanometallate intercalates

General remark: unless otherwise stated, the manipulation and work-up of suspensions and wet slurries was always performed inside the CO_2-free box.

Synthesis of ZnAl-[$Cr^{III}(CN)_6$] [6]: An aqueous suspension of 250 mg of LDH **1** (0.66 mmol) in 10 mL were mixed with a pale yellow solution of 105 mg of $K_3[Cr(CN)_6]$ (0.32 mmol) in 15 mL of degassed milli-Q water under an Ar overpressure and the resulting white suspension was stirred during 4 days in inert conditions. Following, the yellow suspension was filtered *in vacuo* under a CO_2-free atmosphere, washed with 1 L of degassed milli-Q water and dried in the evacuated antechamber of the CO_2-free box in the presence of P_2O_5 and NaOH pellets. As a result, a white powder (**6**) was recovered. A smell of bitter almonds is quickly perceived upon opening the storing vial.

IR (KBr pellet) ν/cm^{-1}: 3416.1 (br); 2177.2 (vw); 2127.7 (sh, w); 1620.9 (m); 1356.6 (w); 755.5 (br); 618.8 (st); 555.3 (m); 453.1 (m); 426.8 (sh, st).

Metallic ratio estimated from EPMA (calculated for $C_6H_{18}N_6O_{18}Al_3Cr_1Zn_6$): Found Zn/Al = 1.98 (2.00); Cr/Al = 0.25 (0.33).

Water content (TG): 19.4%

Empirical Formula: $[Zn_{1.99}Al_{1.01}(OH)_6][Cr(CN)_6]_{0.24}(CO_3)_{0.15}\bullet 3.4(H_2O)$

FW = 380.13

Synthesis of CoAl-[$Cr^{III}(CN)_6$] [7]: A solid mixture of 493 mg of $K_3[Cr(CN)_6]\cdot 3H_2O$ (1.30 mmol) and 1.000 g of **5** (3.14 mmol) were placed in a Schlenk flask and the air inside thoroughly replaced by an inert atmosphere using a standard vacuum/Ar manifold technique. The powder was then suspended in 145 mL of degassed milli-Q water and vigorously stirred under Ar at room temperature for 5 days. The brownish suspension was filtered *in vacuo* under a CO_2-free atmosphere and washed with 1 L of degassed milli-Q water. A little methanol was added to aid fast drying. The solid was left to dry overnight *in vacuo* over P_2O_5 and NaOH pellets to yield a very fine ochre pink solid **7**.

IR (KBr pellet) ν/cm^{-1}: 3450.1 (br); 2179.2 (w); 2129.1 (m); 1618.0 (m); 1359.6 (m); 609.4 (st, br); 453.2 (st); 418.5 (st).

Metallic ratio estimated from EPMA (calculated for $C_6H_{18}N_6O_{18}Al_3Cr_1Co_6$): Found Co/Al = 1.57 (2.00); Cr/Al = 0.20 (0.33).

Water content (TG up to 225ºC): 15.9%

Empirical formula: $[Co_{1.83}Al_{1.16}(OH)_6][Cr(CN)_6]_{0.23}(CO_3)_{0.23}\bullet 3.2(H_2O)$

FW=362.35

Synthesis of hybrid LDH-bimetallic cyanides

Synthesis of ZnAl-$[Cr^{III}Ni^{II}(CN)_6Cl_2]$ [8]: A clear green solution of 862 mg of $NiCl_2{\cdot}6H_2O$ (3.60 mmol) in 20 mL of a degassed mixture of milli-Q water/ethylenglycol 1 : 1 was added on top of 190 mg of **6** (0.50 mmol) with the help of a cannula and always under inert Ar conditions. The greenish-white mixture was left to stand stirring for 5 days. No clear changes could be observed with time. The slurry was then filtered in CO_2-free conditions and washed with 1 L of water and dried *in vacuo* in the presence of both NaOH and P_2O_5 pellets. This afforded a pastel greyish-green lumpy powder **8**.

IR (KBr pellet) ν/cm^{-1}: 3447.7 (br); 2169.4 (w); 2124.4 (w); 1617.7 (m); 1106.9 (w); 669.7 (br); 617.1 (st); 553.3 (m); 494.0 (m); 426.8 (sh, st).

Metallic ratio from EPMA (calculated for $C_6H_{24}N_6O_{24}Al_4Cl_2Cr_1Ni_1Zn_8$): Found Zn/Al = 1.45 (2.00); Cr/Al = 0.19 (0.25); Ni/Al = 0.35 (0.25); Cl/Al = 0.46 (0.50).

Water content (TG up to 232ºC): 13.9%

Empirical formula: $[Zn_{1.78}Al_{1.22}(OH)_6][(Cr(CN)_6)_{0.24}Ni_{0.42}Cl_{0.56}](CO_3)_{0.39}\bullet 2.9(H_2O)$

FW = 420.59

Synthesis of ZnAl-$[Cr^{III}Ni^{II}(CN)_6](NO_3)_2$ [9]: 1 g of $Ni(NO_3)_2{\cdot}6H_2O$ (3.44 mmol) was placed in a flask and 16 mL of a milli-Q water/ethylenglycol 1 : 1 were added on top. The crystalline deep green solid was allowed to slowly dissolve in the solvent mixture whilst continuously bubbling Ar through the system. The clear

green solution was then injected into a flask containing 113 mg of neat **6** (0.30 mmol) under Ar. The greenish slurry was then vigorously stirred for 5 days at room temperature. No apparent colour changes could be observed. Finally the vessel was placed in a CO_2-free glove box, and its content filtered *in vacuo* and washed with 1 L degassed milli-Q. As a result, a greenish-grey wet powder remained on the filter paper. After drying overnight over P_2O_5 and NaOH pellets, solid **9** was recovered as a pastel green powder.

IR (KBr pellet) ν/cm^{-1}: 3453.9 (br); 2171.5 (m); 2125.2 (m); 1616.1 (m); 1384.7 (st); 1363.4 (st); 777.2 (br); 617.1 (st); 555.4 (st); 484.05 (m); 426.2 (sh, st).

Metallic ratio from EPMA (calculated for $C_6H_{24}N_8O_{30}Al_4Cr_1Ni_1Zn_8$): Found Zn/Al = 1.85 (2.00); Cr/Al = 0.25 (0.25); Ni/Al = 0.29 (0.25).

Water content (TG up to 240ºC): 15.3%

Empirical formula: $[Zn_{1.95}Al_{1.05}(OH)_6][(Cr(CN)_6)_{0.27}Ni_{0.31}](NO_3)_{0.86}\bullet 2.8(H_2O)$

FW = 444.88

Synthesis of CoAl-$[Cr^{III}Ni^{II}(CN)_6](NO_3)_2$ [10]: 2 g of $Ni(NO_3)_2{\cdot}6H_2O$ (6.88 mmol) were placed in a flask with 30 mL of a milli-Q water/ethylenglycol 1 : 1. The green salt was allowed to slowly dissolve in the solvent mixture whilst continuously bubbling Ar through the system. The clear green solution was then transferred with the help of a cannula into a flask, previously sparged with Ar, containing 200 mg of neat **7** (0.55 mmol). The slurry was then left to stir for 5 days at room temperature. By the fifth day, the solid in suspension appeared to have not changed colour. The reaction flask was finally placed inside a CO_2-free glove box. A pink solid was recovered by *in vacuo* filtration followed by washing with 1 L degassed milli-Q water. The wet solid was dried overnight over P_2O_5 and NaOH pellets. Compound **10** was recovered as a brown-pink powder.

IR (KBr pellet) ν/cm^{-1}: 3438.0 (br); 2167.6 (w); 2134.8 (w); 1612.2 (m); 1384.7 (st); 1357.7 (st); 833.11 (m); 607.5 (st); 424.3 (st).

Metallic ratio from EPMA (calculated for $C_6H_{24}N_8O_{30}Al_4Cr_1Ni_1Zn_8$): Found Co/Al = 1.50 (2.00); Cr/Al = 0.20 (0.25); Ni/Al = 0.23 (0.25).

Water content (TG): 12.8%

Empirical formula: $[Co_{1.80}Al_{1.20}(OH)_6][(Cr(CN)_6)_{0.24}Ni_{0.28}](CO_3)_{0.10}\bullet 2.5(H_2O)$

FW = 399.57

Synthesis of CoAl-$[Cr^{III}Ni^{II}(CN)_6](Cl)_2$ [11]: 60 mL of a 1.5 M (5.260 g) NaCl (aq.) solution were exhaustively degassed by continuously bubbling Ar during 1 hr. The clear solution was then transferred with the help of a cannula into a flask, previously flushed with Ar, that contained 60 mg of compound **10** (0.15 mmol). The mixture was left to stir under an inert atmosphere during 4 days. Finally, the brownish slurry was filtered *in vacuo* inside the CO2-free box and the solid was dried over P_2O_5 and NaOH pellets. **11** was isolated as a pale pink powder.

IR (KBr pellet) ν/cm^{-1}: 3438.0 (br); 2167.6 (w); 2134.8 (w); 1612.2 (m); 1085.7 (w, br); 607.5 (st); 424.3 (st).

Metallic ratio from EPMA (calculated for $C_6H_{24}N_6O_{24}Al_4Cl_2Cr_1Ni_1Co_8$): Found Co/Al = 1.47(2.00); Cr/Al = 0.19 (0.25); Ni/Al = 0.25 (0.25).

2

Dichalcogenide-based materials

3 Introduction

Standing in water, but dying of thirst
This is my thanks and this is my curse
Try as I might, the fruit on the trees
All remain beyond reach, beyond wishes or pleading for
One last chance

Tantalus, *Arena*

1 Transition Metal Dichalcogenides

Transition metal dichalcogenides (TMDCs) constitute a classical inorganic family of binary compounds of general formula MX_2, where M stands for a transition metal and X stands for a chalcogen (S, Se or Te). While one may straight away appreciate how there is a long list of binary combinations that fit this definition, the term TMDC has been traditionally restricted to the dichalcogenide compounds of groups IV (Ti, Zr or Hf), V (V, Nb or Ta), VI (Mo or W) or VII (Tc or Re).[1] This is so because group IV, V, VI, and VII TMDCs form a structurally and chemically very well defined family. The research presented in this dissertation will focus in this short-listed group of TMDCs, thus the term TMDC will be used to refer strictly to the mentioned compounds.

The most characteristic structural feature of the TMDC family is their *layered* architecture, where the term *layered* designates the existence of parallel MX_2 layers that stack one on top of the other (see Figure 3.1 for an example of the Ta-S system). Each MX_2 plane is three atoms thick, stacked in such a way that a central metal atom sheet is terminated above and below by a chalcogen one. All three of the atomic sheets exhibit a hexagonal bi-dimensional close packing distribution

1 Wilson, J. A.; Yoffe, A. D. *Adv. Phys.* **1969,** *18,* 193–335.

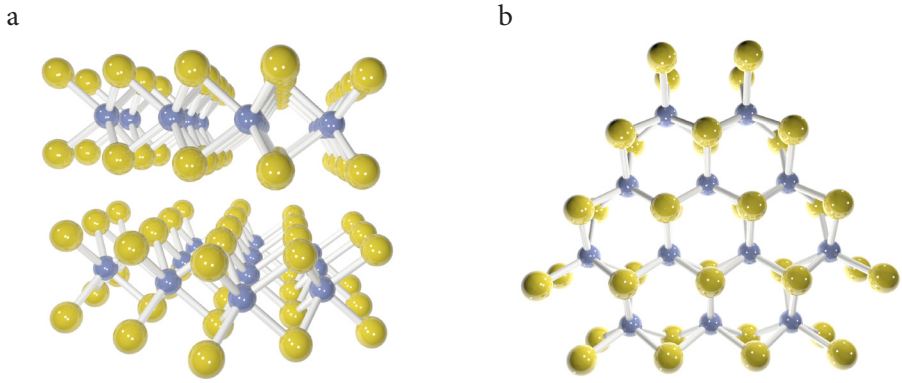

Figure 3.1 3D rendered views based on X-Ray crystallography data of 2H-TaS_2. **a**. Bi-layer stack showing the relative orientation of the two crystallographically non-equivalent TaS_2 planes in a 2H crystal. **b**. Perspective view along the *c* axis of a single layer with trigonal prismatic coordination. S atoms are represented by the yellow spheres whilst the lilac ones stand for Ta.

in the crystallographic *ab* plane (*basal* plane). Following the classical notation for close packed structures,[2] an individual MX_2 layer may present either an AbC- or an AbA-type internal stacking, where the capital letters refer to the chalcogen and the lower-case ones refer to the metal.[3] Notice how in the AbA stacking for instance, both chalcogen sheets appear eclipsed in the view along the stacking direction. This is illustrated in the right panel of Figure 3.1. As a result, the metal is always coordinated by six chalcogen atoms and the coordination geometry can be either octahedral (O_h) or trigonal prismatic (D_{3h}), respectively (view Figure 3.2).

The final crystal structure is obtained by stacking these octahedral/trigonal triatomic layers on top of one another in the crystallographic *c* direction (stacking direction). A wide variety of polytypes originate from the orderly stacking of layers with a certain periodicity. In this context, the nomenclature of the different polymorphs aids in the classification of the distinct piling orders. Each polytype is labelled with a three character prefix, for instance 4Hb. The number indicates the

2 For instance a hexagonal close packing may be described by the sequence ABABAB and a cubic close packing may be referred to as ABCABCABC. Thus, for example a trigonal prism coordination layer of two directly superposed chalcogen sheets is designated by a capital letter dyad such as AA, BB, or CC.

3 *For further details refer to*: Brown, B.; Beerntsen, D. *Acta Cryst.* **1965,** *18,* 31–36.

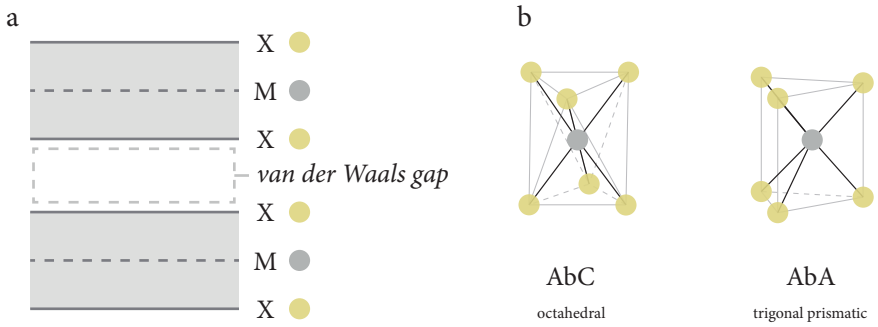

Figure 3.2 Scheme illustrating the general structural features of the TMDC layers. *Left*: a stack of two TMDC layers made out of chalcogen (X, yellow) and metal (M, grey) sheets. *Right*: coordination spheres of the metal atoms within a TMDC layer. Grey lines highlight the coordination geometry and do not indicate chemical interactions.

number of layers contained in the crystallographic unit cell, the following capital letter refers to the unit cell symmetry (T for trigonal, H for hexagonal and R for rombohedral) and a final lower case letter is appended only in the case that the first two do not uniquely identify the polymorph. Figure 3.3 (on page 70) shows a collection of frequently studied TMDC polytypes, mainly TaS_2 ones, with different stacking orders, coordination moieties and cell symmetries. Among them, only one polytype is purely octahedral, namely the 1T phase. On the other hand, there are several entirely trigonal prismatic ones (2H and 3R are examples included in Figure 3.3). The rest are mixed coordination phases where layers of different coordination spheres alternate. It is also important to notice that there are many possible polytypes that may be theoretically obtained by simply permuting the stacking order, yet only a few of them have been detected experimentally. It is noteworthy to mention how different TMDCs exhibit their own characteristic set of polymorphic structures. A compilation of the crystallographic data reported in the literature for several common group V dichalcogenides may be viewed in Table 3.1 (see page 71).

Thus, while the individual planes are robust entities bound by strong M-X bonds, the inter-plane interactions are always very weak. Going into a higher level of detail regarding the M-X bond, there is a gradation in the covalent character of

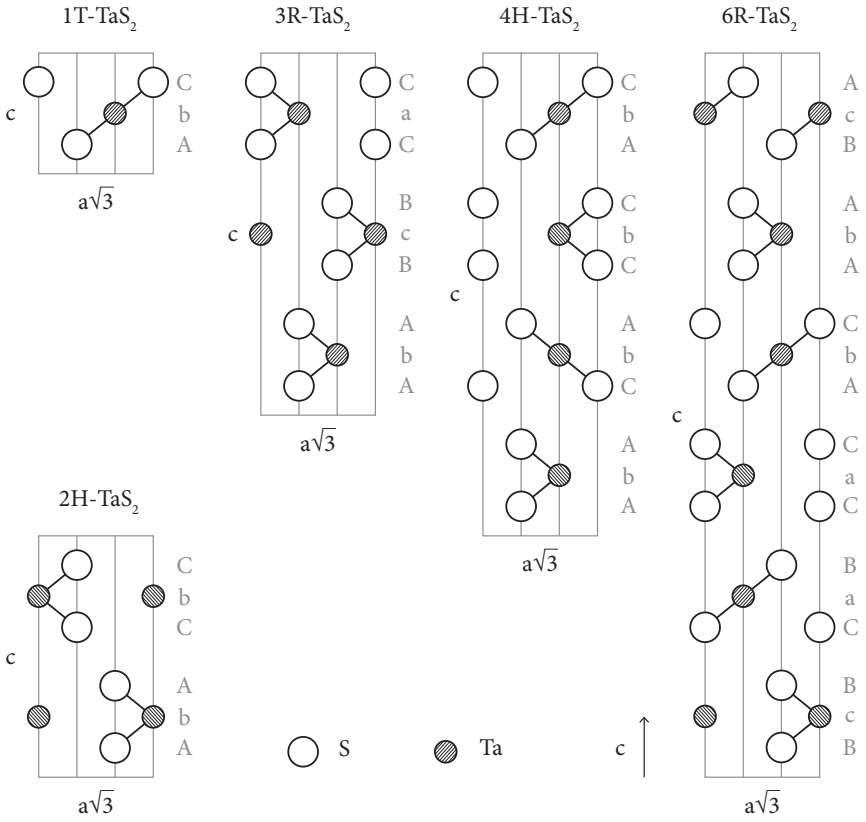

Figure 3.3 Sectional views along the (1120) plane of the most common polytypes of TaS_2. Grey outlines have been drawn to indicate the unit cell boundaries. Solid lines represent covalent bonds: straight lines depict octahedral coordination and acute angles indicate trigonal prismatic coordination.

this interaction with the sequence being Te > Se > S, being the sulphides the most ionic. Similarly, covalency decreases in going down within a group of metals.[4] On the other hand, the interactions that hold the layers together are frequently referred to as *van der Waals* interactions, even though in some cases they may also have a slight covalent or Coulombic character. Therefore, the small structural void that is located between the MX_2 layers is known as the *Van der Waals gap*. This structural characteristic makes these materials extremely anisotropic or even strictly bi-dimensional in some cases.

4 Friend, R.; Yoffe, A. *Adv. Phys.* **1987,** *36,* 1–94.

System	Label	Coordination	Space group	a = b /Å	c / Å	α = β /°	γ /°	Refs.
TaS_2	1T	O_h	P-3m	3.36	5.90	90	120	5
	2H	D_{3h}	$P6_3/mmc$	3.315	12.10	90	120	5
	3R	D_{3h}	R3m	3.32	17.9	90	120	5
	4Hb	O_h, D_{3h}	-	3.332	23.62	90	120	6
	6R	O_h, D_{3h}	R3m	3.335	35.85	90	120	5
$TaSe_2$	1T	O_h	P-3m1	3.4769(4)	6.2722(16)	90	120	7, 8
	2H	D_{3h}	$P6_3/mmc$	3.43(1)	12.71(4)	90	120	3
	3R	O_h, D_{3h}	R3m	3.4348(4)	19.177(4)	90	120	7, 8
	4Ha	D_{3h}	P-6m2	3.4362(4)	25.399(9)	90	120	7, 8
	4Hb	O_h, D_{3h}	$P6_3/mmc$	3.4575(4)	25.143(5)	90	120	3, 7, 8
	4Hc	D_{3h}	$P6_3/mc$	3.436	25.532	90	120	8
	6R	O_h, D_{3h}	R3m	3.4558(3)	37.826(7)	90	120	7, 8
$NbSe_2$	2H	D_{3h}	$P6_3/mmc$	3.45(1)	12.54(4)	90	120	3
	3R	D_{3h}	R3m	3.45(1)	18.88(4)	90	120	3
	4H	D_{3h}	P-6m2	3.44(1)	25.24(4)	90	120	3

Table 3.1 Unit cell parameters and coordination modes (point groups) of a selection of Ta and Nb dichalcogenide known polytypes extracted from a variety of literature references (see refs. column).

In fact, it is the layered anisotropy that confers TMDCs their very special properties. For instance, TMDCs are ideal systems for the study of (quasi)bi-dimensional superconductivity and charge density waves (CDWs) as charge carriers and phonons seem to couple in a unique fashion.[1,9] In that which concerns

5 Jellinek, F. *J. Less-Common Met.* **1962,** *4,* 9–15.

6 Di Salvo, F.; Bagley, B.; Voorhoeve, J.; Waszczak, J. *J. Phys. Chem. Sol.* **1973,** *34,* 1357–1362.

7 Bjerkelund, E.; Kjekshus, A. *Acta Chem. Scand.* **2007,** *21,* 1–14.

8 Huisman, R.; Jellinek, F. *J. Less-Common Met.* **1969,** *17,* 111–117.

9 a) Wilson, J. A.; Di Salvo, F. J.; Mahajan, S. *Adv. Phys.* **1975,** *24 (2),* 117-201. (b) Wilson, J. A.; Di Salvo, F. J.; Mahajan, S. *Phys. Rev. Lett.* **1974,** *32,* 882–885.

the electrical properties, the conductivity perpendicular to the MX_2 planes is at least 100 times lower than the in-plane conductivity and it is also suggested that the movement of the carriers between layers takes place by hopping mechanisms rather than by band-type ones as occurs along the planes (*vide infra*, see section 2.3 on page 78). Following the same trend, thermal conductivity is lower too, once measured perpendicular to the layers.

On a more applied sense, the weak inter-layer interactions have important implications in the mechanical properties of TMDCs. Indeed these materials have been traditionally used as solid-state lubricants thanks to their very low shear resistance derived from the weak interlayer van der Waals forces.[10]

In addition, TMDCs exhibit generally high optical absorption coefficients (in the order of 10^5 cm^{-1}).[1, 11] For some semiconducting members of the family, this feature coexists with direct band gaps which are compatible with the solar spectrum. Therefore, some TMDCs have been proposed as potential candidates for integration in photoelectrochemical devices.[12] Finally, TMDCs are also remarkable in the field of catalysis. Molybdenite (MoS_2) for instance is one of the most widely used compounds in the heterogeneous hydrodesulfurization of natural gas and petroleum compounds.[13] Its high performance in such process is once again attributed to the layered architecture. Though the nature of the sites of catalytic activity is still somehow uncertain, it is generally assumed that the basal planes of the layered structure do not contribute to the catalytic activity. Thus it is believed that it is in the plane edges or rims where the heterogeneous reactions take place.[14]

---

10 a) Rapoport, L.; Bilik, Y.; Feldman, Y.; Homyonfer, M.; Cohen, S. R.; Tenne, R. *Nature* **1997,** *387,* 791–793. (b) Cohen, S. R.; Rapoport, L.; Ponomarev, E. A.; Cohen, H.; Tsirlina, T.; Tenne, R.; Levy-Clement, C. *Thin Solid Films* **1998,** *324,* 190–197. (c) Cohen, S. R.; Feldman, Y.; Cohen, H.; Tenne, R. *Appl. Surf. Sci.* **1999,** *144-145,* 603–607.

11 Grasso, V.; Mondio, G. *Electronic Structure and Electronic Transitions in Layered Materials*, Ed. D. Reidel, Dordrecht, 1986.

12 a) Tributsch, H. *Naturforsch.* **1977,** *32a,* 972 (b) Aruchamy, A. *Photoelectrochemistry and Photovoltaics of Layered Semiconductors,* Ed. Kluwer Academic Publishers, Dordrecht, **1992** (c) Djemal, G.; Müller, N.; Lachish, U.; Cahen, D. *Sol. Energ. Mater.* **1981,** *5 (4),* 403-416. (d) Kline, G.; Kam, D.; Canfiled, D.; Parkinson, B. A. *Sol. Energ. Mater.* **1981,** *4 (3),* 301-308. (e) Pathak, V. M.; Patel, K. D.; Pathak, R. J.; Srivastava, R. *Sol. Energ. Mat. Sol. C.* **2002,** *73,* 117–123. (f) Delphine, S. M.; Jayachandran, M.; Sanjeeviraja, C. *Crystallography Reviews* **2011,** *17(4),* 281-301.

13 Topsøe, H.; Clausen, B. S.; Massoth, F. E., *Hydrotreating Catalysis, Science and Technology*, Ed. Springer-Verlag, Berlin, 1996.

14 Daage, M.; Chianelli, R. R. *J. Catal.* **1994,** *149,* 414-427.

2 Electrical properties

2.1 Different composition, different properties

Despite the profound structural and chemical resemblance of the different layered TMDCs, the entire family of compounds covers a wide spectrum of electrical properties. By changing the metal and the chalcogenide out of which the TMDC is made, one may encounter anything from electrical insulators (such as HfS_2), through semiconductors (like MoS_2, WS_2 or in general the rest of Mo and W dichalcogenides) and semi-metals (for instance WTe_2 and TeS_2) to true metals (for example TaS_2, NbS_2 and VSe_2).[1]

An in-depth study of the electronic nature of TMDCs requires a detailed study of their band structures. Overall, the degree of filling of the d bands which lie around the bonding/antibonding gap provides with a good estimation of the electrical properties. A scheme roughly illustrating the band structure of a selection of TMDCs at the bonding/antibonding region is shown in Figure 3.4. In general terms, the band structure of layered TMDCs presents a filled wide valence band with a marked chalcogen p character just below the energy of the Fermi level. In addition, the octahedral crystal field splitting of the d orbitals of the metal into t_{2g} and e_g symmetry groups allows them to mix with the p orbitals coming from the chalcogen ligands. This originates, a higher-lying wide band based on a mixture of t_{2g} (d_{xy}, $d_{x^2-y^2}$ and d_{z^2}) and e_g (d_{xz} and d_{yz}) metal orbitals with chalcogen p ones on the one hand.

On the other hand, a narrower lower-lying band, which is principally metal d_{z^2} in character, is also created. This band is totally isolated for perfect octahedral coordination. In fact, it is these bands that confer TMDCs their rich electrical properties. Depending on the particular M, X binary combination and also depending on the coordination mode (*vide infra* section 2.2 on page 75) the p-d_{z^2} energy gap changes in such a way that they may be completely separated (1T-ZrS_2) or totally (2H-MoS_2) or partially (1T/2H-NbS_2) overlapped. The picture is completed by the transition metal electronic configuration that defines the band filling (up to the Fermi level). Arising from this delicate band structure equilibrium, anything from a p-d gap semiconductor to a d-band metallic conductor may occur.

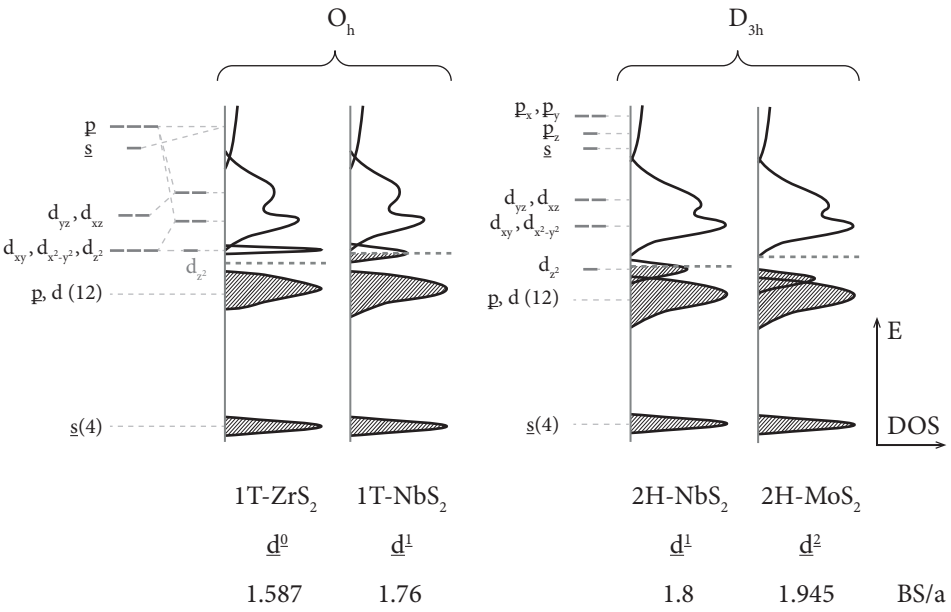

Figure 3.4 Band model comparison for different disulphides with distinct electronic configuration (composition) and metal coordination geometries (polytypes). The hatched bands indicate electronic occupation and the Fermi level (E_F) is marked by a dashed line. Note that orbitals coming from the chalcogen are underlined.[15]

In view of this situation one may appreciate how the band filling is one of the main factors that affect the properties of the different TMDCs. Consequently, the electrical properties of different isostructural TMDCs are better discussed by groups of metals with equal electronic configuration. To begin with, group IV (d^0) dichalcogenides are generally semiconductors (for example $ZrSe_2$)[16] or semimetals at best ($TiSe_2$, $TiTe_2$, and $HfTe_2$)[17] whenever the top of the chalcogen p valence band and the bottom of the transition metal d conduction band get to overlap. Group V dichalcogenides (d^1) should all in theory present metallic conductivity if one considers an undistorted octahedral coordination geometry. Nevertheless this is not the case, and with the exception of 2H-NbS_2 all other

15 Figure adapted from reference 4: Liang, *NATO Advanced Study Institute* **1984**, Cambridge.

16 Klipstein, P. C.; Friend, R. H. *J. Phys. C* **1984,** *17,* 2713.

17 a) Friend, R. H.; Jérome,D.; Yoffe, A. D. *J. Phys. C* **1982,** *15,* 2183. (b) Klipstein, P. C.; Guy, D. R. P.; Marseglia, E. A.; Meakin, J. I.; Friend, R. H.; Yoffe, A. D. *J. Phys. C* **1986,** *19,* 4953.

group V dichalcogenides show strong temperature-dependent structural distortions associated to the structure of their Fermi surfaces and the appearance of periodic lattice distortions-charge density waves (PLD-CDW, *vide infra* see section 3 on page 78). These distortions open gaps in their band structures, making them exhibit anomalously low electrical conductivities and only medium carrier mobilities. In that concerning group VI (d^2) dichalcogenides they all adopt the lower-symmetry trigonal prismatic coordination geometry. They have a further d electron and hence a completely filled d_{z^2} band. Therefore they are all semiconducting with open gaps of around 1 eV between the d_{z^2}-p valence band and the higher-in-energy d conduction band (for instance 2H-MoS_2 present a 4 eV band gap, see Figure 3.4).

By using optical absorption semi-empirical or self-consistent methods,[1, 18] the dispersion of the band structure along characteristic wave vectors of some TMDCs, namely TiS_2, may be proposed. An example of the band model for bulk 2H-TaS_2 across several directions in the first Brillouin zone may be observed in Figure 3.5. In this particular case, two bands cross the Fermi level, fact which justifies the metallic conductivity observed for this analogue. Also important to note in view of this band model is the fact that there is no remarkable band dispersion in the out-of-plane Γ-A section. This once again points in the direction of a quasi-bidimensional systems. The perpendicular band dispersion is calculated to be of up to around ½ eV.[4]

2.2 Different polytypes, different properties

The quasi-bidimensionality of the layered TMDCs make them almost completely insensitive to the layer stacking order. Oppositely, their properties are extremely dependent on the coordination point symmetry. So technically, discarding the stacking effects, the heading should be rather interpreted as '*different coordination symmetry, different properties*'.

18 a) Mattheiss, L. F. *Phys. Rev. B* **1973,** *8,* 3719. (b) Fang, C. M.; De Groot, R. A.; Haas, C. *Phys. Rev. B* **1997,** *56,* 4455–4463. (c) Isomaki, H.; Boehm, von, J. *J. Phys. C: Sol. State Phys.* **2000,** *14,* L75. (d) Umrigar, C.; Ellis, D. E.; Wang, D. S.; Krakauer, H.; Posternak, M. *Phys. Rev. B* **1982,** *26,* 4935–4950. (e) Clerc, D. G.; Poshusta, R. D.; Hess, A. C. *J. Phys. Chem.* **1996,** *100,* 15735–15747. (f) Sharma, S.; Nautiyal, T.; Singh, G. S.; Auluck, S.; Blaha, P.; Ambrosch-Draxl, C. *Phys. Rev. B* **1999,** *59,* 14833.

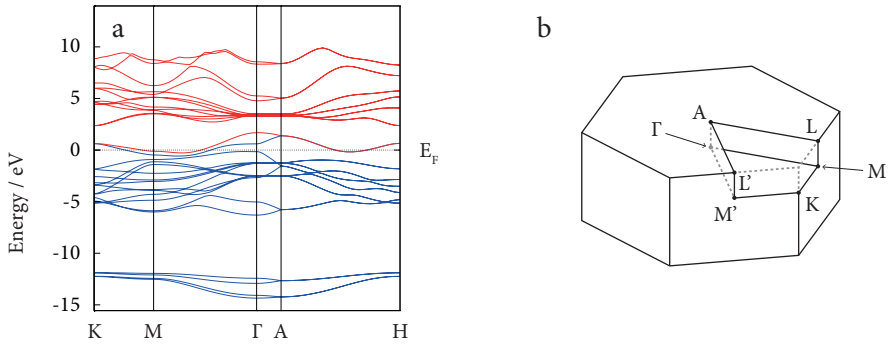

Figure 3.5 a. Calculated band dispersion for bulk 2H-TaS_2. **b**. First Brillouin zone of an hexagonal Bravais lattice, such as the ones adopted by layered TMDCs, highlighting the characteristic points of maximal symmetry.

In this context it is important to be able to quantify the geometrical deviations from the ideal octahedral and ideal trigonal prismatic extremes. The ratio between lattice constant *a* and the *basal spacing* (*BS* = *c* / number layers in unit cell; in analogy to the LDH systems, recall section 1, Chapter 1, page 13) provides with a quantitative value of such distortions. This ratio reaches a value of ≈ 1.63 for perfect octahedral coordination and gradually increases as the trigonal distortion augments. Angle-resolved photoemission spectroscopy (ARPES) experiments in accordance with theoretical calculations have concluded that such trigonal distortion greatly affects the position of the d_{z^2} band and hence the electrical properties of the different polytypes.[19] In this way the *BS*/*a* ratio is an important parameter in the determination of the d_{z^2} band positions and allows for the classification of the distinct polymorphic structures and also to get an intial taste of their electrical properties (recall Figure 3.4).

A clarifying case study to illustrate how different coordination modes may affect the electronic properties of a TMDC is that of TaS_2. On the one hand, the octahedrally coordinated Ta in the 1T-TaS_2 polytype (*BS*/*c* = 1.75) should exhibit metallic conductivity. Yet it behaves optically and magnetically as a semiconductor. In this case, the presence of an incommensurate (IC) or of a nearly-commensurate

19 a) Takahashi, N.; Matsui, F.; Akasaka, M.; Nakanishi, K.; Nozawa, Y.; Hamada, Y.; Namba, H.; Daimon, H. *Mem SR Cent Ritsumeikan Univ* **2005,** 105–107. (b) Bovet, M.; Van Smaalen, S.; Berger, H.; Gaál, R.; Forro, L.; Schlapbach, L.; Aebi, P. *Phys. Rev. B* **2003,** *67,* 125105.

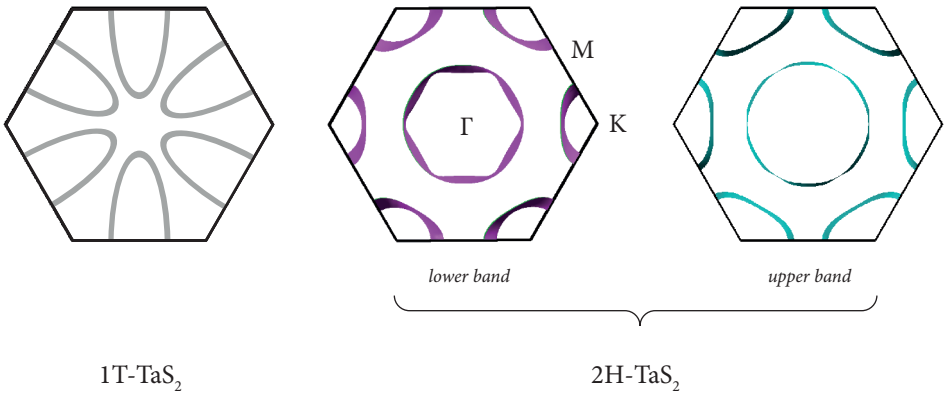

Figure 3.6 Schematic representation of the Fermi surface projections for bulk 1T and 2H-TaS_2 along the Γ-A direction of the first Brillouin zone. Note the *electron-like* structure of the 1T polymorph (with an electron pocket at the zone centre) as opposed to the *hole-like* character of the 2H.

(NC) charge order structure even at room temperature, as seen by electron microscope diffraction patterns,[20] suggests that this polytype may be particularly susceptible to Fermi-surface driven structural distortions. As a consequence, only very faint metallic properties are observed at best.[4] On the other hand, TaS_2 can also be synthesized with a trigonal prismatic coordination (for instance 2H-TaS_2; *BS/c* = 1.83). In this case the D_{3h} coordination symmetry breaks the degeneracy of the d orbitals in such a way that the d_{z^2} comes lowest in energy (review Figure 3.4). Thus, the d-character band that originates from these orbitals lies lower in energy than the one in the 1T type polytypes. In addition, the PLD distortions in the 2H phase generally occur below room-temperature. As a result, the 2H structures show rather better metallic properties than the 1T polytype.

The difference in electronic structure is also reflected in the Fermi surfaces of the 1T and 2H polytypes of TaS_2 shown in Figure 3.6.[21] While the Fermi surface for 1T-TaS_2 has cylindrical electron pockets at the centre of the zone faces, the 2H

20 Spijkerman, A.; De Boer, J.; Meetsma, A.; Wiegers, G.; Van Smaalen, S. *Phys. Rev. B Cond. Matter Mat. Phys.* **1997,** *56,* 13757–13767.

21 Schematic representation of the data presented in reference 4 and 9a.

polytype has a hole-like character for the two bands at the Fermi level, with hole surfaces centred at the singular points Γ, K and M of the Brillouin zone.

2.3 Anisotropic behaviour

It is particularly noteworthy how the structural bidimensionality directly manifests in the electrical properties of the bulk material. Indeed, there is a dramatical difference between the thermal variation of the conductivity measured along the basal layers with respect to the one measured orthogonally. As an example the resistivity profiles measured along the two normal directions in a 4Hb-TaS_2 single crystal are presented in Figure 3.7.[9a] Note the two anomalies in both profiles at around 315 and 22 K that correspond to the onset of two CDW transitions of the octahedral and the trigonal prismatic layers respectively.[6, 22] This depicts the fact that the two types of layers behave independently in the establishment of CDW distortions and supports the idea of strict bidimensionality with only very weak inter-layer interactions. It is moreover suggested that in view of such a low conductivity as measured perpendicular to the basal planes, the carriers must move in this direction by a hopping process rather than by band conduction mechanisms.[1, 4, 23, 24]

3 Superconductivity and CDWs

Exciting as the electrical properties described may seem, what has really tantalized scientists over the history are other more exotic behaviours that some of these layered TMDC present, namely superconductivity and CDWs.

It was back in the 50s that Peierls described how a one-dimensional chain of metal atoms is intrinsically unstable and will hence naturally distort to lower its band energy.[25] This phenomenon opens up a gap (Peierls gap) at the Fermi level and sets up a wavevector that spans the Fermi surface. As a result, an uneven spatial distribution of free charge carriers is generated giving rise to a stabilization

22 Narayan, J. *Appl. Phys. Lett.* **1976,** *29,* 223

23 Bulaevskiĭ, L. N. *Physics-Uspekhi* **1975,** *18,* 514–532.

24 Mott, N. F.; Davis, E. A. *Electronic Processes in Non-Crystalline Solids*, Oxford University Press, **1979.**

25 Peierls, R. E. *Quantum Theory of Solids*, Oxford University Press, **1955**.

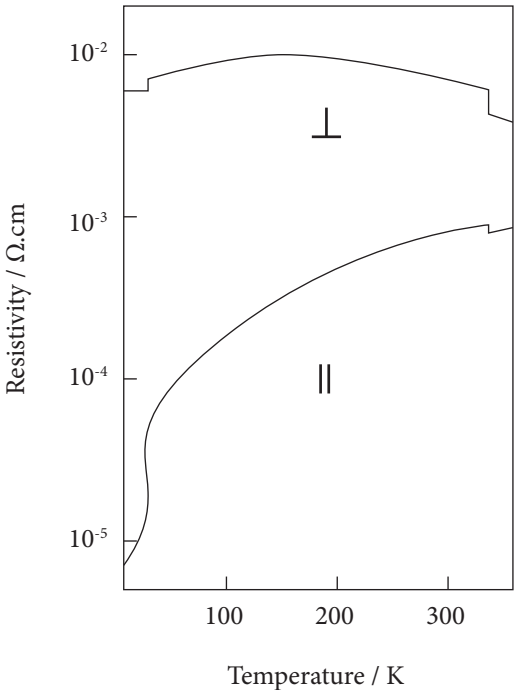

Figure 3.7 Scheme illustrating the electrical resistivity of 4Hb-TaS_2 measured parallel to the *ab* crystallographic plane (||) and along the stacking *c* direction (⊥).

of the conduction electrons by a lattice phonon induced PLD.[26] While in the one-dimension such electron-phonon coupling causes a metal to turn into insulator, in three dimensions it may result in a metal turning superconducting.[27] In two-dimensions the interplay between both phenomena appears to be more complex. Indeed, the investigation of the coexistence of superconductivity with competing magnetic or charge order has drawn much attention in the condensed matter community for over half a century.[28]

In this context of quasi-bidimensionality is where one may find layered TMDCs. Many metallic TMDCs exhibit CDWs, particularly at the low

26 Gruener, G. *Density Waves in Solids*, Addison-Wesley, Reading, MA, **1994**.

27 Di Salvo, F. J. *Electron-Phonon Interactions and Phase Transitions*. Ed. T. Riste, Plenum Press, New York and London, **1977**.

28 a) Moncton, D. E.; Axe, J. D.; Di Salvo, F. J. *Phys. Rev. B* **1977,** *16,* 801. (b) Tsuei, C.; Kirtley, J. R. *Rev. Mod. Phys.* **2000,** *72,* 969. (c) Flouquet, J.; Buzdin, A. *Phys. World* **2002,** *15,* 41.

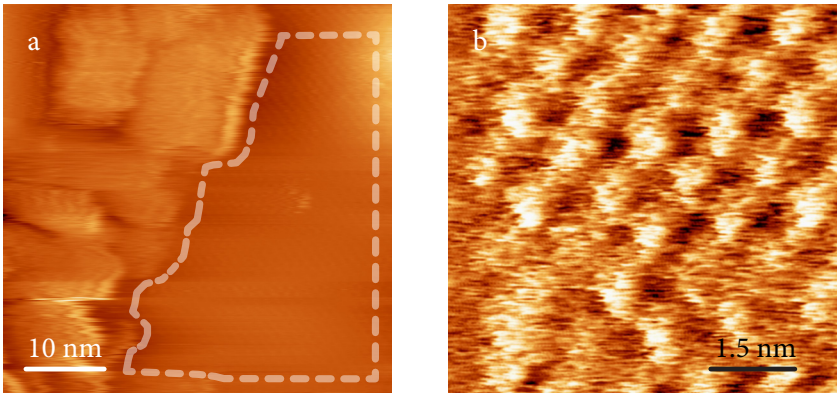

Figure 3.8 CDW at the surface of a 1T-TaS_2 crystal as seen by ambient conditions STM. a. Topography image of a region with a CDW structured surface highlighted by the dashed borderline. **b**. Electrical current close-up image of the CDW lattice.

temperatures. In the presence of such CDWs, the conductivity of these systems is reduced. For some TMDCs, as is the case of group V dichalcogenides, the d_{z2} band stabilization due to this distortion is so favourable that CDWs are very pronounced. In 1T-TaS_2 and 1T-$TaSe_2$ for instance, CDWs are visible at room temperature and the presence of one-electron oxidized (Ta^{5+}) or reduced (Ta^{3+}) Ta centres may be considered. This may be even evidenced by XPS experiments.[29] Furthermore, CDWs can be directly observed by scanning the surface of a TaS_2 crystal with the tip of an STM (see Figure 3.8) For the different TMDC analogues with different band structures, contrasting phases are formed in distinct temperature ranges and with varying periodicities. Whilst CDW are typically not commensurate with the crystal lattice,[30] in special contexts, namely when the amplitude of the PLD distortion builds up at lower temperatures, they may be commensurate.[31] Under these circumstances, the pinning of the CDW to the crystal lattice occurs and the CDW is said to be *locked-in*.

The same electron-phonon interaction that is responsible for PLD-CDWs in TMDCs also accounts for the electron pairing in transition metal d bands, as

29 a) Pollak, R. A.; Eastman, D. E.; Himpsel, F. J.; Heimann, P.; Reihl, B. *Phys. Rev. B* **1981,** *24,* 7435–7438. (b) Hughes, H. P.; Scarfe, J. A. *J. Phys. Cond. Matter* **1996,** *8,* 1457–1473.

30 In this case the CDW has no preferred phase relation to the lattice.

31 *Refer to* section 2.2 in reference 4.

described by the Bardeen-Cooper-Schrieffer (BCS) theory of superconductivity.[32] However, among the vast library of TMDC materials only the group V dichalcogenides and within them only the metallic polytypes that exhibit trigonal prismatic coordination are type-II superconductors at low temperatures. This is due to the fact that the octahedrally coordinated polytypes present such strong PLD-CDWs that they exhibit very low charge mobilities at room temperature. In this way, most of the group V trigonal prismatic dichalcogenides exhibit superconducting features below a specific superconducting transition temperature (T_{SC}).[1, 33] However, amid the group of superconducting TMDC analogues, a great dispersion of T_{SC} may be observed. Once again the trend follows in that the compounds that present the strongest and higher temperature PLD-CDWs are the ones with lowest T_{SC}. This a direct consequence of the Fermi-surface destruction below such transitions, as confirmed by specific heat experiments.[44] Indeed, it was found that T_{SC} is enhanced under applied pressures high enough to annihilate the PLD-CDW.[34] In this line, 2H-$NbSe_2$, which exhibits a weak PLD-CDW, presents a high T_{SC} of 7.1 K,[35] in contrast with for instance 2H-$TaSe_2$ that switches to the superconducting state (*aka.* Meissner state)[36, 37] only below 0.14 K. The T_{SC} together with the CDW for the different group V trigonal prismatic dichalcogenides are summarized in Table 3.2.

4 Easy to exfoliate materials

The structural bi-dimensionality of TMDCs has a key practical implication: they are very easy to exfoliate. There is an alternation along the crystallographic *c* axis of covalent bonds within the MX_2 planes with van der Waals inter-plane forces, which are one to two orders of magnitude weaker,[38] that arise from the

32 Bardeen, J.; Cooper, L. N.; Schrieffer, J. R. *Phys. Rev.* **1957,** *106,* 162–164.

33 For a succinct overview on superconductivity view: Poole, C. P., Jr; Farach, H. A.; Creswick, R. J.; Prozorov, R. *Superconductivity*, Academic Press, San Diego, California,**1995**.

34 a) Berthier, C.; Molinié, P.; Jérome, D., *Sol. State Commun.* **1976,** *18,* 1393. (b) Friend, R. H.; Beal, A. R.; Yoffe, A. D. *Phil. Mag.* **1977,** *35,* 1269.

35 Garoche, P.; Veyssie, J. J.; Manuel, P.; Molinié, P. *Sol. State Commun.* **1976,** *19,* 455.

36 Meissner, W.; Ochsenfeld, R. *Naturwissenschaften* **1933,** *21 (44),* 787–788.

37 For a short overview on how superconductivity relates to magnetism and how it may be pictured by conventional magnetic characterisation techniques see Appendix 4.1.

38 a) Rydberg, H.; Dion, M.; Jacobson, N.; Schröder, E.; Hyldgaard, P.; Simak, S.; Langreth, D.; Lundqvist, B. *Phys. Rev. Lett* **2003,** *91,* 126402. (b) Langreth, D. C.; Dion, M.; Rydberg, H.; Schröder, E.; Hyldgaard, P.; Lundqvist, B. I. *Int. J. Quantum Chem.* **2004,** *101,* 599–610.

interaction of chemically saturated chalcogen atoms. It is therefore easy to cleave along the van der Waals gap, as virtually no dangling bonds are generated in the process. The tearing of a MX_2 sheet on the other hand has less-favourable energy implications.

System	T_{SC} / K	T_{CDW} / K	References
2H-TaS_2	0.6-0.8	78.0	40, 41, 42, 43, 44
4Hb-TaS_2	1.1	317, 22	42, 43, 44
2H-$TaSe_2$	0.15	121, 90	43, 44
4Hb-$TaSe_2$	1.1	75	43, 44
2H-NbS_2	6.3	-	4
2H-$NbSe_2$	7.2	33.5	40, 44
4Ha-$NbSe_2$	6.3	-	42

Table 3.2 Superconducting transition temperatures (T_{SC}) and CDW transition onset temperatures (T_{CDW}) extracted from specific heat capacity data for some group V dichalcogenides.[39]

Indeed, single crystals usually grow in the form of thin platelets with high aspect ratio habits, which may be readily cleaved with sticky tape to yield thin specimens only a few nanometers thick in the stacking direction *c*. These thin TMDC samples exhibit strong light absorption coefficients in the colour spectrum and the colour under transmitted light changes with thickness in a different manner for each different analogue.[1] The bulk crystals have highly reflecting facets too. As a result, even in the case of the thin cleaved samples, a high rate of reflection occurs given the fact that the refractive index (n) is still above $n \sim 2$.[1]

Having delivered such a description, the comparison to graphene is inescapable. As a matter of fact it is thanks to the recent advances in sample preparation, detection and manipulation of graphene that other bi-dimensional

39 Adapted from reference 4 and updated from alternative sources indicated in the references column.

40 Coleman, R. V.; Eiserman, G. K.; Hillenius, S. J.; Mitchell, A. T.; Vicent, J. L. *Phys. Rev. B* **1983,** *27,* 125.

41 Garoche, P.; Manuel, P.; Veyssle, J. J.; Molinié, P. *J. Low Temp. Phys.* **1978,** *30,* 323.

42 Meyer, S. F.; Howard, R. E.; Stewart, G. R.; Acrivos, J. V.; Geballe, T. H. *J. Chem. Phys.* **1975,** *62,* 4411.

43 van Maaren, M. H.; Schaeffer, G. M. *Phys. Lett.* **1967,** *24A,* 645.

44 Harper, J.; Geballe, T. H.; Di Salvo, F. J. *Phys. Rev. B* **1977,** *15,* 2943.

crystals are experiencing a better degree of recognition. Nonetheless atomically thin samples of TMDCs offer properties that are not found in graphene. While graphene exhibits good conductivity and high carrier mobilities ($> 10^6$ $cm^2 \cdot V^{-1} \cdot s^{-1}$ at 2 K and $> 10^5$ $cm^2 \cdot V^{-1} \cdot s^{-1}$ for BN-encapsulated graphene at r.t.),[45, 46] TMDCs present sizable bandgaps making them exhibit anything from metallic conductivity materials to semiconductivity (see section 2 on page 73) and outweighing the former in the design and fabrication of FET and optoelectronic devices. Other thickness-dependent properties of TMDC layers are also currently attracting a great deal of attention making them consolidate as the versatile heirs of the graphene lore.

5 Intercalation and hybrid materials

The layered structure of a TMDC exhibits a series of interlayer sites in the van der Waals gap available for occupation by extrinsic guest species. In particular, there are two types of interlayer site: a first class of site is characterized by an octahedral chalcogen coordination and the second one in which the chalcogen atoms above and below the void define a tetrahedral coordination sphere (see Figure 3.9).[4] A third more rare possibility is a trigonal prismatic site achieved by rotation of adjacent sandwiches only observed in intercalation of very specific chemical species.[47] These sites provide TMDCs with the capability of hosting a wide variety of chemical species as long as the interactions with the chalcogen-surrounded cavity are favourable. As a matter of fact, the van der Waals gap is said to posses an effective negative charge density accumulated at the chalcogen terminated MX_2 layer surfaces. This is in accordance with the electron donor nature of most of the species that have been successfully intercalated in neutral TMDCs.[4] In this line, three main types of guest species have historically attracted most of the attention regarding the intercalation in neutral TMDC hosts: organic Lewis bases (pyridine for example) and simple inorganic nitrogen-based molecules

45 Elias, D. C.; Gorbachev, R. V.; Mayorov, A. S.; Morozov, S. V.; Zhukov, A. A.; Blake, P.; Ponomarenko, L. A.; Grigorieva, I. V.; Novoselov, K. S.; Guinea, F.; Geim, A. K. *Nat. Phys.* **2012,** *8,* 172

46 Mayorov, A. S.; Gorbachev, R. V.; Morozov, S. V.; Britnell, L.; Jalil, R.; Ponomarenko, L. A.; Blake, P.; Novoselov, K. S.; Watanabe, K.; Taniguchi, T.; Geim, A. K. *Nano Lett.* **2011,** *11,* 2396–2399.

47 Rouxel, J. in *Intercalated Layer Materials*, Ed. F. Levy, Dordrecht: D. Reidel, **1979**, Vol. 6, p. 210.

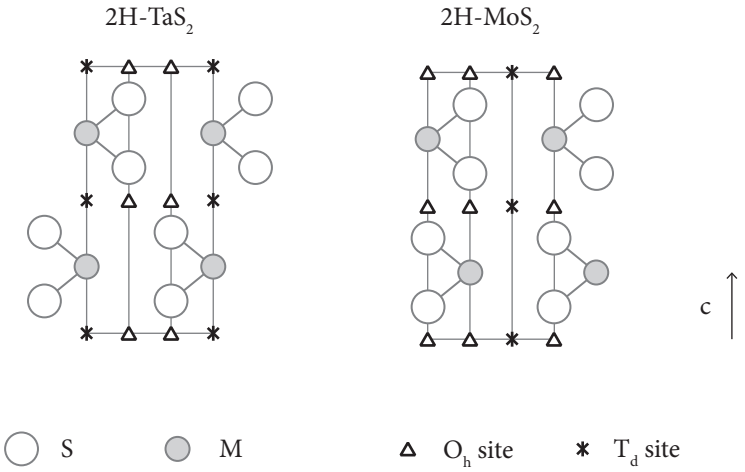

Figure 3.9 Examples of coordination sites in the van der Waals gaps of two TMDCs.

(ammonia or hydrazine for instance), alkali metal atoms (Li, Na, K, Rb),[48] heavier metals (Ag, Ca, In, Sn and Pb)[49] and 3d transition metal atoms (Ti, V, Cr, Mn, Fe, Co, Ni, Rh)[50] and simple complexes (such as metallocenes).[51]

Much research indeed has been devoted to the intercalation of simple metal atoms at TMDCs. In the hybrid materials formed by intercalation of single atom donors, alkali metals and 3d transition metals, the guest species occupy typical well-defined sites: alkali metals and the 3d transition metals occupy octahedral sites preferentially, while tetrahedral sites are preferred by silver or copper. This gives rise to ordered sheets of guest atoms between MX_2 planes and also to order-disorder transitions as seen by Raman scattering or X-Ray diffraction studies.[52] These materials have been readily obtained by a variety of methods including: (i) by soaking pristine TMDC crystals in metal/ammonia solutions, organometallic

48 a) Rüdorff, W.; Sick, H.H. *Angew. Chem.* **1959,** *71,* 127. (b) Bayer, E.; Rüdorff, W. *Z. Naturforsch.* **1972,** *27b,* 1336.

49 Di Salvo, F.; Hull, G., Jr; Schwartz, L.; Voorhoeve, J.; Waszczak, J. *J. Chem. Phys.* **1973,** *59,* 1922–1929.

50 a) Parkin, S. P.; Beal, A. R. *Phil. Mag. B* **1980,** *42(5),* 627-642. (b) Negishi, H.; Shoube, A.; Takahashi, H.; Ueda, Y.; Sasaki, M.; Inoue, M. *J. Mag. Mag. Mat.* **1987,** *67(2),* 179-186.

51 a) Dines, M. B. *Science* **1975,** *188,* 1210–1211. (b) Clement, R.; Davies, W.; Ford, K.; Green, M.; Jacobson, A. *Inorg. Chem.* **1978,** *17,* 2754–2758.

52 a) Suter, R. M.; Shafer, M. W.; Horn, P. M.; Dimon, P. *Phys. Rev. B* **1982,** *26,* 1495–1498. (b) Leonelli, R.; Plischke, M.; Irwin, J. C. *Phys. Rev. Lett.* **1980,** *45,* 1291–1294.

solutions,[53] or molten alkali/alkalihalide mixtures;[54] (ii) by delaminating the host structure in the presence of the alkali metal;[55] (iii) by electrochemical processes;[56] (iv) or by UHV methodologies.[57] However, softer chemical methods involving the use of simple bases (NaOH for instance) may also be employed (see section a of Chapter 4 (p. 113)). In any case, it is of interest to mention how a complete charge transfer from the metal to the conduction band of the TMDC host (assuming a rigid band model) generally occurs upon intercalation (see Equation 3.1). This has a big impact on both the structure and properties of the resulting electrostatically bound stack and the specific implications will be discussed in detail in the following section 3 of Chapter 4 (p. 112). The intercalation of alkali metals in TMDCs has had a big impact in industry too since it was understood it could be used in a reversible manner in TMDC/Li batteries.[58]

$$MX_2 + A \longrightarrow A^{y+}(MX_2)^{y-}$$

Equation 3.1 Internal redox process upon TMDC intercalation with an alkali metal (A).

In that regarding the intercalation of molecular species, much has been explored too. Great scientific impact was generated by the first intercalation of pyridine in TaS_2.[59] Since that discovery an entirely new physics regarding Lewis-base-intercalated hybrid superconductors has been developed.[60] The facile insertion of these molecules in the van der Waals gap of TMDCs make these materials very easy to access via simple immersion in a liquid of guest molecules

53 Murphy, D.; Di Salvo, F.; Hull, G., Jr; Waszczak, J. *Inorg. Chem.* **2001,** *15,* 17–21.

54 Omloo, W.; Jellinek, F. *J. Less-Common Met.* **1970,** *20,* 121–129.

55 Gee, M. A.; Frindt, R. F.; Joensen, P.; Morrison, S. R., *Mater. Res. Bull.* **1986,** *21,* 543.

56 a) Thompson, A.H. *Physica B+C* **1980,** *99(1-4),* 100-106. (b) Gerhards, A. G.; Roede, H.; Haange, R. J.; Boukamp, B. A.; Wiegers, G. A., *Synth. Met.* **1984,** *10,* 51. (c) Folinsbee, J. T.; Jericho, M. H.; March, R. H.; Tindal, D. A. *Can. J. Phys.* **1981,** *59,* 1267.

57 a) Starnberg, H. I.; Hughes, H. P. *J. Phys. C Sol. State Phys.* **1987,** *20,* 4429–4436. (b) Ohuchi, F. S.; Jaegermann, W.; Pettenkofer, C.; Parkinson, B. A. *Langmuir* **1989,** *5,* 439–442.

58 Whittingham, M. S. *Science* **1976,** *192,* 1126–1127.

59 Gamble, F.; Di Salvo, F.; Klemm, R. A.; Geballe, T. *Science* **1970,** *168,* 568–570.

60 a) Gamble, F. R.; Osiecki, J. H.; Cais, M.; Pisharody, R.; DiSalvo, F. J.; Geballe, T. H. *Science* **1971,** *174,* 493–497. (b) Gamble, F.; Osiecki, J.; DiSalvo, F. *J. Chem. Phys.* **1971,** *55 (7),* 3525–3530.

or via the exposure to a suitable vapour pressure. In addition, the high quality of the resulting crystals has allowed for the precise determination of the sites that the guest molecules occupy within the layered structure and the orientation within those sites.[61] Also appealing is the reversibility of the intercalation process of the volatile molecules introduced.[62] In this case it is also suggested that a partial charge transfer from the donor guest species to the MX_2 layers is produced. The partial band filling after intercalation may be confirmed by different techniques, namely optical absorption or transport measurements.[63, 64] The intercalation of sizeable organic molecules allowed for the controlled separation of the MX_2 planes permitting the study of nearly isolated layers in the case of the very long chain amines (around 60 Å in length).[61b]

More recent research in this field has focused in the intercalation of other more complex chemical species. New organic-MX_2 hybrid materials have been accessed via delamination/flocculation or electrochemical procedures starting from the pristine TMDCs or via ionic exchange starting from the alkali metal intercalates previously described (*vide supra*).[65, 66, 67] The delamination approach has also been employed for the encapsulation of polymeric species in new composite materials.[68, 69] In addition, inorganic molecular guest species such as cationic polyoxometalates (POMs) have also been inserted in TMDC hosts.[70]

Intercalation in TMDCs and specially in group V dichalcogenides is of great interest since in many cases PLD-CDWs are suppressed, causing an increase of T_{SC}.[4] In other cases such as 2H-NbS_2, where no CDWs exist, the intercalation

61 a) Schöllhorn, R.; Sick, E.; Weiss, A. *Z. Naturforsh. B* **1973,** *28,* 168. (b) Gamble, F. R.; Geballe,T. H. *Treatise on Solid State Chemistry: Inclusion Compounds*, Plenum, New York, **1976**, Vol. 3, Chpt. 3. (c) Acrivos, J. W. in *Intercalated Layer Materials*, Ed. F. Levy, Dordrecht: D. Reidel, **1979**, Vol. 6, Chpt. 2. (d) Riekel, C.; Hohlwein, D.; Schöllhorn, R. *J. Chem. Soc., Chem. Commun.* **1976,** *863–864.*

62 Sarma, M.; Beal, A. R.; Nulsen, S.; Friend, R. H. *J. Phys. C Sol. State Phys.* **1982,** *15,* 4367–4378.

63 Beal, A. R.; Liang, W. Y. *Phil. Mag.* **1973,** *27,* 1397.

64 Klipstein, P. C.; Friend, R. H.; Yoffe, A. D. *Phil. Mag. B* **1985,** *52,* 611.

65 Divigalpitiya, W.; Frindt, R.; Morrison, S. *Science* **1989,** *246,* 369–371.

66 Hauptmann, A.; Lerf, A.; Biberacher, W. *Z. Naturforsch.* **1996,** *51b,* 1571.

67 Figueroa, E.; Brill, J.; Selegue, J. *J. Phys. Chem. Sol.* **1996,** *57,* 1123–1127.

68 Murphy, D.; Hull, G., Jr *J. Chem. Phys.* **1975,** *62,* 973–978.

69 a) Wang, L.; Kanatzidis, M. *Chem. Mater* **2001,** *13,* 3717–3727. (b) Yang, D.; Westreich, P.; Frindt, R. F. *Nanostruct. Mat.* **2004,** *12,* 467–470.

70 a) Lerf, A.; Lalik, E.; Kolodziejski, W.; Klinowski, J. *J. Phys. Chem.* **1992,** *96,* 7389–7393. (b) Nazar, L.; Jacobson, A. *J. Mater. Chem.* **1994,** *4,* 1419–1425.

of Lewis bases leads to some band filling and a consequent reduction of the density of state at E_F leading to a drop in T_{SC}.[71] Besides, the rich intercalation chemistry investigated has provided with powerful tool for the study of quasi-bidimensionality in these systems. Indeed, layer superconductivity is suggested by the fact that the intercalation of long chain amines, for which the number of carbon atoms was varied between 9 and 18, yielded materials with an approximately equal T_{SC} of around 3 K).[60a, 40] This is in contrast to the expected fall in T_{SC} should the Josephson coupling of Cooper pairs between layer be strong enough. Additionally, the fact that the intercalation of paramagnetic guest species (i.e. bis(cyclopentadienyl)chromium(III)) leads to similar T_{SC} as in the case of diamagnetic ones (i.e. bis(cyclopentadienyl)cobalt(III)) provides with an extra piece of evidence to support the idea that Cooper pairs do not tunnel across the van der Waals gap or they would otherwise be affected by the magnetic field located at the paramagnetic centres.[51a, 72] Therefore, the attractive interactions that give rise to the superconducting behaviour are thought to come from the intra-layer electron-phonon coupling with just minor contributions of inter-layer interactions.

However, that described in this section is just a small taste of the massive amount of research carried out concerning the intercalation of TMDCs. The topic has been the subject of many review articles and books covering the different areas previously outlined in greater detail.[4, 73] Yet, to the date little has been reported on multifunctional host-guest combinations involving TMDCs. In view of all the interesting properties intrinsic to specific TMDCs previously presented and also in view of their versatile intercalation potential, one may appreciate how it is an unbeatable opportunity to bring together different properties that have never before naturally coexisted in a material.

---

71 Hamaue, Y.; Aoki, R., *J. Phys. Soc. Jap.* **1986,** *55,* 1327.

72 Gamble, F. R.; Thompson, A. H., *Sol. State Commun.* **1978,** *27,* 379.

73 *For instance*: (a) Liang, W. Y. *Intercalation in Layered Materials*, Ed. M.S. Dresselhaus, Perseus Publishing, New York, **1986**. (b) Levy, F.A. (Ed.) *Intercalated Layered Materials, Physics & Chemistry of Materials with Layered Structures*, Kluwer Academic Publishers, Dordrecht, **1979**. (c) T. Hibma, *Intercalation Chemistry*, Eds.: Whittingham, M. S.and Jacobson, A. J., Academic Press, New York, **1982**.

4 Synthesis of TMDCs and simple intercalates

The synthesis of layered TMDCs has been exhaustively studied in the past. Indeed, from the very many TMDC analogues, only MoS_2 occurs naturally in an appreciable abundance. Even so, naturally occurring MoS_2 is normally found in the 3R or 2H phases.[74] So the demand for different MoS_2 polytypes and also for a wide range of different TMDC analogues is not by far covered by the natural ores. Thus the synthesis of pure TMDC powders and especially the growth of good quality large TMDC single crystals has been a very active field during the past half century within the context of materials science.

1 Polycrystalline materials

The synthesis of a binary TMDCs of general formula MX_2 has been traditionally performed by reacting stoichiometric amounts of the elemental constituents M and X inside evacuated silica tubes at high temperatures (see Equation 4.1).[75]

$$M + 2X \xrightarrow[in\ vacuo]{\Delta} MX_2$$

Equation 4.1 Generic equation for the ceramic synthesis of TMDC systems.

More recently, some alternative lower-temperature methods have been investigated. In this context, several synthetic approaches based on the solid-state metathesis of inorganic compound precursors have been proposed as rapid and more convenient approaches for the production of simple or mixed-metal TMDCs.[76] In addition, the solvothermal reaction of soluble precursors has also been explored as a potential alternative for the low-temperature synthesis of highly

74 a) Newberry, R. J. *Am. Miner.* **1979,** *64,* 758–767. (b) Newberry, R. J. *Am. Miner.* **1979,** *64,* 768–775.

75 a) Leith, R. M. A.; Terhell, J. C. J. M. in *Preparation and Crystal Growth of Materials with Layered Structures*, Ed. Leith, R. M. A., D. Reidel: Dordrecht, The Netherlands, ***1977***, pp. 141-223. (b) Brauer, G. *Handbook of Preparative Inorganic Chemistry*, Academic Press, New York, **1965**, Vols. 1 and 2.

76 a) Bonneau, P. R.; Shibao, R. K.; Kaner, R. B. *Inorg. Chem* **1990,** *29,* 2511–2514. (b) Bonneau, P. R.; Jarvis, R. F., Jr; Kaner, R. B. *Inorg. Chem.* **1992,** *31,* 2127–2132. (c) Bonneau, P. R.; Kaner, R. B. *Inorg. Chem.* **1993,** *32,* 6084–6087.

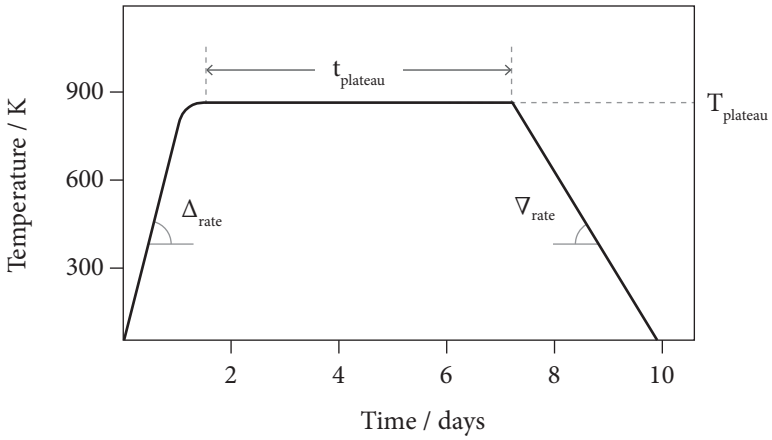

Figure 4.1 Temperature profile of a typical ceramic TMDC synthesis..

crystalline materials.[77] Though the methods reported do achieve remarkable improvements in the temperatures required and the times employed, none of the methods reported yield the homogeneity and crystal size attainable by the traditional ceramic approach. Furthermore, all the low-temperature syntheses required more complex and resource-consuming purification processes and some of them involved handling harmful precursors. Thus, the traditional ceramic approach was the method of choice for the synthesis of TMDCs.

1.1 The ceramic synthesis

The ceramic synthesis of TMDCs is a solid-state technique in which the elemental components in fine powder form are intimately mixed in first place and then sintered at high temperatures (typically between 500 and 1100 ºC) during long reaction times (generally several days, see Figure 4.1). As a result, free-flowing polycrystalline powder samples of TMDCs are obtained. In general, the samples are composed of micrometer size hexagonal prismatic crystallites with high aspect ratio habits. In order to avoid the formation of the metallic oxides the solid reacting mixture must be placed inside an evacuated quartz ampoule during the thermal treatment. The control of the different experimental parameters

77 a) Xuefeng, Q.; Yadong, L.; Yi, X.; Yitai, Q. *Mat. Chem. Phys.* **2000,** *66,* 97–99. (b) Chen, X.; Fan, R. *Chem. Mater.* **2001,** *13,* 802–805.

(temperature ramps and plateaus, reactions times, etc.) allows for the selective recovery of specific TMDC polytypes with particular crystallite morphologies.

In general terms and regardless of the MX_2 system considered, it is well established how the octahedral coordination geometry is stable at higher temperatures, while the trigonal prismatic coordination is thermodynamically favoured at lower temperatures.[78] This makes the cooling stage of the ceramic process (cooling rate, ∇_{rate}) a particularly crucial step for the isolation of the target polytype, since the system gradually passes through different regions of stability of the different coordination geometries. In other words, whereas the synthesis of a pure 1T polytype required a rapid ice-quenching from the sintering temperature in order to trap the metastable octahedral coordination, the isolation of the purely trigonal prismatic phases involved a slow and much more controlled cooling ramp. Less critical, though also important to some extent, were the heating ramp (Δ_{rate}), the plateau temperature ($T_{plateau}$), the reaction time ($t_{plateau}$) and the degree of packing of the reagents inside the ampoule.

It goes without saying that in order to be able to perform intercalation chemistry with TMDCs in a controlled manner later on, it is important to be aware of the polytype that is being handled. Of particular interest to this work are the trigonal prismatic polytypes of group V TMDCs, as they are the ones less affected by CDWs and thus exhibit higher T_{SC} (recall previous section 3 on page 78, Chapter 3). Unfortunately, the trigonal prismatic polymorphs are the hardest ones to isolate as suggested by the complex coordination geometry equilibria that occur during the ceramic cooling step. Yet strangely, the literature is full of references describing the facile one-step synthesis of pure 2H TMDCs.[59, 60] On the contrary our experimental results show that metastable octahedral contamination usually occurs and mixed coordination phases are obtained during the process (4Hb, 6R, etc.). In this way, one may demonstrate how several annealing stages following the initial sintering procedure were normally required if one wants to access the a pure trigonal prismatic coordination polytype. An example of a very exhaustive procedure for the transformation of a mixture of TaS_2 phases to the pure 2H polytype was described by Wang *et al.* (shown in Figure 4.2).[69a] During this multi-step procedure, the temperature is very gradually left to drop stopping

78 Di Salvo, F.; Bagley, B.; Voorhoeve, J.; Waszczak, J. *J. Phys. Chem. Sol.* **1973,** *34,* 1357–1362.

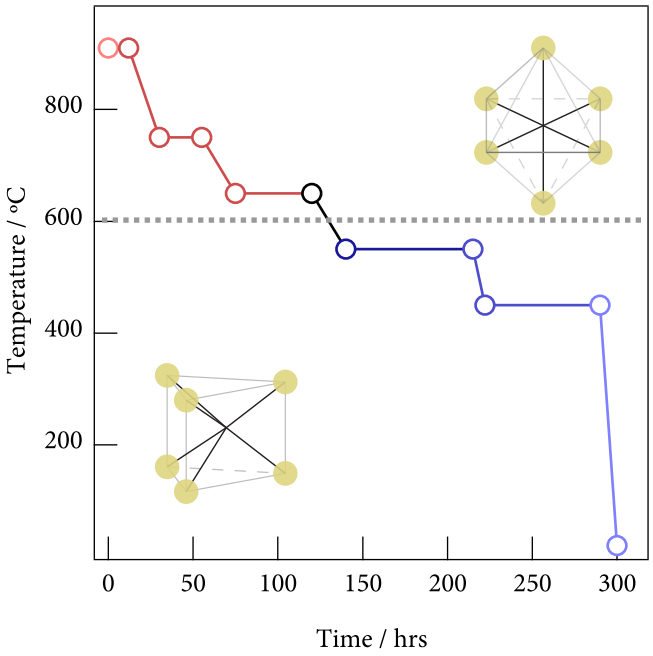

Figure 4.2 Multi-step annealing procedure proposed by Wang *et al.* for the isolation of 2H-TaS_2. The approximate regions of thermodynamic stability of the different coordination geometries are highlighted.

at certain temperature plateau where the equilibrium between coordination geometries is reached.

Next, a general overview of how the ceramic approach may be used for the synthesis of TMDCS in the pure 2H phase is provided. Due to the fact that different MX_2 systems exhibited different sensitivity to the experimental conditions, the synthesis of each TMDC analogue (or small group of analogues) is best discussed separately.

a. The system tantalum-sulfur

The synthesis of TaS_2 seemed particularly susceptible to subtle experimental changes. In order to illustrate the large variability of TaS_2 samples, a survey of the distinct crystallographic phases and sample morphologies obtained under

a

Test	Δ_{rate} / °C.min^{-1}	$T_{plateau}$ / °C	∇_{rate} / °C.min^{-1}	Load packing[79]
A	4.5	900	1.5	disperse
B	0.2	950	1.6	disperse
C	1	950	0.3	disperse
D	4.5	900	1.5	tightly packed
E	1	950	0.3	disperse
F	5	900	5	disperse

b

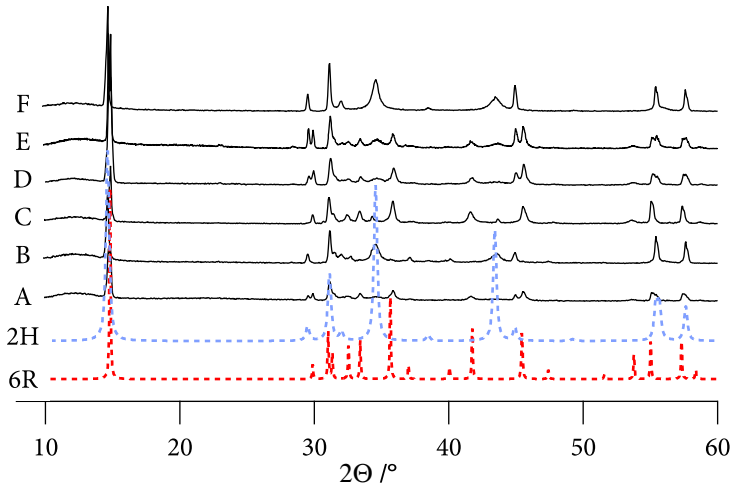

Figure 4.3 a. Range of experimental parameters surveyed in the synthesis of the TaS_2 system. The parameter naming is in accordance to that defined in Figure 4.1 **b**. Experimental XRPD patterns corresponding to the different tests listed in **a**. and simulated patterns of polytypes 2H and 6R.

different experimental conditions was conducted.[79] The initial conditions tested corresponded to those reported in the literature for the synthesis of pure 2H-TaS_2 (conditions A).[59, 60] Variations were then performed with respect to this starting point. A collection of the experimental parameters surveyed together with the XRPD profiles of the resulting polycrystalline materials are showed in Figure 4.3. The qualitative comparison of the experimental XRPD patterns (*continuous*) with the simulated ones (*dashed*) permits appreciating how the resulting materials are

79 The reagents were either evenly distributed along the ampoule's length (*disperse*) or accumulated at one end (*tightly packed*).

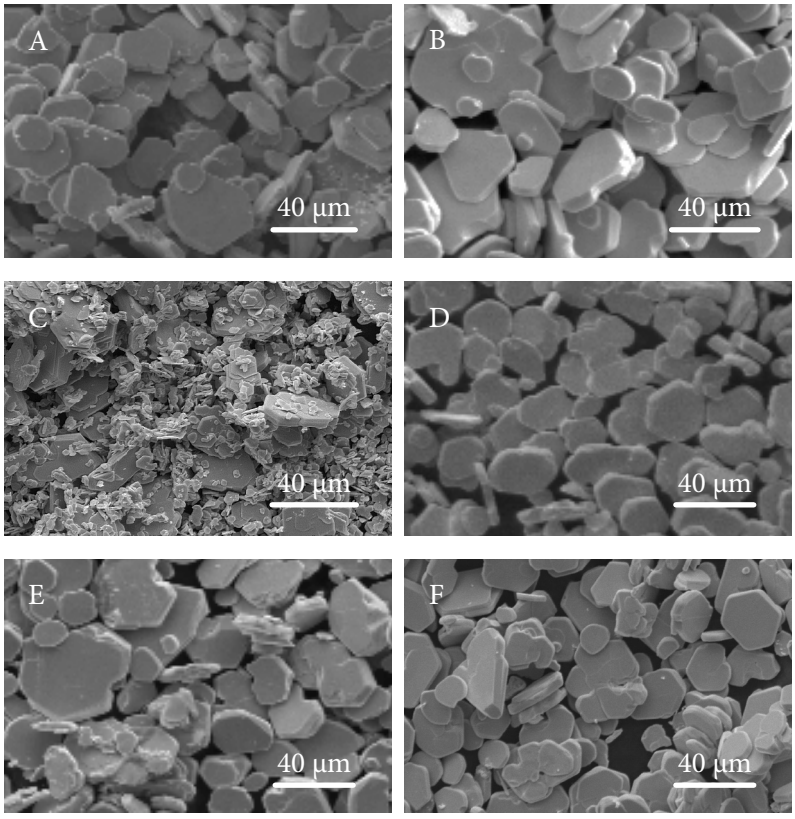

Figure 4.4 SEM images of polycrystalline TaS_2 samples corresponding to tests A - F described in Figure 4.3 a.

composed of a mixture of different polytypic phases (namely 2H and 6R) and how the nature of that blend varied as the set of testing conditions were changed. Likewise, the crystallite morphology and sizes of the resulting samples were also sensitive to the experimental parameters. The inspection of the samples via SEM permitted identifying a big dispersion both in size and homogeneity (view Figure 4.4). Among all the experimental conditions surveyed, the conditions of test F afforded the best and most homogeneous hexagonal crystallite morphologies and the most pure 2H phase.

However, it may be appreciated how a single-step ceramic process is not sufficient to achieve a high degree of polymorphic purity. A high purity 2H-TaS_2 sample (**1**) could only be achieved by the thermal annealing of the polycrystalline

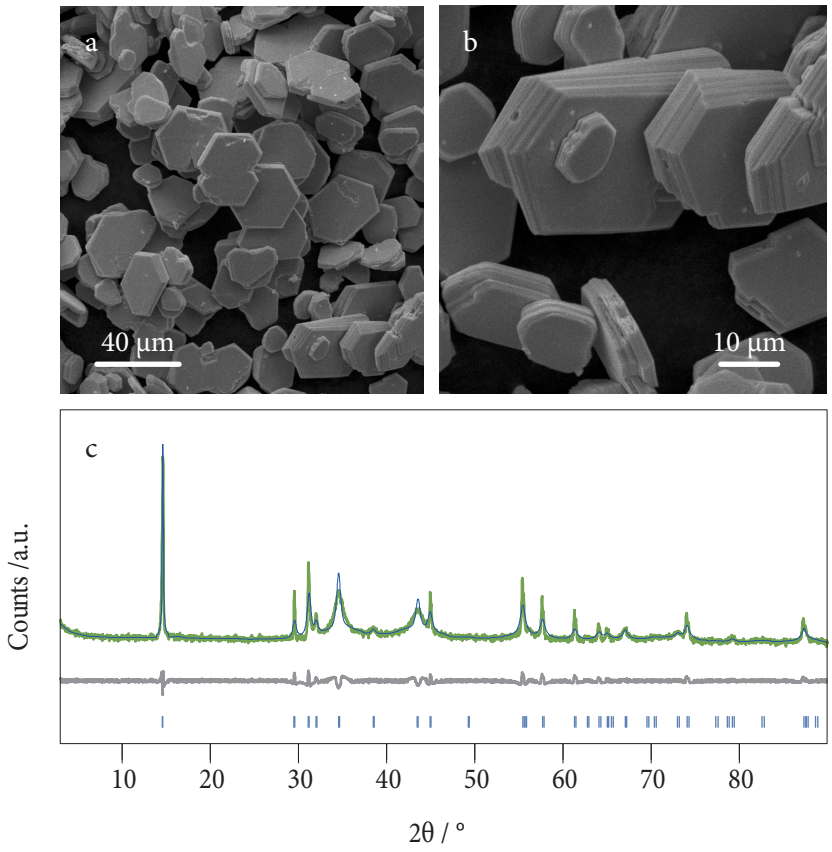

Figure 4.5 Characterisation of a TaS_2 sample annealed following the thermal treatment described in Figure 4.2. **a**. SEM image showing crystallite morphology. **b**. Close-up SEM image of the layered edges and vertex of a few hexagonal TaS_2 platelets. **c**. Le Bail refinement of the XRPD pattern.

sample synthesized in the first step under conditions F. The annealing step was accomplished by resealing the material back inside a new evacuated quartz ampoule and by either keeping the system at 450 ºC during two weeks or by following the multi-step process shown in Figure 4.3.[69a, 70b] The latter allowed for a better reproducibility than the former, so unless otherwise stated it was the standard annealing process employed. In this way, a two-step procedure (sintering + annealing) guaranteed a very homogeneous sample made out of hexagonal platelets of around 40 µm long as seen by SEM (Figure 4.5, *top*). The crystallites exhibited much more defined facets in comparison with those obtained after the

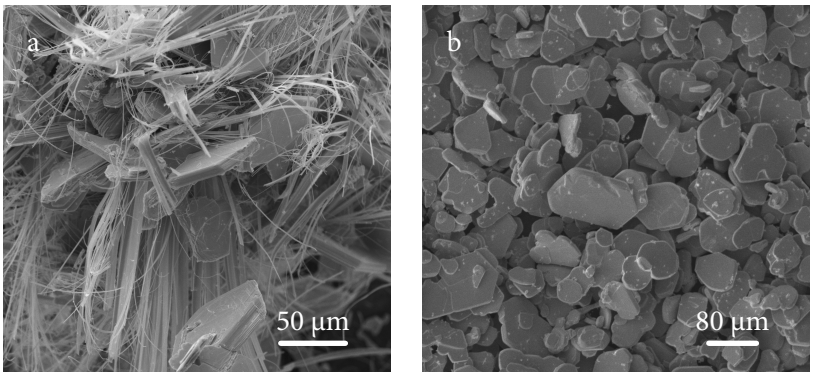

Figure 4.6 SEM images of polycrystalline two $TaSe_2$ samples synthesized under the same reaction conditions (Δ_{rate} = 1.5 ºC.min^{-1}, $T_{plateau}$ = 900 ºC) and varying cooling ramps. **a**. Ice-quenched to room temperature. **b**. Slow cool-down step (∇_{rate} = 1.5 ºC.min^{-1}).

first step. The phase purity was confirmed by conducting Le Bail refinements on the experimental XRPD patterns of **1** (Figure 4.5).[80] The data showed an excellent fit to a single-phase model (R_{wp} = 0.2236; R_{Bragg} = 0.040 and gof = 4.86, where R_{wp} is the weighted-profile R-factor)[81] with a hexagonal cell with *a* = 3.3105(2) Å and *c* = 12.071(1) Å in agreement with that described for TaS_2 layers with trigonal prismatic Ta coordination in 2H-TaS_2 (recall Table 3.1 on page 71).

Finally, the chemical composition was confirmed by the combination of elemental analysis data with EPMA data. Both techniques were consistent with the 1Ta : 2S stoichiometry in most occasions. Only for some samples an excess of S could be observed. In those cases the excess S could be selectively removed by *in vacuo* sublimation at 300 ºC. As a matter of fact, this purification step could be more conveniently performed *in situ* inside the first ampoule containing the TaS_2 non-annealed mixture just after the first sintering step.

b. The system tantalum-selenium

A similar scenario was found in the case of $TaSe_2$. The same experimental conditions tried out for TaS_2 yielded extremely heterogeneous samples in the

80 Le Bail, A.; Duroy, H.; Fourquet, J. L. *Mater. Res. Bull.* **1988,** *23,* 447–452.

81 Young, R. A. *The Rietveld Method*, Oxford University Press, Oxford, **1993**, pp. 1–38.

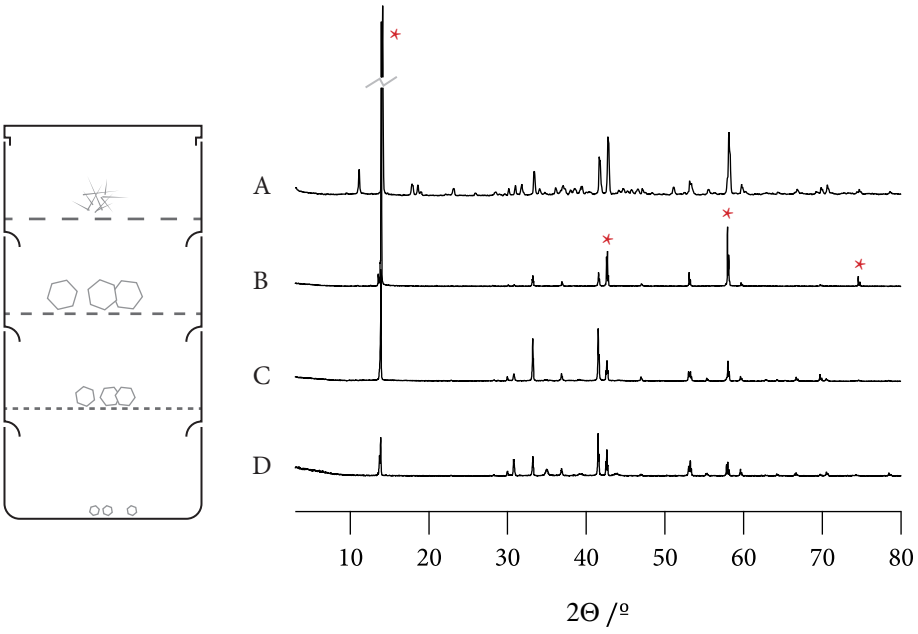

Figure 4.7 Separation of different crystallite forms present in $TaSe_2$ annealed reaction mixtures by simple sifting. The corresponding XRPD patterns are shown in the *left* hand side. The out-of-plane peaks have been marked with an asterisk: (002), (006), (008) and (0010) from *right* to *left*.

case of the selenium analogue. Indeed, while a very clean platelet-like 1T phase was obtained by ice-quenching, two clearly different crystal habits (needle- and platelet-like) were always observed whenever the synthesis was aimed at the trigonal prismatic polytypes (see Figure 4.6). Though a variation of the synthetic conditions could help to minimize the amount of needle-like crystallites, these were always present in slowly-cooled samples. The two types of crystallites persisted even after performing long annealing treatments.

In order to ascertain the nature of the two types of crystallites, the distinct crystal habits could be successfully segregated by the use of manually operated metal sieves. In this way, 4 different fractions (A - D) were isolated from the crude reaction mixture, the first three being held back by the 500 μm (mesh 1, A), the 250 μm (mesh 2, B) or the 75 μm (mesh 3, C) opening sieve in turn, and the rest being collected at the bottom (D, see Figure 4.7). Whilst the mesh 1 sieve retained most of the needle-like structures held together in the form of bunches together

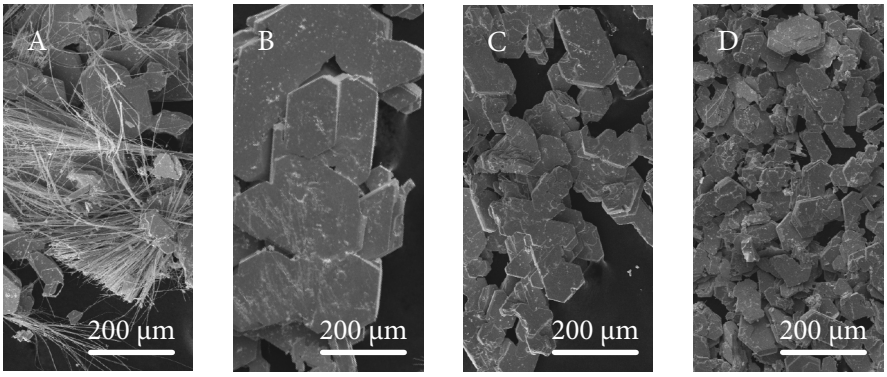

Figure 4.8 SEM images of the different sifted fractions (described in Figure 4.7) of a $TaSe_2$ annealed sample.

with some of the larger hexagonal crystallites, fractions B, C and D were mainly composed of platelet-like crystallites (view Figure 4.8). Indeed, the powder pattern of fraction A is totally different from the profiles of fractions B - D. The pattern of A fails to refine within the hexagonal/trigonal crystal system. On the contrary, B, C and D exhibit exactly the same peaks and in the exact same positions and are well described by a CdI_2-type lattice model (2H-type lattice). The difference between the three diffractograms may be ascribed to the preferred orientations of the crystallites on the flat plate sample holder on which they were deposited for X-Ray data collection (θ-θ reflection geometry experiment). In this context it is easy to appreciate how the relative intensity of out-of-plane reflections (marked with an asterisk in Figure 4.7) with respect to the rest of the peaks decreases as the crystallite aspect ratio decreases (B > C > D, Figure 4.8) The powder patterns of B - D were refined by the Le Bail method to a single phase model in the $P6_3/mmc$ space group symmetry within the hexagonal crystal system and with resulting unit cell parameters of a = 3.4362(1) Å and c = 12.7043(4) Å (R_{wp} = 0.1808; R_{Bragg} = 0.0518 and gof = 2.70).

The 1Ta : 2Se stoichiometry of fractions B - D phase was once here confirmed by EPMA, depicting an homogeneous chemical composition throughout. On the contrary, the fibres observed in fraction A depicted a higher Se content (Se/Ta = 2.5). This confirms the different chemical nature of such needle-like crystallites

and is in accordance with the completely discordant XRPD patterns with respect to the rest of the fractions isolated.

Though fractions B to D seemed coincident both chemically and structurally, only type-D $TaSe_2$ specimens (**2**) were used as starting materials in subsequent chemical process. The choice was based upon the enhanced crystallite homogeneity of fraction D. In addition, the crystallite size was more reasonable for later intercalation purposes. In this context, too large crystals present deeper van der Waals voids which are more difficult to access by guest species, thus hindering total bulk intercalation.

c. The niobium dichalcogenides

Oppositely to the other systems previously described, both NbS_2 and $NbSe_2$ exhibited an enhanced robustness to the ceramic process experimental conditions. For the latter systems, a smaller degree of contamination of mixed coordination polytypes was found even in the event of slow cool-down ramps. The resulting polycrystalline samples also presented more homogeneous crystallite morphologies and more reproducible XRPD patterns. Nevertheless, the two step ceramic approach was here also employed for the synthesis of high quality polycrystalline samples of $NbSe_2$ (**3**) and NbS_2 (**4**). The Le Bail refinements of the XRPD patterns of samples **3** and **4** depicted an excellent fit in both cases to a pure 2H polytype model. Table 4.1 sums up the cell refinements of all the successfully isolated 2H TMDC polycrystalline samples.

Alias	System	Space group	a /Å	c / Å	α /º	γ /º	R_{wp}	R_{Bragg}	gof
1	2H-TaS_2	$P6_3/mmc$	3.3105(2)	12.071(1)	90	120	22.36	4.03	4.86
2	2H-$TaSe_2$	$P6_3/mmc$	3.4362(1)	12.7043(4)	90	120	18.08	5.18	2.70
3	2H-$NbSe_2$	$P6_3/mmc$	3.44577(3)	12.5449(4)	90	120	17.32	5.93	1.81
4	2H-NbS_2	P-6m2	3.4441(1)	12.5483(6)	90	120	18.13	5.60	3.29

Table 4.1 Le Bail unit cell refinement parameters and discrepancy indices of the XRPD patterns of 2H TMDCs accessed via the two-step ceramic process. All of the have been fit in the hexagonal crystal system where a = b and α = β. R coefficients are given as percentages.

2 Large TMDC single crystals

The polycrystalline materials so far described are the starting point of a rich intercalation chemistry, finding application not only in a wide range of fields within materials science but also within the context of industry (*vide supra* section 1, Chapter 3, page 72). However, other more fundamental aspects of research in TMDCs require for large crystal sizes. Large single crystals provide with the possibility of macroscopically manipulating these systems to study their anisotropic properties or to integrate them in devices. Their high aspect ratio crystal habits permit identifying the relative orientation of the atomic structure within the well-defined facets. Thus it is easy to manually wire bond them along specific crystallographic directions or to place them within an external magnetic filed at a given relative orientation. In addition, their large basal plane areas make them convenient candidates for exfoliation of large surface-area flakes or for performing surface chemistry.

In this way, the synthesis of large single TMDC crystals has fuelled much research in the past. The high melting points (generally above 1000 ºC) of these systems, which are also close to the decomposition limit, have generally hindered crystallization from the molten state.[1] That traditionally reported in the literature suggests that TMDC crystals are best obtained by the chemical vapour transport (CVT).[82] However, alternative vapour transport methods derived from the CVT approach, namely the direct vapour transport (DVT) method, may also be employed.[83]

The CVT reactions have been widely utilized in the past for the crystallisation of non-volatile compounds. The method relies in the reversible transformation of the different non-volatile components into volatile entities.[84] For this purpose, the technique involves the use of a *transport agent*, which is a chemical species that reacts with the different components to generate the mentioned volatile

82 a) Hicks, W. T. J. *Electrochem. Soc.* **1964,** *111,* 1058. (b) Greenaway, D. L.,; Nitsche, R. *J. Phys. Chem. Sol.* **1965,** *26,* 1445. (c) Domingo, G.; Itoga, R. S.; Kannewurf, C. R. *Phys. Rev.* **1966,** *143,* 536. (d) Kershaw, R.; Vlasse, M.; Wold, A. *Inorg. Chem* **1967,** *6,* 1599–1602. (e) Conroy, L. E.; Park, K. C. *Inorg. Chem* **1968,** *7,* 459–463. (f) Dalrymple, B.; Mroczkowski, S.; Prober, D. *J. Cryst. Growth* **1986,** *74,* 575–580.

83 Al-Hilli, A. A.; Evans, B. L. *J. Cryst. Growth.,* **1972,** *15 (2),* 93 - 101.

84 a) Schäfer, H. *Chemical Transport Reactions*, Academic Press, 1964. (b) Gruehn, R.; Glaum, R. *Angew. Chem. Int. Ed* **2000,** *39,* 693–716. (c) Gruehn, R.; Glaum, R. *Angew. Chem* **2000,** *112,* 706–731.

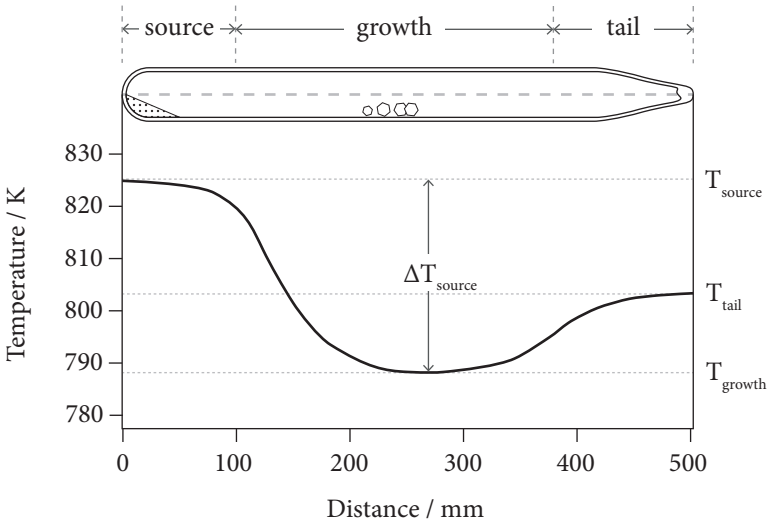

Figure 4.9 Scheme illustrating the temperature profile established along the silica tube during a typical CVT single crystal growth experiment.

molecular compounds. Common transport agents are iodine, bromine or chlorine, though hydrogen halides or elemental dichalcogenides are sometimes also used.[85, 86] The components are placed at one end (*source* zone) of a sealed reaction vessel (generally a fused silica ampoule) under very low pressures. Next, a temperature gradient is set along the length of the reaction vessel, causing the volatile species to migrate from the source zone where they are produced. The temperature of each zone of the ampoule is set by independent heating elements of a split tube multi-zone tubular furnace.[87] A typical CVT temperature gradient may be observed in Figure 4.9. This temperature gradient provokes the release of the parent components in a different region of the vessel (*growth* zone) where the thermal conditions favour the splitting of the volatile species into the original components. This depends on the thermodynamics of the reaction between the transported solid and the transport agent. For instance, when the reaction is endothermic, the solid will be transported from the hotter end to the cooler one

85 Krabbes, G.; Oppermann, H.; Wolf,. E. *Z. Anorg. Allg. Chem.* **1976,** *423,* 212.

86 Schäfer, H. *Z. Anorg. Allg. Chem.* **1982,** *486,* 33.

87 a) Otto, C. A. *Electric Furnaces*, George Newnes, **1958**. (b) Sunil, K.; Ittyachen, M. A. *In. J. Pure Appl. Phys.* **1997,** *35 (6),* 384-386.

where the volatile species is unstable in favour of the parent components. This is the case of most TMDCs as may be inferred from previous studies in which single crystals always develop in the cold zones of the reaction vessel.[82] In view of the well-established iodine vapour transport mechanism of group IV and V metals,[88] it is suggested that pentaiodide volatile species are responsible for the migration of the solid TMDCs. In addition, the chalcogenide atoms are mostly present as X_2 species in the high temperature range that is often used for transport reactions.[89] Equation 4.2 illustrates the solid-vapour equilibrium for a generic TMDC CVT process and Figure 4.10 provides with a visual scheme of the transport process.

$$MX_{2}(s) + \tfrac{5}{2} I_{2}(g) \rightleftarrows MI_{5}(g) + X_{2}(g) \quad \Delta H_{T,P} > 0$$

Equation 4.2 Generic CVT mechanism proposed for a TMDC-I_2 system.

The synthesis of TMDC single crystals via the CVT approach was first reported back in the 60s.[90] The synthetic procedure was later greatly improved by Kershaw *et al.*[82d] In this report, iodine is suggested as the most convenient transport agent, though it is also conjectured that some intercalation may occur. Nevertheless, previous studies demonstrate that no remarkable iodine take-up occurs even in the presence of higher iodine concentrations.[82] The transport agent partial pressure inside the reaction vessel has also an important effect in the chemical vapour equilibria.[89] For instance, classical thermodynamic calculations for the WSe_2 analogue have permitted realising how relatively low iodine partial pressures favour the transport of the solid TMDCs from the source zone.[91] Hence, iodine was the transport agent of choice and both in order to avoid the potential inclusion of molecules of transport agent in the layered crystals and also to enhance the migration of solid material inside the reaction vessel, the concentration was best kept low (~ 1 mg cm^{-3}, grams per unit inner volume of the reaction ampoule).

Other experimental parameters such as the reaction vessel geometry (shape, length and internal volume), the inner pressure/vacuum, the temperature profiles,

88 Jeffes, J. H. E.; Marples, T. N. R. *J. Cryst. Growth* **1972,** *17,* 46–52.

89 Schmidt, P.; Binnewies, M.; Glaum, R.; Schmidt, M. in *Advanced Topics on Crystal Growth,* Ed. Ferreira, S. O., InTech, **2013**, Chapter 9.

90 Brixner, L. H. *J. Inorg. Nucl. Chem.* **1962,** *24,* 257.

91 Sunil, K.; Ittyachen, M. A. *Bull. Mat. Sci.* **1997,** *20 (2),* 231-238

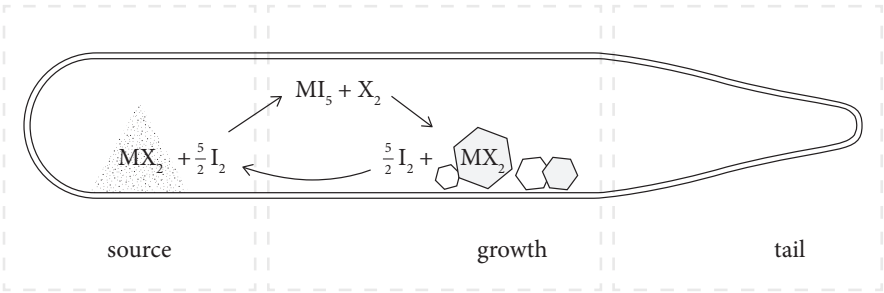

Figure 4.10 Cartoon illustrating the CVT process in a TMDC-I_2 system.

the heating and cooling rates and the use of crystallisation seeds have also been surveyed in the past.[82, 92] Based on the findings reported by these previous TMDC CVT studies, a series of basic experimental requirements were initially fixed. In that which concerns the CVT system, fused silica ampoules of *ca.* 75 cm^{-3} of inner volume and 18 mm in external diameter were employed as the reaction vessel and they were thoroughly cleaned with distilled water and different organic solvents prior to being used. It is also worthwhile mentioning that a three-zone (source, growth and tail) temperature profile with independent heating elements was employed (such as the one introduced in Figure 4.9). This allowed for two separate temperature gradients to be generated in such a way that the coolest part of the tube (growth zone) remains at the centre of the tube rather than at the end (two-zone configuration). In turn, it permited the crystals to grow in an isolated manner and prevents them from crowding at the round edge of the tube. The crystal quality is said to be greatly improved by the three-zone configuration.[82d] Finally, particular care was also taken to evacuate the silica ampoule down to a pressure of under 10^{-4} mbar (in a typical experiment the internal pressure was approximately $5{\cdot}10^{-5}$ mbar) prior to being flame-sealed, assuring the facile sublimation of the volatile components inside the vessel and at the same time guaranteeing an oxygen-free atmosphere. Now regarding the thermal treatment of the CVT system, a basic three-stage process was always followed. An example of the typical thermal variations that take place at each zone of the furnace can be seen in Figure 4.11. An initial *inverse* temperature gradient ($T_{growth} > T_{source}$)

92 a) Gobrecht, J.; Gerischer, H.; Tributsch, H. *J. Electrochem. Soc.* **1978,** *25,* 1086. (b) Fan, F. R.; White, H. S.; Wheeler, B.; Bard, A. J. *J. Electrochem. Soc.* **1980,** *27,* 518.

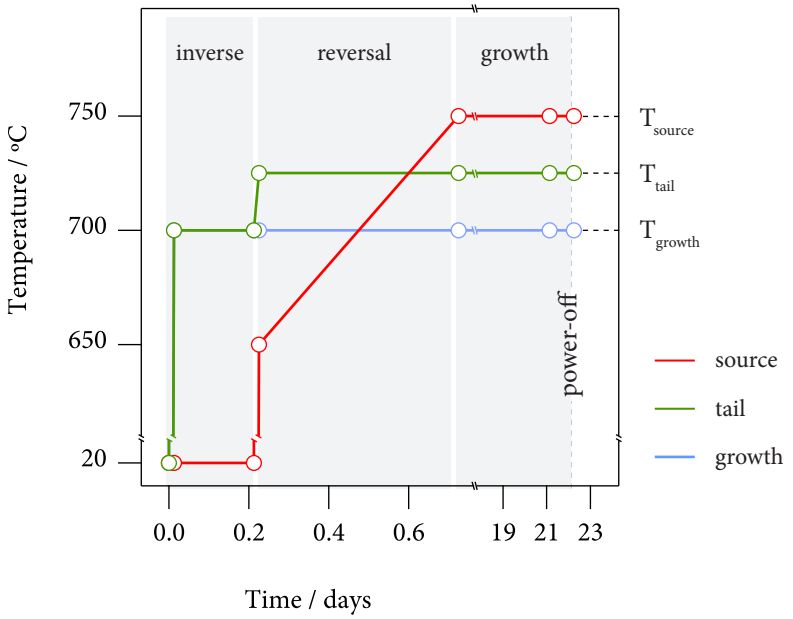

Figure 4.11 Scheme illustrating the temperature variations in the three independently-heated sections of a split-tube furnace (source, growth and tail) during a typical CVT single crystal growth experiment. The three stages of the CVT process are highlighted by the shaded areas.

was always established in order to wipe out as many nucleation centres from the growth zone as posible. Next, the temperature of the source zone is very gradually raised during the gradient *reversal* stage until the final thermal difference is reached ($\Delta T_{growth} = T_{source} - T_{growth} > 0$). The temperature of the tail is rapidly raised to confine the crystal groth in the cenrtal region. During this step, the migration towards the growth zone is very slowly engaged and nucleation occurs. The final stage is a stationary growth step where conditions are kept constant, allowing the crystals to reach the desired size. At the end of the process the heating elements were simply turned off.

As in the case of the synthesis polycrystalline materials, the temperature variations could be finely adjusted for the growth of specific polytypic phases. In this way, some investigation was carried out in order to elucidate what were the best conditions to synthesise large single crystals of pure trigonal prismatic coordination phases. In this occasion, with the exception of TaS_2, all Ta and Nb

analogues were found to yield similar results. Thus, the synthesis was optimized independently for the case of TaS_2.

2.1 Tantalum disulphide

The CVT growth of TaS_2 large crystals has been previously looked into by Conroy *et al.*[93] On that note, the specific synthesis of 2S or 1S phases was controlled on the basis of seeding techniques.[94] Yet, the phase control solely based upon the fine tuning of the thermal conditions was desirable. Other than the mentioned report, there are very few publications devoted to the CVT synthesis of TaS_2 polymorphs. In this way, the seminal works published by Kershaw *et al.* on different TMDC analogues also served as a good starting point for the current investigation.[82d]

As expected, the variation of the thermal parameters involved in the three-stage CVT process gave rise to the growth of different size, different habit and different polytype crystals. Among the list of parameters that could be tuned, the temperature gradient at the growth stage (ΔT_{growth}) and the temperature of the growth zone during the same stage (T_{growth}) were found to have the greatest influence in the crystalline phase and morphology of the resulting TaS_2 crystals. The list of conditions tested are listed in Table 4.2 (page 111). In order to analyse the polymorphic composition of the isolated crystals, a sample of a few crystals extracted from the growth zone of each test ampoule was finely *sliced* to powder. Note that the word *sliced* rather than the term grinded has been here used. Indeed TMDC crystals exhibited an enhanced lubricity, fact which made it impossible to grind them with pestle and mortar.[95] By contrast, the crystals could be easily cut into small pieces suitable for XRPD analysis, with the help of a sharp razor blade. It is noteworthy how under most of the conditions explored, a mixture of 4Hb and 2H polytypes in the form of long shiny ribbons was produced. Even more strangely, if the temperature at the growth zone (T_{growth}) was reduced in an attempt to stabilize the trigonal prismatic coordination, the pure 4Hb phase (**5**) was isolated. For T_{growth} = 700 ºC (conditions D), the crystal habits are much more bulkier than in higher temperature tests and exhibit layered facets (see Figure

93 Conroy, L. E.; Pisharody, K. R. *J. Sol. Stat. Chem.* **1972,** *4,* 345–350.

94 At the time when Conroy *et al.* published their studies, the polytype were named according to the number of layers in the unit cell n and adding an S: 1S, 2S, etc.

95 Wilson, J. A.; Yoffe, A. D. *Adv. Phys.* **1969,** *18,* section 3, p. 217.

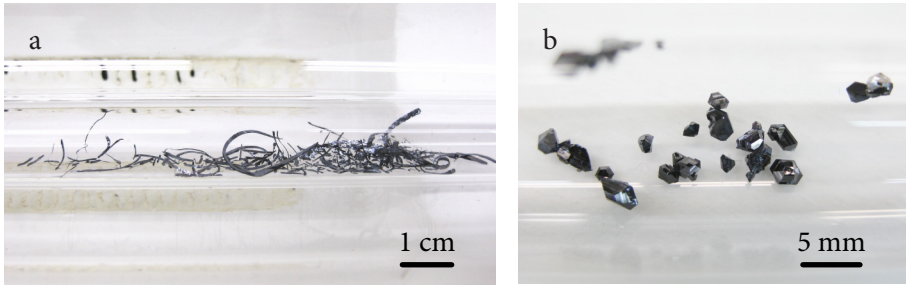

Figure 4.12 Photographs of the growth zone of two different TaS_2 CVT tests. Different crystal morphologies result from different CVT conditions: thin long ribbons for conditions B (**a**) and bulk crystal habits for conditions D (b, see Table 4.2)

4.12). The Le Bail refinements of the corresponding XRPD pattern provides with excellent figures of merit for the fitting (R_p = 8.47, R_{wp} = 12.22) to a single-phase 4Hb model. However, the detailed inspection of the higher T_{growth} tests A - C permitted one to distinguish at least 4 different types of crystal morphology: non-faceted flakes, ribbons, high-aspect ratio triangular prisms and hexagonal prisms (see inset photographs in Figure 4.13). Though all four crystal types were found in test conditions A to C, A was found to have a higher content of ribbon-like structures together with undefined shape flakes, B was primarily made out of triangular-habit crystals and C exhibited predominately hexagonal prisms. While all the diffraction peaks exhibited by the ribbon-, hexagon- and triangle-like crystals could only be indexed assuming a mixed 2H/4Hb phase, the XRPD patterns showed by the flakes could be associated to a pure 2H polytype. The Le Bail refinement of the latter suggested that the unit cell parameters were a = 3.3137(2)Å and c = 12.076(1)Å (R_p = 10.25, R_{wp} = 14.52), in good agreement with that reported for the 2H phase of TaS_2.[96] Thus it is concluded that, at least for the experimental conditions surveyed, the best way to isolate pure large 2H-TaS_2 crystals (**6**) is to carry out a manual Pasteur-like separation of samples prepared under CVT conditions A.

The diameter of the reaction ampoule was pointed out by some theoretical studies as an important experimental parameter in the isolation of big size and

96 Meetsma, A.; Wiegers, G. A.; Haange, R. J.; de-Boer, J. L. *Acta Cryst.* **1990,** *C46,* 1598–1599.

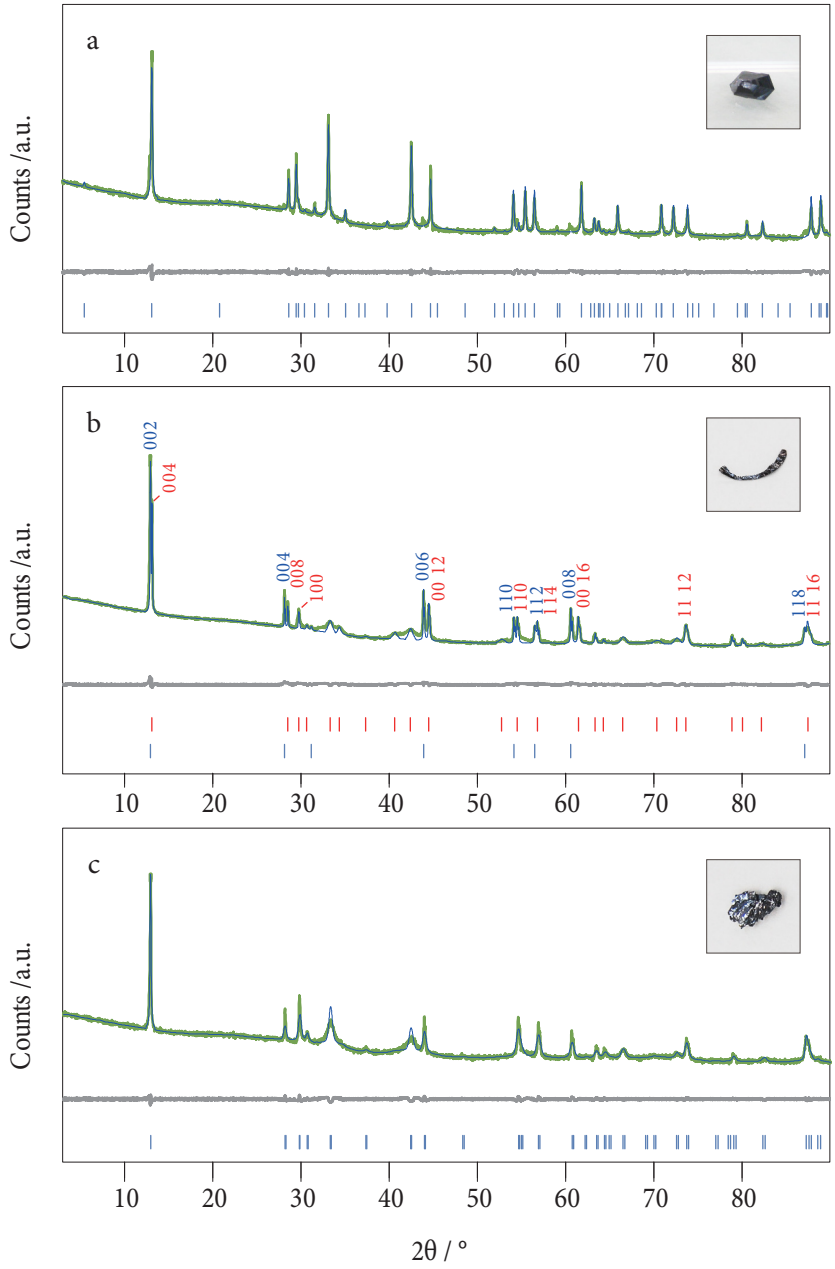

Figure 4.13 Three different crystal habits found in CVT test conditions A - C and their corresponding XRD patterns (*green*) and Le Bail unit cell refinements (*blue*): 4Hb pyramid (**a**), 2H/4Hb ribbon (**b**), 2H flake (**c**). The most prominent peaks at b have been tagged with the corresponding (*hkl*) indices of the 2H (*blue*) and 4Hb (*red*) phase components.

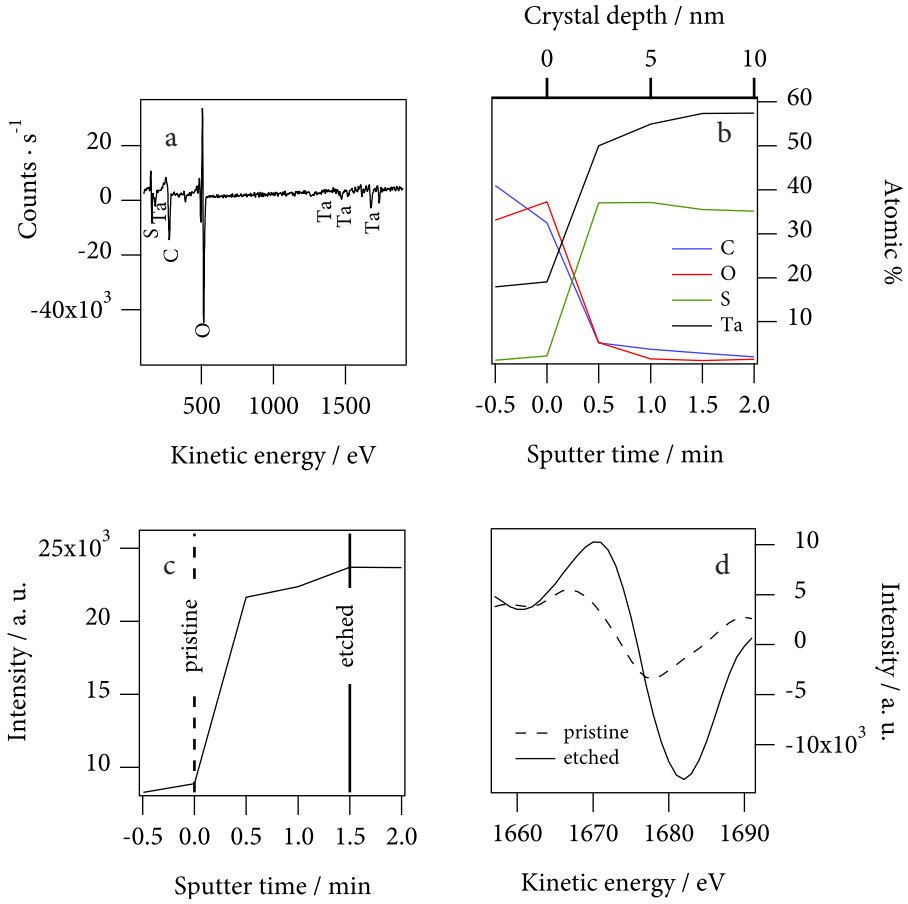

Figure 4.14 AES analysis of the surface of a TaS_2 crystal. **a**. Full range AES spectrum of the surface of a TaS_2 crystal. **b**. Depth profile study of the composition as a function of the sputtering time. **c**. Evolution of the intensity of the Ta peak as the outer layers of the crystal are gradually sputtered away. **d**. Ta peak shape coming from the outer layers and from the bulk crystal.

good quality crystals.[97] Yet, no difference was observed among the same process carried out in 18 and 9 mm OD fused silica ampoules.

The chemical analysis via EPMA allowed for the probing of the bulk composition of the crystals obtained under different conditions. In all cases and regardless the crystal habit and the polytypic nature of the specimen, the

97 Zuo, R.; Wang, W. *J. Cryst.Growth* **2002,** *236,* 695–710.

data depicted a non-ideal stoichiometry far from the expected 1Ta : 2S ratio. However, it is well-established how TMDCs tarnish with time, in such a way that it may be observed how nanometer-thick oxide layer generally covers the whole surface of the crystal. A surface chemical probing technique as is Auger electron spectroscopy (AES) was here employed for these means.[98] These experiments were conducted in collaboration with Dr Sergio Tatay (Unité Mixte de Physique CNRS/Thales, France). Indeed, AES spectra of the surface of as-synthesized of **5** exhibit remarkable impurities of C, O and N. Following, an ion milling of the outermost layers of the crystal with Ar^+ ions was performed. The electron probe of the resulting surface revealed that the underlying material, characteristic of the bulk composition, was basically Ta and S. A depth profile of the atomic percentage content of the different elements present in the crystal as a function of the etch duration is showed in Figure 4.14. The etch duration has been roughly converted to sample depths (*top* axis of Figure 4.14b) taking into account an estimated etch erosion of 5 nm min^{-1}. In addition, it is observed that the shape and position of the Ta peak changes with etching time. This can be due to the presence of different Ta species: TaO_x at the very surface and TaS_2 in the bulk. The difference between the ideal stoichiometry and the observed one may be ascribed to surface artifacts such as potential species reduction under the electron beam, or preferred sputtering of S with respect to Ta, as has been previously reported for other sulfur-containing materials.[99]

2.2 Tantalum diselenide and niobium dichalcogenides

The Nb dichalcogenide family was particularly easy to grow in the form of large high-aspect-ratio hexagonal prisms. In particular, the $NbSe_2$ system could be easily obtained as flat hexagonal plates of over one centimetre in length (**7**) by employing the CVT conditions D (Table 4.2). These crystals displayed mirror-like polished facets. In the case of $TaSe_2$ and NbS_2, large single crystals with relatively flat faces (**8** and **9** respectively) could also obtained by setting the exact same

98 A short description of the AES technique has also been included in Appendix 4.2 on page 285.

99 a) Graedel, T. E.; Franey, J. P.; Gualtieri, G. J.; Kammlott, G. W.; Malm, D. L. *Corrosion Science* **1985,** *25,* 1163–1180. (b) Fominski, V. Y.; Nevolin, V. N.; Romanov, R. I.; Smurov, I. *J. Appl. Phys.* **2001,** *89,* 1449.

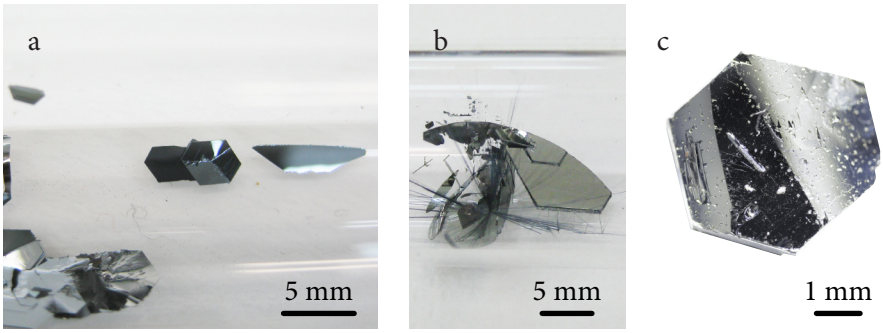

Figure 4.15 Photographs of CVT-grown crystals of 2H-$TaSe_2$ **6** (**a**) and 2H-$NbSe_2$ **7** (**b**) inside the reaction ampoules and an isolated 2H-NbS_2 **8** (**c**).

conditions. In the former case some of the specimens recovered exhibited the typical spiral-like growth features (see Figure 4.15a).[1, 100]

The high aspect ratio crystal habits in which this group of analogues grew under the conditions described was indicative of a pure trigonal prismatic coordination phase as pointed out by Di Salvo *et al.*[6] Nevertheless, XRPD studies of ground samples were carried out in order to ascertain the exact polytypes that had been isolated. In this way, samples **7**, **8** and **9** could be successfully fitted by the Le Bail method to a 2H pure phase model. Details of the exact lattice parameters are listed in Table 4.2. In conclusion, experimental conditions D that had been originally optimized for the TaS_2 systems prove as universal conditions for the isolation of the 2H phase of tantalum diselenide and the niobium dichalcogenides. This allows for the simultaneous crystal growth of the three systems in the same CVT process and thus permits optimising resources.

100 a) Yousefi, G. H. *J. Mat. Sci. Lett.* **1990,** *9,* 1216–1217. (b) Sumesh, C. K.; Patel, K. D.; Pathak, V. M.; Srivastava, R. *J. Ovonic Res.* **2008,** *4,* 61–68. (c) Patel, A.; Bhayani, M.; Jani, A. *Chalcogenide Letters* **2009,** *6,* 491–502. (d) Agarwal, M.; Patel, J.; Patel, H. *Bull. Mat. Sci.* **1979,** *1,* 107–112.

System	Test	Experimental conditions						Crystal charcateristics			
		$\Delta T_{inverse}$ / °C	$v_{reversal}$ / °C·h^{-1}	ΔT_{source} / °C	T_{growth} / °C	ΔT_{tail} / °C	t_{growth} / h	a / Å	c / Å	Polytype	Habit
TaS_2	A[82d]	875	1	50	750	125	120	3.3137(2)	12.076(1)	2H	flake
	A	875	1	50	750	125	120	3.342(4)	12.06(2)	2H	ribbon
								3.316(8)	23.88(3)	4Hb	
	B	875	1	75	750	125	120	3.331(8)	12.07(3)	2H	triangular prism
								3.324(6)	23.94(5)	4Hb	
	C[82f]	875	1	30	770	30	17280	3.324(5)	12.07(3)	2H	ribbon
								3.328(8)	23.95(4)	4Hb	
	C	875	1	30	770	30	17280	3.316(2)	12.105(7)	2H	hexagonal prism
								3.312(6)	24.03(5)	4Hb	
	D	700	0.01	50	700	25	21600	3.33841(7)	23.7602(5)	4Hb	pyramid
$TaSe_2$	D	700	0.01	50	700	25	21600	3.43910(5)	12.7067(2)	2H	hexagonal plate
	B	875	1	75	750	125	120	3.4353(1)	25.475(1)	4H	ribbon
$NbSe_2$	D	700	0.01	50	700	25	21600	3.29(1)	12.07(4)	2H	hexagonal plate
NbS_2	D	700	0.01	50	700	25	21600	3.44538(7)	12.5467(2)	2H	hexagonal plate

Table 4.2 CVT thermal conditions tested for the synthesis of group V dichalcogenides and resulting polytypic phases deduced from Le Bail refinements of XRPD data. All the refined cells presented belong to the hexagonal crystal system (α = 90°; β = 120°). The parameter nomenclature is consistent with the labels in Figure 4.9.

3 Simple alkaline earth metal intercalates

A further appealing aspect of TMDCs is their versatile red-ox chemistry. By effect of soft reducing agents, electrochemical processes or even solid-state doping, these layered materials undergo a facile reduction. This process is said to be a *topotactic reduction* since the individual layers acquire a negative charge (MX_2^{-n}) that needs to be compensated by countercationic species.[101] This means that intercalation occurs simultaneously to the red-ox exchange, yielding a new layered lattice in which MX_2 sheets alternate with monoatomic cations that is, depending on the intercalation method employed, sometimes accompanied by solvent molecules. A side effect of this cation interlayer inclusion is that the whole structure swells, in other words, the basal spacing between MX_2 planes expands. In addition, the charged layers are also better stabilized by polar or protic solvents than the parent neutral ones. In this context, the topotactic reduction of TMDCs is a good starting point if one wants to perform intercalation chemistry with charged species as it facilitates subsequent ionic exchange steps or sheet delamination for stable colloid formation.

Following, the intercalation of TMDCs with alkaline earth metal cations is discussed. The description will be focused in the analogues introduced in the previous section, namely the Ta and Nb dichalcogenides. In this way, special emphasis will be made on the most convenient methods reported in the literature together with some newly developed approaches to the synthesis of simple metal intercalates will also be described. A final section will be devoted to the analysis of the particular physical and chemical properties of simple metal intercalates TMDCs.

3.1 Synthesis and structural considerations

The intercalation techniques addressed in this work may be divided in two main categories that will be discussed separately: the *wet* methods and the *dry* methods.

101 *Topotactic transition*: a transition in which the crystal lattice of the product phase shows one or more crystallographically equivalent, orientational relationships to the crystal lattice of the parent phase. From *Compendium of Chemical Terminology*, 2nd ed. (the "Gold Book"), compiled by A. D. McNaught and A. Wilkinson, Blackwell Scientific Publications, Oxford, **1997**. *doi:10.1351/goldbook.T06395*.

a. Metal intercalation via wet chemical methods

TMDCs undergo a topotactic reduction reaction when immersed in aqueous solutions of metal hydroxides or mild inorganic reducing alkaline earth salts (i.e. sodium dithionite, $Na_2S_2O_4$). This topotactic chemical transformations have been extensively visited by different authors since the 70s.[102] Though the precise nature of the reduction mechanism remains somehow uncertain, a likely explanation points at the presence of reducing X^{2-} ions in the medium, arising from the residual hydrolysis of pristine MX_2 slabs.[102c] In any case, the reaction yields an intercalation compound of general formula: $A_x[MX_2]\cdot nH_2O$ (where A is an alkaline-earth metal and x = 0.24 – 0.33). On this note, it has been well described how the fine tuning of the reaction conditions (fundamentally the pH value, the reaction time and the molar ratio r = NaOH/TaS_2) allowed for the reproducible synthesis of alkaline metal intercalates with a fixed metal content (x) and a well-defined T_{SC}. For example, the x = 0.33 Na-intercalated TaS_2 has a relatively high T_{SC} of 4.5 K and is easily obtained according to the method reported by Biberacher *et al.*[102c] The synthesis of this particular intercalate (**10**) required the immersion a sample of 2H-TaS_2 (**1**) in a NaOH aqueous solution of pH ~ 12.7 in a ratio of r ~ 5 for over an hour. Hence the $Na_{0.33}TaS_2$ system was used throughout the investigation as a reference compound for assessing the improvements introduced in the synthetic process.

It is important to highlight how important the starting neutral TMDC was in order to control the intercalation process. In this way, pure 2H polytypic samples with regular hexagonal μ-crystallites were easy to intercalate in a reproducible and homogeneous manner. Oppositely, the intercalation of phase mixtures lead to the preferred intercalation of some crystallites with respect to other ones depending on their polymorphic nature. As a result, heterogeneous materials are obtained.

As previously mentioned, the intercalation of A^+ guest species also promotes an expansion of the MX_2-MX_2 interlayer space that is confirmed by the increase in the length of the c parameter of the unit cell.[102] The structural change may also be evidenced at the microscopic scale since the crystals clearly swell in the direction

102 a) Whittingham, M. *Mat. Res. Bull.* **1974,** *9,* 1681–1689. (b) Schöllhorn, R.; Sick, E.; Lerf, A. *Mat. Res. Bull.* **1975,** *10,* 1005–1012. (c) Biberacher, W.; Lerf, A. *Mat. Res. Bull.* **1982,** *17,* 633–640. (d) Rao, G. V. S.; Shafer, M. W.; Tsang, J. C. *J. Phys. Chem.* **1975,** *79,* 553–557.

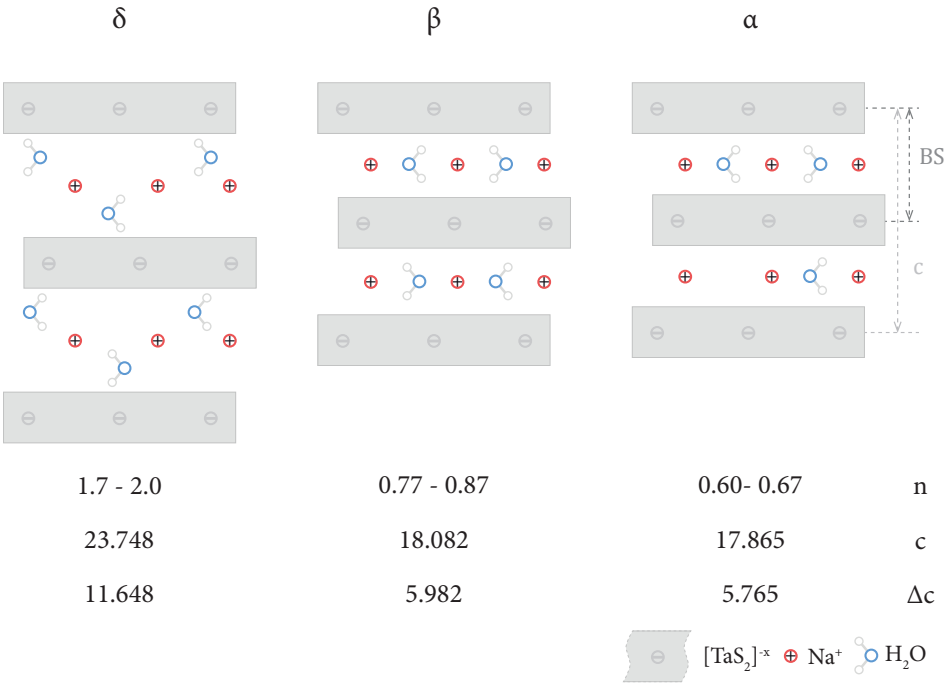

Figure 4.16 Cartoon representation of three common phases (α, β and δ) of the 2H-$Na_{0.33}TaS_2 \cdot nH_2O$ with different hydration degrees. Crystallographic (*c*, Δ*c*) and water content (**n**) data were extracted from reference 103a.

perpendicular to the basal planes. On the other hand, the in-plane lattice parameter *a* remains almost unaffected, which indicates that the MX_2 in-plane structure is preserved. This expansion ($\Delta c = c_{Na_xTaS_2} - c_{TaS_2}$) normally exceeds that expected for the intercalation of the plain cations since A^+ is generally accompanied by a variable amount of water molecules. The number of water molecules per unit formula has found to be dependent on the relative humidity of the atmosphere in which the metal intercalates are stored.[103] This leads to the formation of different BS phases. For instance, in the case of 2H-$Na_{0.33}TaS_2$, three phases named α, β, and δ with *c* = 17.87, 18.08 and 23.75 Å respectively may be obtained depending on the hydration degree of the layered structure (see Figure 4.16).[103a] Whilst both α

103 a) Johnston, D. *Mat. Res. Bull.* **1982,** *17,* 13–23. (b) Johnston, D. *J. Less-Common Met.* **1982,** *84,* 327–347.

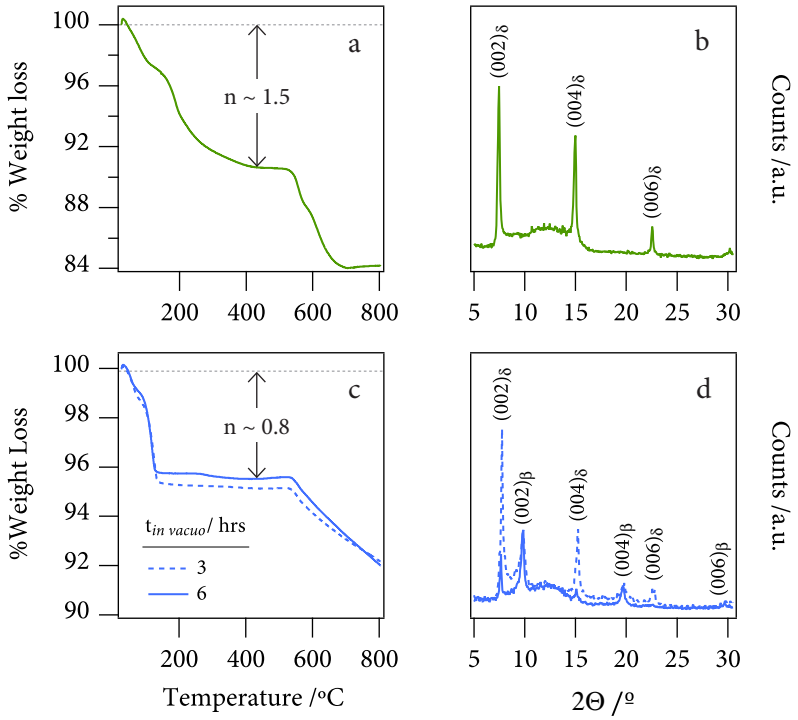

Figure 4.17 TG data (**a**) and XRPD patterns (**b**) of a 2H-$Na_{0.33}TaS_2 \cdot nH_2O$ sample dried in ambient conditions (δ phase, *green*). The same characterisation (c: TG, d: XRPD) for an anlogous sample dried *in vacuo* during 3 and 6 hrs is also provided (mixture of β and δ phases, *blue*).

and β phases are said to contain a monolayer of water molecules in the interlayer space, it is suggested that the δ phase contains a water bi-layer. The water content could be easily extracted from thermogravimetric (TG)[104] data and was in good agreement with XRPD patterns. In general, it could be observed how samples dried in ambient conditions yielded pure δ phases. In contrast, it was difficult to isolate pure hydration phases when intercalated samples were dried *in vacuo*. This was easily confirmed by collecting the XRPD patterns in the range $5^o < 2\theta < 30^o$, where the out-of-plane (00*l*) reflections are observed. Figure 4.17 illustrates the hydration phase equilibria that occur in 2H-$Na_{0.33}TaS_2$ prepared by the procedure described by Biberacher *et al.* (**10**).[102c] Interestingly, whereas samples dried in air

104 TG experiments needed to be carried out in a N_2 atmosphere to prevent weight increments due to oxidation processes as mentioned in reference 102a.

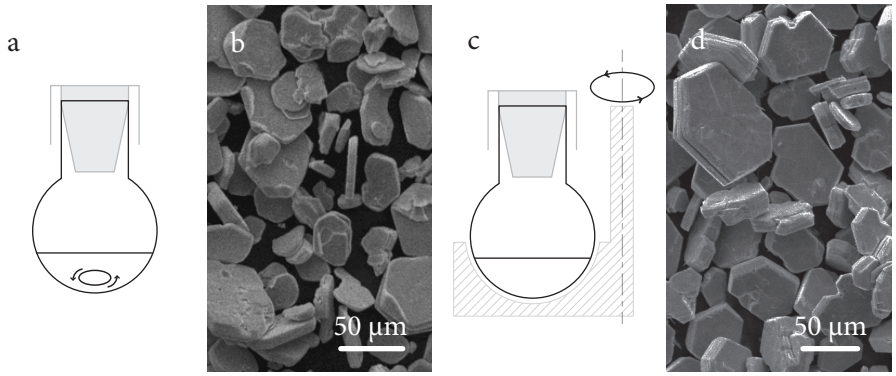

Figure 4.18 Schematic representation of the mechanical stirring (**a**) and orbital shaking (**c**) stirring modes and SEM images of the resulting polycrystalline δ-2H-$Na_{0.33}TaS_2$ (b and d respectively).

exhibited around 1.7 water molecules per unit formula and a unique BS typical of the δ phase (BS_δ = ½ = 11.8 Å), vaccum-dried ones normally showed a mixture of at least two (00*l*) reflection families (BS_δ = 23.2 Å; BS_β = 18.0 Å) and a much lower water content. Even more, a quantitive conversion fron the δ to the β phase could not be achieved via conventional evacuation methods in reasonable time periods ($t_{in\ vacuo}$ < 24 hrs).

Concerning the experimental reaction setup, it was observed that conventional stirring techniques such as the ones involving stirring with magnetic bits, provoked substantial erosion in the pristine hexagonal platelets. Once again taking the 2H-$Na_{0.33}TaS_2$ system synthesized by the B method as a case study, it can be confirmed from SEM images that the individual crystallites of Na-intercalated samples exhibit more rounded vertex and less well-defined factes in comparison with the parent neutral TaS_2 material (see Figure 4.18a). In addition, XRPD patterns collected from the same eroded samples depicted a severe decrease in the overall crystallinity of the material. Though this may be associated to an increment in the turbostratic disorder inherent to the intercalation process in the basal planes, it is suggested that the effect may be enhanced by particle abrasion. Thus alternative approaches for shaking the reaction mixture in a milder fashion were sought for. In this context, the external stirring via an orbital shaker (see Appendix 4.5, section 1.10 on page 301) could avoid the interal milling of the sample produced by the stirring bit. Indeed the use of orbital stirring allowed

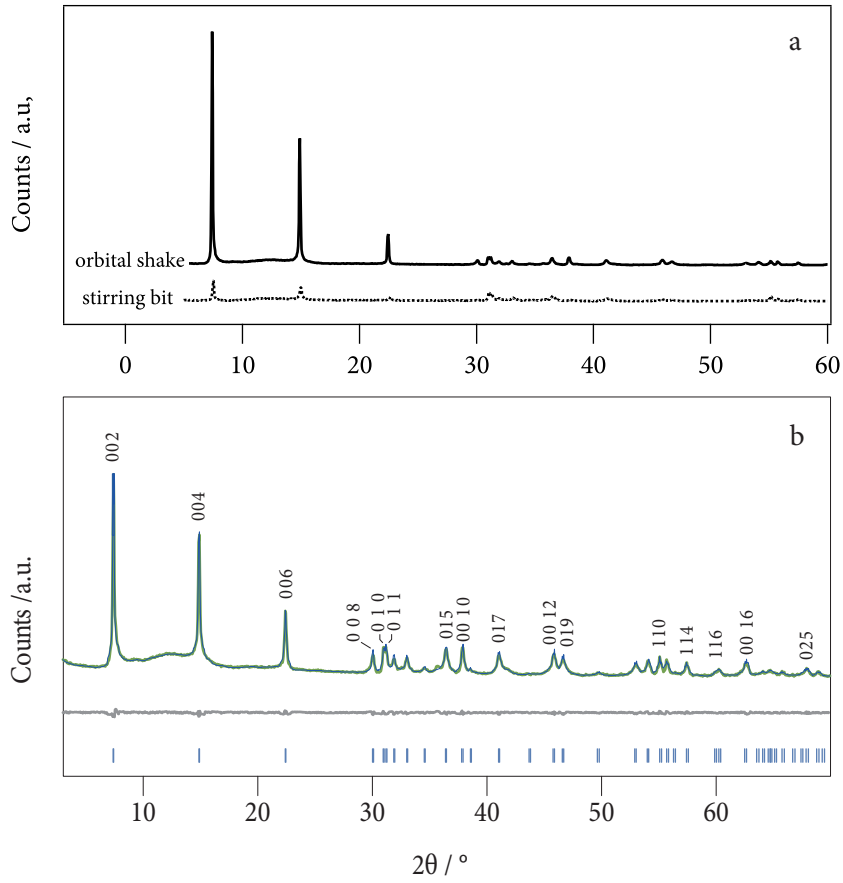

Figure 4.19 a. XRPD patterns of polycrystalline δ-2H-$Na_{0.33}TaS_2$ synthesized by mechanical stirring (*dashed*) and orbital shaking (**11**, *continuous*). **b**. Le Bail fit of **11** (*blue*). The most prominent reflections have been tagged with their corresponding Miller indices.

for the successful isolation of δ-2H-$Na_{0.33}TaS_2$ samples (**11**) with less eroded crystal morphologies. The inspection of polycrystalline samples of **11** revealed almost unspoilt hexagonal prismatic plaquettes. Yet, minor crevasses along the crystallographic *ab* plane of each crystallite were difficult to avoid. These features gave the platelets a characteristic book-fore-edge-like appearance. More interestingly, crystallinity was also enhanced by the use of this technique as denoted by the comparison of XRPD patterns collected in the same conditions of δ-2H-$Na_{0.33}TaS_2$ samples prepared by the two methods (see Figure 4.19a). In this way, samples prepared by traditional stirring exhibited weaker intensities and

broader profiles of the reflection peaks. These problems have generally hindered the determination of accurate structural models for intercalation complexes of layered dichalcogenides.[105] By contrast, the XRPD pattern of **11** displays peaks which are prominent enough for phase indexation and overall profile fitting. Indeed, the presence of a pure δ-2H-$Na_{0.33}TaS_2$ was confirmed using the Le Bail method to fit the data to a single-phase hexagonal model in the $P6_3/mmc$ space group (R_{wp} = 12.11, R_{exp} = 3.92; see Figure 4.19). Unit cell parameters (a = 3.3285(2) Å, *c* = 23.743(1) Å) were in good agreement with that reported for the δ phase of the *x* = 0.33 Na-intercalate.[103a] The Na/Ta metal ratios could be estimated from EPMA analysis (*x* = 0.39) and were also in excellent agreement with the theoretical value (*x* = 0.33). The elemental analysis data seem to support the hypothesis that some sulphur hydrolyses from the MX_2 layers to act as the reaction catalyst (*vide supra*), reflecting a slightly minor sulphur content in the Na-intercalated sample when compared with the theoretical values expected for the non-hydrolysed sample (22.1 and 25.4%, respectively).

A different and also unprecedented approach for the alkali-metal intercalation of TMDCs is the hydrothermal (HT) technique. The use of the HT procedures was inspired by the fact that such technique could lead to intercalation in static conditions, this is with no need of stirring. Moreover, it was also expected that the higher temperatures and higher pressures would lead to faster intercalation velocities and thus shorter reaction times. Therefore, a higher crystallite quality could be envisioned. In this way, the precursor materials were loaded inside a teflon lined autoclave in the optimum stoichiometric ratios and pH value established by Biberacher *et al.* for the synthesis of $Na_{0.33}TaS_2$ (*vide supra*). With the aim of roughly monitoring the kinetics of the HT reaction, three identical autoclave vessels were mounted in the same way and placed inside an oven at a temperature of approximately 110 °C. Each of them were be taken out of the oven at increasing reaction times and the reaction mixtures were isolated. Then, in order to study the HT effect over the reaction, a parallel control test was also carried out by setting an identical autoclave to those thermally treated and leaving the reacting mixture to evolve at room temperature. The results are plotted in Figure 4.20. Curiously, the resulting hydration phase was the β one with an estimated *c* of 18.03 Å. This occurred even having taken the precaution of air drying the resulting samples.

105 Wong, H. V.;Evans, J. S. O.; Barlow, S.; Mason, S. J.; O'Hare, D. *Inorg. Chem.* **1994,** *33,* 5515.

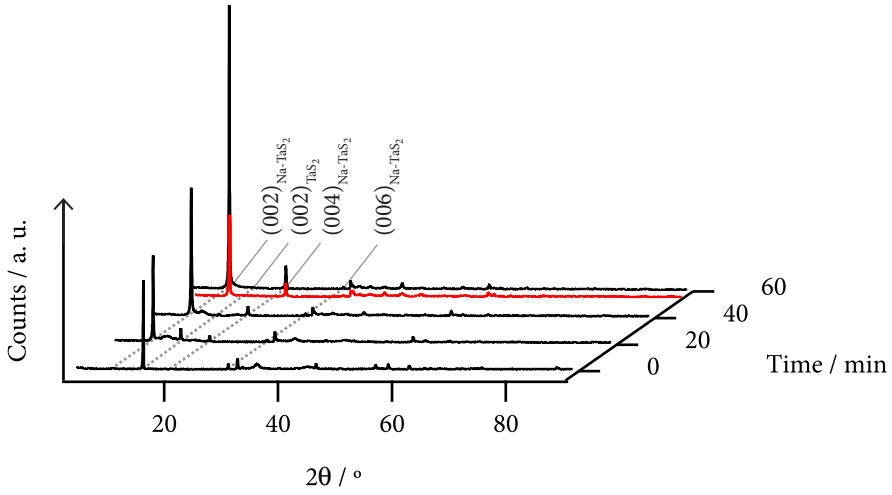

Figure 4.20 XRPD patterns of HT-synthesized β-2H-$Na_{0.33}TaS_2$ at different reaction times (T = 110 ºC). A control test sample treated at room temperature is shown by the *red* profile. Guides to the eye have been drawn at the positions of the (00*l*) reflections of the precursor and the intercalate.

This result seemed to be reproducible and the β (and some other times the α one, *vide infra*) phase appears to be favoured by the HT methodology. In the plot it may also be appreciated how the powder pattern for t = 20 min some low-intensity 2H-TaS_2 precursor diffraction peaks are left. In contrast, for t = 40 min the pattern corresponds to pure β-2H-$Na_{0.33}TaS_2$, which indicates that the reaction had finalized at some point in the range 20 min < t < 40 min. This fact indicates that a great improvement has not been achieved regarding the reaction speed. Yet, typical HT synthesis durations could be shortened to 30 min instead of the 60 min with the conventional approach. The results are in good agreement with more detailed studies on the kinetics of these topotactic reduction processes employing classical reaction setups.[106] On the other hand, cristallinity seems to be greatly improved by the HT technique as seen from the comparison of the r. t. and the HT profiles for t = 60 min. Next, the influence of the temperature over the HT reaction was looked at. In principle, no effect was observed by varying the temperature in the 90 - 120 ºC. However, higher temperatures resulted in highly hydrolysed

106 Rao, G. S.; Shafer, M. W. *J. Phys. Chem.* **1975,** *79,* 557–560.

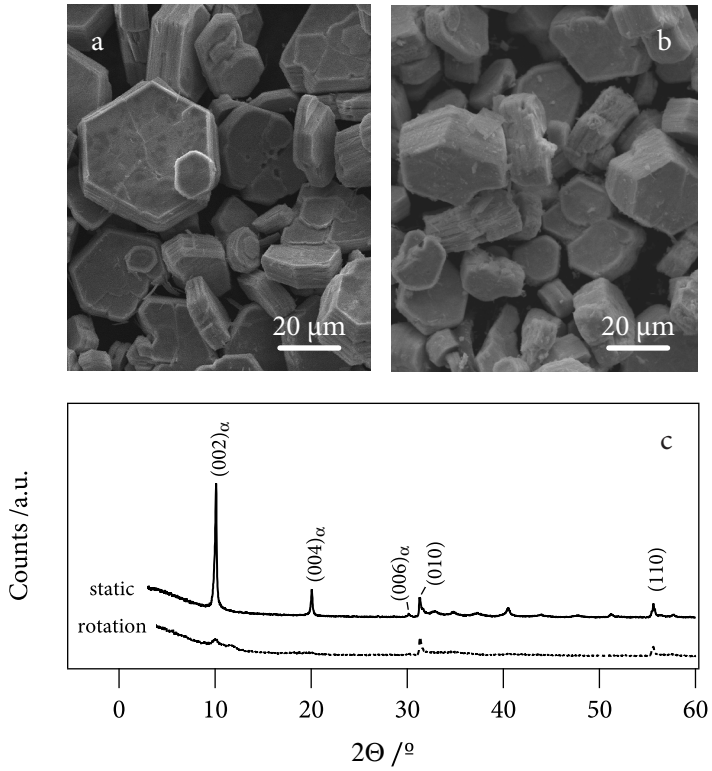

Figure 4.21 Comparison of α-2H-$Na_{0.33}TaS_2$ samples prepared in HT static and HT rotation modes as seen by SEM (**a**: rotation, **b**: static) and XRPD (**c**).

samples, which displayed almost featureless XRPD patterns, thus a temperature of around 105 ºC is suggested as adequate for building up enough inner pressure whilst avoiding sample degradation. Finally, the effect that the static reaction medium had on the crystallinity and morphology of the intercalated samples was assessed. This was determined by carrying out parallel tests in conventional and rotatory ovens both at 105 ºC and during 30 min. The rotatory oven was specially designed and included a rotating axis where individual autoclaves vessels could be mounted (see Appendix 4.5, section 2.3 on page 302). SEM images depicted some crystallite erosion both when the autoclave was shaken in the rotatory oven and when the reacting solution was left to stand inside the oven. However, the hexagonal morphology was preserved in both cases (see Figure 4.21). Yet, XRPD clearly demonstrated how the stirring effect in the HT approach had an even

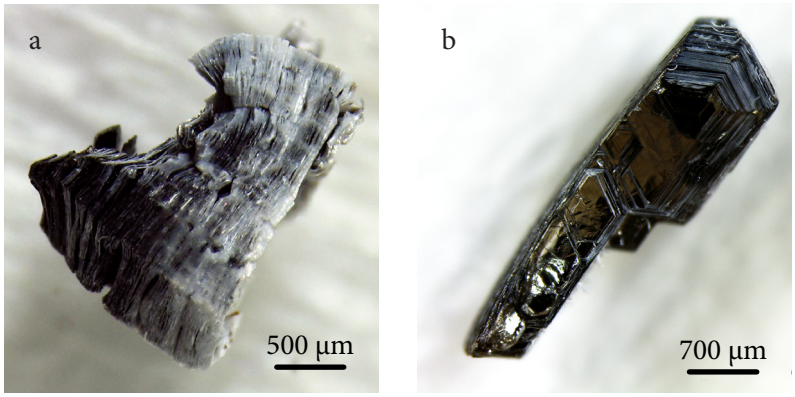

Figure 4.22 Optical microscope images of large single 2H-TaS_2 crystals intercalated by the HT approach (T = 105 ºC) with Na^+ cations in aerobic (**a**) and inert (N_2, **b**) atmospheres.

greater destructive effect than at ambient pressures. This was confirmed by XRPD. While the patterns exhibited by the α-2H-$Na_{0.33}TaS_2$ prepared in static mode (**12**) could be associated to a pure α phase (c = 17.67 Å), those corresponding to the shaken samples only displayed low-intensity peaks coming from the in-plane reflections (010) and (110). The chemical compositions of **12** were studied by EPMA. An average value of x = 0.41 could be inferred from the Na/Ta metallic ratios and was consistent within experimental error with the metal content found in samples that had been synthesized by conventional reaction methodologies.

The HT approach also turned out as a very useful tool in the intercalation of alkali metals in larger single crystals of TMDCs. While the traditional methodologies proved inefficient for the homogeneous intercalation of large crystals. It is suggested that the diffusion process of the redox active species into the deep crystal core may be difficult in the case of large crystals. However, this problem seemed to be overcome by the use of the high autogenous pressures such as the ones generated inside the autoclave in the HT process. In this way, a few single 2H-TaS_2 flakes were sealed inside a teflon autoclave containing an aqueous NaOH solution (pH ~ 12.7) in the molar ratio r = NaOH/TaS_2 = 5. After 30 min at 105 ºC the crystals had swollen remarkably, much in the fashion of that observed for polycrystalline samples. However, the resulting crystals displayed disordered stacks of layers separated by deep crevasses and also, the dark colour characteristic of TaS_2 seemed to have been bleached out (see Figure 4.22). This

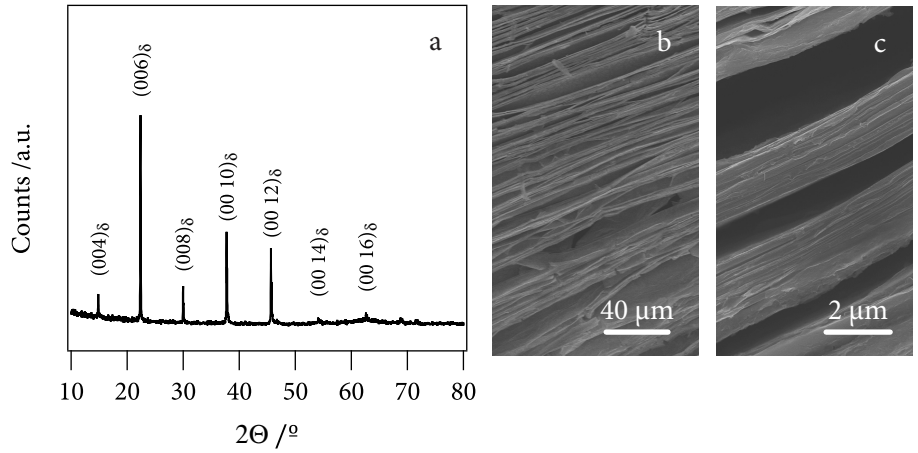

Figure 4.23 a. XRPD (flat plate, reflection configuration) pattern of a large single 2H-TaS_2 crystal intercalated with Na^+ ions (**13**). **b**. and **c**. Different magnification SEM images of the swollen profile of the intercalated crystal along the crystallographic *c* axis.

was thought to be indicative of the oxidation of TaS_2 to white Ta_2O_5. Indeed, the hypothesis was confirmed by repeating the same reaction but replacing the inner aerobic conditions by a N_2 atmosphere. The crystals recovered in this occasion (**13**) showed much cleaner dark facets and no evidences of white Ta_2O_5 could be detected. The XRPD patterns of these single crystals exhibit a unique set of (00*l*) reflections indicative of a δ-2H-$Na_{0.33}TaS_2$ as suggested by the estimated unit cell parameter $c = 23.83$ Å (view Figure 4.23). The chemical analysis via EPMA was also in accordance with the composition of polycrystalline samples of δ-2H-$Na_{0.33}TaS_2$ in so far a Na/Ta ratio of $x = 0.43$ could be inferred from the experimental data.

Next, the alkali-metal intercalation of other TMDCs was addressed. In this way, the topotactic reduction of $TaSe_2$ and $NbSe_2$ was investigated. Though the reaction had already been described by Schöllhorn *et al.*,[102b] the reduction of these systems seemed much more challenging than for the TaS_2 system as intercalation could not be accomplished . This observation is in agreement to that previously reported by Rao *et al.*[102d] In that study it is concluded that while alkali metal hydroxides intercalate in TaS_2 within 1hr, Nb analogues typically require periods of at least 12 hr. However, the prolonged treatment of TMDCs with concentrated aqueous metal hydroxides generally lead to the chemical decomposition of the

layered structures. This is especially remarkable in the case of the metal selenides in which a red floating residue (Se) builds up right from the start of the reaction. Anyhow, no further details are given on the viability or on the kinetics of the Na intercalation in the $TaSe_2$ system. Yet the intercalation of the $TaSe_2$ system may be of interest given the peculiar electronic and superconducting properties that it exhibits (review Chapter 3). Thus, an investigation was conducted to ascertain whether Na intercalation on the $TaSe_2$ could be achieved and what were the optimum reaction conditions. The reaction was initially carried out employing the reference method proposed by Biberacher *et al.* for TaS_2 but starting with 2H-$TaSe_2$ polycrystalline samples (**2**). Preliminary tests indicated that little intercalation had taken place as the samples recovered after 1 hr presented identical XRPD patterns to the parent material **2**. Higher reaction temperatures (T) were also explored but to no avail, since the system $TaSe_2$ was severely damaged degraded and large amounts of red residue appeared upon heating the reaction medium (T > 30 ºC). Hence a more in depth qualitative study of the reaction dynamics was carried out. For this reason, several aliquots were extracted from the reaction medium at different times (t_r) and were conveniently washed and isolated. In order to determine the intercalation reaction coordinate x (Na/Ta molar ratio) in an accurate manner, the metallic content of each isolated specimen was determined by induced coupled plasma optical emission spectroscopy (ICP-OES). This method provided with the required sensitivity for the quantification of small Na concentrations during the early stages of the intercalation reaction. The results of the reaction dynamics as viewed by ICP-OES have been plotted in Figure 4.24a. ICP data confirms the slow kinetics of the intercalation reaction, where intercalation ratios of $x \sim 0.2$ are reached only after 150 min of reaction time. Ta/Se ratios remained constant throughout the reaction, confirming the ideal 1Ta : 2Se stoichiometry and discarding hydrolysis processes at least before t_r = 180 min. Upon reaching that stage, the intercalation speed (gradient of the curve) had diminished remarkably, though it is clear how the equilibrium had still not been reached. At higher Na concentrations, the reaction coordinate could be more easily followed by EPMA (shown in Figure 4.25). The data for t_r > 2 hr show how x continues to increase until $t_r \sim 4$ hrs. At that point a value of $x \sim 0.4$ was reached and the intercalation process appeared to stop. From the structural point of view , the modifications occurring during the reduction reaction were followed by XRPD (Figure 4.24b and c). It may be observed how 15 min after the start of

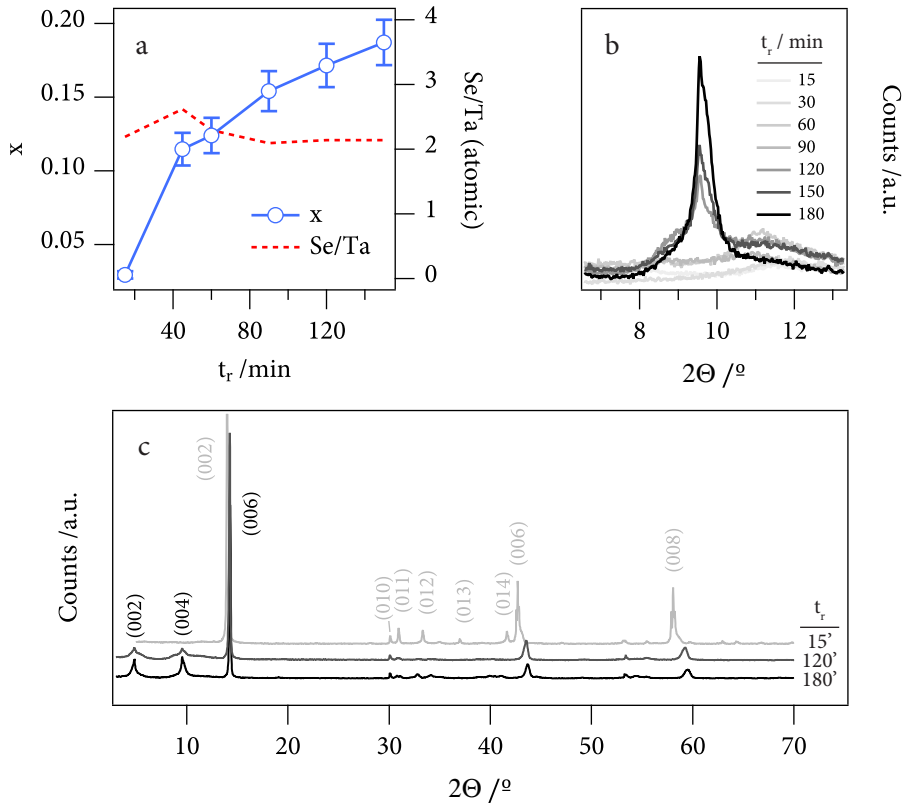

Figure 4.24 Kinetics of the intercalation of Na^+ in 2H-$TaSe_2$(**2**) followed in terms of the Na/Ta ratio *x* as determined by ICP-OES (**a**) and in terms of the intensity of the (004) reflection peak as viewed by XRPD (**b**). The line connecting the points in **a** are just a guide to the eye.

the reaction, the pattern could be ascribed to that of pure 2H-$TaSe_2$ (**2**). Note that the XRPD patterns were collected in a θ-θ reflection configuration, fact which made the out-of-plane (00*l*) peaks stand out with respect to the in-plane ones. As the reaction progresses, it may be observed how as the in-plane reflections remain still, the out-of-plane peaks shift to the right. In addition, a couple of lower angle out-of-plane features start to appear. In contrast, with the TaS_2 system, these low-angle out-of-plane peaks exhibited low relative intensities even past t_r = 180 min. Already at t_r = 120 min the peaks positions cease to evolve, suggesting that a complete topotactic transformation had been accomplished. This means that the Na uptake for t_r > 2 hr happens with no apparent structural change. From that

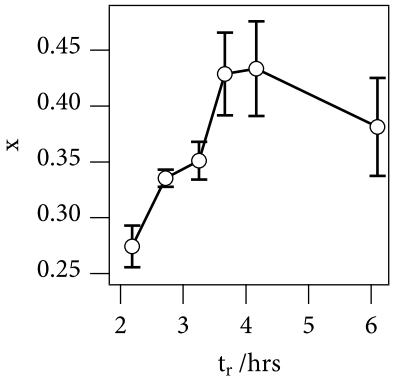

Figure 4.25 Reaction coordinate *x* of the intercalation of Na^+ in $TaSe_2$ for $t_r > 2$ hrs as monitored by EPMA.

point onwards, the only variation of the XRPD patterns that could be observed was the increase of relative intensities of the low-angle peaks (view Figure 4.24b). Unfortunately, the profile shown by the intercalated samples displayed exceedingly broad peaks that prevented the successful indexation of the pattern. Therefore it can only be suggested that the lower angle peaks might belong to the (00*l*) family. Assuming a hexagonal 2H-type structure, these reflections permit estimating a unit cell *c* paramter of 36.9 Å (assuming a 2H lattice, BS = 18.5 Å). This value is larger than that found for the intercalation of other TMDCs and also for what had already been reported for $TaSe_2$.[102b]

The same behaviour could be observed for the reaction of 2H-$NbSe_2$ (**3**) with NaOH aqueous solutions confirming the slower and less favourable kinetics in contrast with the intercalation process of the sulphides such as 2H-TaS_2 (**1**).

b. Metal intercalation via dry solid-state methods

Hitherto the traditional approach for the synthesis of Na-intercalated phases has been described. However, the intercalation of alkali metals in TMDCs can also be achieved by solid-state methodologies, namely by exposing the pristine crystals to the gaseous intercalants at low pressures (recall section 5, Chapter 3, page 83). These solvent-free approaches result in higher quality materials, however, the methods and equipment required hinders their large scale application.

A different all-dry approach consists in the ceramic reaction of stoichiometric mixtures of the elemental constituents of a TMDC together with simple inorganic salts. In this way, Na_xTaS_2 intercalates (**14**) could also be prepared by the sintering a mixture of Ta and S and ultrapure NaCl at high temperatures according to the methodology previously reported by Fang *et al.*[107] The current approach being a one-step approach permits saving both time and resources and most importantly, it greatly improves the integrity of the precursor Na-intercalated material in comparison with the wet methods. While compound $Na_{0.33}TaS_2$ crystallites synthesized via basic reduction (**11**, **12**) exhibited rounded crystallite vertex and a decrease in the overall crystallinity of the sample if compared with TaS_2 pristine samples, the XRPD pattern of **14** showed extremely intense and sharp diffraction peaks that depicted an enhanced crystallinity (see Figure 4.26). The large aspect ratio of the sample crystallites resulted in preferred orientation of powder specimens, making it difficult to observe diffraction peaks other than the (00*l*) family in a θ-θ reflection geometry experiment (Figure 4.26a). Nevertheless, indexation of the mentioned reflections by assuming a hexagonal symmetry allowed for the identification of two very similar phases with the following c-axis unit cell parameters: c_A = 12.08980(19) Å and c_B = 11.9497(2) Å (see Table 4.3).

Phase	a = b / Å	c / Å	α / º	β = γ / º	BS / Å
A	3.31708(14)	12.08980(19)	90	120	6.04
B	3.313(2)	11.9497(2)	90	120	5.97

Table 4.3 Unit cell parameters from Pawley refinements of compound **14**.

Phase A coincides with that described in the literature for single crystals of Na_xTaS_2.[107] On the other hand, phase B shows a BS that is very similar to that reported for 2H-TaS_2.[96] This evidences the fact that most Na^+ ions remain away from the bi-dimensional galleries. In order to diminish the effect of preferred orientation and try to enhance the in-plane family of reflections the sample was loaded into a glass capillary and a transmission XRPD pattern was collected (Figure 4.26b). Though still faint, transmission data permitted identifying the (100) and (010) reflections. A Pawley refinement of the whole pattern revealed an

107 Fang, L.; Wang, Y.; Zou, P.; Tang, L.; Xu, Z.; Chen, H.; Dong, C.; Shan, L.; Wen, H. *PRB* **2005,** *72,* 1–8.

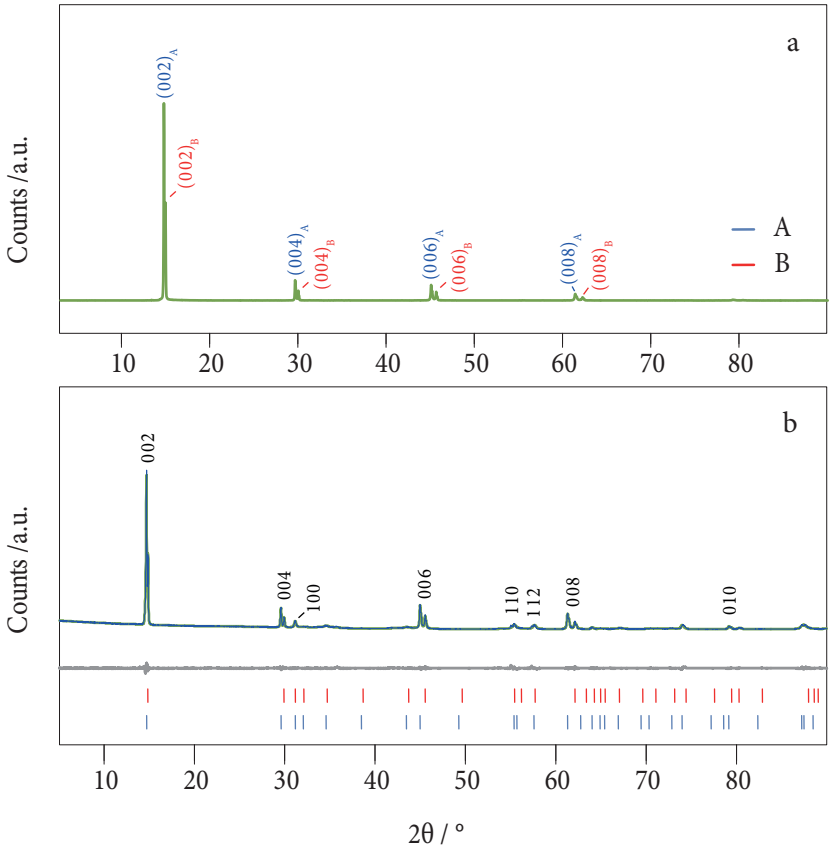

Figure 4.26 XRPD patterns of 2H-$Na_{0.015}TaS_2$ (**14**) recorded in the θ - θ reflection geometry (**a**) and in tranmission geomtry (**b**). The Pawley pattern fit is shown by the *blue* line in b..

excellent fit to a two-phase model (R_{wp} = 0.1469 and gof = 1.815) with a hexagonal cell with a ~ 3.31 Å in agreement with that described for TaS_2 layers with trigonal prismatic Ta coordination such as 2H-TaS_2. Homogeneous morphology of the isolated Na_xTaS_2 microcrystals was confirmed with SEM (see Figure 4.27). High aspect ratio crystals were approximately 100 μm in length and 20 μm in thickness. Given the small ratio of Na in the isolated sample, EPMA lacked sensitivity and was not a suitable probe for stoichiometry determination. Thus, the chemical composition of the bulk samples of **14** was determined via quantitative X-Ray Photoemission Spectroscopy (XPS) chemical studies. The XPS technique also permitted to conduct experiments on the surface of selected single crystals

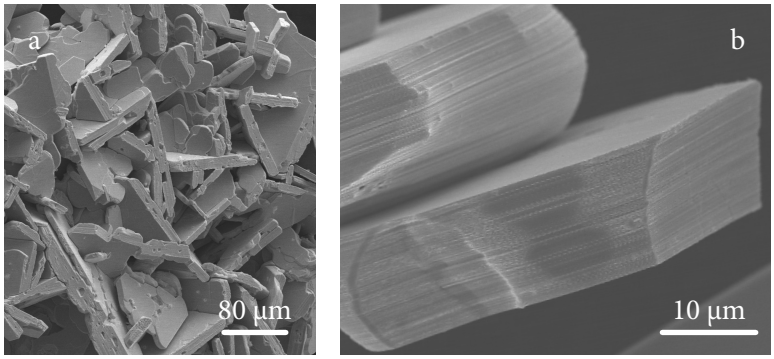

Figure 4.27 Different magnification SEM images of $Na_{0.015}TaS_2$ (**14**).

extracted from the bulk sample. Na : Ta stoichiometries for the different crystals analysed were coincident within experimental error. In this way, an overall x = Na/Ta ratio of 0.015 ± 0.005 could be inferred from XPS data. This is once again consistent with the intercalation limits reported in the literature for solid-state-synthesized Na_xTaS_2.[107] Etching studies were carried out in order to confirm the homogeneous composition of the crystals and to discard the influence of surface ionic adsorption. In this line, XPS data show that the composition remained constant no matter how deep the crystal was away.

Alternatively, the synthesis of large single crystal TMDC intercalates via the CVT approach has also been reported in the literature. In this context the I_2-transport reaction of mixtures of TaS_2 with elemental transition metals (TM) for the fabrication of crystals of general formula $(TM)_xMX_2$ have been very recently reported.[108] This relatively new solid-state approach motivated the investigation of the previously described reaction of NaCl, Ta and S but employing the CVT technique. In this way, pre-sintered 2H-TaS_2 **1** was intimately mixed with ultrapure NaCl and vacuum sealed inside a fused silica ampoule together with the transport agent I_2 (~ 1 mg cm^{-3}). The thermal treatment of the CVT system following the optimum conditions previously described (experimental conditions D, Table 4.2 on page 111) affords large single crystals of general formula 4Hb-Na_xTaS_2 (**15**).

108 a) Zhu, X.; Sun, Y.; Zhang, S.; Lei, H.; Li, L.; Zhu, X.; Yang, Z.; Song, W.; Dai, J. *Sol. State Comm.* **2009,** *149,* 1296–1299. (b) Zhu, X.; Sun, Y.; Zhang, S.; Wang, J.; Zou, L.; DeLong, L. E.; Zhu, X.; Luo, X.; Wang, B.; Li, G.; et al. *J. Phys. Cond. Matter.* **2009,** *21,* 1–7. (c) Li, L. J.; Sun, Y. P.; Zhu, X. D.; Wang, B. S.; Zhu, X. B.; Yang, Z. R.; Song, W. H. *Sol. State Comm.* **2010,** *150,* 2248–2252.

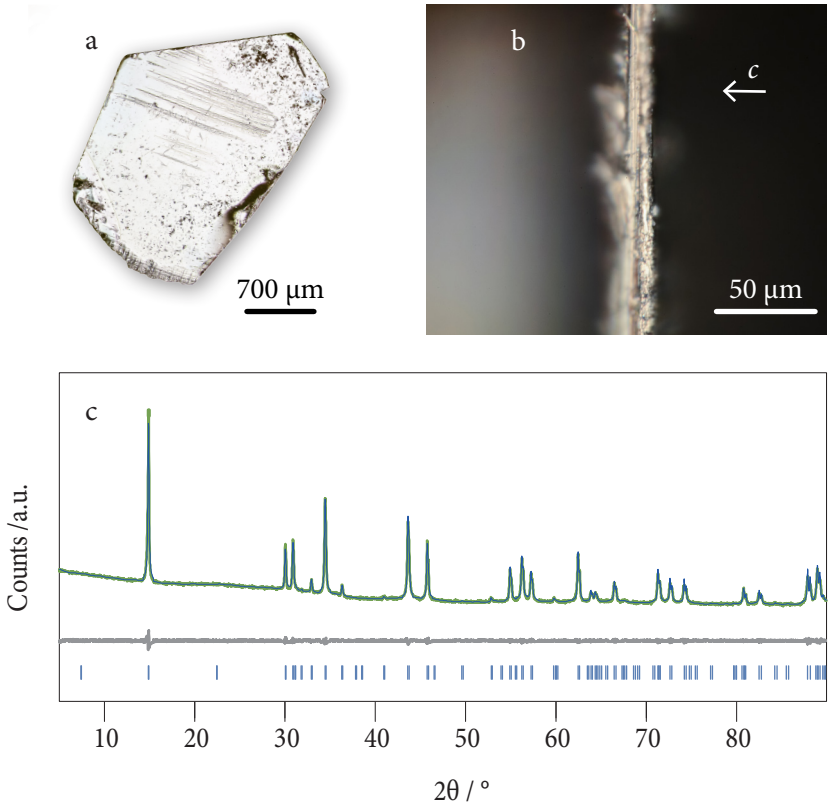

Figure 4.28 Characterisation of a specimen of 4Hb-$Na_{0.02}TaS_2$ (**15**): photograph along the basal plane (**a**) and along the crystallographic *c*-axis (**b**); XRPD experimental pattern (**c**, *green*, **15**) and corresponding Le Bail fit (**c**, *blue)*.

All the crystals had a few square millimetres of surface area along the basal plane (corresponding to the *ab* crystallographic plane) and were several ten microns thick (Figure 4.28a and b). EPMA spectra confirmed the intercalation of Na atoms and the total absence of chlorine contaminants. Intercalation ratios varied very slightly from one crystal to another in the range $0.01 < x < 0.05$. Phase purity was confirmed on the basis of the Le Bail fit of the XRPD pattern to a single-phase model with $a = 3.33922(5)$ Å and $c = 23.7637(3)$ Å, in good accordance with that previously reported for a 4Hb -type lattice (see Figure 4.28c). Interestingly, the great proximity of the basal planes suggested by this unit cell (BS = 5.94 Å) depicts that literal intercalation does not occur— but rather doping— and most of the Na

atoms are located outside of the interlayer space such as in the case of $Na_{0.015}TaS_2$ (**15**).[96] This experiment provides with the first proof of concept that the reductive 'intercalation' TMDCs may be achieved by the use of alkali-metal halides in CVT conditions. Further experiment will be devoted to the polytype control of the resulting single crystals.

3.2 Properties of metal intercalates

In addition to the structural change, the intercalation reaction of TMDCs with alkali metals has an dramatic effect on their physical properties as a result of the charge transfer to the MX_2 layers. In fact, the resulting solid is characterised by the mixed valence state of the metal atoms (M), in which a fraction of the original M(IV) centres have been reduced to M(III). This induces both a charged state of the TMDC planes and a modification of the electronic configuration, with important implications in the solvent-assisted exfoliation properties and the T_{SC} respectively.

a. Wet delamination of metal intercalates

After undergoing reduction, the individual TMDC layers may be described as anionic $[MX_2]^{x-}$ units. The charged nature of the planes favour the stabilising interaction with polar or protic solvent molecules and at the same time it makes homologous $[MX_2]^{x-}$ repel each other. In addition, the BS expansion facilitates the access of further solvent molecules to the bi-dimensional galleries. These characteristics may be profited from to segregate the individual layers of the intercalated material via vigorous shaking in certain solvents or solvent mixtures.

The process begins with the initial swelling of the layered structure by the diffusion of new solvent molecules into the interlayer spacing. This event yields swelled structures with very large interlayer separations and promotes a drastic reduction of the intensity of the interactions operating across the stack of $[MX_2]^{x-}$-Na^+ planes. Upon the vigorous shaking or the ultrasound treatment of the initial suspension, the layered stacks break down and give rise to the individual solvated layers. The favourable interactions between the charged $[MX_2]^{x-}$ layers and the solvent molecules results in the formation of a stable sol of highly anisotropic bi-dimensional nano-sheets (2DNs). Figure 4.29 shows a schematic representation

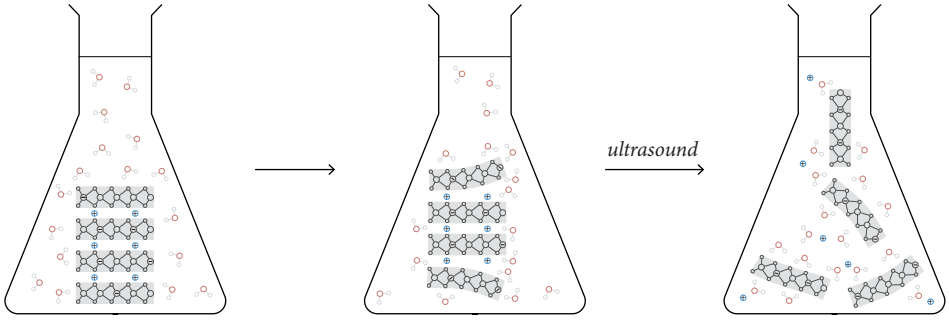

Figure 4.29 Cartoon representation of the wet delamination of an alkali-metal TMDCs generic intercalate.

of this process. These sols exhibit different colours under transmitted light characteristic of the TMDC exfoliated. For example, while the TaS_2 system normally gave rise to golden yellow colloids, the $TaSe_2$ system produced reddish sols. In this line, they displayed structured UV-Visible (UV-Vis) spectra with strong absorption coefficient (ε_λ) bands that could be fitted to a Lambert-Beer absorption model (see Figure 4.30). From the linear fit of the absorbance (ABS) at the maximum of the specific optical bands, a value of $\varepsilon_{272\ nm} = 2.95 \pm 0.01\ g^{-1}\ L\ cm^{-1}$ for $[TaS_2]^{0.33-}$ and of $\varepsilon_{141\ nm} = 3.21 \pm 0.08\ g^{-1}\ L\ cm^{-1}$ for the $[TaSe_2]^{-0.45}$ could be extracted. It has been previously suggested for other colloidal systems that a good fit to the Lambert-Beer law indicates that the suspended 2DNs are approximately monodispersed and that inter-particle interactions are almost negligible, this supporting the presence of single monolayers.[109]

The delamination of the $Na_{0.33}TaS_2{\cdot}nH_2O$ system has been exhaustively studied by Nazar *et al.*[70b] In this report it is described how when crystals of $Na_{0.33}TaS_2$ are placed in NMF (N-Methylformamide) and then H_2O is added (or the other way round), the solid begins to swell rapidly. A high degree of delamination was then attained by applying periodic cycles of mechanical stirring and sonication. It is suggested that the material is best delaminated when the H_2O : NMF mixture was 1 : 1 (v/v). For that mixture ratio, the maximum dispersion stability was reported. As a matter of fact, the procedure allows for the quantitative delamination of **11** to afford sols that do not sediment before several weeks. It is important to

109 Han, J. B.; Lu, J.; Wei, M.; Wang, Z. L.; Duan, X. *Chem. Commun.* **2008,** *5188.*

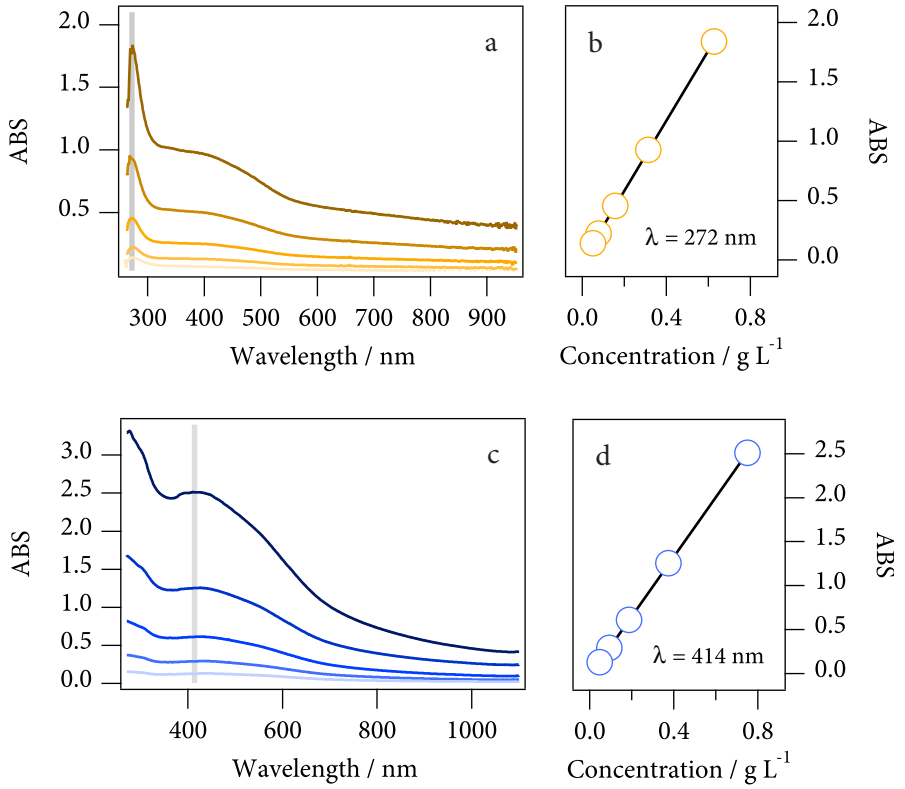

Figure 4.30 UV-Vis spectra of stable sols obtained by sonication of $Na_{0.33}TaS_2$ (**a**) or $Na_{0.45}TaSe_2$ (**c**) in a mixture of H_2O : NMF 1 : 1. The Beer fitting of the most characteristic absorption bands of $[TaS_2]^{-0.33}$ and $[TaSe_2]^{-0.45}$ is plotted in **b** and **d** respectively..

emphasize that the process yielded cleaner sols when performed under an inert N_2 atmosphere. Amorphous white by-products, which could be generally ascribed to TaO_x species, were commonly obtained otherwise. It may be concluded that in order to avoid further oxidation of the 2DNs, the delamination of **11** and in general of any TMDC intercalate needed to be performed under an inert atmosphere.

In order to confirm the success of the exfoliation process and extract direct information concerning the size of the exfoliated layers in the formamide dispersion, Dynamic Light Scattering (DLS) studies were conducted. Despite the average hydrodynamic diameter of dispersions resulting from the exfoliation of inorganic lamellae solids is commonly biased towards the larger particles, Figure

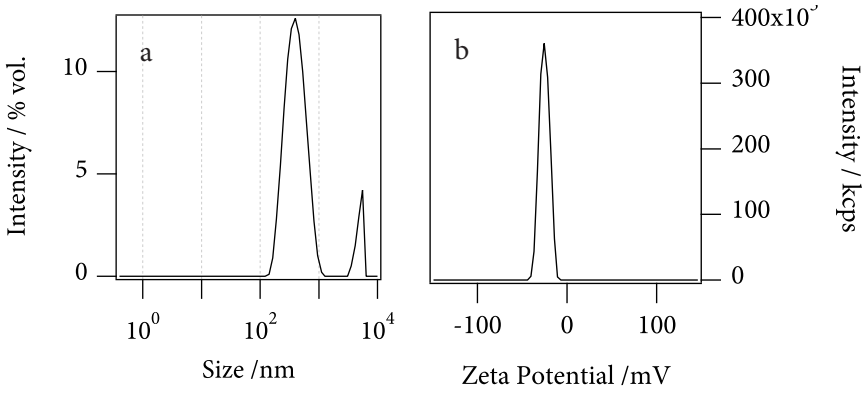

Figure 4.31 DLS studies of stable sols of $[TaS_2]^{-0.33}$ prepared by wet delamination of compound **11** (1.5 g L^{-1} in NMF : H_2O, 1:1). **a**. Hydrodynamic diameter volume distribution. **b**. Particle zeta potential distribution.

4.31 shows a homogeneous Gaussian distribution of the particles' size, centred around 400 nm.[110] Nevertheless, it is important to note the asymmetric peak that shows at the higher end of the size scale. This is typical of a much bigger size particle distribution that lies out of the measuring range and reflects a higher degree of complexity of the sample size distribution. The zeta potential of the 2DN sols of **11** was also in the range of a typical moderately stable colloid (ζ = -25.4 mV, see Figure 4.31b).[111]

Another powerful technique for the characterization of both the morphology and the atomic structure of the suspended 2DNs is high-resolution transmission electron microscopy (HRTEM). Figure 4.32 shows different magnification HRTEM images of the $[TaS_2]^{0.33-}$ 2DNs isolated by dropping a freshly prepared sol of **11** on a carbon-coated copper TEM grid. The exfoliated 2DNs show defined facets and a weak homogeneous transmission intensity, revealing a uniform and relatively small flake thickness. However, some thickness dispersion could be deduced from the slightly different ratio of transmitted electrons exhibited by different 2DNs. Figure 4.33 shows a selected area electron diffraction (SAED) pattern

110 Q. Wu, A. Olafsen, O. B. Vistad, K. D. Knudsen, J. Roots, J. S. Pedersen, P. Norby, *J. Mat. Chem.* **2007,** *17,* 965-971.

111 *For instance*: (a) Greenwood, R.; Kendall, K. *J. Eur. Ceram. Soc.* **1999,** *19,* 479–488. (b) Smith, R. J.; King, P. J.; Lotya, M.; Wirtz, C.; Khan, U.; De, S.; O'neill, A.; Duesberg, G. S.; Grunlan, J. C.; Moriarty, G.; Chen, J.; Wang, J.; Minett, A. I.; Nicolosi, V.; Coleman, J. N. *Adv. Mater.* **2011,** *23,* 3944–3948.

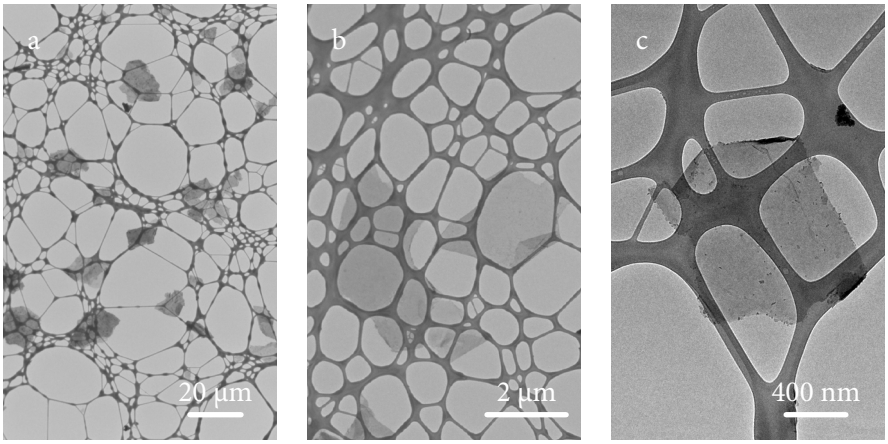

Figure 4.32 HRTEM images of a sample of $[TaS_2]^{-0.33}$ 2DNs casted on a C-coated Cu grid.

acquired from two specimens that displayed different transmission intensities. It is important to highlight that special care needed to be taken once focusing the electron beam in selected areas of the 2DNs since remarkable sample degradation took place during long exposure times. The thinnest flakes with lower optical contrasts appeared to be specially sensitive to electron beam burns. Indeed, whilst thin samples such as the one shown in Figure 4.33e were irreversibly blemished after performing SAED experiments, no evidence of sample degradation could be observed in thicker ones (Figure 4.33d for instance). Concerning the atomic structure, the SAED patterns of both 2DNs exhibit a hexagonal arrangement of reflections as expected for the in-plane symmetry intrinsic to the 2H-TaS_2 layers. Indexation of the SAED pattern assuming a hexagonal closed packed structure (hcp) and a 001 zone vector (theoretical pattern shown in Figure 4.33c) provides a reproducible *a* value of around 2.9 Å, in agreement with that estimated from the indexation of the powder diffraction patterns of the bulk samples ($a \sim 3.3$ Å for **11**). This point confirms that these 2DNs do not experiment a significant chemical change during the exfoliation process, thus the internal atomic structure of the 2H-TaS_2 layers from the pristine layered bulk material are retained. The atomic periodicity may also be directly imaged at higher magnifications. Figure 4.34 shows high magnification HRTEM images of the same $[TaS_2]^{0.33-}$ 2DNs, where the Ta atom hexagonal lattice exhibits a remarkable transmission intensity. S atoms appear as much lower-contrast owing to their smaller Z number. Hence,

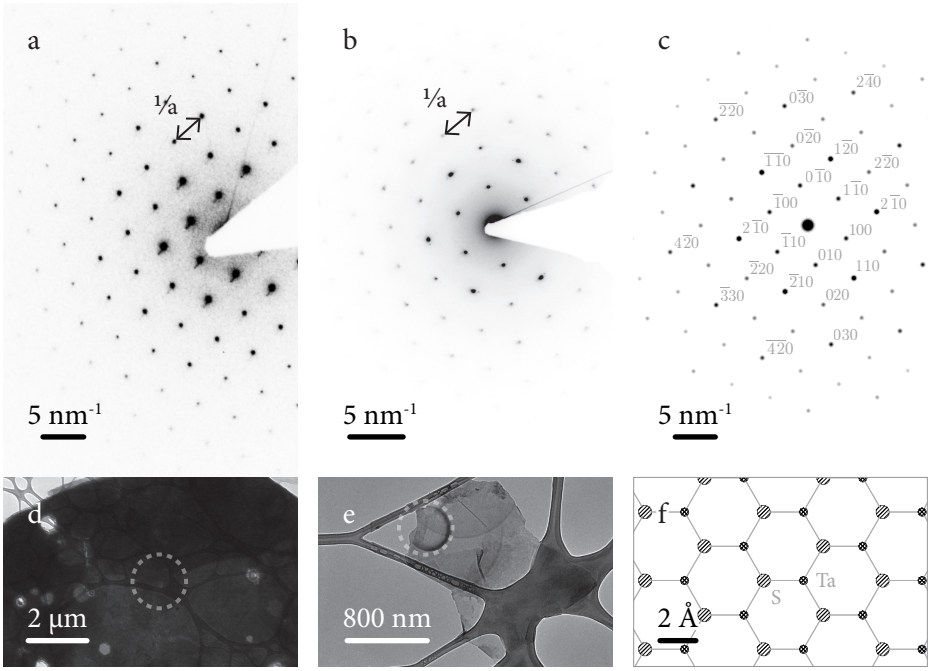

Figure 4.33 SAED patterns collected from of a thicker (**a**) and a thinner (**b**) $[TaS_2]^{0.33-}$ 2DN shown by TEM images below (**d**, **e**). The beam foci selected for electron diffraction are marked with a dashed circle. **c**. Theoretical model of the electron diffraction of a 2H-TaS_2 crystal for the 001 zone vector. **f**. View of the structure of single layer 2H-TaS_2 along the latter zone vector.

the spots corresponding to the S sites are sometimes difficult to appreciate by the naked eye, yet they may be identified by plotting the transmission intensity along specific crystallographic directions. Figure 4.34c displays a line profile along what is assumed to be the 120 (or symmetry equivalent) crystallographic direction which goes alternatively through Ta and S atoms. Indeed two different alternating intensities are here observed regardless of the background signal. In point of fact, the distance between the intensity maxima are in agreement with the distance expected for the Ta-Ta and Ta-S distances along the 120 direction projected in the 001 plane ($d_{Ta\text{-}Ta}^{120}$ = 5.7 Å, $d_{Ta\text{-}S}^{120}$ = 1.9 Å). A further piece of information that may be extracted from the intensity line profiles is the number of layers present. Though a simple examination of the flake edge may provide information regarding the number of MX_2 planes in some particular cases (see the four-step edge in Figure 4.34a), this is often unclear. By contrast, uneven HRTEM intensity

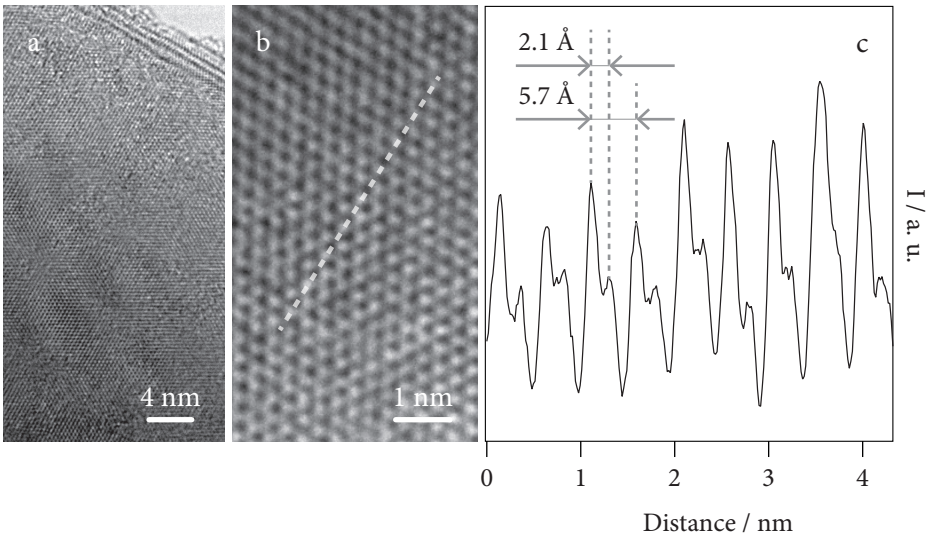

Figure 4.34 High magnification HRTEM images showing the atomic lattice of selected $[TaS_2]^{0.33-}$ 2DN. **a**. Flake edge of a 4 layer thick 2DN. **b**. Atomic resolution image of a single (or few odd number) layer flake. **c**. Line profile of the transmission intensity along the dashed line marked in (**b**).

maxima of the M and X sites taken a 001 zone vector depict unmistakably the presence of a single or a very small odd number of layers of a 2H-type stacking sequence (CdI_2-type, ABAB) due to the uneven integral electron absorption of the different atomic sites in the hexagonal lattice.[112] This is the case of the line profile shown in Figure 4.34c, which confirms the nanometer-thick nature of the flakes in the sol. Oppositely, a specimen with an even number of layers or made out of more than just a few layers would project along the crystallographic *c* axis to produce an HRTEM image with no contrast between adjacent atom maxima.

Following, the delamination of $Na_{0.015}TaS_2$ (**14**) was addressed. To the best of knowledge, no previous studies on the solvent-based exfoliation of such Na-intercalates have been reported. In order to investigate the wet exfoliation of **14**,

112 Coleman, J. N.; Lotya, M.; O'neill, A.; Bergin, S. D.; King, P. J.; Khan, U.; Young, K.; Gaucher, A.; De, S.; Smith, R. J.; Shvets, I. V.; Arora, S. K.; Stanton, G.; Kim, H.-Y.; Lee, K.; Kim, G. T.; Duesberg, G. S.; Hallam, T.; Boland, J. J.; Wang, J. J.; Donegan, J. F. ; Grunlan, J. C.; Moriarty, G.; Shmeliov, A.; Nicholls, R. J.; Perkins, J. M. ; Grieveson, E. M.; Theuwissen, K.; McComb, D. W.; Nellist, P. D.; Nicolosi, V. *Science* **2011,** *331,* 568–571.

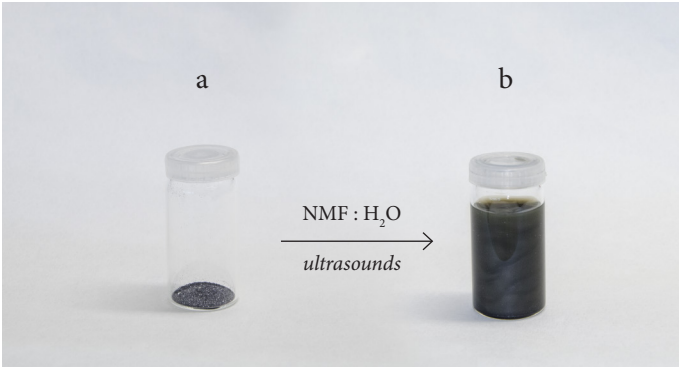

Figure 4.35 Photographs of pristine $Na_{0.015}TaS_2$ **14** (a, 40 mg) and of the same vial after sonication in 15 mL of a mixture of NMF : H_2O, 1 : 1 (**b**). Note the *pearl effect* exhibited by the 2DN sol.

delamination tests using the optimum conditions described for **11** were carried out. In this way, pristine polycrystalline samples of $Na_{0.015}TaS_2$ were immersed in a degassed mixture of H_2O : NMF 1 :1 (v/v) under an argon inert atmosphere and were treated with recurrent cycles of mechanical stirring and sonication. Indeed, it was found out that the behaviour of **14** was comparable to that of other Na-intercalated phases synthesized by wet techniques. Upon immersion in the swelling mixture, the powder puffed up and started to disaggregate across the entire container, probably due to the incorporation of an increasing number of solvent molecules into the bi-dimensional galleries. After immersion in an ultrasound bath, the suspension attained stability and exhibited a characteristic glossy texture upon being stirred (Figure 4.35). The more diluted sols were less opaque and exhibited the characteristic golden yellow appearance under transmitted light that has been already described for $[TaS_2]^{0.33-}$ (see Figure 4.36a). A more quantitative estimate of the degree of dispersion was established by sonicating increasing amounts of **14** in the same volume (40 mL) of the mentioned solvent mixture for 60 min and then allowing the resultant colloidal suspension to stand for 2 h. This allowed the thicker layers that had not substantially delaminated to sediment. The sol was then decanted off to discard the bulkier crystallites and dried *in vacuo* for weighing and consequent delamination quantification. Following this procedure, stable sols with a maximum effective colloidal concentration of 0.35 g L^{-1} could be achieved (see Table 4.4). Qualitative stability experiments were also conducted on the $[TaS_2]^{0.015-}$ sols. For this purpose a freshly prepared 0.35 g L^{-1} suspension was left

Figure 4.36 a. Photograph showing a $[TaS_2]^{0.015-}$ sol (0.3 g L^{-1}) prepared from compound **14** under transmitted white LED light. Frames **b** to **h** show the sedimentation of a $[TaS_2]^{0.015-}$ sol followed by the naked eye. Photographs were taken of the freshly prepared sol (**b**) and at t = 2 hrs (**c**), 4 hrs (**d**), 6.5 hrs (**e**), 10 hrs (**f**), 2 days (**g**) and 1 week (**h**).

to stand and was observed for over a week. Figure 4.36 shows how no significant sedimentation occurs before 4 hours of having prepared the sol. In addition, it is clear how even after a few days, there is still a remarkable concentration of suspended 2DNs in the solvent mixture. The complete sedimentation of the sol

Load / mg	Dispersed /mg	% dispersion	Concentration / $g.L^{-1}$
14	12	88	0.30
22	14	64	0.35
37	11	30	0.28

Table 4.4 Delamination studies to estimate the degree of dispersion of compound **14** in NMF : H_2O, 1 : 1 by sonication.

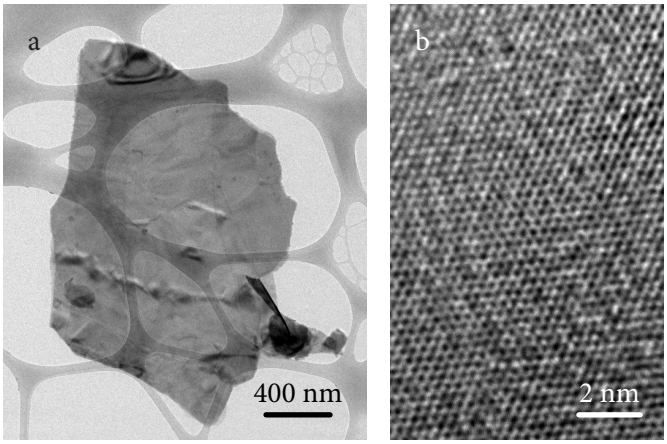

Figure 4.37 HR-TEM images of a sample of $[TaS_2]^{-0.015}$ (**14**) 2DNs casted on a C-coated Cu grid.

is only achieved one week after the initial preparation. The exfoliated 2DNs that could be found in this sol appeared as high aspect ratio flakes as seen by HR-TEM. Figure 4.37 shows an example of the morphology (a) and atomic structure (b) 2DNs found in a delaminated sample of **14**. As in the case of $[TaS_2]^{0.33-}$, $[TaS_2]^{0.015-}$ 2DNs appeared as very low contrast flakes when deposited over C-coated Cu TEM grids. In addition, the lattice parameter *a* that could be calculated from SAED data of selected 2DNs of **14** (2.8 Å) was in agreement with the one extracted for $[TaS_2]^{0.33-}$ 2DNs.

The possibility of having stable sols of charged 2DNs that retain the structure and hence the properties of the parent TMDCs has very important chemical designing implications, since it opens the door for carrying the intrinsic 2D superconductivity into a different hybrid layered heterostructure. This sets the basis for the so-called *delamination/flocculation* synthetic technique. In other words, the described $[TaS_2]^{x-}$ sols may be conveniently re-stacked into a new layered solid in the presence of a concentrated solutions of a cationic counterpart of choice. Figure 4.38 shows a schematic representation of how a solid-state TMDC may give rise to a new hybrid structure by flocculation in the presence of a soluble counterionic part (A^+). One may appreciate how this technique is equivalent to the more traditional direct ionic exchange processes (i.e. zelotitic

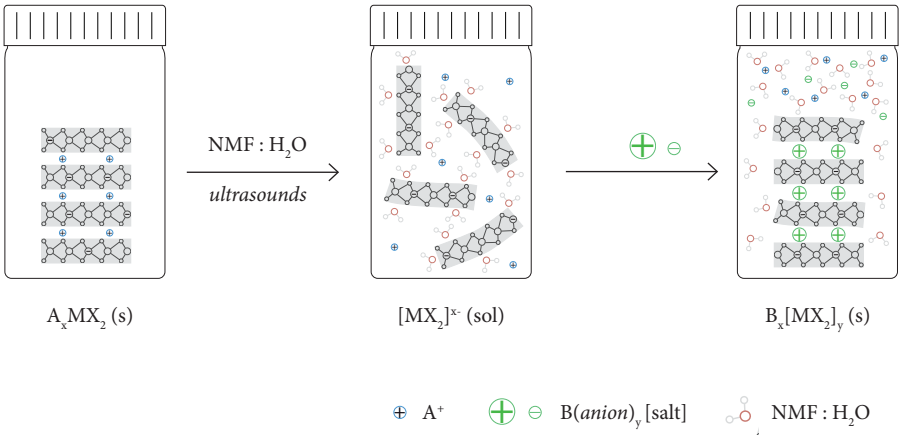

Figure 4.38 General delamination/flocculation approach for the synthesis of hybrid TMDC materials starting from a simple metal (A) intercalate and a cationic functional species B^+.

exchange)[113] in which the solid-state host remains unaltered. However, the direct ionic exchange procedures present major drawbacks in the design of more complex hybrid materials. Indeed, they are limited by several experimental conditions, namely, the long reaction times imposed by the guest substitution step, which is in turn limited by the molecular diffusion into the solid host structure. This disqualifies the use of molecular counterparts that exhibit poor chemical stability and also narrows the suitable range of size and charge of the guest entities. The delamination/flocculation strategy overcomes these limitations, allowing for the fast encapsulation of sensitive systems between the host layers and thus expanding the chemical designing possibilities.

b. Physical properties: superconductivity

Up to this point no experimental characterization of the superconducting properties of TMDCs has been presented. The reason for this is that most TMDCs exhibit very low T_{SC}, typically below 2K. This places the superconducting state of these materials out of the reach of conventional liquid helium cryogenic techniques. Fortunately, the topotactic reduction of TMDCs changes the scenario. It has already been pointed out how the intercalation reaction of alkaline metals

113 *For instance*: Colella, C. *Min. Dep.* **1996,** *31 (6),* 554 - 562.

is accompanied by a suppression of CDWs and a consequent increase in T_{SC}. This allows for the convenient study of the superconducting properties of metal intercalates. Following, several case studies will be used in order to illustrate how the superconductivity operates in these TMDC intercalates. For this purpose the relationship between magnetism and superconductivity has been exploited in such a way that the superconducting properties of the different materials will be inferred from magnetometry measurements (review Appendix 4.1 on page 279). The discussion will be focused in those materials that are of intest for their use as precursors in the synthesis of the hybrid layered materials, namely Na-intercalates **11**, **14** and **15**.

The facile intercalation of the TaS_2 system together with the relatively high temperature superconducting transition makes it an exceptionally convenient system for the study of the variation of the superconducting properties upon intercalation. In this line, for the 2H-TaS_2 system T_{SC} increases from 0.8 K for the neutral pristine TaS_2, up to 4.5 K, for the $x = 0.33$ sodium-intercalated material.[102c] The superconducting behaviour of **11** was surveyed via SQUID magnetometry by recording the thermal variation of the AC susceptibility (see Figure 4.39a and b). The data show perfect diamagnetism in the high temperature range and a sharp transition to the superconducting state below 4.5 K. The sudden downfall to negative values in the in-phase component and equally sharp peak in the out-of-phase signal observed for **11** nicely match that previously reported for $Na_{0.33}TaS_2$. Magnetization curves were also recorded and allowed for the determination of the two critical fields that are characteristic of a type II superconductor: H_{c1} = 170 Oe; H_{c2} = 10.9 kOe (Figure 4.39c).

The properties of the system $Na_{0.015}TaS_2$ (**14**) were analogous to those described for **11**. The variation of AC susceptibility with temperature of powder samples of **14** showed diamagnetic behaviour in the high temperature range and a sharp transition to the superconducting state below 3.2 K indicative of a pure and crystalline Na_xTaS_2 2H phase with $0 < x < 0.05$.[107] This ties in correctly with the value of $x = 0.015$ determined by XPS data (*vide supra* XPS data on page 127). AC magnetization curves recorded under increasing DC external fields are shown in Figure 4.40. The data allowed for the rough estimation of the type II superconductor upper critical field (H_{c2}) at which 100% volume of the material

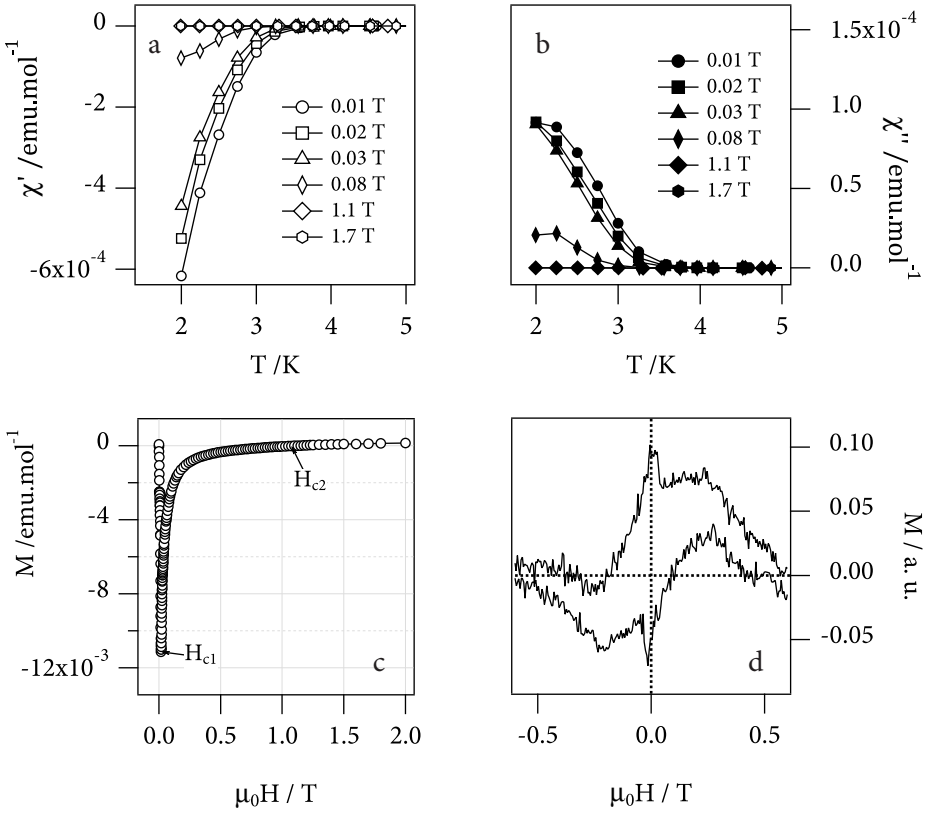

Figure 4.39 SQUID magnetometry characterization of polycrystalline 2H-$Na_{0.33}TaS_2$ (**11**). **a**. Thermal variation of the in-phase component of the AC susceptibility measured at increasing DC applied fields. **b**. Out-of-phase component of the AC susceptibility. **c**. Magnetization curve measured at 2 K showing the typical features of a type II superconductor: lower and upper critical fields (H_{c1} = 170 Oe and H_{c2} = 10.9 kOe). **d**. Hysteresis loop measured at 2 K.

had switched to the normal state. A value of 1.6 kOe could be extracted from the onset point of both the asymptotically decreasing out-of-phase curve and the increasing in-phase component.

It is worthwhile reminding that the TMDC crystals that are currently being discussed are not only structurally anisotropic but that the superconductivity is also essentially bi-dimensional. This fact may pass unnoticed when dealing with polycrystalline samples. However, thanks to the availability of large single crystals grown by the CVT method, the anisotropic nature of the superconductivity at

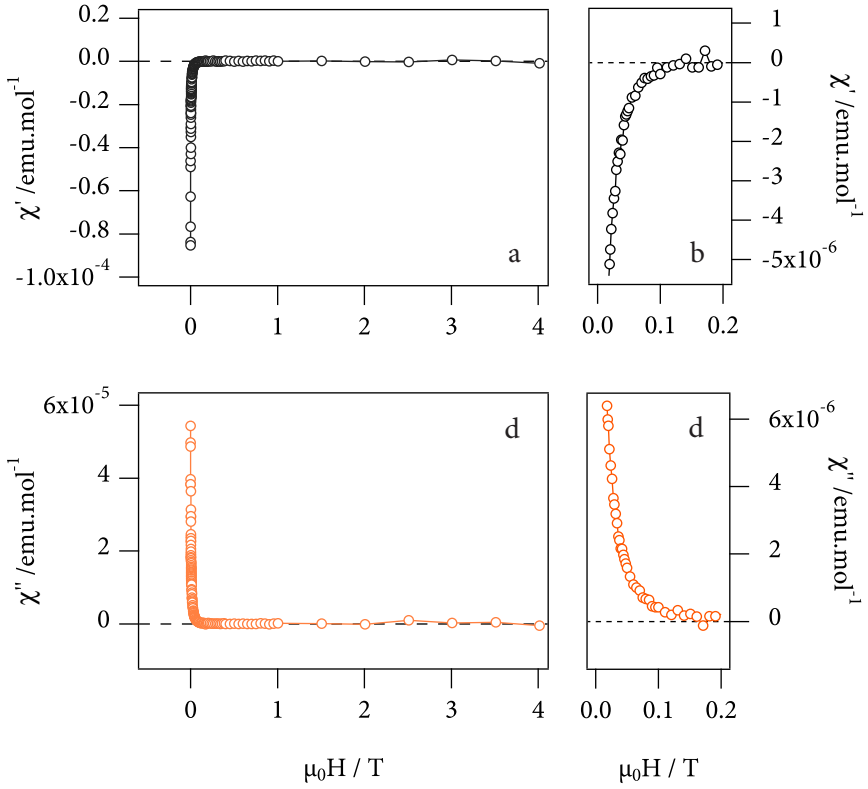

Figure 4.40 AC magnetization curves of Na_xTaS_2 (**14**) measured at 2 K showing the in-phase (**a**) and out-of-phase (**c**) components. On the *right* hand side are the *x*-intercept regions of both in-phase (**b**) and out-of-phase (**d**) components where superconductivity is totally suppressed by the external field..

metal intercalate $Na_{0.02}TaS_2$ (**15**) may be directly witnessed. The AC magnetic susceptibility of **15** as a function of the angle formed by the AC magnetic field *H* and the basal plane of the crystal (crystallographic *ab* plane containing the TaS_2 sheets) is shown in Figure 4.41. The susceptibility observed is very anisotropic, showing the strong bi-dimensional character of the superconductivity in this material. In good agreement with that expected, the diamagnetic response becomes maximum when h is perpendicular to the TaS_2 layers. However, a more detailed study of thermal variation of the AC susceptibility at the extreme orientations ($\theta = 0^o$ and $\theta = 90^o$) permit appreciating how the parallel ($\chi_{||}$) and perpendicular ($\chi_{\perp}$) susceptibilities exhibit a slightly different T_{SC}. Figure 4.42a and b show respectively

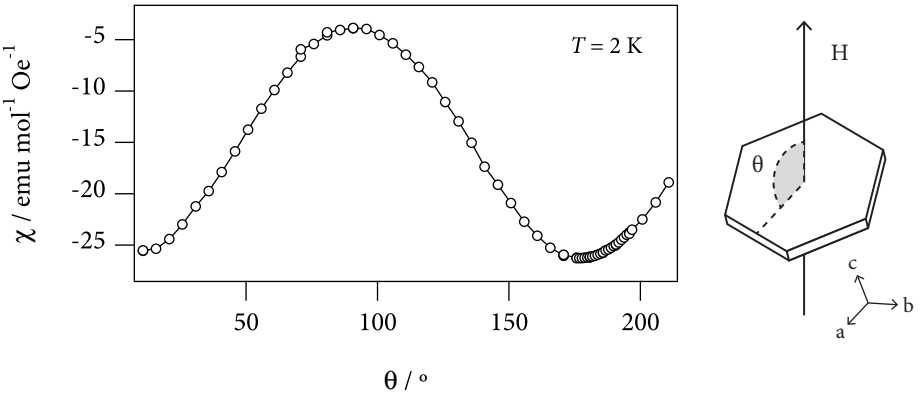

Figure 4.41 AC magnetic susceptibility of $Na_{0.02}TaS_2$ (**15**) measured at 2 K as a function of the orientation (θ) of the basal plane of the crystal with respect to the AC magnetic field.

the dependence of $\chi_{||}$ and $\chi_{\perp}$ of a single crystal with the temperature. One may appreciate how when *H* is co-planar to the superconducting planes, the onset of the superconductivity occurs at approximately 3.75 K. Oppositely, when the field is perpendicular to the TaS_2 layers, a large diamagnetic response starts to manifest already at approximately 5 K. Furthermore, $\chi_{\perp}$ shows an additional step below 3.6 K. Whereas the transition occurring at higher temperature may be attributed to the onset of superconductivity inside the TaS_2 planes, the low temperature anomaly might be indicative of a bulk transition to a 3D superconducting state. It is suggested that below that temperature a state in which Cooper pairs are free to move between adjacent TaS_2 layers is attained.

Finally, the diamagnetic superconducting response could also be pictured via magnetization measurements. The magnetization curves of a specimen of compound **15** measured at different temperatures in the paralel and perpendicular orientations are shown in Figure 4.42c and d respectively. Both plots show a hysteretic behaviour which is typical of a type II superconducting material and that is characteristic of the pinning of vortices. In agreement with the AC data, there is a strong dependence of the superconducting behaviour with the relative orientation of the magnetic field with the crystal structure. In this way, the low critical field reaches a value of H_{c1} = 40 Oe when H perpendicular to the TaS_2 layers. By contrast, it almost doubles to a value of H_{c1} = 75 Oe when the field is

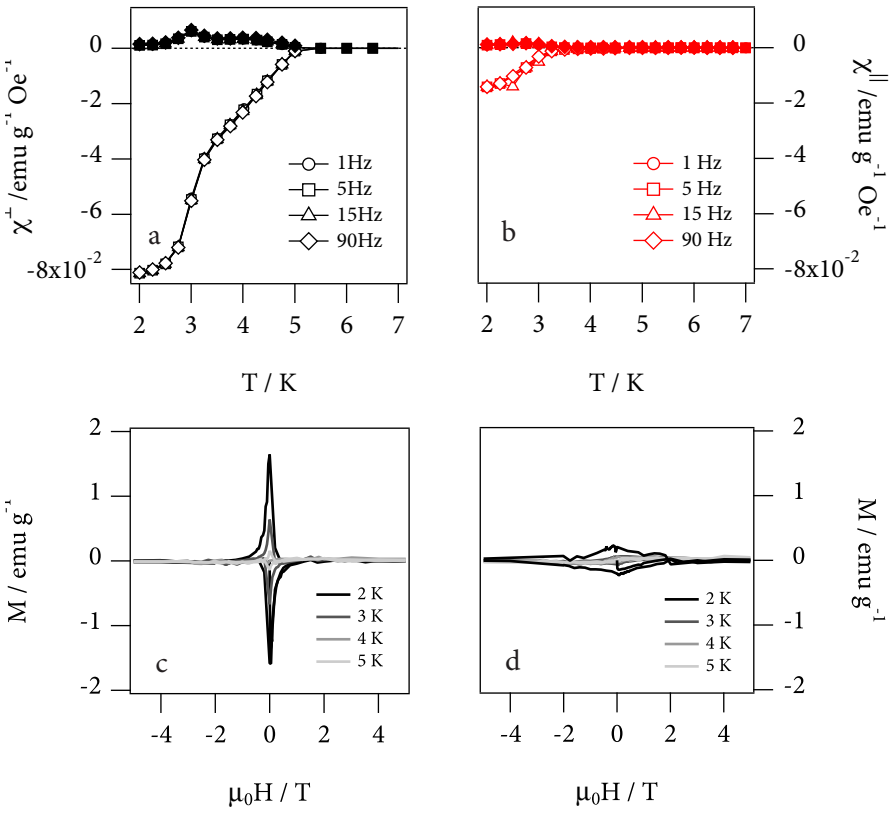

Figure 4.42 Magnetic measurements of a single crystal of compound **15** in the parallel (θ = 0º) and perpendicular (θ = 90º) orientations with respect to the applied field. *Top*: AC susceptibility measured in the perpendicular (**a**) and parallel (**b**) orientations. *Bottom*: Magnetic hysteresis curves measured at several temperatures for the same perpendicular (**c**) and parallel (**d**) conformations..

oriented parallel basal plane. In addition, the hysteresis becomes broader and H_{c2} considerably larger (from around 13 kOe to approximately 40 kOe) in the latter situation.

4 Conclusions

In this chapter, the synthesis of neutral TMDCs has been exhaustively explored. Different approaches for the fabrication of high quality starting materials have

been discussed, making special emphasis in the synthesis of homogeneous and crystalline powder materials and also in the synthesis of large single crystals. In particular, the optimum synthetic conditions for obtaining trigonal prismatic coordination polytypes with clean superconducting transitions have been investigated herein. In this way, the synthetic conditions for the synthesis of group V disulphides and diselenides in their 2H polymorphs have been optimized. Crystal size control allowed to prepare samples with average crystal sizes (along the basal plane) ranging from the tens of microns to several millimetres.

Next, the intercalation of these systems with alkali metal atoms has been addressed. Special attention has been dedicated to the intercalation of superconducting 2H-TaS_2. New synthetic approaches for the isolation of 2H-Na_xTaS_2 ($0.01 \leq x \leq 0.33$) polytypically pure intercalation samples have been studied in depth. As a result, minimum crystallinity loss with respect to the pristine neutral TMDC has been achieved. By contrast, the selenides were found to be less readily intercalated and further studies need to performed in order to master the topotactic reduction process.

A final section has been devoted to the study of the special properties exhibited by the alkali metal TMDC intercalates introduced previously. The expected T_{SC} increase due to the partial charge transfer to the MX_2 layers was confirmed by SQUID magnetometry. In addition all the samples synthesized exhibited excellent exfoliation properties in agreement to that previously reported for this type of materials. The materials and methods here introduced provide with the fundamental background required for understanding the design and synthesis of new hybrid multifunctional materials. In particular, the following two chapters will be devoted to the exploration of the delamination/flocculation technique presented in this section for the combination of superconductivity with other magnetic functionalities.

5 Experimental procedures and recipes

AES experiments

The AES experiments were conducted in collaboration with Dr Tatay-Aguilar in a laboratory at Unité Mixte de Physique CNRS/Thales (France).

The Auger analysis was carried out using a Physical Electronic PHI 680 Auger nanoprobe with a Schottky emission cathode and multi- channel plate detector. The beam voltage acceleration was 5 kV, the beam current 10 nA and the incident angle 30 degrees. For short beam exposition times, these conditions allowed the analysis of the surface of the TaS_2 crystals with little degradation.

Determination of elemental content via ICP-OES

A spectro Arcos model ICP-OES was used for the high accuracy determination of the metal content of selected samples.

Samples were previously dissolved in autoclaves following a certified alkaline fusion digestion procedure optimised for TMDCs: ITA 31 01 (UNE-EN ISO 9001:2008, AENOR, certificate registry no. ER-0915/2007).

Synthesis of polycrystalline metal dichalcogenides

Synthesis of 2H-TaS_2 [1]: 2.422 g of tantalum (13.4 mmol) and 0.858 g of sulphur (26.8 mmol) were intimately mixed with the help of pestle and mortar and flame sealed inside an evacuated quartz ampoule (length = 25 cm; internal diameter = 15 mm; wall thickness = 1.5 mm). The system was transferred to a ceramic muffle (see Appendix 4.5,section 2.2 on page 302) and thermally treated as follows: 1) heated from room temperature up to 900 ^{o}C at 5 ^{o}C.min^{-1}; 2) kept at 900 ^{o}C during nine days; 3) cooled down to room temperature by powering off the muffle. The resulting black solid was purified from traces of elemental sulphur by simple sublimation *in vacuo* at 300 ^{o}C during two days. Finally, the resulting powder was thermally treated following a multi-step annealing procedure described by Wang

et al.[69] The final free-flowing blueish black polycrystalline powder **1** was stored under an N_2 atmosphere.

Elemental analysis % (calculated for TaS_2): C = 0.0 (0.00); H = 0.0 (0.0); N = 0.0 (0.0); S = 27.3 (27.2).

Empirical formula: TaS_2; FW = 245.08.

Synthesis of 2H-$TaSe_2$ [2]: 2.422 g of tantalum (13.4 mmol) and 2.116 g of selenium (26.8 mmol) were exhaustively mixed. The resulting reddish black powder was sintered, purified and annealed in the same conditions used for compound **1**. The final mixture of needle- and block-like crystals was sifted using a set of 3 stainless-steel sieves of different pore sizes (mesh 1: 500 μm, mesh 2: 250 μm, mesh 3: 75 μm). A free-flowing grey polycrystalline sample of compound **2** was recovered by joining the smaller particle size fractions that passed across all three meshes and by the fractions held back by meshes 2 and 3. The fraction held back by the larger mesh was discarded. The resulting solid material was best stored under an N_2 atmosphere.

Elemental ratio estimated by EPMA (calculated for $TaSe_2$): Ta/Se = 0.52 (0.50).

Empirical formula: $TaSe_2$; FW = 338.87.

Synthesis of 2H-$NbSe_2$ [3]: the same procedure as for compound **1** was here employed but this time mixing 1.244 g of tantalum (13.4 mmol) and 2.116 g of selenium (26.8 mmol). The resulting free-flowing greenish black polycrystalline powder **3** was also stored under an N_2 atmosphere.

Elemental ratio estimated by EPMA (calculated for $NbSe_2$): Nb/Se = 0.60 (0.50).

Empirical formula: $NbSe_2$; FW = 250.83.

Synthesis of 2H-NbS_2 [4]: the same procedure as for compound **1** was here employed but this time mixing 1.244 g of tantalum (13.4 mmol) and 0.858 g of sulphur (26.8 mmol). The resulting free-flowing blueish black polycrystalline powder **4** was also stored under an N_2 atmosphere.

Elemental analysis % (calculated for NbS_2): C = 0.08 (0.00); H = 0.00 (0.00); N = 0.01 (0.00); S = 35.72 (40.84).

Elemental ratio estimated by EPMA (calculated for NbS_2): Nb/S = 0.49 (0.50).

Empirical formula: NbS_2; FW = 157.04.

Synthesis of single-crystalline metal dichalcogenides

Synthesis of 4Hb-TaS_2 [5]: 1g of **1** (4 mmol) together with 275 mg of freshly sublimed I_2 were loaded into a 500 mm long fused silica ampoule (internal diameter = 15 mm; wall thickness = 1.5 mm). The mixture was thoroughly stashed at one end of the ampoule and the vessel was then exhaustively evacuated (~ $5{\cdot}10^{-5}$ mbar) and flame-sealed. The quartz tube was finally placed inside a three-zone split-tube furnace placing the starting material edge in the leftmost part (*source* zone) of the furnace (see Appendix 4.5, section 2.4 on page 302). Firstly, the central (*growth*) and rightmost (*tail*) zones were heated to 700 ºC while keeping the heating elements of the source zone inactive. Following, the temperature of the source zone was risen to 650 ºC. Next comes the temperature reversal stage, when the temperature of the *source* zone is gradually increased at a speed of $0.01^{o}C{\cdot}min^{-1}$ until a gradient of 50 ºC with respect to the *growth* zone (700 ºC) was reached. Simultaneously the temperature of the *tail* zone was also risen to 725 ºC. These temperature gradients were maintained constant during 15 days and the muffle was eventually switched off and left to cool down at ambient conditions. Pyramid-like crystals of **5** were recovered from the growth zone of the ampoule. They exhaustively rinsed with diethyl ether until a clear supernatant was observed and stored under an N_2 atmosphere. Phase purity was confirmed by fitting the XRPD pattern by the Le Bail method to a single crystallographic phase: a = 3.33841(7) Å, c = 23.7602(5) Å, $\alpha = 90^{o}$, $\gamma = 120^{o}$; R_{wp} = 12.6.

Synthesis of 2H-TaS_2 [6]: an analogous procedure as the one for compound **5** was followed with a few modifications of the temperature values set and the heating speeds of the different CVT stages. To begin with, the *growth* and *tail* zones were heated to 875 ºC while keeping the heating elements of the source zone inactive. Following, the temperature of the source zone was risen to 800 ºC. During the

temperature reversal stage, the temperature of the *growth* zone is gradually cooled down at a speed of $1^{o}C{\cdot}min^{-1}$. A gradient of 125 ºC was finally established between the *source* zone (875 ºC) and *growth* zone (750 ºC). A gradient of 50 ºC was also set between the rightmost (*tail)* and growth regions. The temperature gradient was maintained constant during 120 hours and the muffle was eventually switched off and left to cool down at ambient conditions. A mixture of ribbon- and flake-like crystals could be observed after cooling down. The flake like specimens (**6**) were isolated from the ribbon-like ones, which where discarded. Finally, the single-crystalline sample of **6** was thouroughly rinsed with diethyl ether and stored under an N_2 atmosphere. Phase purity was confirmed by fitting the XRPD pattern by the Le Bail method to a single crystallographic phase: a = 3.3137(2) Å, c = 12.076(1) Å, $\alpha = 90^{o}$, $\gamma = 120^{o}$; R_{wp} = 14.5.

Synthesis of 2H-$NbSe_2$ [7]: 1g of **3** (4 mmol) was processed using the same CVT procedure and the same experimental conditions used for the growth of **5**. As a result, homogeneous hexagonal-like crystals of **7** with a high aspect ratio and several millimetres in length appeared in the *growth* zone. Occasionally some bunches of needle-like formations appeared in the growth zone, but these were easy to separate from the platelets and were discarded. The isolated crystals of **7** were thoroughly rinsed with diethyl ether before storing in a N_2 atmosphere. Phase purity was confirmed by fitting the XRPD pattern by the Le Bail method to a single crystallographic phase: a = 3.29(1) Å , c = 12.07(4) Å, $\alpha = 90^{o}$, $\gamma = 120^{o}$; R_{wp} = 8.5.

Synthesis of 2H-$TaSe_2$ [8]: 1g of **2** (4 mmol) was processed using the same CVT procedure and the same experimental conditions used for the growth of **5**. This resulted in the growth of very homogeneous samples of hexagonal flake-like crystals of **8**. These crystals were recovered from the *growth* zone of the ampoule and thoroughly rinsed with diethyl ether and then stored in a N_2 atmosphere. Phase purity was confirmed by fitting the XRPD pattern by the Le Bail method to a single crystallographic phase: a = 3.43910(5) Å , c = 12.7067(2) Å, $\alpha = 90^{o}$, $\gamma = 120^{o}$; R_{wp} = 7.7.

Synthesis of 2H-NbS_2 [9]: 1g of **4** (4 mmol) was processed using the same CVT procedure and the same experimental conditions used for the growth of **5**. After the CVT process, millimetre long hexagonal prisms could be observed in

the *growth* zone of the fused silica vessel. The crystal habit in this occasion was bulkier than that observed for crystals **7** and **8**. Single-crystalline specimens of **9** was thoroughly rinsed with diethyl and finally stored in a N_2 atmosphere. Phase purity was confirmed by fitting the XRPD pattern by the Le Bail method to a single crystallographic phase: a = 3.44538(7) Å , c = 122.5467(2) Å, $\alpha = 90^o$, $\gamma = 120^o$; R_{wp} = 12.6, gof = 6.6.

Synthesis of simple metal intercalates

Synthesis of 2H-$Na_{0.33}TaS_2 \cdot nH_2O$ [10]: 10 mL of a freshly prepared aqueous solution of NaOH (20 mg dissolved in 10 mL of deionized water) were adjusted to pH ~ 12.7 and were added onto 450 mg (1 mmol) of **1**. The mixture was mechanically stirred during 1 hr. **10** was recovered from the resulting yellowish slurry by *in vacuo* filtration and the solid material was then washed thoroughly with a few millilitres of ultrapure milli-Q water. Finally, the grey moist powder was dried overnight in ambient conditions. The resulting glittering dark microcrystalline solid was stored under a N_2 atmosphere.

Elemental analysis % (calculated for $Na_{0.33}TaS_2$): C = 0.0 (0.0); H = 0.0 (0.0); N = 0.0 (0.0); S = 25.4 (26.2).

Elemental ratio estimated by EPMA (calculated for $Na_{0.33}TaS_2$): Na/Ta = 0.33 (0.32).

% H_2O weight (TG loss for T < 400 ^{o}C) = 4.5 - 10

Empirical formula: $Na_{0.33}TaS_2 \cdot nH_2O$; FW = 252.67 + 18.02 × n.

Synthesis of δ-2H-$Na_{0.33}TaS_2 \cdot 1.9H_2O$ [11]: the same reagents and concentrations as in the synthesis of **10** were here employed. However, this time the mixture was stirred in an orbital shaker (Appendix 4.5, section 1.10 on page 301) during 1 hr at 273 rpm. **11** was recovered from the green-yellow crude slurry by *in vacuo* filtration and the solid material was then washed thoroughly with milli-Q water. The microcrystalline solid was dried overnight in ambient conditions and the resulting free-flowing solid was best preserved in a N_2 atmosphere.

Elemental analysis % (calculated for $H_{3.8}O_{1.9}Na_{0.33}TaS_2$): C = 0.0 (0.00); H = 0.3 (0.4); N = 0.0 (0.0); S = 22.1 (24.5).

Elemental ratio estimated by EPMA (calculated for $Na_{0.33}TaS_2$): Na/Ta = 0.32 (0.33).

% H_2O weight (TG loss for T < 400 ºC) = 9.4

Empirical formula: $Na_{0.33}TaS_2 \cdot 1.9H_2O$; FW = 286.91.

Synthesis of α-2H-$Na_{0.33}TaS_2 \cdot 0.8H_2O$ [12]: 10 mL of a freshly prepared aqueous solution of NaOH (20 mg dissolved in 10 mL of deionized water) were adjusted to pH ~ 12.7 and were placed inside a PTFE-lined autoclave together with 450 mg (1 mmol) of **1**. The PTFE autoclave was properly sealed with its corresponding stainless-steel and placed inside an oven that had been pre-heated at 105 ºC. The reaction mixture was left to stand at a constant temperature of 105 ºC during 1 hr. The autoclave was then left to cool down to room temperature and the crude mixture was filtered *in vacuo*. The solid was thoroughly washed with ultrapure milli-Q water and left to dry overnight at ambient conditions. Compound **12** was recovered as a dark microcrystalline solid and it was stored under N_2 atmosphere.

Elemental ratio estimated by EPMA (calculated for $H_{1.6}O_{0.8}Na_{0.33}TaS_2$): Na/Ta = (0.33).

% H_2O weight (TG loss for T < 400 ºC) = 5.6

Empirical formula: $Na_{0.33}TaS_2 \cdot 0.8H_2O$; FW = 267.09.

Synthesis of 2H-$Na_{0.33}TaS_2$ [13]: 20 mg of NaOH were dissolved in 10 mL of deionized water and the pH of the solution was adjusted to ~ 12.7. The solution was exhaustively degassed and then placed inside an O_2-free box (Appendix 4.5, section 1.8 on page 300). 300 μL of the previous freshly prepared solution were sealed inside a PTFE-lined autoclave together with 6 mg (24 μmol) of **6** in the form of large single crystals. The latter step was carried out inside the O_2-free box. The PTFE autoclave was then removed form the box and placed inside an oven that had been pre-heated at 105 ºC. The reaction mixture was left to stand at a constant temperature of 105 ºC during 30 min. The autoclave was then left to cool down to room temperature and the crystals were recovered by *in vacuo* filtration in

ambient conditions. Finally, the intercalated crystals **15** were thoroughly washed with ultrapure milli-Q water and left to dry overnight at ambient conditions. Single crystals **15** had a swollen appearance with respect to the parent crystals **6**. The crystals were preserved under N_2.

Elemental ratio estimated by EPMA (calculated for $Na_{0.33}TaS_2$): Na/Ta = 0.43 (0.33).

Hydration water molecules inferred from XRPD data: *c* (expected for δ phase) = 23.83 (23.748 Å).

Empirical formula: $Na_{0.43}TaS_2 \cdot 1.9H_2O$; FW = 290.41.

Synthesis of $Na_{0.015}TaS_2$ [14]: the procedure described by Fang *et al.* was followed with minor modifications. A 1 : 2 : 0.15 molar ratio mixture of 2.422 g of tantalum (13.4 mmol), 0.858 g of sulphur (26.8 mmol) and 0.117 g of sodium chloride (2 mmol) was prepared with the help of pestle and mortar and put into an Ar-flushed fused silica ampoule (length = 25 cm; internal diameter = 15 mm) The ampoule was then evacuated until reaching an internal pressure of approximately $5 \cdot 10^{-5}$ mbar. The system was transferred to a ceramic furnace and thermally treated as follows: 1) heated from room temperature up to 900° C at 5 °C·min^{-1}; 2) constant heating at 900 °C during 48 hrs; 3) cooled from 900 °C down to 700 °C at 2 °C·min^{-1} 4) cooled down to room temperature. The resulting black glittery solid was purified from traces of elemental sulphur by simple sublimation at 300 °C during two days. Finally, the resulting powder was thoroughly washed with distilled water to eliminate the excess of non-intercalated salt crystals. The final free-flowing dark microcrystalline solid **14** was stored under Ar atmosphere.

Elemental ratio estimated by XPS (calculated for $Na_{0.015}TaS_2$): Na/Ta = 0.015 (0.015).

Elemental ratios estimated by SEM-EPMA (calculated for $Na_{0.015}TaS_2$): Na/Ta = 0.008 (0.015); S/Ta = 1.98 (2.00).

Empirical formula: $Na_{0.015}TaS_2$; FW = 246.63.

Synthesis of 4Hb-Na_xTaS_2 [15]: 1g of **1** (4 mmol) together with 117 mg (2 mmol) of ultrapure NaCl (99.999% trace metals basis) and 275 mg of freshly sublimed

I_2 were loaded into a 500 mm long fused silica ampoule (internal diameter = 15 mm; wall thickness = 1.5 mm). Following, the CVT procedure employed in the synthesis of **5** was used. As a result, large hexagonal plate-like crystals **15** developed in the *growth* zone. The crystals were recovered, thoroughly rinsed with diethyl ether and finally dried *in vacuo*. Samples were stored in a N_2 atmosphere.

Elemental analysis % (calculated for $Na_{0.01}TaS_2$): C = 0.0 (0.00); H = 0.0 (0.0); N = 0.0 (0.0); S = 27.7 (26.1).

Elemental ratio estimated by EPMA: Na/Ta ratio was found to vary in the range 0.01 - 0.05 depending on the single crystal selected.

Empirical formula: Na_xTaS_2; FW = 245.08 + 22.99 × x.

5 Insertion of SMMs in superconducting TaS_2 hosts

The combination of molecule-based materials with solid-state extended hosts has already been introduced in Chapter 2. This approach is revisited in this section but this time by the use of a different layered solid-state component: a TMDC. It has already been described how once exfoliated through soft chemistry methods, TMDCs or their intercalation derivatives may be segregated into single lamellae, yielding stable 2DN suspensions. It has also been proved that the individual layers retain the original composition and structure and hence allow for the incorporation of intrinsic superconductivity in hybrid synthetic structures. As a matter of fact, pioneering works in the field of multi-functionality by chemical design have recently exploited the delamination/flocculation technique for the synthesis of superconducting-ferromagnetic materials.[114] This seminal study has opened the door for the unprecedented combination of new functionalities. This is the case of single-molecular magnetism and superconductivity, that remains unexplored to the date.

1 Single-molecule magnetism

Single molecule magnets (SMMs) are a family of metal-organic molecules that exhibit slow relaxation of the magnetization at the molecular scale below a certain temperature, known as the blocking temperature (T_b).[115] This means that SMMs show a hysteretic behaviour even in the absence of long-range magnetic ordering. In other words, the magnetic hysteresis of SMMs has a purely molecular character.[116]

In the case of the more classical polynuclear SMMs, the latter is a consequence of the combination of the magnetic exchange interactions that operate between metal centres within the molecule itself and the magnetic anisotropy of the

114 Coronado, E.; Martí-Gastaldo, C.; Navarro-Moratalla, E.; Ribera, A.; Blundell, S.; Baker, P. *Nat. Chem.* **2010,** *2,* 1031–1036.

115 T_b is defined as the temperature below which the relaxation of the magnetisation becomes slow compared to the time scale of a particular measuring technique.

116 a) Gatteschi, D.; Caneschi, A.; Pardi, L.; Sessoli, R. *Science* **1994,** *265,* 1054–1058. (b) Thomas, L.; Lionti, F.; Ballou, R.; Gatteschi, D.; Sessoli, R.; Barbara, B. *Nature* **1996,** *383,* 145–147.

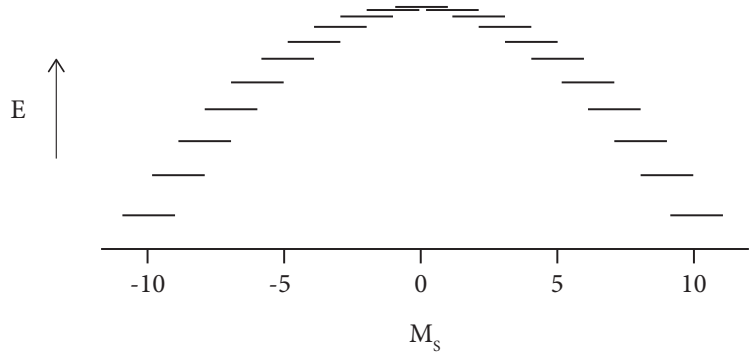

Figure 5.1 Schematic representation of the energies of the spin microstates that correspond to the S = 10 ground state multiplet as a function of magnetic quantum number M_S.

molecule. These lead to a large ground spin state multiplet (dimensionless total molecular spin state S; z projection M_S) whose energies split up in zero-field in the presence of a uniaxial anisotropy as $-DM_S^2$ (where D is the zero field splitting parameter of the magnetic cluster). Figure 5.1 illustrates the energy splitting of a hypothetical S = 10 ground spin state cluster. It is well known that a phonon-induced transitions may only happen between spin projections so that $\Delta M_S = \pm 1$ or $\Delta M_S = \pm 2$. Hence, a uniaxial spin anisotropy (accounted by a $D < 0$) effectively creates an energy barrier (U) toward relaxation of the magnetization. The molecular magnetic moment must overcome this barrier as it switches between inverse orientations of the z component of the magnetic moment. Equation 5.1 defines U as a function of S and D. This slow relaxation of the magnetization reflects both in large magnetic hystereses (with occasional quantum tunnelling steps) and in characteristic shifts in the position and intensity of the AC magnetic susceptibility maxima as the AC frequency is varied.[117]

$$U = S^2 |D|$$

Equation 5.1 General expression of the energy barrier for the spin switching in a SMM

Regarding their chemical nature, single-molecule magnetism has been traditionally based on large metal clusters with an organic shell and a core of metal atoms generally bridged by oxo (O^{2-}) ligands. Mn_{12} is the archetype of this

117 Gatteschi, D.; Sessoli, R. *Angew. Chem. Int. Ed.* **2003,** *42,* 268–297.

first-generation SMMs.[118] Nowadays the family of SMMs has greatly expanded and it involves molecules of very different composition and chemical topologies: organic single-ion magnets (SIMs), inorganic SIMs and POM-capped metal clusters for example.[119] In any case, due to their molecular nature, SMMs present some important advantages over more traditional metallic or metal oxide superparamagnetic nanoparticles, including the uniformity of particle size, the solubility in organic solvents and the chemical versatility in terms of molecular design. It is thanks to these properties that single-molecule magnetism have been successfully incorporated into new chemically designed hybrid materials.[120]

2 Combination of superconductivity and SMM by chemical design

In the current study, the hybrid solid-state/molecular route has been used as a tool for the design of layered superconductors that host single molecule magnets (SMMs) in their bi-dimensional galleries.[121] Besides the natural interest linked to the organization of magnetic clusters within the interlamellar space offered by a layered host, address the prospective physical implications which might result from the presence of magnetic sites in close proximity with a superconducting lattice was also addressed. The aim of the work was to explore the mutual influence between these two components, in other words, the effect that the strong diamagnetism of a superconductor (SC) below its transition temperature might have on the relaxation dynamics of the SMM cluster and, at the same time, the effect that the large spins of the SMM have on the superconducting properties of a type-II layered SC. The controlled integration of SMMs in direct contact with 2D superconducting layers might contribute to the development of hybrid architectures for sensing and manipulating mesoscopic spins, with possible

118 Lis, T. *Acta Crystallogr. B* **1980,** *36,* 2042.

119 a) Ishikawa, N.; Sugita, M.; Ishikawa, T.; Koshihara, S.-Y.; Kaizu, Y. *J. Am. Chem. Soc.* **2003,** *125,* 8694–8695. (b) AlDamen, M.; Clemente-Juan, J.; Coronado, E.; Martí-Gastaldo, C.; Gaita-Ariño, A. *J. Am. Chem. Soc.* **2008,** *130,* 8874–8875. (c) Fang, X.; Kögerler, P.; Speldrich, M.; Schilder, H.; Luban, M. *Chem. Commun.* **2012,** *48,* 1218.

120 Cardona-Serra, S.; Clemente-Juan, J. M.; Coronado, E.; Martí-Gastaldo, C.; Navarro-Moratalla, E. *Eur. J. Inorg. Chem.* **2013,** *10 - 11,* 1903 - 1909.

121 Coronado, E.; Martí-Gastaldo, C.; Navarro-Moratalla, E.; Burzurí, E.; Camón, A.; Luis, F. *Adv Mater.* **2011,** *23,* 5021–5026.

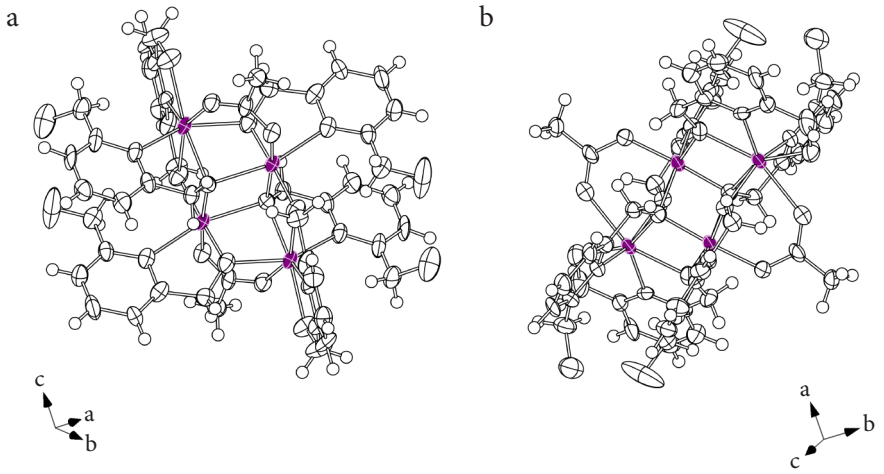

Figure 5.2 Two perspective ORTEP representations of the Mn_4 SMM cluster highlighting the Mn_4 pseudo-cubane core (*lilac* atoms).

applications in the field of quantum information.[122] Notice that the combination of conductivity and single-molecule magnetism has been already attempted. Still, the materials reported behave as semiconductors at best.[123]

Among the library of layered inorganic solids available, we focused on the TMDC family. The versatile intercalation chemistry of TMDCs along with their well-known superconducting properties make these systems ideal candidates for the aim of this work. In particular, tantalum disulphide (TaS_2) was the analogue of choice. The election was motivated by the facile and robust topotactic reduction of this system to higher T_{SC} intercalates which are in turn easy to exfoliate. In this way, bulk δ-2H-$Na_{0.33}TaS_2$ may be delaminated in certain solvents down to its constituent $[TaS_2]^{0.33-}$ anionic layers. The charged nature of these superconducting and highly anisotropic 2DNs provide the colloid with stability and also allows for the direct electrostatic re-stacking with a cationic SMM soluble species. This permits the combination of the intrinsic bi-dimensional superconductivity provided by the $[TaS_2]^{0.33-}$ layers with the magnetic bi-stability features of cationic

122 Imamoglu, A. *Phys. Rev. Lett.* **2009,** *102,* 083602.

123 Hiraga, H.; Miyasaka, H.; Nakata, K.; Kajiwara, T.; Takaishi, S.; Oshima, Y.; Nojiri, H.; Yamashita, M. *Inorg. Chem.* **2007,** *46,* 9661–9671.

single molecule magnets (SMMs) in a new layered hybrid solid-state/molecular material.

As far as the choice of the SMM is concerned, a conveniently charged and robust molecular unit should be selected. In this way, we chose the Mn_4 tetranuclear cluster: $[Mn_4(OAc)_2(pdmH)_6]^{2+}$ (pdmH = deprotonated pyridine-2,6-dimethanol; $C_5H_4NO_2$).[124] This system is composed of a central tetramer of $(Mn^{2+})_2/(Mn^{3+})_2$ ions bridged through the alkoxide groups of pyridinedimethanol ligands in a μ_2 fashion (see Figure 5.2). This divalent cation shows a ground spin state S = 8 ± 1 and superparamagnetic blocking below 2.5 K. Regardless of their higher blocking temperatures, we discarded the use of other single-molecular magnets belonging to the Mn_{12} family because of their poor chemical stability.[125] The chemical robustness of Mn_4-type clusters has also been demonstrated through its use in the design of a wide range of magnetic materials of different crystal packings.[126] On the other hand, it has also been shown that this unit can be combined with conducting or even superconducting counterparts.[127]

3 Synthetic process

The delamination/flocculation synthetic technique was here employed (recall Figure 4.38 on page 140). This methodology allowed for the exchange of the Na^+ intercalated atoms in δ-2H-$Na_{0.33}TaS_2$ by $[Mn_4]2+$ in a rapid an efficient manner. This synthetic approach results in the fast crashing of the hybrid material out of the colloid, fact which helped to prevent any possible side reactions of the SMM entity from taking place.

For this purpose, compound **11** was employed as a source of $[TaS_2]^{0.33-}$ 2DNs. It is important to re-emphasize that in order to accomplish the exfoliation process

124 Yoo, J.; Brechin, E.; Yamaguchi, A.; Nakano, M.; Huffman, J.; Maniero, A.; Brunel, L.-C.; Awaga, K.; Ishimoto, H.; Christou, G.; et al. *Inorg. Chem.* **2000,** *39,* 3615–3623.

125 Mannini, M.; Pineider, F.; Sainctavit, P.; Joly, L.; Fraile-Rodríguez, A.; Arrio, M.-A.; Cartier Dit Moulin, C.; Wernsdorfer, W.; Cornia, A.; Gatteschi, D.; et al. *Adv. Mater.* **2009,** *21,* 167–171.

126 a) Miyasaka, H.; Nakata, K.; Sugiura, K.; Yamashita, M.; Clerac, R. *Angew. Chem. Int. Ed.* **2004,** *43,* 707. (b) Miyasaka, H.; Nakata, K.; Lecren, L.; Coulon, C.; Nakazawa, Y.; Fujisaki, T.; Sugiura, K.-I.; Yamashita, M.; Clérac, R. *J. Am. Chem. Soc.* **2006,** *128,* 3770–3783.

127 a) Shiga, T.; Miyasaka, H.; Yamashita, M.; Morimoto, M.; Irie, M. *Dalton Trans* **2011,** *40,* 2275–2282. (b) Hiraga, H.; Miyasaka, H.; Clérac, R.; Fourmigué, M.; Yamashita, M. *Inorg. Chem.* **2009,** *48,* 2887–2898. (c) Bosch-Navarro, C.; Coronado, E.; Martí-Gastaldo, C.; Rodríguez-González, B.; Liz-Marzán, L. M. *Adv. Funct. Mat.* **2012,** *22,* 979–988

in a clean way, the swelling solvents were previuosly degassed and the ultrasound treatment was performed in an inert atmosphere. The careful addition of an acetonitrile solution containing a fixed concentration of $[Mn_4(OAc)_2(pdmH)_6]^{2+}$ cations (**16**) to a freshly prepared sol of **11**, triggered attractive electrostatic interactions between the oppositely charged species coexisting in solution and drove the assembly of the new layered hybrid superstructure of formula $[TaS_2][Mn_4(OAc)_2(pdmH)_6]_{0.15}$ (**17**).Worthwhile mentioning is that in order to discard a mere co-precipitation of both components, a range of $[Mn_4]^{2+}$: $[TaS_2]^{0.33-}$ non-equivalent concentration ratios were explored. As a matter of fact all of the concentrations tested lead to homogeneous phases with the same stoichiometry within experimental error as analysed by EPMA (see Table 5.1).

$[Mn_4]$ /mM	Mn_4 molar excess	% Ta		% Mn	
		exp.	*theor.*	*exp.*	*theor.*
2.14	× 1	63.5		36.5	
2.14	× 2	78.9	60	21.1	40
3.21	× 2	65.9		34.1	

Table 5.1 Variation of the relative metallic content of hybrid material **17** as seen by EPMA (*exp.*) with respect to the Mn_4 flocculating concentration (mmol per L of acetonitrile). The theoretical values calculated from ideal electrostatic compensation are indicated (*theor.*).

If no extra care was taken during filtration and isolation steps, hybrid compound **17** was recovered as a powder sample. By contrast, the isolation of the final hybrid material could also be achieved in the form of free-standing large surface area highly oriented macroscopic flakes. The slow controlled sedimentation of the flocculated material allowed for the individual crystallites to pack in a co-planar orientation within high aspect ratio thin scales (**18**) that could be easily scooped from the filter surface. Figure 5.3 shows SEM images comparing the hybrid SC-SMM compound synthesised in the form of powder (**17**) and in the form of oriented scales (**18**). These samples were specially well-suited for the characterization of anisotropic physical properties such as the two-dimensional

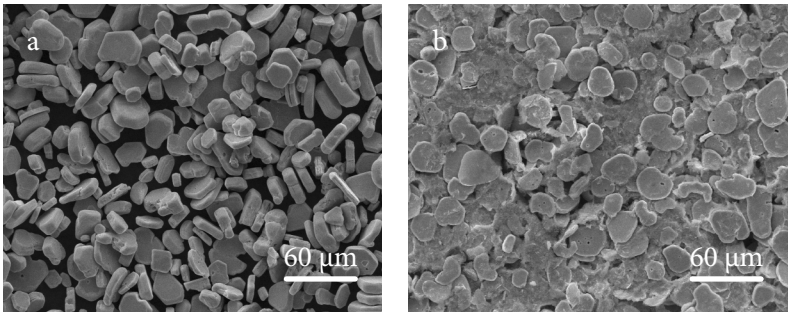

Figure 5.3 SEM images of hybrid $[Mn_4]_{0.15}TaS_2$ samples isolated as a powder (**17**, **a**) and as an oriented flakes (**18**, **b**).

superconductivity since the basal planes of each individual crystallite were approximately parallel to the flake surface (*vide infra* section 4.3 on page 164).

4 Physical properties and characterization

4.1 XPS experiments

XPS experiments were performed and provided evidence of the presence of Mn_4 clusters with binding energies that are in good agreement with the expected bonding states. Figure 5.4 shows a comparison between the XPS data obtained for pristine SMM sample **16** and the one obtained for hybrid compound **17**.

The Mn 2p³⁄₂ (up) and Mn 3s (down) signals exhibited by **17** coincide with the spectra collected for **16**. Taking into account the oxidation states that may be inferred from the spectra (Figure 5.4g), the XPS experiment provides a strong indication of the presence of the unaltered Mn_4 core within the TaS_2.

4.2 Structural studies

The direct comparison between the X-Ray diffraction data collected from ground samples of the starting materials (**11** and **16**) and the re-stacked hybrid (**17**) confirms that the diffraction profile observed for the latter is not merely a superposition of the XRPD patterns of the precursors. This supports the generation

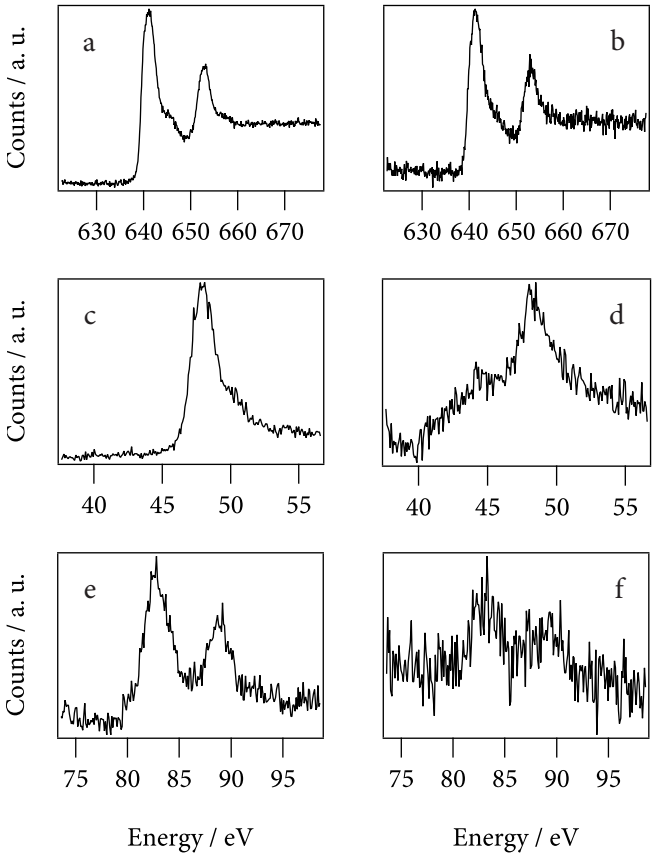

g

Compound	Mn 2p ³⁄₂	Mn 3s' – Mn 3s"	Mn 3s	Mn 3p
			spin energy splitting	
16	641. 2 (Mn^{2+}) 642.7 (Mn^{4+}) 645.2 (sat. Mn^{2+})	83.3 - 89.7 84.8 - 88.9	6.4 (Mn^{2+}) 4.08 (Mn^{4+})	48.64 (Mn^{2+}/Mn^{3+}) 50.60 (Mn^{4+})
17	641.3 (Mn^{2+}) 642.86 (Mn^{4+}) 645.1 (sat. Mn^{2+})	83.2 - 90.0 84.6 - 88.2	6.7 (Mn^{2+}) 3.6 (Mn^{4+})	48.68 (Mn^{2+}/Mn^{3+}) 50.0 (Mn^{4+})

Figure 5.4 XPS high resolution scans of **16** (2p³⁄₂: **a**; 3p: **c**; 3s: **e**) and **17** (2p³⁄₂: **b**; 3p: **d**; 3s: **f**) collected in the Mn binding energy region. **g**. Mn 2p³⁄₂, Mn 3s and Mn 3p experimental binding energy estimated values (in eV) and chemical state assignment (*in brackets*) extracted from previous.

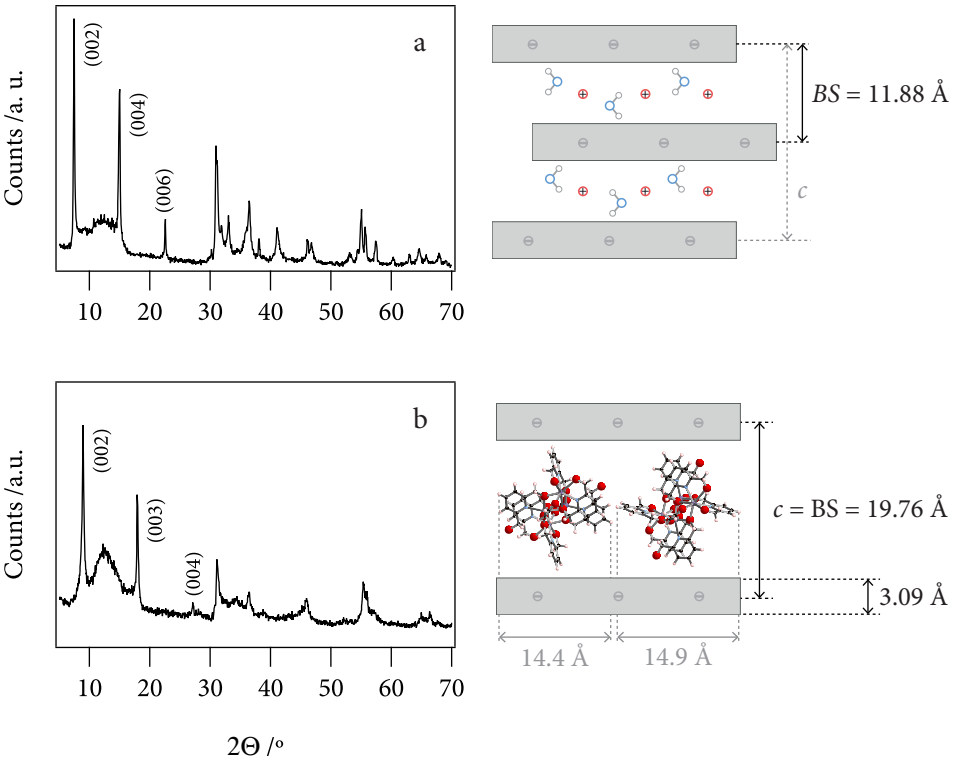

Figure 5.5 Structural model ascribed to the powder patterns observed for δ-2H-$Na_{0.33}TaS_2$ (**11**, **a**) and $[Mn_4(OAc)_2(pdmH)_6]_{0.15}[TaS_2]$ (**17**, **b**).

of a novel layered crystalline phase in the solid state from the combination of the ionic nano-sheets in solution (see Figure 5.5).

Due to the delamination/flocculation methodology employed, **17** presents a bigger number of stacking defects and overall disorder than the starting components, as denoted by the weaker intensity and broader profile of the reflection lines. These problems have generally hindered the determination of accurate structural models for intercalation complexes of layered dichalcogenides.[105] Still, two sharp intense diffraction peaks and a broader less intense one, which can be indexed as (002), (003) and (004) reflections by assuming a hexagonal unit cell, are observed at low angular values and permit estimating a crystallographic *c* axis value of 19.8 Å. In contrast with the neutral host and the δ-Na^+-intercalated 2H polytypes (with basal spacing, BS = *c*/2, of 6.1 Å and 11.8 Å, respectively), this

value suggests the formation of a 1H phase (BS = *c*) with an eclipsed packing of the TaS_2 slabs in the solid-state. This is the result of the exfoliation and subsequent re-assembly of a layered structure with the Mn_4 complex in solution. This stacking periodicity provides a BS of *ca.* 19.8 Å for **17**, in excellent agreement with the addition of the thicknesses of one TaS_2 layer (3.1 Å),[128] and the average size of the Mn_4 complex (*ca.* 15 Å in diameter assuming a spherical model).

4.3 Coexistence of SMM behaviour and SC

Following, the magnetic characterisation of the synthesised materials is presented. The study described in this section was performed in collaboration with Prof. Fernando Luis from ICMA (Instituto de Ciencia de Materiales de Aragón, Universidad de Zaragoza).

The AC magnetic susceptibility (Figure 5.6) performed on bulk powder samples of the hybrid material (**17**) clearly show the coexistence of a diamagnetic response, characteristic of the superconductivity, and a paramagnetic one, which can be attributed to the Mn_4 clusters. The AC susceptibility of **17** is dominated by the transition to the superconducting state at T_{SC} = 4.2 K, and is frequency independent above 2 K Nevertheless, though masked by the enormous diamagnetic susceptibility of the superconducting layers, a maximum is observed in the out-of-phase component. This is clearly shifted to lower temperatures in comparison with the reference cluster **17** and shows a frequency dependence that can be described with an Arrhenius law, indicating the existence of the slow and thermally activated magnetic relaxation typical of SMMs. Indeed, the activation E_a of *ca.* 10.4 K estimated for the Mn_4 clusters in the hybrid material is typical of a superparamagnetic regime.

In order to discard the presence of spin glass behaviour a Mydosh frequency shift parameter value of ϕ = 0.25 could be extracted from the out-of-phase maxima according to Equation 5.2 (where T_b is the temperature of the χ" maxima and *f* is the frequency). This is in excellent agreement with that expected for superparamagnetic behaviour ($0.1 \leq \phi \leq 0.3$).[129] The Arrhenius fit (see Figure 5.7) suggests an activation energy of U / k_B = 10.4(4) K. This barrier value is lower

128 Bruce, D. W.; O'Hare, D. *Inorganic Materials,* John Wiley & Sons, **1997**

129 Mydosh, J. A. *Spin Glasses: An experimental introduction*; Taylor & Francis, London, **1993**

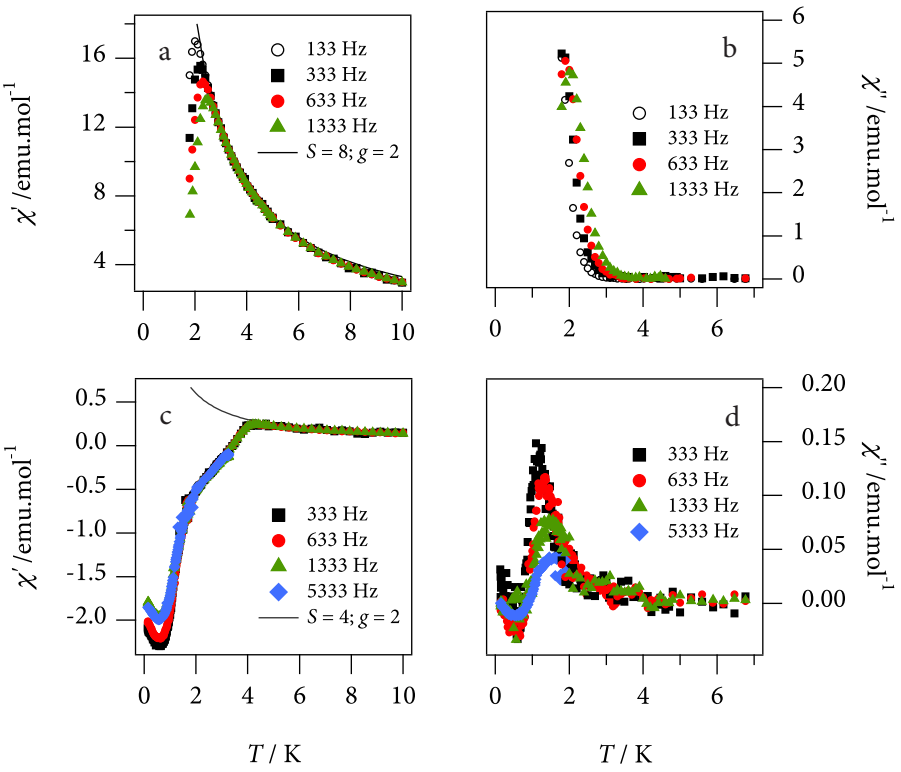

Figure 5.6 AC magnetic susceptibility study of the SMM material **16** (in-phase: **a**; out-of-phase: **b**) and of the hybrid material **17** (in-phase: **c**; out-of-phase: **d**). The solid lines show the predicted susceptibility of anisotropic spins $\chi = N_A(gS\mu_B)^2/3k_B(T-\theta)$ for two different values of g and S, the Weiss temperature being $\theta = 0.3$ K for **16** and ≈ 0 for **17**.

than the one estimated for **16** and explains why the AC susceptibility of **17** is almost frequency independent above 2 K. In fact, the activation energy of **17** is approximately half of that estimated for the starting pure SMM material **16** ($U / k_B = 20(1)$ K).[124] This suggests that the magnetic relaxation of Mn_4 clusters is strongly influenced by the presence of the superconducting host, becoming faster as the clusters are inserted in between TaS_2 layers.

$$\phi = \frac{\Delta T_b}{T_b \Delta (\log f)}$$

Equation 5.2 Mydosh frequency shift parameter.

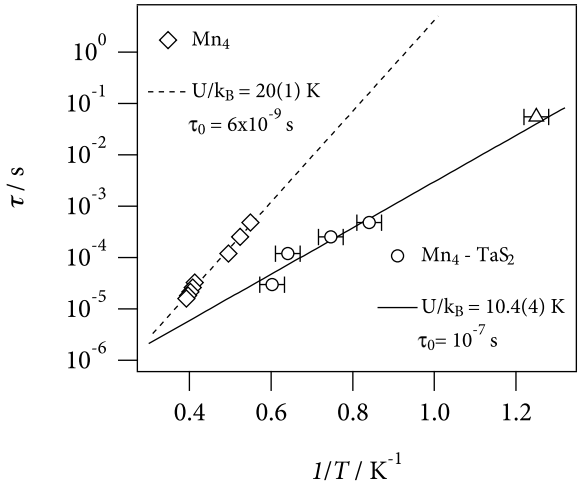

Figure 5.7 Arrhenius fitting of **16** (*dashed*) and **17** (*continuous*) extracted from the out-of-phase AC signal shown in Figure 5.6. The triangular marker showed in the plot of **17** represents a data point estimated from the temperature dependence of the remnant magnetization measured below 1 K (see Figure 5.8f).

The change in the magnetic behaviour of Mn_4 clusters in the hybrid material is also confirmed by the hysteresis loops measured on **16** and **17** at very low temperatures (view Figure 5.8). At $T = 0.35$ K, the coercive field of the Mn_4 sample **16** ($\mu_0 H_c = 0.33$ T) is about ten times larger than that of the hybrid material **17** ($\mu_0 H_c = 0.035$ T). Figure 5.8 shows the variation with temperature of the coercive fields (H_c) of samples **16** and **17**. Still, the hysteresis loops further clearly confirm the coexistence of a diamagnetic response with a super-paramagnetic one.

This faster magnetic relaxation may arise from two possible scenarios: a change in the structure of magnetic energy levels of the molecular cluster, that is, of the magnetic anisotropy associated with the different environment; or, alternatively, a faster tunnelling rate associated with the screening of intermolecular dipolar interactions by the superconducting layers. Further measurements of the magnetic relaxation in the presence of strong DC fields ($H > H_{c1}$ for $[TaS_2]^{0.33-}$) were performed in order to discriminate amongst these two situations.[130] When the external field becomes larger than the lower critical field of the superconducting

130 The whole set of AC thermal variation curves are shown in Appendix 4.3 on page 289.

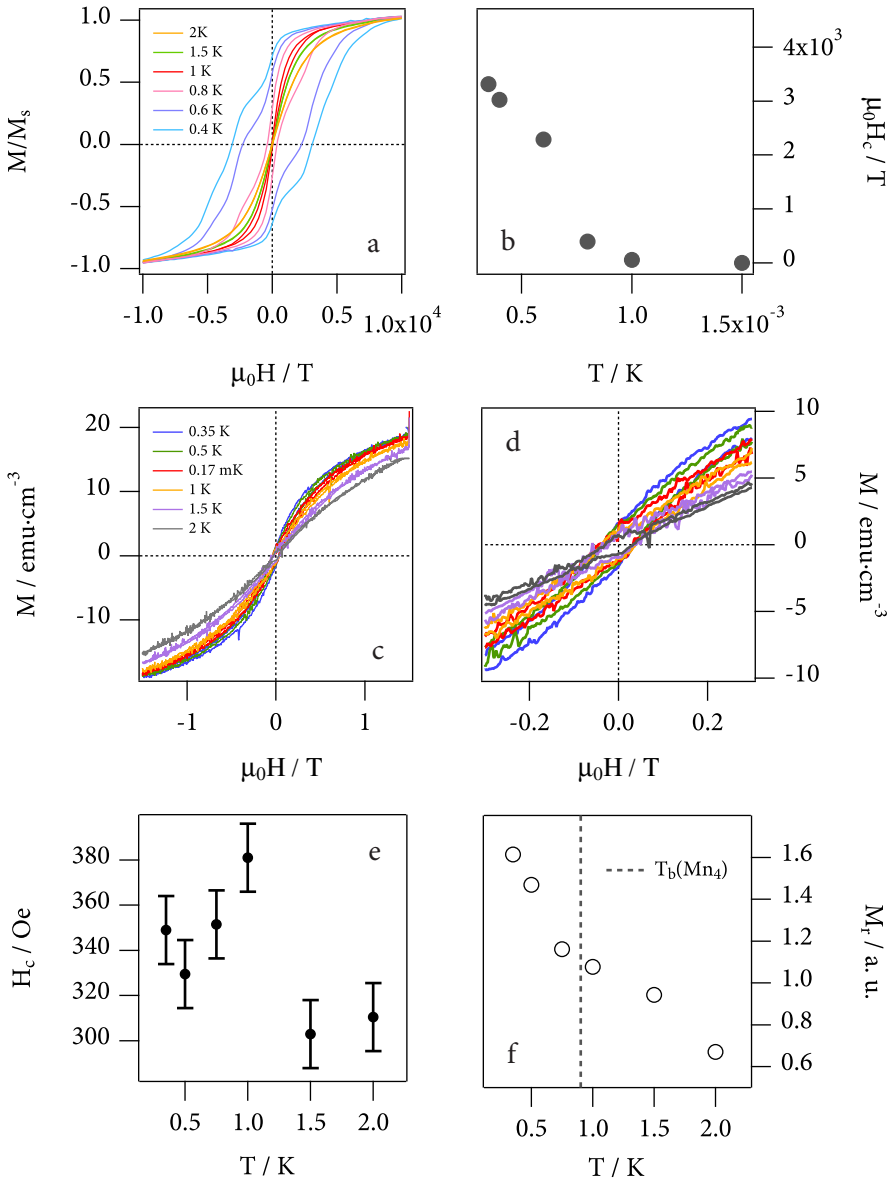

Figure 5.8 Magnetic hysteresis loops of samples **16** (**a**) and **17** (**c**: full range; **d**: zoom-in of the central region) measured at different temperatures (T ≤ 2 K) with a μ-Hall sensor. **b** shows a plot of the variation of the coercive field of compound **16** as a function of the temperature. **e** and **f** show the coercive and remnant field values respectively of compound **17** determined from the hysteresis loops. T_b is a guide to the eye suggesting the blocking temperature for the Mn_4 clusters in hybrid **17**.

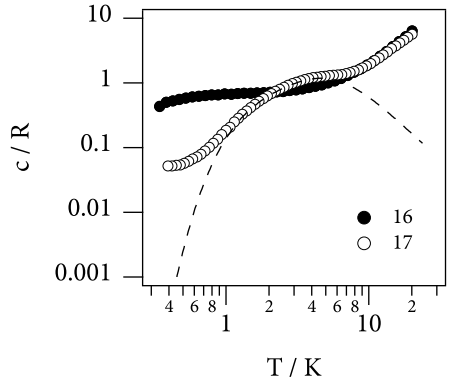

Figure 5.9 Specific heat data of the reference SMM **16** (*hollow markers*) and of the hybrid material **18** (*filled markers*) measured as a function of temperature and under zero applied field. The dashed line shows the calculated profile for Mn_4 cluster (S = 8 and D/k_B = -0.358).

$[TaS_2]^{0.33-}$ component (H_{c1} ~ 170 Oe for **11**; recall part b of section 3.2, Chapter 4, page 140) the interactions are no longer screened and the relaxation rate is mainly determined by the strength of the magnetic anisotropy. The data measured on **17** remain different from those measured on the reference sample **16** at all fields, even for H = 3000 Oe when it is clear that T_{SC} of the superconducting fraction becomes smaller than 1.8 K. Under these conditions the relaxation of the clusters should not be affected by the superconductivity of TaS_2. Therefore, we must conclude that the magnetic anisotropy of Mn_4 clusters is greatly modified by their insertion into TaS_2 layers.

This assumption is additionally supported by comparing the specific heat data of compounds **16** and **17**. Figure 5.9 shows the specific heat data. In order to allow a direct comparison between the two, the specific heat per mol of Mn_4 clusters has been plotted for the two samples. The specific heat of a magnetic material provides direct information on the structure of magnetic energy levels and thus enables to ascertain if important changes in the anisotropy parameters have occurred. The experimental data reflect that the Schottky anomaly in **17** is markedly lower and shifted towards lower temperatures compared with the anomaly measured for **16**. This confirms that the zero-field splitting associated with the magnetic anisotropy of Mn_4 clusters becomes smaller as they are inserted into TaS_2. It also suggests that the net molecular spin, which determines the number of energy levels populated

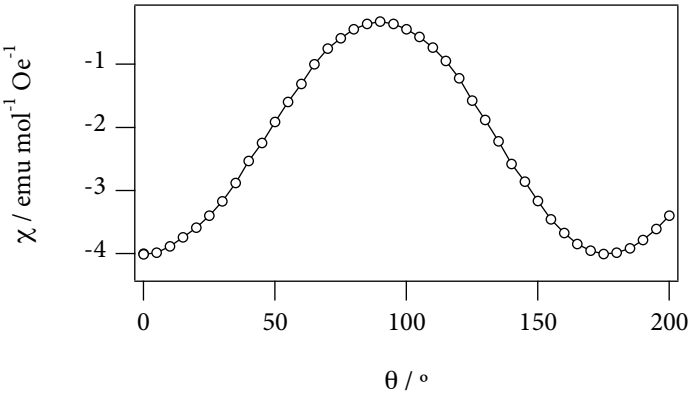

Figure 5.10 AC magnetic susceptibility of a single oriented flake of **18** measured at 2 K as a function of the sample orientation (θ) with respect to the AC magnetic field.

at these temperatures and thus the magnetic entropy change, might also be lower in the latter sample. This is confirmed by magnetization isotherms recorded for 17 that reach a magnetization value of M ≈ 3.5 μ_B per Mn_4 cluster at 2 K and 5 T, clearly below the saturation magnetization of **16** (16 μ_B). From the susceptibility values (Figure 5.6), we estimate a ground state S = 4 for the clusters in **17**, that is, half the value S = 8 found in the starting material **16**. A final remark concerning the specific heat profile of hybrid **17** is the absence of a well-defined lambda peak. This is once again typical of strongly two-dimensional superconducting materials as opposed to three-dimensional bulk superconductivity. The intrinsic two-dimensional nature of superconductivity in TaS_2 and Na-intercalated materials make them exhibit a very high level of entropy above T_{SC}, hence the maximum smears in such a way that is hardly observable.[131]

Interestingly, the isolation of the hybrid compound in the form of highly oriented flakes (**18**) provided with new insights into the magnetic behaviour of this material. In view of the angle-dependent AC susceptibility measured for a single flake, it is evident that the magnetic susceptibility of the hybrid sample is strongly anisotropic (see Figure 5.10). In this line, a co-parallel orientation of the pellet

131 a) Geballe, T.; Menth, A.; Di Salvo, F.; Gamble, F. *Phys. Rev. Lett* **1971,** *27,* 314–316. (b) Benda, J. *Phys. Rev. B* **1974,** *10,* 1409–1420. (c) Meyer, S.; Howard, R.; Stewart, G.; Acrivos, J. V.; Geballe, T. H. *J. Chem. Phys.* **1975,** *62,* 4411–4419. (d) Schlicht, A.; Schwenker, M.; Biberacher, W.; Lerf, A. *J. Phys. Chem. B* **2002,** *105,* 4867–4871.

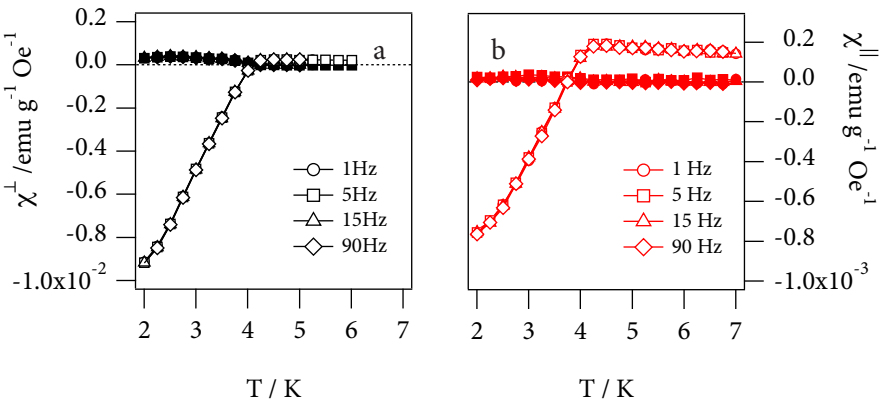

Figure 5.11 AC magnetic susceptibility of a single oriented flake of **18** measured at 2 K in perpendicular (**a**) and parallel (**b**) orientations with respect to the AC magnetic field. Note that the *y*-axis range in **b** is almost one order of magnitude smaller than in **a**.

with the external applied field leads to maximum shielding whilst an orthogonal one reduces the Meissner response. Additionally, while the overall susceptibility suggests bulk diamagnetism, the maximum and minimum values are closer to zero than those observed for the pure Na_xTaS_2 single crystals **15** (*vide supra* Figure 4.41 on page 144),[132] signalling the presence of an additional paramagnetic component. The response of the magnetic Mn_4 clusters can be clearly seen above T_{SC}, as shown in Figure 5.11. This paramagnetic contribution appears to be nearly independent of θ, meaning that the magnetic anisotropy axes of the Mn_4 clusters are not aligned. It is worth noticing also that the critical temperature is coincident (T_{SC} = 4 K) for the two orientations. Individual flakes of **18** exhibit no evidence of the double transition that could be observed for instance in **15** when the AC magnetic field lies co-parallel to the TaS_2 planes. A likely interpretation is that the intercalation of the clusters hinders the establishment of quantum coherence between Cooper pairs in adjacent layers, thus enhancing the bi-dimensional character of the superconductor.

The magnetization isotherms of **18** measured from 2 K down to 350 mK is shown in Figure 5.12 and in Figure 5.13. Both sets of data confirm once again

132 A direct comparison with the values obtained for the actual precursor material **11** may not be established due to the large influence of the crystallite orientation and the impossibility to control this parameter in a polycrystalline sample.

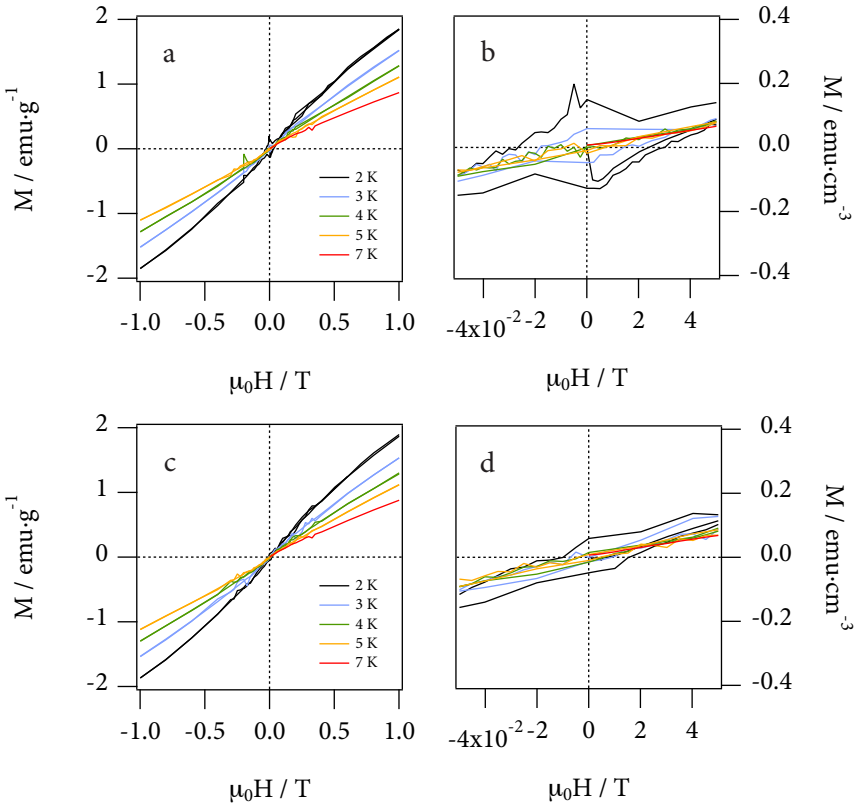

Figure 5.12 Magnetic hysteresis curves of **18** measured in a SQUID magnetometer at several temperatures and in a perpendicular (**a**, **b**: zoom-in) or parallel (**c**, **d**: zoom-in) orientation of the TaS_2 layers with respect to the external applied field.

the coexistence of a two-dimensional superconducting fraction, with a highly anisotropic and hysteretic magnetization, and a nearly isotropic paramagnetic fraction. In the parallel orientation, the typical features of the superconducting behaviour are very subtle and very difficult to appreciate since they are obscured by the presence of the strong paramagnetic response coming from the Mn_4 clusters. The SQUID data shown in Figure 5.12 for the perpendicular orientation permit estimating a value of H_{c1} = 40 Oe which is in excellent agreement with the value inferred from the measurement performed on powder samples **17** (35 Oe). In addition, the value is similar to the one suggested for precursor material **11** (170 Oe) knowing that a direct comparison may not be established

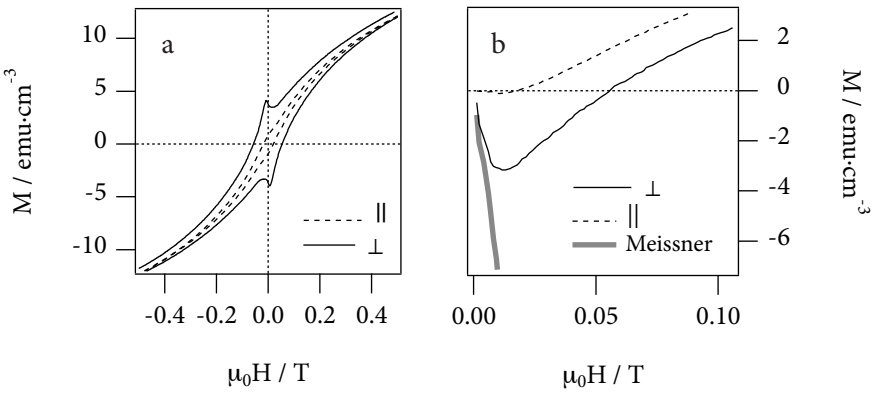

Figure 5.13 a. Magnetic hysteresis curves of a single oriented flake of **18** measured at 350 mK in a μ-Hall sensor in perpendicular (**a**) and parallel (**b**) orientations with respect to the AC magnetic field. **b**. Initial magnetization curves in the low-field region for both orientations and comparison with the ideal Meissner response.

due to the orientation issue. The magnetic hysteresis is considerably enhanced with decreasing temperature below 2 K (Figure 5.13). One may also observe an increase of H_{c1} from the values measured at 2 K. At T = 350 mK, H_{c1} = 104 Oe (118 Oe) for the parallel (perpendicular) orientation. This could be attributed to the enhancement of the hysteresis due to the onset of magnetic memory in the Mn_4 clusters. However, the low temperature hysteresis in the hybrid is still dominated by the response of the superconducting fraction. Hence, extra evidence is required to support this hypothesis. Figure 5.13 also permits to appreciate how when the field is orthogonal to the TaS_2 planes, the magnetization is close to the expected value for a perfect diamagnetic material (Meissner response: M = (-¼π)H, when expressed in emu·cm^{-3}). Notice that a reduction from this limit is expected on account of the flat shape of the specimen, which favours the formation of an intermediate or a mixed state.[133] By contrast, when the field is parallel to the TaS_2 and sample planes, the diamagnetic response is strongly reduced. This is yet a further piece of evidence that suggests the material behaves as a collection of superconducting layers with thicknesses smaller than or comparable to the penetration depth.

133 M. Tinkham, *Introduction to Superconductivity*, Dover Publications, New York, **2004**.

Finally, it is important to emphasize that whilst the relaxation and/or the intrinsic magnetic properties of the Mn_4 clusters experience modifications once nested in between TaS_2 layers, the superconducting behaviour of the dichalcogenide layers remains totally unaltered. Not only T_{SC} = 4.2 K found for **17** is almost coincident with T_{SC} = 4.5 K of the precursor material **11**, but also the value of H_{c1} seems to change little (*vide supra*). The fact that T_{SC} and H_{c1} of the hybrid remain close to the values measured on the precursor material suggests that the superconductivity of each TaS_2 layer is little affected by the intercalation of Mn_4 clusters.

5 Conclusions

The hybrid solid-state/molecular approach has been here employed for the synthesis of the first material combining superconductivity and SMM properties. The exhaustive magnetic characterization of the hybrid samples confirms that superconductivity and SMM behaviour coexist in this chemically engineered material. Interestingly, the magnetism of the Mn_4 clusters suffers large changes as they are inserted in between the TaS_2 layers, experimenting a change in the spin ground state. In particular, the magnetic anisotropy becomes weaker, leading to a faster magnetic relaxation, and the molecular spin becomes smaller.

In addition, a step further in the synthesis of TMDC hybrid materials is herein reported, consisting in the isolation of highly oriented plaquettes with anisotropic properties that mimic the behaviour of the parent solid-state precursor compounds.

The synthesis of this new material represents the first successful attempt to insert a functional molecule into this class of layered chalcogenide superconductors. On the other hand, it extends the realm of the hybrid strategy that arises from the combination of molecule-based components with solid-state inorganic structures.[134, 135] It is also a natural extension of the very recent superconducting-ferromagnetic material, proving the versatility of the layered dichalcogenide strategy for the combination of superconductivity with other interesting

134 See Chapter 2

135 Coronado, E.; Martí-Gastaldo, C.; Navarro-Moratalla, E.; Ribera, A.; Galán-Mascarós, J. *J. Mater. Chem.* **2010,** *20,* 9476–9483.

properties.[114] Finally it is also suggested that, although the presence of Mn_4 clusters in between TaS_2 host layers does not seem to affect the superconducting bulk properties, these high spin clusters may act as a vortex pinning centres. Future studies will be devoted to analyse the vortex dynamics in these hybrid superconductors.

6 Procedures and experimental recipes

Very low temperature physical characterization

The low temperature magnetic characterisation of the materials synthesized was performed in the laboratory of Prof. Fernando Luis from in Zaragoza (Spain).

Hysteresis loops were measured between 350 mK and 7 K using a home-made micro-Hall magnetometer working in a ^{3}He refrigerator. The sample, mixed with Apiezon N grease to ensure thermalization at these very low temperatures, was deposited directly on the edge of one of the two Hall crosses.

The AC susceptibility was also measured, from 333 Hz up to 13 kHz, using a home-built mutual inductance susceptometer thermally anchored to the mixing chamber of a ^{3}He-^{4}He dilution refrigerator, which gives access to temperatures ranging from 0.09 K up to 3.5 K. A lock-in amplifier amplifies the voltages arising from in-phase and out-of-phase magnetic signals. The errors involved in the determination of the output signal's phase have been determined separately by measuring a reference signal and are found to be smaller than 0.01 deg. for any frequency.

Finally, specific heat data were also measured between 350 mK and 20 K on compact pellets using a commercial Physical Properties Measurement System (PPMS).

Material density calculations

In many magnetization plots presented throughout this chapter, the magnetic moment has been normalized per unit of sample volume, namely per cm^3. The calculation was performed diving the corrected long magnetic moment by the sample density, calculated from the unit cell volume extracted from XRPD data. In our case, the unit cell volume of the hexagonal unit cells of compounds were as follows: $V_{2H\text{-}Na_{0.33}TaS_2}$ = 225.9 Å^3; $V_{Mn4\text{-}TaS_2}$ = 188.0 Å^3. This corresponds to a theoretical density of: $\rho_{2H\text{-}Na_{0.33}TaS_2}$ = 3716.9 kg·m^{-3}; $\rho_{Mn4\text{-}TaS_2}$ = 3883.4 kg·m^{-3}.

XPS experiments

Analysis of the samples was performed using a Thermo Scientific K-Alpha ESCA instrument equipped with aluminium $K_{\alpha 1}$, $K_{\alpha 2}$ monochromatized radiation at 1486.6 eV X-ray source. Due the non conductor nature of samples was necessary to use an electron flood gun to minimize surface charging. Neutralization of the surface charge was performed by using both a low energy flood gun (electrons in the range 0 to 14 eV) and a low energy Argon ions gun. The XPS measurements were carried out using monochromatic Al-Kα radiation (hν=1486.6 eV). Photoelectrons were collected from a take off angle of 90º relative to the sample surface. The measurement was done in a Constant Analyser Energy mode (CAE) with a 100 eV pass energy for survey spectra and 20eV pass energy for high resolution spectra. Charge referencing was done by setting the lower binding energy C 1s photo peak at 285.0 eV C1s hydrocarbon peak.[136] Surface elemental composition was determined using the standard Scofield photoemission cross sections.

Syntheses

Synthesis of $[Mn_4(OAc)_2(pdmH)_6](ClO_4)_2$ [16]: polycrystalline samples of this compound were obtained according to the method previously described by Yoo *et al.*[124]

IR (KBr pellet) ν/cm^{-1}: 3423,4 (m, br), 2913,1 (w), 2650,7 (w), 1604,5 (m, sh), 1578,3 (m, sh), 1462,4 (m, sh), 1445,8 (m, sh), 1387,0 (m, sh), 1330,6 (m, sh), 1237,7 (w, sh), 1205,0 (w, sh), 1161,0 (w, sh), 1103,6 (st, sh), 1070.9 (s, br), 1008,9 (m, sh), 928,1 (w, sh), 790,5 (m, br), 743,2 (w), 690,7 (m, sh), 669,5 (m, sh), 624,4 (m, sh), 574,0 (m), 547,7 (m), 530,8 (m), 478,9 (m), 453,1 (m), 443,9 (m), 434,5 (m).

Elemental analysis % (calculated for $C_{46}H_{54}N_6O_{24}Cl_2Mn_4 \cdot 2.5H_2O$): C = 38.9 (39.2); H = 4.1 (4.2); N = 5.36 (5.96)

Empirical formula: $C_{46}H_{54}N_6O_{24}Cl_2Mn_4 \cdot 2.5H_2O$; FW = 1410.66

136 *Journal of Electron Spectroscopy and Related Phenomena* **1995**, *74*, 201-206

Synthesis of $[Mn_4(OAc)_2(pdmH)_6]_{0.15}[TaS_2]$ [17]: 222 mg (0.88 mmol) of **11** were suspended in 150 mL of a 1 : 1 (v/v) degassed mixture of ultrapure Milli-Q water and N-methylformamide. At this stage, sedimentation of the solid material occurred at once was the suspension left to stand. Following, the exfoliation process of **11** was carried out under an Ar atmosphere in three successive steps: 1) mechanical stirring during 3 min ; 2) ultrasonic bath treatment during 60 min ; 3) mechanical stirring during 5 min. Upon completion of the exfoliation step, the yellowish grey suspension had attained stability and exhibited a remarkable 'pearl effect' when stirred. The final flocculation stage involved the drop-wise addition of a solution of **16** in acetonitrile (0.15 mmol in 75 mL) over the delaminated stable sol of **11**. The addition was performed whilst gently stirring the reaction medium. The addition rate was controlled via Ar pressure and the use of cannula transferring procedures. The resulting slurry was allowed to stir for 20 minutes and finally left to stand for another 40 min until partial sedimentation. The yellowish supernatant was decanted off and the flocculated solid was then washed thrice by re-suspending/decanting with fresh acetonitrile (100 mL). *In vacuo* drying of the material yielded a glittering grey powder that was best preserved under an Ar atmosphere.

Elemental ratio estimated by EPMA (calculated for $C_{6.9}H_{8.1}Mn_{0.6}N_{0.9}O_{2.4}TaS_2$): Na/Ta = 0.00 (0.00), Mn/Ta = 0.57 (0.60).

% H_2O weight (TG loss for T < 200 °C) = *negligible*

Empirical formula: $[C_{46}H_{54}Mn_4N_6O_{16}]_{0.15}TaS_2$; FW = 439.92

Synthesis of oriented flakes of $[Mn_4(OAc)_2(pdmH)_6]_{0.15}[TaS_2]$ [18]: the delamination and flocculation steps were carried out in the same way as was done for **17**. Once the hybrid material was precipitated, it was well re-suspended in fresh acetonitrile and transferred to a membrane filtration set-up (see Appendix 4.5, section 1.11 on page 301) with a frit and a PTFE membrane of 0.2 µm of pore size. The suspension was poured into the top reservoir cup and the precipitate was left to settle by effect of gravity. Once the supernatant was clear, vacuum was established in the bottom conical drain vessel and the acetonitrile was left to filter through. Two additional aliquots (20 mL) of fresh acetonitrile were passed through the solid subsequently. The resulting black slurry was left to dry in the

air current and finally *in vacuo*. Large relatively robust flakes could be scraped off the PTFE membrane. Samples prepared by this technique presented the same chemical composition as the powder specimens **17** within experimental error.

6 Magnetic superconductors by insertion of SCO complexes between TaS_2 layers

The re-stacking of charged $[TaS_2]^{x-}$ 2DNs with molecular counterparts has so far allowed for the combination of superconductivity with a manifold of other molecule-intrinsic properties such as single-molecule magnetism (see Chapter 5).Yet, a hybrid compound that blends superconductivity with spin crossover switching has still not been reported. Here we continue to exploit the solid-state/molecule-based hybrid approach for the synthesis of a layered TaS_2-based material that hosts Fe^{2+} complexes with a spin switching behaviour. The chemical design and synthetic aspects of the exfoliation/re-stacking approach are discussed, highlighting how the material can be conveniently obtained in the form of highly oriented easy-to-handle flakes. The likely sensitivity of the intercalated Fe^{2+} complexes to external stimuli such as light opens the door for the study of synergistic effects between the superconductivity and the spin crossover switching at low temperatures.

1 Introduction

1.1 The spin crossover phenomenon

More than eight decades ago, Cambi *et al.* first reported the unusual magnetic behaviour of the tris(N,N-dialkyldithiocarbamato)iron(III) complexes under different conditions.[137] However, it was not until the avenue of ligand field theory that a solid interpretation of these result was provided.[138] Indeed, already in the mid 50s, Orgel suggested that the anomalous magnetic behaviour observed many years earlier could be explained by a equilibrium of spin states.[139]

---

137 a) Cambi, L.; Szegö, L. *Ber. Deutsch. Chem. Ges.* **1931,** *64,* 167. (b) Cambi, L.; Malatesta, L. *Ber. Deutsch. Chem. Ges.* **1937,** *70,* 2067.

138 Schäfer, H.L.; Gliemann, G. *Einfürung in die Ligandenfeldtheorie*, Akademische Verlagsgesellschaft, Frankfurt/Main, **1967**.

139 Orgel, L. *Tenth Solvay Conference*, Brussles, **1956**.

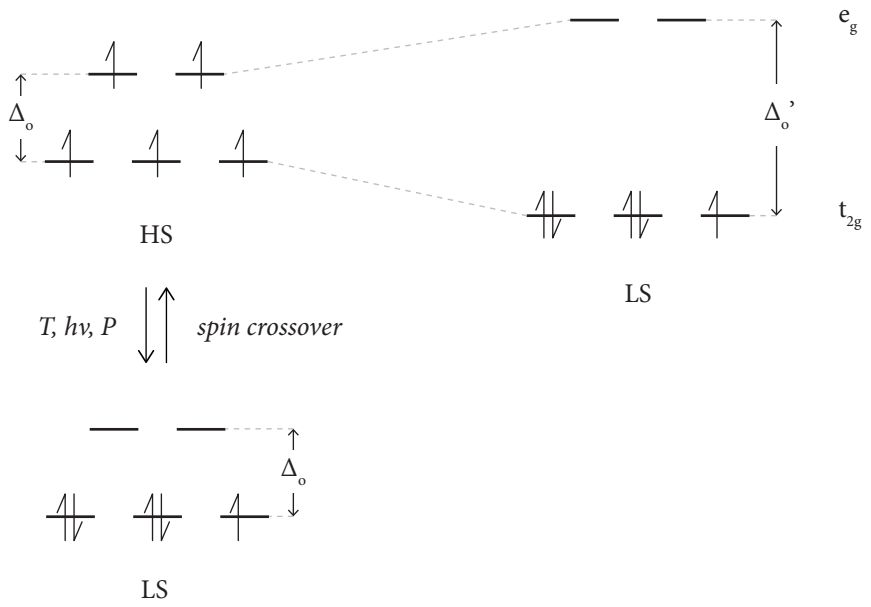

Figure 6.1 Scheme illustrating different splitting energies (Δ_o, Δ_o') in hypothetically different octahedral (O_h) ligand fields and the SCO phenomenon provoked by different external stimuli in the same O_h ligand field.

Nowadays it is well established that the so called spin crossover (SCO) phenomenon is a spin transition or spin equilibrium that occurs in some metal complexes wherein external stimuli (namely temperature, pressure or light irradiation) cause the spin state of the molecule to change.[140] In most metal complexes the spin ground state is either low spin (LS) or high spin (HS) depending on the magnitude of the ligand field splitting (Δ) and the electron pairing energy.[141] This means that for weaker ligand fields, the energy involved in populating the higher-energy e_g levels following Hund's rule is smaller than the pairing energy and the complex will remain HS. The opposite situation rules the case of the higher ligand fields. However, there are some compounds in which this equilibrium is subtly balanced and depending on the external conditions,

140 Gütlich, P.; Goodwin, H. A. *Spin Crossover in Transition Metal Compounds*. Springer-Verlag, Berlin, **2004**.

141 Cotton, F. A.; Wilkinson, G.; Gaus, P. L. *Basic Inorganic Chemistry*, Wiley, **1995**.

the pairing energy may or may not be overcome resulting in the complex having either a LS or HS character.

These SCO transitions happen to be gradual in some cases and more abrupt in others. Sometimes a magnetic hysteresis is even exhibited, which indicates strong cooperativity between neighbouring SCO metal centres. In the latter case a bi-stability region may occur, where both spin states may coexist in stable and metastable states. Big efforts have been devoted to the control of the hysteresis range via chemical design.[142]

1.2 Spin crossover properties in hybrid materials

SCO transitions are of importance as they may be profited from for practical switching or displaying applications. On a more fundamental note, much research has already been devoted to the understanding of spin transition processes in solid materials and also to the investigation of pathways for the control of such phenomena by either chemical design or external stimuli.[143]

Recent activity in the field has been focused in the design of new materials in which SCO properties are blended with other chemical or physical properties.[144] For instance, the interplay between magnetism and SCO has been extensively addressed during the past few years.[145] Electrical conductivity is another property that has also drawn much attention during the past decades in the field of molecule-based materials.[146] Much effort has been dedicated to the synthesis of conducting or even superconducting organic phases composed of charge transfer

142 *For instance:* Galán-Mascarós, J. R.; Coronado, E.; Forment-Aliaga, A.; Monrabal-Capilla, M.; Pinilla-Cienfuegos, E.; Ceolin, M. *Inorg. Chem.* **2010,** *49,* 5706–5714.

143 a) Real, J. A.; Andrés, E.; Muñoz, M. C.; Julve, M.; Granier, T.; Bousseksou, A.; Varret, F. *Science* **1995,** *268,* 265–267. (b) Létard, J.-F.; Guionneau, P.; Rabardel, L.; Howard, J. A. K.; Goeta, A. E.; Chasseau, D.; Kahn, O. *Inorg. Chem.* **1998,** *37,* 4432–4441. (c) Létard, J.-F.; Guionneau, P.; Nguyen, O.; Costa, J. S.; Marcén, S.; Chastanet, G.; Marchivie, M.; Goux-Capes, L. *Chem. Eur. J.* **2005,** *11,* 4582–4589. (d) Bonhommeau, S.; Molnár, G.; Galet, A.; Zwick, A.; Real, J. A.; McGarvey, J. J.; Bousseksou, A. *Angew. Chem. Int. Ed.* **2005,** *44,* 4069–4073.

144 a) Gaspar, A. B.; Ksenofontov, V.; Seredyuk, M.; Gütlich, P. *Coordination Chemistry Reviews* **2005,** *249,* 2661–2676. (b) Niel, V.; Thompson, A. L.; Muñoz, M. C.; Galet, A.; Goeta, A. E.; Real, J. A. *Angew. Chem. Int. Ed.* **2003,** *42,* 3760–3763.

145 a) Clemente-León, M.; Coronado, E.; López-Jordà, M.; Desplanches, C.; Asthana, S.; Wang, H.; Létard, J.-F. *Chem. Sci.* **2011,** *2,* 1121–1127. (b) Clemente-León, M.; Coronado, E.; López-Jordà, M. *Dalton Trans.* **2010,** *39,* 4903–4910.

146 Akamatu, H.; Inokuchi, H.; Matsunaga, Y. *Nature* **1954,** *173,* 168. (b) Coronado, E.; Day, P. *Chem. Rev.* **2004,** *104,* 5419–5448.

complexes or radical ions.[147] As a matter of fact, the combination of SCO transitions and electrical conductivity has already been explored in the past using an all-molecular approach. As conducting precursors, radical anions as well as metal complexes with redox active ligands have been used.[148, 149] Still, this approach has always afforded hybrid materials with very poor electrical conductivities. In fact, all the reported materials behave as insulators or as semiconductors. Thus, no real SCO metallic conductor has been so far reported, nor a SCO hybrid material exhibiting superconducting properties.

With the aim of extending the hybrid solid-state/molecule-based strategy to the intercalation of other magnetic molecules between superconducting TMDC layers, this chapter explores the insertion of a spin crossover (SCO) complex. In this context, the delamination/flocculation strategy appeared as an unexplored though promising approach to accomplish the task of combining superconductivity with SCO switching. Once again TMDCs play an important role as versatile building blocks for the introduction of superconductivity in hybrid media. The strategy here suggested makes use of a TMDC solid-state part and molecular SCO building blocks for the assembly of a new hybrid material.

2 Design, synthesis and structure

As layered solid state host, $Na_{0.015}TaS_2$ **14** was this time the material of choice. Traditionally, Na-intercalated materials for the synthesis of hybrid materials (such as compound **11**) were accessed via a two-step process that began with the synthesis of pure 2H-TaS_2 and ended with the wet topotactic reduction of the pristine neutral material (*vide supra* section 3.1, Chapter 4, page 113). This is the approach followed for the synthesis of the SMM-SC hybrid material described

147 a) Williams, J.M.; Ferraro, J.R.; Thorn, R.J.; Carlson, K.D.; Geiser, U.; Wang, H.H.; Kini, A.M.; Whangbo, M.H. *Organic Superconductors. Synthesis, Structure, Properties and Theory*, Ed. Grimes, R. N., Prentice Hall, Englewood Cliffs, NJ, **1992**. (b) Ouahab, L. *Coord. Chem. Rev.* **1998,** *178–180,* 1501–1531. (c) Coronado, E.; Galan-Mascarós, J. R. *J. Mater. Chem.* **2005,** *15,* 66–74

148 a) Takahashi, K.; Cui, H.-B.; Okano, Y.; Kobayashi, H.; Einaga, Y.; Sato, O. *Inorg. Chem* **2006,** *45,* 5739–5741. (b) Faulmann, C.; Jacob, K.; Dorbes, S.; Lampert, S.; Malfant, I.; Doublet, M.-L.; Valade, L.; Real, J. A. *Inorg. Chem* **2007,** *46,* 8548–8559. (c) Takahashi, K.; Cui, H.-B.; Okano, Y.; Kobayashi, H.; Mori, H.; Tajima, H.; Einaga, Y.; Sato, O. *J. Am. Chem. Soc* **2008,** *130,* 6688–6689. (d) Nihei, M.; Takahashi, N.; Nishikawa, H.; Oshio, H. *Dalton Trans.* **2011,** *40,* 2154–2156.

149 a) Djukic, B.; Lemaire, M. T. *Inorg. Chem* **2009,** *48,* 10489–10491. (b) Djukic, B.; Seda, T.; Gorelsky, S. I.; Lough, A. J.; Lemaire, M. T. *Inorg. Chem.* **2011,** *50,* 7334–7343.

in the previous Chapter 5. On the other hand, starting from precursor material **14** permits saving both time and resources and most importantly, it greatly improves the integrity of the precursor Na-intercalated material. It has already been described how whilst $Na_{0.33}TaS_2$ crystallites synthesized via basic reduction exhibited rounded crystallite vertex a lower crystallinity material **14** exhibited improved crystal morphology and lower degree of defects. Still, both precursors displayed equivalent physical properties notwithstanding these differences.

As SCO cationic species we focused in the classical Fe^{2+} octahedral complexes of N-donor ligands.[150] A big number of these compounds present clean SCO transitions with large bi-stability regions in the pure state. In particular, $Fe(PyimH)_3](ClO_4)_2$ (PyimH = 2-(1H-Imidazol-2-yl)pyridine; $C_8H_7N_3$) not only presents a relatively abrupt spin transition above room temperature but it may also be switched by light radiation stimuli in its pure perchlorate salts.[151] The proposed precursor materials are simple single-ion complexes that live up to the few requisites imposed by the delamination/flocculation approach: they are to some extent compatible with the polar protic solvents that will be employed for the wet exfoliation of the host material.

As mentioned, the synthetic strategy employed was the delamination/flocculation technique (recall Figure 4.38 on page 140). This required the deconstruction of the precursor layered material **14** in its constituent layers. As described in the previous chapter, polycrystalline samples of compound **14** were immersed in degassed water : N-methylformamide, 1 : 1 (v/v) mixtures under an argon inert atmosphere and were treated with recurrent cycles of mechanical stirring and ultrasound treatments to yield a stable $[TaS_2]^{0.015-}$ 2DN sol. It is also important to underline how crucial it is to carry out the exfoliation process under inert conditions. The argon atmosphere not only favoured a clean delamination process but also prevented oxidation processes in the subsequent flocculation step.

The Fe^{2+} complex $[Fe(PyimH)_3](ClO_4)_2$ (**19**) was obtained as a burgundy crystalline powder in excellent yields and chemical composition was coherent with the proposed formula elemental, XRPD and FT-IR studies (see experimental

150 Sacconi, L. *Coord. Chem. Rev.* **1972,** *8,* 351.

151 a) Goodgame, D.; MacHado, A. *J. Chem. Soc. D, Chem. Commun.* **1969,** *23,* 1420–1421. (b) McGarvey, J. J.; Lawthers, I. *J. Chem. Soc., Chem. Commun.* **1982,** *16,* 906.

section). The synthetic procedure was optimised in collaboration with Monica Giménez-Marqués (ICMol, Valencia).

The flocculation of the $[Fe(PyimH)_3]$-TaS_2 hybrid **20** was performed under an argon inert atmosphere to prevent the oxidation of the redox-active counterparts involved in the reaction. In this way, solvents were thoroughly degassed and reaction vessels were conveniently flushed with Ar. The controlled addition of a solution of $[Fe(PyimH)_3](ClO_4)_2$ in NMF over a freshly prepared sol of $[TaS_2]^{0.015-}$ 2D sheets was carried out by cannula transfer procedures. This results in the immediate re-stacking assembly of a layered superstructure built up from the intercalation of Fe^{2+} cationic complexes in between the anionic layers of TaS_2. The flocculation of **20** always occurred under an excess of $[Fe(PyimH)_3]^{2+}$. It is important to realize that the process is driven by attractive electrostatic interactions between the oppositely charged species that coexist in solution until electroneutrality is achieved. Thus, the excess $[Fe(PyimH)_3]^{2+}$ remained soluble in the supernatant and needed to be discarded by decantation. The fine tuning of the cation's solution addition rate may conveniently enhance the crystallinity of the resulting material by helping to reduce the degree of disorder associated to the rapid intercalation of the clusters within the host's interlamellar space. As a result, the isolation of a pure crystalline phase of general formula $[Fe(PyimH)_3]_y[TaS_2]$ was achieved. The theoretical stoichiometry expected from electro-neutrality calculations suggests an approximate value of $y = 0.007$. Yet, the empirical formula estimated on the basis of SEM-EPMA metal analysis, reflected a larger proportion of Fe with respect to the proposed one. The chemical composition estimation by SEM-EPMA is shown in Table 6.1.

Thus, a value of $y = 0.10$ could be inferred from metallic ratio data extracted from SEM spectra. This metallic ratio was found to be constant despite the flocculated slurry being always thoroughly rinsed with fresh solvent in order to wash away remaining precursor co-precipitated impurities. In addition, no Na or

Na/Ta	Cl/Ta	Fe/Ta
0.00	0.00	0.10

Table 6.1 Chemical composition of hybrid polycrystalline sample **20** relative to the Ta content as extracted from SEM EPMA spectra.

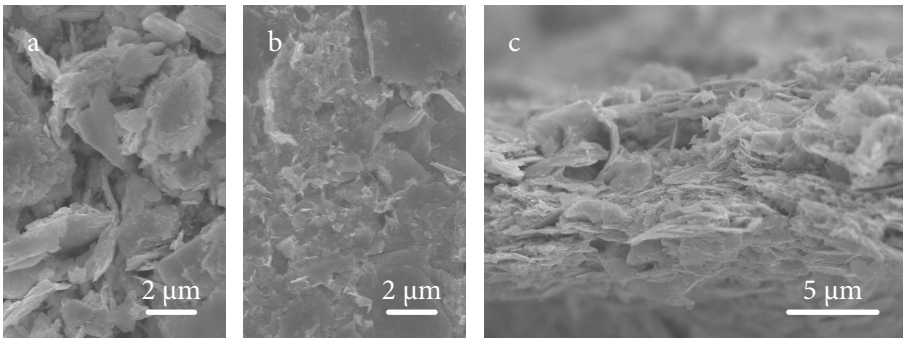

Figure 6.2 SEM images of hybrid sample $[Fe(PyimH)_3]_{0.1}TaS_2$ as polycrystalline powder (**20**, a) and free-standing highly oriented flakes (**21**, b: *top* view, c: side view).

Cl could be detected by EPMA, thus ruling out the presence of Na-intercalated **14** or perchlorate salt **19** precursor leftovers. The mismatch between the theoretical and the experimentally calculated metallic ratios may be explained by a redox process that involves the partial reduction of the $[TaS_2]^{0.015-}$ nano-flakes. As a result, the nano-layers acquire a higher charge, namely 0.2-, and require a larger number of countercations for electrostatically re-stacking. Due to the fact that the whole process was carried out under an inert atmosphere, it is proposed that the reducing agent came from the reaction medium itself. This hypothesis is consistent with Mössbauer and XPS studies,[152] which clearly revealed the presence of oxidized Fe^{III} species in the final hybrid (*vide infra*). This means that a certain proportion of these Fe species are trapped inside the layered structure of the final hybrid along with other pristine Fe^{II} complexes. The remaining excess Fe complex molecules are discarded in the supernatant solution.

As already described for the flocculation of the SMM-SC material (**17**), hybrid compound **20** could be isolated as a random-oriented polycrystalline sample by conventional filtration techniques. On the contrary, free-standing highly oriented macroscopic flakesc ould be obtained from the slow controlled sedimentation of the flocculated material followed by vacuum filtration on 0.2 µm pore size PTFE membranes. The thin scales yielded exhibited large surface areas (typically several $mm^2 \times 5$ µm thick) that could be easily removed from the filter surface. The closer examination by SEM (see Figure 6.2) revealed that the flocculated high

152 Notice that according to Mössbauer, the proportion of Fe^{3+}/Fe^{2+} is small (~ 0.2).

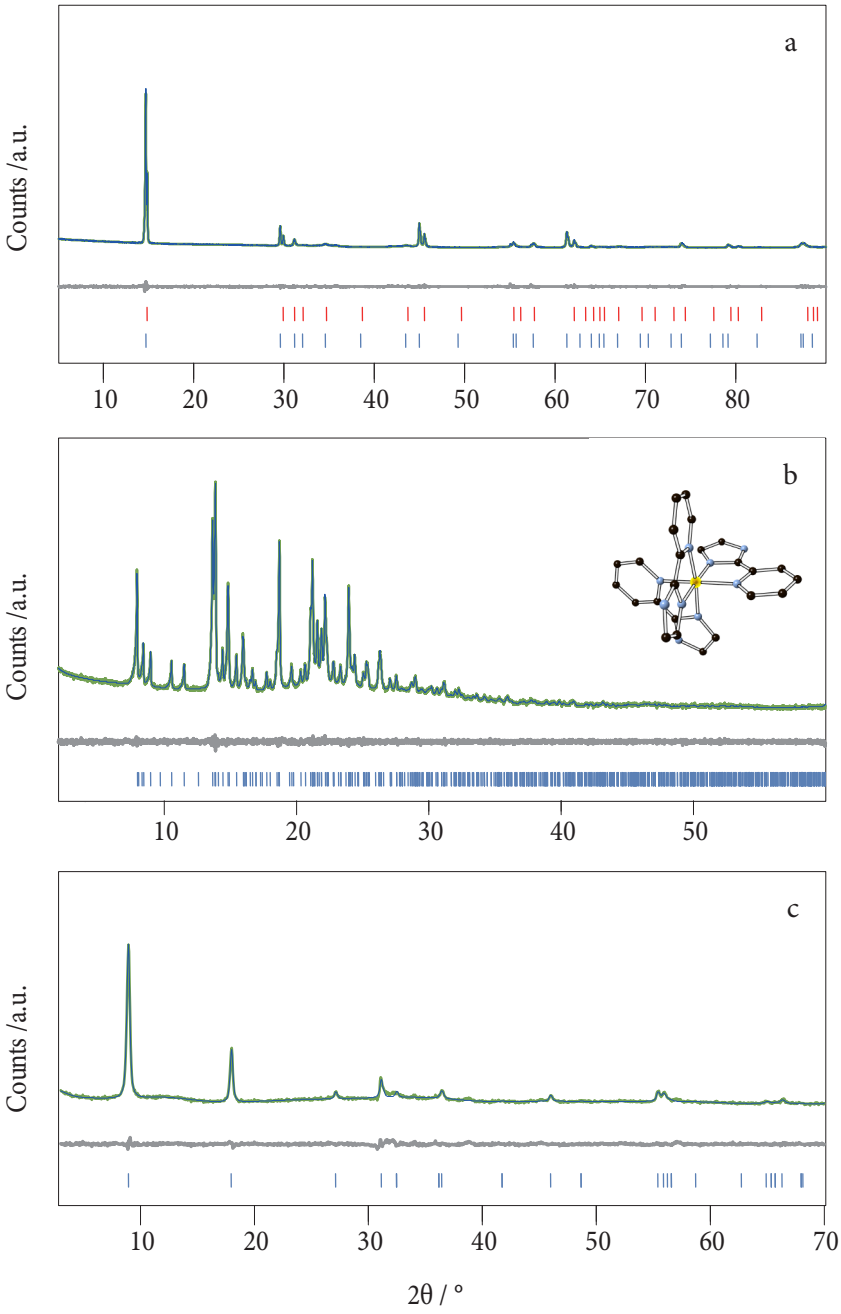

Figure 6.3 XRPD patterns and corresponding Pawley refinements of precursor compounds **14** (**a**) and **19** (**b**) and hybrid sample **20** (**c**).The inset at (**b**) shows the SCO molecular structure viewed along the *a*-axis of a single crystal of **19** (C: *black*, N: *blue*, Fe: *orange*)

aspect ratio layers appear to have the same orientation, with the crystallographic *c* axis normal to the flake plane as opposed to powder samples where crystallite orientation was random. These samples were most convenient for conducting transport measurements and prevented the preparation of pressed pellets that has been reported to destroy superconductivity in TMDCs.[114, 131b, 131c] They are also ideal candidates for the characterization of anisotropic physical properties such as two-dimensional superconductivity.

The evaluation of the XRPD profiles collected from powder samples of **20** together with those of the starting materials (**14** and **19**) confirms that the diffraction pattern observed for the hybrid material is not just an additive superposition of the precursors. This agrees with the creation of a different and pure layered crystalline phase from the combination of the ionic 2DNs and the Fe^{2+} complexes in solution (see Figure 6.3). Furthermore the Pawley refinement of the X-Ray diffraction data indicates that there is a unique layered-dichalcogenide-type crystalline phase present in **20** in contrast to starting material **14** where two different phases are found in the Pawley refinement (see Table 6.2).

Sample	*a*, *b* / Å	*c* / Å	α, β / º	γ / º	BS / Å
$\mathbf{14}_A$	3.31708(14)	12.08980(19)	90	120	6.04
$\mathbf{14}_B$	3.313(2)	11.9497(2)	90	120	5.97
2H-TaS_2 [96]	3.315	12.10	90	120	6.50
19	12.8058(11)	63.702(7)	90	120	-
$[Fe(PyimH)_3](ClO_4)_2 \cdot H_2O$ [153]	12.7633(5)	63.459(5)	90	120	-
20	3.3150(6)	9.863(19)	90	120	9.86

Table 6.2 Unit cell parameters exctracted from the Pawley refinements of compounds **14**, **19** and **20** and those of analogous compounds extracted from single crystal diffraction data.

This reinforces the idea of quantitative exfoliation of the phase mixture into individual $[TaS_2]^{0.015-}$ and successful restacking to produce a totally different layered material. As observed for previously described flocculated materials, **14** presents a bigger number of stacking defects and overall disorder than the starting components. This is suggested by the weaker intensity and broader full

153 Coronado, E.; Giménez-Marqués, M.; Mínguez Espallargas, G. *(unpublished work).*

widths at half maximum (FWHM) of its diffraction peaks in comparison to the precursor materials'. It has already been mentioned that these complications have impeded in the past the postulation of consistent structural models for the intercalation compounds of layered dichalcogenides.[105] However, in our case the Pawley refinement of the diffractogram of **20** permitted estimating the following hexagonal (α = 90º, β = 120º) unit cell: a = 3.3150(6) Å, c = 9.863(19) Å. It is presumed that the 2H stacking conformation of the layers with an alternating packing of two crystallographically distinct TaS_2 slabs turns into a phase with a single TaS_2 layer in the unit cell as has already been discussed for the SMM-SC hybrid **17** (review recall section 4.2, Chapter 5, page 161). Such a single-layer stacking periodicity provides a BS = c of *ca.* 9.86 Å for **20**. This is in good accordance with the addition of the thicknesses of one layer of TaS_2 (3.1 Å)[128] and the size of the Fe^{2+} complex inserted with its C_3 axis perpendicular to the TaS_2 planes, as estimated from X-ray single crystal diffraction experiments. In addition, the hexagonal a axis of 3.3150(6) Å supports that the hybrid layered structure is sustained by unaltered TaS_2 individual planes.[96] Unfortunately, the structural data does not permit giving any further information regarding the distribution of the SCO cations within the bi-dimensional space afforded by the TaS_2 planes. Nevertheless, in view of the stoichiometry of the hybrid material together with the surface charge density of the $[TaS_2]^{0.2-}$ planes, it is evident that Fe^{2+} centres are further apart from each other than in the precursor perchlorate salt (see Figure 6.4). Simple surface charge calculations, taking into account the 2H-TaS_2 in-plane structure, permit establishing that each SCO molecule bearing two positive charges occupies an average area of 200 $Å^2$ within the inter-layer gallery. This suggests an efficient segregation of the Fe^{2+} complexes, which should have a direct effect over the co-operativity of the SCO phenomenon.

3 Mösbauer spectrocopy experiments

Mössbauer spectroscopy was carried out by Prof. João C. Waerenborg from the Chemistry Department at IST/ITN, Instituto Superior Técnico (Universidade Técnica de Lisboa, Portugal).The Mössbauer experiments were carried out for 100% ^{57}Fe enriched samples of **19** and **20** in order to study the SCO transitions (see Figure 6.5). The 295 K spectrum of **19** consist of three absorption peaks which may be fitted with two quadrupole doublets while at 4 K only one doublet is observed.

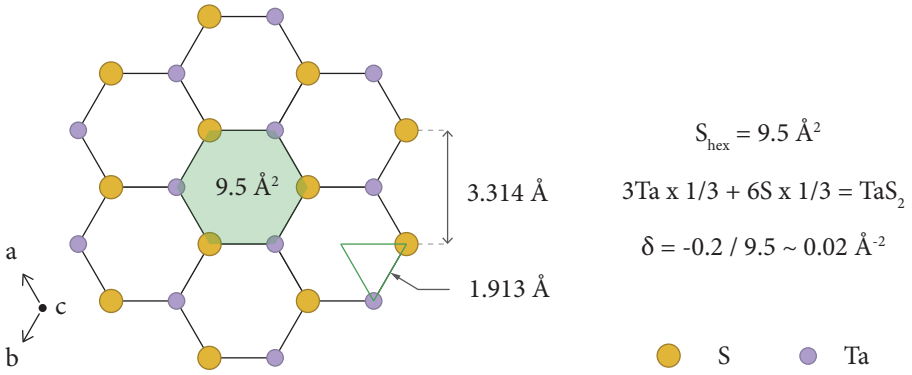

Figure 6.4 $[TaS_2]^{0.2-}$ surface density charge (δ) calculations based on the 2H in-plane crystal structure extracted from XRPD data (Table 6.2).

The estimated isomer shifts (IS) relative to α-Fe at 295 K and quadrupole splittings (QS) are shown in Table 6.3. The doublet with lower IS and QS, corresponds to LS Fe^{II} (S = 0), and the doublet with higher IS and QS detected at 295 K, to HS Fe^{II} (S = 2) in agreement with reported results for similar Fe^{II} SCO complexes such as the $[Fe(bpp)_2]^+$ species: $[Fe(bpp)_2](BF_4)$,[154] $[Fe(bpp)_2](CF_3SO_3)_2{\cdot}H_2O$,[155] $[Fe(bpp)_2][MnCr(ox)_3]_2$.[156] The spectra of **19** evidences a spin crossover transition showing that all the Fe^{II} is LS at 4 K and only approximately 15% is HS at 295 K. As reported by Vijayalakshimi *et al.*, this compound was also found to mainly exhibit LS state at room temperature.[157] Since our sample was 100% enriched in ^{57}Fe, a spectrum with better statistics could be obtained, which allowed the detection of the HS state at 295 K.

The 4 K spectrum of **20** reveals, in addition to both doublets assigned to LS and HS Fe^{II}, the presence of a sextet with broad peaks. This sextet becomes more evident at 2 K. The IS (~ 0.48 mm/s) and magnetic hyperfine field B_{hf} (50.1 - 51.6 T) estimated for this sextet (Table 6.3) are typical of HS Fe^{III}. Mössbauer

154 Buchen, Th.; Gütlich, P.; Goodwin, H. A. *Inorg. Chem.* **1994,** *33,* 4573-4576.

155 Buchen, Th.; Gütlich, P.; Sugiyarto, K. H.; Goodwin, H. A. *Chem. Eur. J.* **1996,** *2,* 1134

156 Coronado, E.; Galán-Mascarós, J.R.; Giménez-López, M.C.; Almeida, M.; Waerenborgh, J. C. *Polyhedron* **2007,** *26,* 1838-1844.

157 Vijayalakshmi, R.; Yusuf, S.M.; Kulshreshtha, S.K. *J. Phys. Chem. Sol.* **2004,** *65,* 975–979.

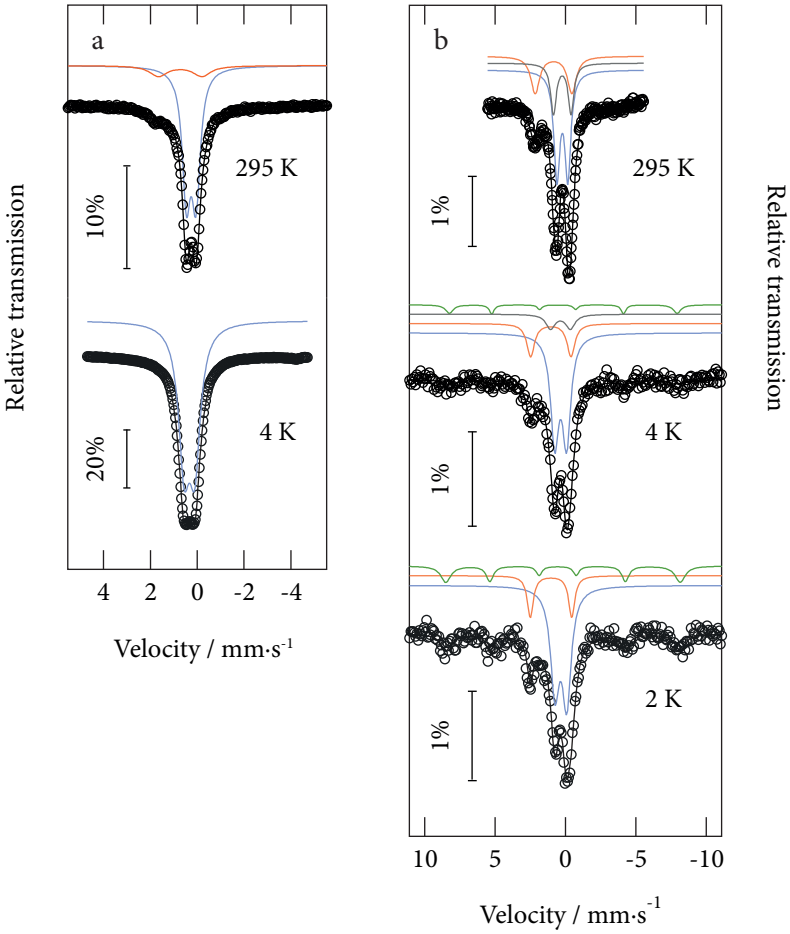

Figure 6.5 Mössbauer spectra of **19** (**a**) and **20** (**b**) recorded at different temperatures.

spectra therefore confirm that Fe^{2+} is partially oxidized even when the synthesis was performed under an inert atmosphere. This further supports the hypothesis of an internal redox event between the host layers and the guest Fe complexes. The fact that the broad peaks of this sextet are only observed at 4 K and below suggest that the sextet results from a slowing down of the relaxation frequency of the Fe^{III} magnetic moments directions below the Larmor precession frequency ($f_L \sim 4\times10^7$ Hz) of the ^{57}Fe nuclei.[158] At temperatures higher than 4 K the relaxation

158 Gütlich, P.; Link, R.; Trautwein, A., *Inorganic Chemistry Concepts 3: Mossbauer Spectroscopy and Transition Metal Chemistry*, Springer-Verlag Berlin, Heidelberg, New York, **1978**.

is faster than f_L and a doublet is observed instead. This slow relaxation is not caused by magnetic ordering but results from a slow spin-spin relaxation of the HS Fe^{III} cations caused by the large Fe^{III} - Fe^{III} distances in **20**. The absence of a magnetic moment for LS Fe^{II} and the spin-lattice relaxation mechanism available to HS Fe^{II} due to spin-orbit coupling, may explain why no slow relaxation is observed for Fe^{II}.[158]

	T / K	IS / mm·s^{-1}	QS / mm·s^{-1}	B_{hf} / T	Γ / mm·s^{-1}	I %	Fe state
19	295	0.37	0.41	-	0.41	85	Fe^{II} LS
		0.87	1.87	-	0.91	15	Fe^{II} HS
	4	0.46	0.45	-	0.58	100	Fe^{II} LS
20	295	0.35	0.78	-	0.51	49	Fe^{II} LS
		0.97	2.60	-	0.75	25	Fe^{II} HS
		0.35	1.25	-	0.48	26	Fe^{III}
	4	0.46	0.84	-	0.70	63	Fe^{II} LS
		1.16	2.86	-	0.66	17	Fe^{II} HS
		0.48	1.40	-	0.78	11	Fe^{III}
		0.48	-0.40	50.1	0.38	9	Fe^{III}
	2	0.45	0.83	-	0.75	62	Fe^{II} LS
		1.15	2.94	-	0.51	17	Fe^{II} HS
		0.49	-0.38	51.6	0.50	21	Fe^{III}

Table 6.3 Estimated Mössbauer parameters of **19** and **20** extracted from spectra taken at different temperatures shown in Figure 6.5. IS: isomer shift relative to metallic α-Fe at 295 K. QS: quadrupole splitting. B_{hf} magnetic hyperfine field. Γ: width. I: relative areas. Estimated errors are ≤ 0.02 mm/s for IS, QS, Γ; ≤ 0.5 T for B_{hf}; and ≤ 2% for I.

The Fe^{III} doublet that is expected at room temperature is not resolved from the LS Fe^{II} doublet due to similar IS and QS values. In order to estimate the fractions of Fe^{II} HS and LS at 295 K the data analysis was performed assuming the presence of three doublets at this temperature. Such a fitting leads to parameters consistent with those observed at 2 K. The IS for each Fe species are lower according to the second order Doppler shift. The relative area of the Fe^{III} doublet is slightly higher

than the relative area of the Fe^{III} sextet at 4 K, which may be explained by a higher recoil-free fraction of Fe^{III} relative to Fe^{II}.

The lower area of the Fe^{III} sextet at 4K when compared to 2 K suggests that at 4 K a fraction of the Fe^{III} still has a relaxation faster than f_L and is giving rise to a doublet. The analysis of the spectra indicates that this fraction corresponds to approximately half of the Fe^{III} (Table 6.3). The estimated fraction of Fe^{II} in LS state is approximately 22 - 23% at 4 and 2 K and approximately 34 % at room temperature evidencing SCO in the 4 - 295 K temperature range.

Mössbauer spectra show that the IS value of LS Fe^{II} in the $[Fe^{II}(PyimH)_3]^{2+}$ complex does not change within experimental error when this complex is inserted between TaS_2 layers. IS of HS Fe^{II} however increases. Such increase normally indicates an increase in the ionic character of the chemical bond (decrease in the 4s electron density of the formal Fe^{2+} or alternatively increase in 3d electron density that results in a higher shielding of the s electrons relative to the Fe nuclei). Furthermore the QS of both LS and HS Fe^{II} are higher in compound **20** than in 2 which means that insertion of the $[Fe^{II}(PyimH)_3]^{2+}$ complex between the TaS_2 layers increase the distortion of the charge distribution around the Fe^{II}. This may explain the different SCO behaviour of $[Fe^{II}(PyimH)_3]^{2+}$ in **20** and in **19** particularly the fact that HS Fe^{II} is still observed at 2 K in **20** while in **19** all the Fe^{II} is LS. It is suggested that this observation may be a direct consequence of the confinement of the metal complexes within the TaS_2 layered architecture.

4 Magnetic properties

The thermal variation of AC susceptibility of hybrid material **20** was recorded in the 2 - 300 K temperature range (Figure 6.6a). The AC behaviour is characterised by a drop of the in-phase AC susceptibility and a maximum in the out-of-phase component, both being long-range frequency independent features. In this case, the sharp fall of the AC susceptibility at T_{SC} is representative of unaltered nano-layers that persist in the re-stacked material. This is demonstrative of how the superconducting properties have been successfully brought into the final material. However, although the in-phase and out-of-phase curves of precursor compound **14** (see AC plot on page 143) and hybrid compound **20** are comparable, they are not identical. Indeed, **20** presents a Meissner superconducting response below 4.5

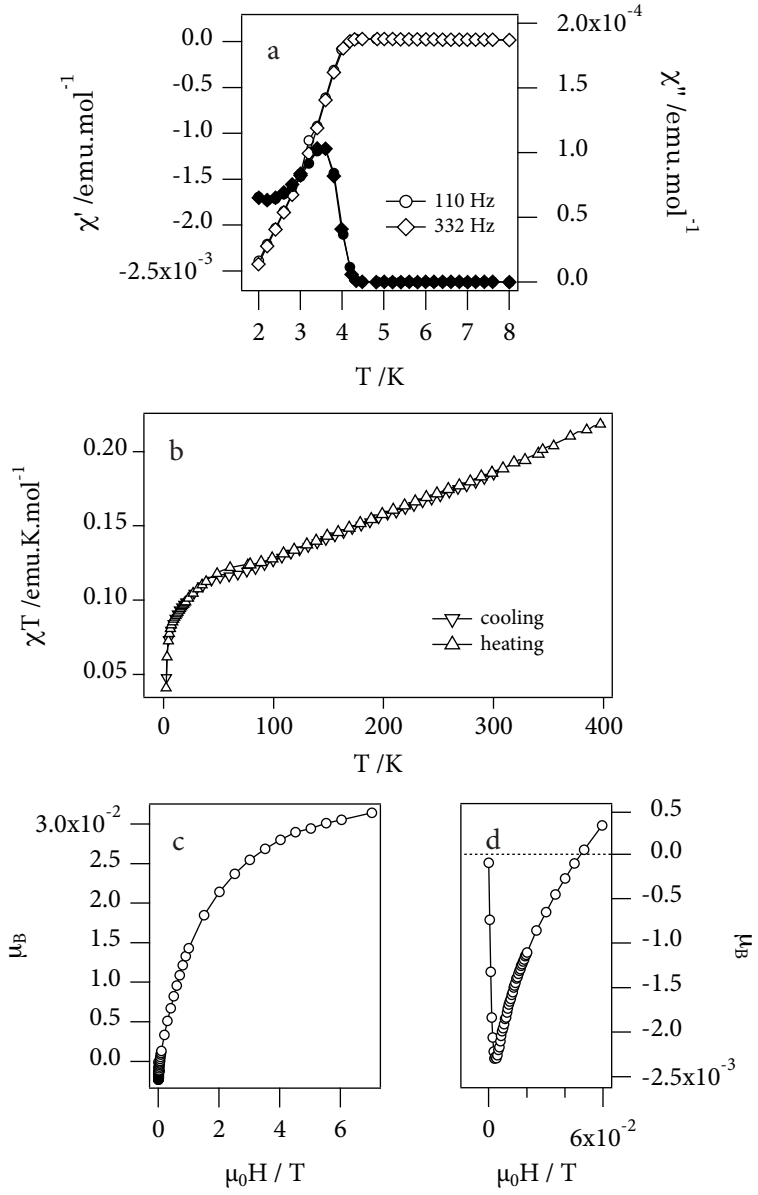

Figure 6.6 a. AC magnetic susceptibility thermal variation of 20 measured from 8 K to 2 K measured at two different frequencies (110 Hz and 332 Hz; in-phase: hollow markers, out-of-phase: solid) at zero external applied field. **b**. χT product versus T heating/cooling cycles of 20 measured under 1000 G of external applied field in the 300 – 2 K temperature range. **c**. Magnetization curve of 20 measured at 2 K (d: low-field region showing the typical features of a type II superconductor).

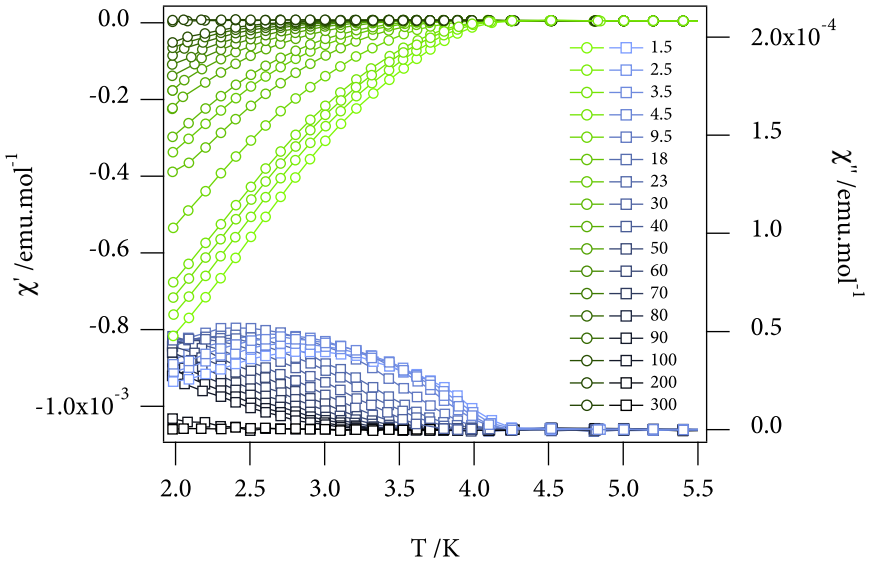

Figure 6.7 AC susceptibility (in-phase: *circles*, out-of-phase: *squares*) thermal variation measured in the 5.5 - 2 K range, recorded under increasing external applied fields in the range of 1.5 mT – 300 mT (specific values listed in graph legend).

K, which defines an increase in the critical temperature of ΔT_{SC} = 1.3 K with respect to the Na-intercalated precursor **14**. The explanation to this increase in the critical temperature may be found in the mentioned partial reduction of the $[TaS_2]^{0.015-}$ to a higher charged state x = 0.2-. This is once again consistent with both a partial oxidation of the Fe^{2+} centres illustrated by Mössbauer spectroscopy and with the non-ideal stoichiometry found in the chemical analysis and XPS results. It is also in perfect agreement with the superconducting critical temperature expected for $[TaS_2]^{0.2-}$ (T_{SC} = 4.3 K) reported in the literature.[107] Field expulsion experiments were conducted in the presence of increasing DC external applied fields in the 2 - 6 K range (see Figure 6.7). In this way, AC susceptibility thermal variations were collected under the effect of varying DC external applied fields. In-phase profiles show how the Meissner effect is gradually annihilated as the external applied field approaches the critical field H_{c2}. At the same time, the peak exhibited by the out-of-phase component at zero applied field is gradually smeared out upon increasing the external DC value. The results also allowed for the estimation of the critical field inherent to the superconducting component of the hybrid material.

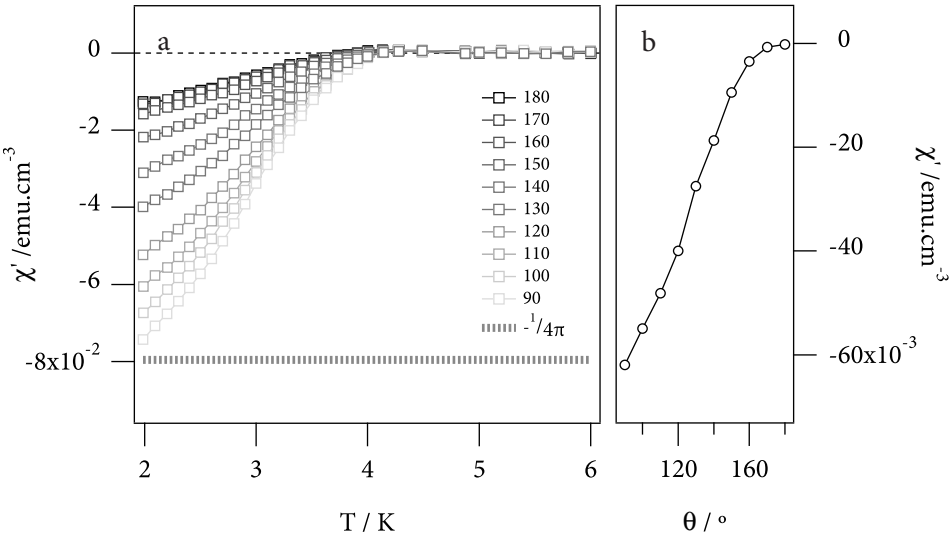

Figure 6.8 In-phase AC response as a function of the relative orientation of a highly oriented flake of sample **21** with respect to the external applied field (**a**). The evolution of the in-phase AC susceptibility value at 2 K is shown in **b**. The sample density was obtained indirectly from the approximate crystal structure (4248.28 $kg \cdot m^{-3}$).

Conventionally, this can be extracted from magnetization studies. However, in our hybrid, the paramagnetic component coming from the paramagnetic Fe centres handicapped such determination. In this case, it is interesting to note how upper critical fields for hybrid sample **20** are subtly higher than for precursor material **14**. Indeed applied fields of around 0.3 T are needed to eliminate the out-of-phase component of the AC susceptibility. Therefore, H_{c2} lies between 2 kOe and 3 kOe. This is consistent with the increase in T_{SC} suggested by the premature onset of the AC response in zero applied field in comparison to the precursor material. Furthermore, the isolation of highly oriented flakes of material **20** allowed for the angle-dependent probing of the material AC response of the material. Figure 6.8 shows a set of AC thermal variations recorded as a function of the angle between the flake normal and the external uniaxial field. It is easy to observe that the strong bi-dimensional anisotropy of the starting material is preserved in the hybrid structure. As a single flat flake of compound **20** was rotated within the DC field, AC response was maximum upon reaching an orthogonal orientation (90º) of the

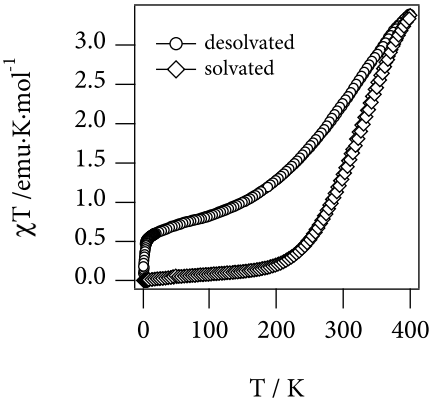

Figure 6.9 χT versus T heating/cooling cycles for precursor salt $[Fe(PyimH)_3](ClO_4)_2 \cdot H_2O$ 20 (*solvated*) and the desolvated complex $[Fe(PyimH)_3](ClO_4)_2$.

crystallographic *c*-axis with respect to the external field axis. At this orientation, the low-temperature susceptibility is close to the limit (-¼π emu·cm^{-3}) expected for perfect diamagnetism. These results neatly show that the superconductivity observed in this material is a bulk effect, which involves nearly 100% of the sample.

Following, the SCO transition was addressed by recording the χT product thermal variation of sample **20** under 1000 G of applied external field (see Figure 6.6b). The evolution of the χT product with temperature resembles to that of precursor material **19** once the solvent molecules have been removed *in vacuo* (Figure 6.9). Indeed, this is a strong evidence of the presence of isolated non-solvated SCO species within TaS_2 planes. A more detailed analysis of the DC profile of hybrid material **20** permits identifying two distinct temperature sections that must be discussed separately: the 4.5 - 400 K region and the 2 - 4.5 K one. On the one hand, the higher temperature range (4.5 - 400 K) shows a gradual decrease of the χT product as the temperature falls. The χT value at 400 K of approximately 0.23 emu·K·mol^{-1} suggests that a complete spin transition to high-spin state has not yet been achieved at that temperature. Taking the 295 K Mössbauer spectra (Fe^{II} HS mol/Fe^{III} mol = 0.96) and the relative spin-only values for Fe^{II} (S = 2) and Fe^{III} (S = ⅝) into account, a ratio of $\chi T[Fe^{II}\ HS]_{295\ K}$ /$\chi T[Fe^{III}]_{295\ K}$ = 0.66 may be deduced. The 295 K χT value of 0.20 emu·K·mol^{-1} may therefore be split into the paramagnetic components coming from the HS Fe^{II} (0.08 emu·K·mol^{-1}) and Fe^{III}

(0.12 emu·K·mol^{-1}) species present in the hybrid material. As a matter of fact, this reveals that at 295 K, around 20% of the Fe^{2+} centres are in their high-spin state according to the spin-only calculation for 0.1 mol Fe per compound formula. This is consistent with Mössbauer data within experimental error. Upon decreasing the temperature, a quasi-linear χT decrease follows. This progressive drop may be attributed to a gradual SCO transition down to 4.5 K. At this point, a χT value of 0.12 emu·K·mol^{-1} is reached. Down the lower temperature range (2 - 5 K), the Meissner effect starts to operate and dominate that part of the profile. The sample diamagnetism starts to build up and describes an abrupt drop of the χT product. Finally, two cooling-heating DC susceptibility cycles were performed and the corresponding susceptibility thermal variations recorded in order to explore potential spin bi-stability regions. The results showed no significant hysteresis in the whole temperature range which indicate the lack of cooperative effects. This is consistent with the structural model proposed of a loose-packed organization of isolated SCO complexes within the bi-dimensional galleries provided by the layered host. Lastly, it is important to mention that the effect that the host Meissner state may exert over the SCO centres is difficult to evaluate via magnetic characterization given the small temperature range in which the superconductivity operates together with the SCO transition and also due to the strong diamagnetic fall at low temperatures.

The magnetization curve of sample **20** was measured at 2 K (see Figure 6.6c and d). It shows a low-field minimum that originates from the diamagnetism coming from the superconducting TaS_2 layers. Upper and lower critical fields characteristic of type II superconductivity could be estimated from such feature and depicted only a subtle variation with respect to the precursor sample **14** (see AC susceptibility plot on page 143). As the applied field is increased above 5 mT, superconductivity is gradually annihilated and finally completely suppressed at H_{c2} ~ 220 Oe. Superconductivity suppression gives way to the observation of a paramagnetic component, which defines a typical Brillouin function attributed to the Fe^{2+} and the Fe^{3+} centres that still remain in their high-spin configuration at 2 K. However, the saturation of the magnetic moment is not achieved even at 5 T so no clear conclusions regarding the remnant HS fraction of the Fe^{II} species could be drawn from these data.

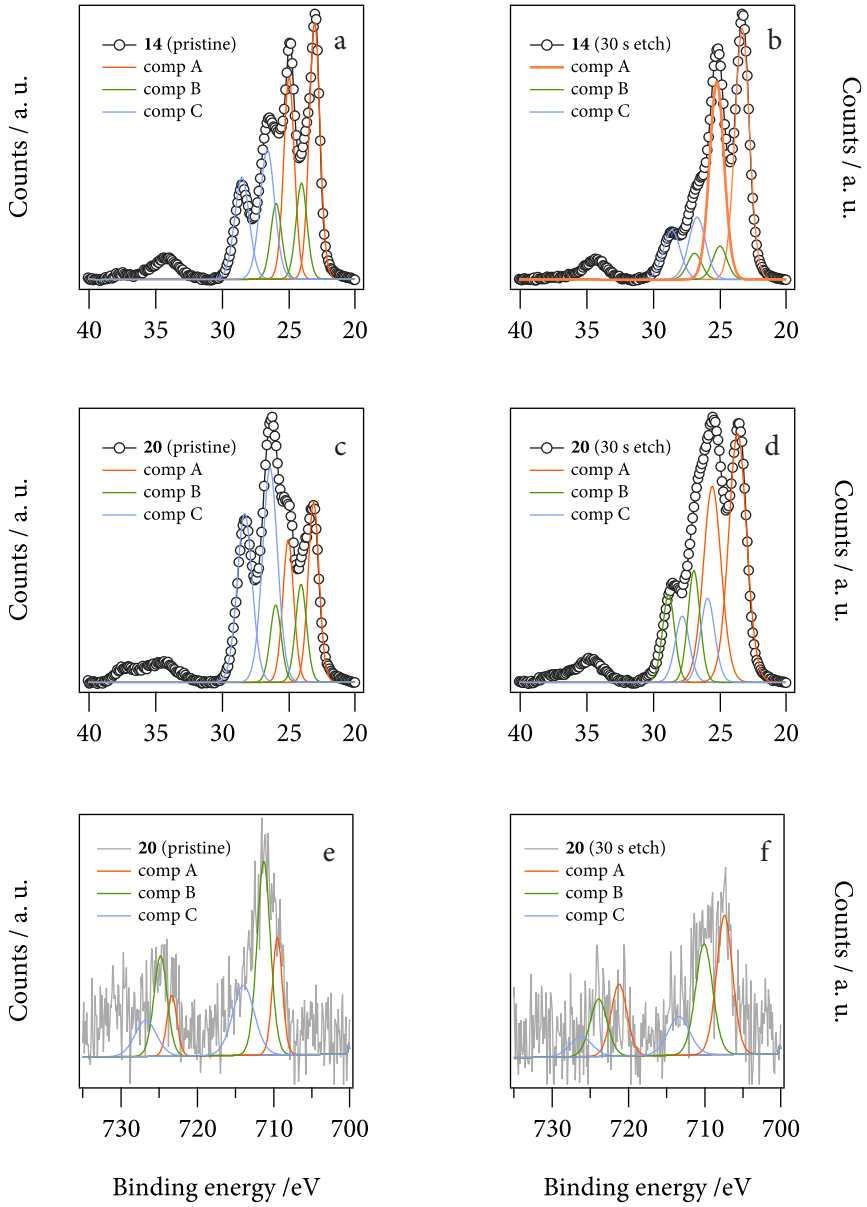

Figure 6.10 XPS spectra and oxidation state analysis of precursor **14** (**a**: as-synthesized, **b**: 30 s etch) and hybrid **20**. (**c, e**: as-synthesized, **d, f**: 30 s etch). The Ta binding energy region is presented in plots **a** - **d** and the Fe region in plots **e** and **f**. The surface etching was performed by a 30 s long Ar^+ ion bombarding.

5 XPS experiments

XPS surface measurements performed on single crystallites of sample **14** and on hybrid **20** in the form of free-standing scales permitted analysing the chemical states of the metallic components of the hybrid (see Figure 6.10). The survey of the Ta binding energy region allowed for the observation of three 4f⁷⁄₂-4f⁵⁄₂ doublets that could be assigned to an equal number of chemical states. Both compounds **14** and **20** exhibit an intense doublet with the 4f⁷⁄₂ peak centred at around 23 eV and anther less intense one positioned at approximately 24 eV. Whilst the latter doublet exactly matches that expected for Ta^{4+} in neutral TaS_2 (23.9 eV), the former is shifted towards lower binding energies, indicating Ta^{3+}. This reflects the n-doped state of the dichalcogenide layers with a Ta^{4+}/Ta^{3+} mixed valence situation.[159] Still, no further distinctions with respect to the different degree of doping between compounds **14** and **20** could be established. On the other hand, a very intense doublet at around 26 eV depicted the presence of a much more oxidized Ta species. According to that reported in the databases, a binding energy of 26 eV coming from the 4f⁷⁄₂ transition may be assigned to tantalum pentoxide (Ta^{5+}).[160] This clearly demonstrates the ready superficial oxidation of the TaS_2 host that may be observed even in freshly prepared samples. In order to discard bulk oxidation of the samples, high aspect ratio samples of **14** (crystals) and **20** (oriented flakes) were etched by Ar^+ bombarding. Indeed, spectra collected after the ion etching exhibited a much weaker Ta^{5+} signal and a dominating 23 eV 4f⁷⁄₂ peak.

The Fe XPS footprint of **20** was also addressed. Despite the 2p signal being weak, the experimental profile allowed for its deconvolution in three different components. Two lower binding energy 2p½-2p³⁄₂ doublets appeared to be especially intense. These could be ascribed to the HS (2p³⁄₂ = 711 eV; 2p½ = 725 eV) and LS (2p³⁄₂ = 709 eV; 2p½ = 723 eV) components of the Fe^{2+} species present in the sample. A particularly high separation between both components (ca. 2 eV) is evidenced in accordance to previous studies on spin crossover Fe^{2+}

159 a) Tison, Y.; Martinez, H.; Baraille, I.; Loudet, M.; Gonbeau, D. *Surf. Sci.* **2004,** *563,* 83–98. (b) Peters, E. S.; Carmalt, C. J.; Parkin, I. P.; Tocher, D. A. *Eur. J. Inorg. Chem.* **2005,** *4179–4185.*

160 *NIST Chemistry WebBook*, NIST Standard Reference Database Number 69, Eds.: Linstrom, P. J.; Mallard, W. G.

compounds.[161] The third component is clearly higher in binding energy ($2p_{3/2}$ = 711 eV) and could therefore be attributed to the Fe^{3+} identified by Mössbauer spectroscopy. Moreover, etching studies confirmed the constant intensity of the Fe^{3+} signal, discarding its presence being due to surface oxidation. On the other hand, the high random variability of the LS/HS ratios on different scans hindered an accurate estimation of spin-state proportions via XPS.

6 Conclusions

In this chapter, the delamination/flocculation of a layered material in presence of a molecular Fe^{2+} complex has been employed for the synthesis of a hybrid multifunctional material that combines superconductivity and a SCO transition. Such functionalities had never before been successfully combined together. Magnetic together with Mössbauer characterisation demonstrate how type II superconductivity and SCO behaviour coexist in this chemically engineered hybrid material. Though superconductivity and SCO occur at complementary temperature regimes, the material is also a good electrical conductor at higher temperatures, namely, above T_{SC}. This means that the material here introduced is a new example of the very few SCO conductors reported.[148, 149] In fact, preliminary results of conductivity measurements show an electrical conductivity as high as 0.93 $S \cdot cm^{-1}$, measured at room temperature on a free-standing highly oriented flake.

The organisation of the SCO complexes in between TaS_2 and the ratio in which they are mixed are always restrained by the electro neutrality of the final structure. As a consequence, the Fe^{2+} centres are diluted within the TaS_2 layered lattice leading to a non-cooperative gradual SCO transition that has been observed by a manifold of techniques in the 2 - 400 K temperature range.

The synthesis of this new material continues to extend the hybrid strategy that arises from the combination of molecule-based components with solid-state inorganic structures described in Chapter 2 and Chapter 5). Moreover, it also revisits the strategy of using TMDCs as a route for the combination of superconductivity with other interesting properties. Indeed, TaS_2 layers have been

161 Mazalov, L. N.; Asanov, I. P.; Varnek, V. A. *Journal of Electron Spectroscopy and Related Phenomena* **1998,** *209–214.*

previously combined with both magnetic LDH layers and single-molecule magnets affording hybrid magnetic superconductors with coexistence of superconductivity and ferromagnetism or single-molecule magnetism (see reference 114 and Chapter 5). The present material constitutes the third example of this class of hybrid superconductors in this case incorporating SCO magnetism.

Finally it is also suggested that the compound here introduced is potentially responsive to external stimuli such as an external applied magnetic field or light. In this line, subsequent investigation will be devoted to the study of the LIESST effect on this hybrid material as an approach to verify whether there is a synergy between superconductivity and SCO in the low temperature region. On the other hand, alternative studies will be devoted to the investigation of the prospective interaction between conductivity and SCO at the higher end of the temperature scale through the study of its magnetoresistive behaviour.

7 Experimental recipes and procedures

XPS experiment

X-ray photoelectron spectroscopy (XPS, K-ALPHA, Thermo Scientific) was used to analyze the filter surface. All spectra were collected using Al-K_α radiation (1486.6 eV), monochromatizedby a twin crystal monochromator, yielding a focused X-ray spot with a diameter of 400 μm, at 3 mA × 12 kV. The alpha hemispherical analyser was operated in the constant energy mode with survey scan pass energies of 200 eV to measure the whole energy band and 50 eV in a narrow scan to selectively measure the particular elements. Charge compensation was achieved with the system flood gun that provides low energy electrons and low energy argon ions from a single source. XPS depth profiles were obtained by sputtering the specimen with a 3 keV Ar^+ ion beam during periods of 30 s. The analysis spot was elliptical in shape with a major axis length of 400 μm. XPS data was analysed with Avantage software; a Shirley background function was used to approximate the experimental backgrounds and surface elemental compositions were calculated from background-subtracted peak areas.

Mösbauer experiments

Mössbauer experiments were carried out in the laboratory of Prof. João C. Waerenborg at IST/ITN, Instituto Superior Técnico in Lisbon (Universidade Técnica de Lisboa, Portugal)

Mössbauer spectra were collected in transmission mode using a conventional constant-acceleration spectrometer and a 25 mCi ^{57}Co source in a Rh matrix. The velocity scale was calibrated using α-Fe foil. The absorbers were obtained by packing the powdered samples into perspex holders. Isomer shifts are given relative to metallic α-Fe at room temperature. The spectra at 4 and 2 K were collected using a bath cryostat with the sample immersed in liquid He. The spectra were fitted to Lorentzian lines using a non-linear least-squares method.

Preliminary transport measurements

The electrical conductivity (σ) measurement of oriented flakes have been measured using a standard four-probe method with Pt wire in a physical properties measurement system (PPMS-9) by Quantum Design. Electrical contacts were made with highly conducting silver and on sample sizes of approximately of $1 \cdot 10^{-2}$ cm^2.

Syntheses

Synthesis of 2-(1H-Imidazol-2-yl)pyridine: the compound was prepared by the Radziszewskias method described in detail by Chiswell, Lions and Morris.[162, 163] Special care needed to be taken as perchlorate salts are potentially explosive.

Synthesis of $[Fe(PyimH)_3](ClO_4)_2 \cdot H_2O$ (PyimH = 2-(1H-Imidazol-2-yl) pyridine; $C_8H_7N_3$) [19]: bulk $[Fe(PyimH)_3](ClO_4)_2 \cdot H_2O$ complex was prepared according to a procedure reported in the literature with some modifications.19 Solutions of PyimH (2.2 g) in previously degassed hot ethanol (20 mL) and $Fe(ClO_4)_2 \cdot 6H_2O$ (1.8 g) in deionized water (10 mL) were mixed and stirred at room temperature for 3 hours under Ar atmosphere. The dark red solution was concentrated to half-volume on heating in an open atmosphere while bubbling Ar. After cooling down to room temperature, the complex was isolated as a polycrystalline powder induced by scratching of the inner surface of the glass. Recrystallization from a 1 : 1 (v/v) mixture of hot ethanol and water afforded dark red crystals.

IR (KBr pellet) ν/cm^{-1}: 3415.4 (br, m), 3056.7 (br, s), 2919.7 (s), 2757.8 (m), 2701.8 (m), 2013.4 (br, w), 1716.7 (m), 1614.2 (s), 1565.9 (m), 1496.5 (m), 1469.5 (s), 1450.2 (m), 1423.2 (w), 1365.4 (w), 1322.9 (w), 1294.0 (w), 1224.6 (w), 1145.5 (s), 1110.8 (s), 1087.7 (s), 1012.5 (m), 966.8 (m), 929.5 (m), 788.8 (s), 752.1 (s), 703.9 (s), 636.45 (s), 626.8 (s), 532.3 (w).

Elemental analysis % (calculated for $C_{24}H_{23}N_9O_9Cl_2Fe_1$): C = 40.3 (40.7); H = 3.3 (4.2); N = 17.8 (17.8)

162 Radziszewski, B. *Ber.* **1882,** *15,* 2706.

163 Chiswell, B.; Lions, F.; Morris, B. *Inorg. Chem.* **1964,** *1,* 110.

Empirical formula: $[Fe(C_8H_7N_3)_3](ClO_4)_2 \cdot H_2O$; FW = 708.25

Synthesis of polycrystalline $[Fe(PyimH)_3]_{0.1}TaS_2$ [20]: The superconducting-SCO hybrid was prepared by exfoliation-flocculation taking care of performing all manipulations under an inert atmosphere. Typically, 100 mg of **14** (0.4 mmol) were suspended in 70 mL of a 1:1 (v/v) mixture of ultrapure Milli-Q water and N-methylformamide (NMF). At this stage, sedimentation of the solid material occurred at once, was the suspension left to stand. The $Na_{0.015}TaS_2$ delamination process was then carried out in three sequential steps: 1) 3 minutes of mechanical stirring; 2) 60 minutes of ultrasonic bath treatment; 3) 5 minutes of mechanical stirring. The suspension was left to stand for 20 minutes to discard the larger particles that settled at the bottom of the flask. Upon completion of the exfoliation procedure, the stable sol exhibited a remarkable 'pearl effect' if stirred. The final flocculation step involved drop-wise addition of 2 mL of a 75 mM **19** solution (0.15 mmol) in NMF, over the delaminated **14** stable suspension under gentle stirring. The addition rate was controlled via Ar pressure and the use of cannula transferring material. Allowing the slurry to stir for 20 minutes, the resulting suspension had lost stability and settled readily at the bottom of the flask once left to stand. The yellowish supernatant was decanted off. At this point the flask was opened to the air. The recovered black solid was then washed thrice by re-suspension-decantation with 20 mL fresh ethanol and immediately dried *in vacuo*. The material was recovered in approximately quantitative yields as glittery light grey thin scales and was best preserved under Ar atmosphere.

Elemental ratio estimated by EPMA (calculated for $C_{2.4}H_{2.1}N_{0.9}Fe_{0.1}TaS_2$): Na/Ta = 0.00 (0.00), Cl/Ta = 0.00 (0.00), Fe/Ta = 0.10 (0.10), Ta/S = 0.78 (0.5).

% H_2O weight (TG loss for T < 200 °C) = *negligible*

Empirical formula: $[Fe(C_8H_7N_3)_3]_{0.1}TaS_2$; FW = 294.2

Synthesis of oriented flakes of $[Fe(PyimH)_3]_{0.1}TaS_2$ [21]: the procedure followed was the one already introduced for the synthesis of **18** (recall symthesis on page 177). The delamination and flocculation steps were carried out in the same way as was done for **20**. Once the hybrid material was precipitated, it was well re-suspended in fresh ethanol and transferred to a membrane filtration set-up (see

Appendix 4.5, section 1.11 on page 301) with a frit and a PTFE membrane of 0.2 μm of pore size. The suspension was poured into the top reservoir cup and the precipitate was left to settle by effect of gravity. Once the supernatant was clear, vacuum was established in the bottom conical drain vessel and the acetonitrile was left to filter through. Two additional aliquots (20 mL) of fresh acetonitrile were passed through the solid subsequently. The resulting black slurry was left to dry in the air current and finally *in vacuo*. Large relatively robust flakes could be scraped off the PTFE membrane. Samples prepared by this technique presented the same chemical composition as the powder specimens **20** within experimental error.

7 Dichalcogenide thin flakes

The rocketing development of graphene science has opened an entire new field that studies the physics underlying atomically-thin layers. These cutting-edge investigations have been achieved thanks to the blooming recent advances regarding sample preparation and flake detection, transfer and manipulation.[164] To the date most of the research in this line has been devoted to graphene itself, leaving aside a plethora of alternative interesting layered materials that match or even outweigh the properties of graphite. Among them, TMDCs hold an important place.[165] Despite the fact that the sticky tape preparation of TMDC thin films had already been reported in a review article by Wilson *et al.* back in year 1969,[1] there has been a general lack of interest in the study of their low-dimensional systems ever since. Yet, it has already been extensively discussed, how layered TMDCs are a vast family of compounds with excellent exfoliation properties and how the different types of analogues offer the researcher with a quasi-continuous range of electrical, optical and magnetic properties from where to choose: from wide band-gap semiconductors to type II superconductors. The access to TMDC atomically-thin flakes opens the door to an entirely new science of low-dimensional physics of well-known old materials.

1 A brief history of exfoliation

Exfoliation of bulk crystals down to the single layer level is nowadays a feasible task for a few types of layered materials made out of weakly interacting lamellae. As exhaustively described in previous Chapter 4 (section 3.2 on page 130) this may be done by employing swelling solvents that solvate individual lamellae to yield stable thin flake sols after sonication. The latter is the method of choice for the clean segregation of electrostatically bound stacks, which occur for instance upon electron doping. However, exfoliation may also be achieved by means of a

164 For a comprehensive up-to-date view of the synthetical and applied aspects of graphene, see: (a) Choi, W.; Lahiri, I.; Seelaboyina, R.; Kang, Y. S. *Critical Reviews in Solid State and Materials Sciences* **2010,** *35,* 52–71. (b) Guo, S.; Dong, S. *Chem. Soc. Rev.* **2011,** *40,* 2644. (c) Huang, X.; Yin, Z.; Wu, S.; Qi, X.; He, Q.; Zhang, Q.; Yan, Q.; Boey, F.; Zhang, H. *Small* **2011,** *7,* 1876–1902.

165 A very recent review of the field may be read at: Xu, M.; Liang, T.; Shi, M.; Chen, H. *Chem. Rev.* **2013,** *DOI: 10.1021/cr300263a*

manifold of distinct 'dry' techniques, namely the micro-mechanical exfoliation method and derived procedures. Either way, thin flakes of varying number of layers may be conveniently obtained and deposited on a variety of substrate surfaces. Whereas the versatility of the 'wet' chemical approach may be profited from for the design and synthesis of a plethora of hybrid materials with multifunctional properties, it generally affords smaller lower aspect ratio flakes with large quantity of surface defects. This effect is inherent to the use of solvating liquid mixtures and physical methods for particle size reduction, such as ultrasounds. For the isolation of unspoilt larger surface area flakes it is mandatory to avoid the use of solvents.

Historically, it was accepted that two-dimensional (2-D) crystals were thermodynamically unstable and could not exist. It was so established more than 70 years ago by Peierls and Landau and more recently corroborated by Mermin that free-standing atomic planes should be thermodinamically stable at the nano-scale and are thus prone to roll up or buckle if left unsupported.[166] Regardless of these suppositions, the fabrication of atomically-thin graphitic films was soon claimed, though no proper justification of the isolation of single-layer graphene was yet given.[167] The method described by Boehm *et al.* constitutes the first example of fabrication of a thin graphitic film from the exfoliation and later reduction of graphite oxide and was the first report of its type of many more to come.[168] Following, a few publications reported the isolation of the so-called mesoscopic graphite by using dry exfoliation techniques.[169] However, only multilayer patches as thin as 10 nm were successfully deposited. It was only after the pioneering works published by Novoselov *et al.* that the rush for graphene was really triggered.[170] The group coming from Manchester reported the repeated peeling of higly-oriented pyrolitical graphite (HOPG) mesas stuck on a photoresist layer

166 a) Peierls, R. E. *Ann. I. H. Poincare* **1935.** *5,* 177-222. (b) Landau, L. D. *Phys. Z. Sowjetunion* **1937.** *11,* 26-35. (c) Mermin, N. D. *Phys. Rev.* **1968,** *176,* 250.

167 Boehm, H. P.; Clauss, A.; Fischer, G.; Hofmann, U. *Proceedings of the Fifth Conference on Carbon* **1962,** *73–80.*

168 For instance: (a) Eswaraiah, V.; Jyothirmayee Aravind, S. S.; Ramaprabhu, S. *J. Mater. Chem.* **2011,** *21,* 6800. (b) El-Kady, M. F.; Strong, V.; Dubin, S.; Kaner, R. B. *Science* **2012,** *335,* 1326–1330.

169 a) Zhang, Y.; Small, J. P.; Amori, M. E. S.; Kim, P. *Phys. Rev. Lett.* **2005,** *94,* 176803. (b) Bunch, J. S.; Yaish, Y.; Brink, M.; Bolotin, K.; McEuen, P. L. *Nano Lett.* **2005,** *5,* 287–290. (c) Ohashi, Y.; Koizumi, T.; Yoshikawa, T.; Hironaka, T.; Shiiki, K. *TANSO* **1997,** *235-238.*

170 Novoselov, K. S.; Geim, A. K.; Morozov, S. V.; Jiang, D.; Zhang, Y.; Dubonos, S. V.; Grigorieva, I. V.; Firsov, A. A. *Science* **2004,** *306,* 666–669.

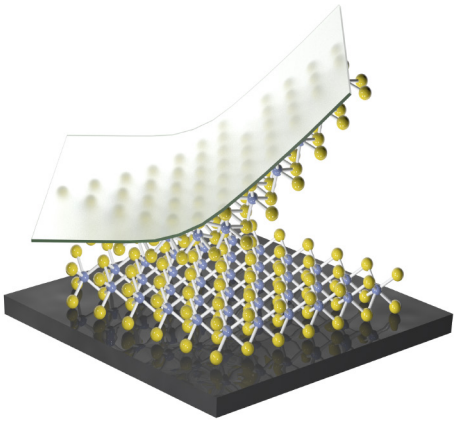

Figure 7.1 Cartoon representation of the mechanical exfoliation process by peeling off superficial metal dichalcogenide layers of a flake with sticky media. Sticky tape or PDMS gel ribbons are prototypical exfoliation tools employed for this purpose..

and the final release of the resulting thin flakes in acetone. The procedure very much resembled a previous patent filed in the US Patent Office in which very thin graphitic films were fabricated by successive peeling off.[171] This method was later improved in such a way that the 'dry' exfoliation of a manifold of layered materials by simply rubbing the surface of crystalline samples against different surfaces was reported.[172] Primitive as may seem, the methodology readily gave access to large surface area flakes of atomically-thin graphene and also to flakes of certain TMDCs. The technique soon expanded and was implemented in a variety of different ways under the generic name of micro-mechanical cleavage or exfoliation or, more informally, Scotch tape method (see Figure 7.1).

The following decade would experience the development of a plethora of different mechanical cleavage approaches for the clean deposition of extended graphene layers as well as many other layered materials on distinct surfaces. The introduction of soft-gel all-dry stamping procedures within the micro-mechanical family of exfoliation techniques has lead to great progress in the transfer of good

171 Rutherford, R. B.; Dudman, R. L. *Ultra-thin flexible expanded graphite heating element* **2003.** *US Patent* 6667100.

172 Novoselov, K. S.; Jiang, D.; Schedin, F.; Booth, T. J.; Khotkevich, V. V.; Morozov, S. V.; Geim, A. K. *Proc. Natl. Acad. Sci. U.S.A.* **2005,** *102,* 10451–10453.

quality extended bi-dimensional crystals.[173] These techniques are based in both the adhesive and viscoelsatic properties of silicone stamps, generally PDMS. In this way, successive thinning of bulk crystals may be achieved by stamp to stamp transferring. In the final step, the thinnest flakes are simply pressed on to a receiver surface. The applied pressure, pressing and peel-off rates and stamp surface structures are all key features that condition the transfer of flakes from the donor to the receiver surface. In this way, TMDC, mica and even heterostructure multilayer systems have been reported to be successfully exfoliated by modification of the micro-mechanical method.[174, 175, 176] Extremely long graphene nano-ribbons have also been successfully deposited by this technique.[177] The PDMS stamp methodology finds direct application in device fabrication due to the easy transfer and integration of the exfoliated structures in electronic circuitry.[178] Another technique which derives from the Scotch tape one is the so-called anodic bonding. At high temperatures and under and electric field it is claimed that single flakes are chemically bonded to the surface of a receiving wafer.[179] This allows for the safe peeling off of the rest of the bulk non-bonded material. The technique has very recently been extended to other layered materials, proving to be a versatile approach.[180]

At the same time, the bottom-up approach is currently attracting interest. In this way, a lot of research is nowadays being devoted to the growth of large-surface-area crystalline films on a variety of surfaces. Epitaxial growth of graphene lead the way for the controlled fabrication of atomically thin films on a variety of

---

173 a) Meitl, M. A.; Zhu, Z.-T.; Kumar, V.; Lee, K. J.; Feng, X.; Huang, Y. Y.; Adesida, I.; Nuzzo, R. G.; Rogers, J. A. *Nature Mat.* **2006,** *5,* 33-38. (b) Meitl, M. A. *Transfer Printing and Micro-scale Hybrid Materials Systems*, ProQuest, **2007.**

174 Castellanos-Gomez, A.; Agraït, N.; Rubio-Bollinger, G. *Appl. Phys. Lett.* **2010,** *96,* 213116.

175 Castellanos-Gomez, A.; Poot, M.; Amor-Amorós, A.; Steele, G. A.; Zant, H. S. J.; Agraït, N.; Rubio-Bollinger, G. *Nano Res.* **2012,** *5,* 550–557.

176 Castellanos-Gomez, A.; Wojtaszek, M.; Tombros, N.; Agraït, N.; van Wees, B. J.; Rubio-Bollinger, G. *Small* **2011,** *7,* 2491–2497..

177 Moreno-Moreno, M.; Castellanos-Gomez, A.; Rubio-Bollinger, G.; Gomez-Herrero, J.; Agraït, N. *Small* **2009,** *5,* 924–927.

178 Ahn, J. H.; Kim, H. S.; Lee, K. J.; Jeon, S.; Kang, S. J.; Sun, Y.; Nuzzo, R. G.; Rogers, J. A. *Science* **2006,** *314,* 1754–1757.

179 a) Balan, A.; Kumar, R.; Boukhicha, M.; Beyssac, O.; Bouillard, J.-C.; Taverna, D.; Sacks, W.; Marangolo, M.; Lacaze, E.; Gohler, R.; et al. *J. Phys. D Appl. Phys.* **2010,** *43,* 374013. (b) Moldt, T.; Eckmann, A.; Klar, P.; Morozov, S. V.; Zhukov, A. A.; Novoselov, K. S.; Casiraghi, C. *ACS Nano* **2011,** *5,* 7700–7706.

180 Gacem, K.; Boukhicha, M.; Chen, Z.; Shukla, A. *Nanotechnology* **2012,** *23,* 505709.

surfaces, namely silicon carbide (SiC) or metal substrates.[181, 182] Whilst in the first case SiC itself acts as a C source, the second method employs an external chemical vapour source to seed the growth of the graphene following the atomic structure provided by the substrate in a chemical vapour deposition (CVD) process. These techniques yield extense graphene films which present high mobilities, though still lower than the ones exhibited by graphene produced by top-down micro-mechanical exfoliation.[183] Yet, the electronic band-structure has already been successfully observed in epitaxially grown layers and the characteristic properties of massless Dirac fermions such as the anomalous quantum Hall effect have also been visualized.[184] Driven by the increasing interest in epitaxially crystallized atomically thin carbon films, attention is gradually being redirected to other bi-dimensional crystals such as TMDCs. On this note, Helveg *et al.* had already reported the fabrication of MoS_2 nano-clusters over a Au surface back in 2000.[185] More recently, big progress has been made in the growth of MoS_2 single or few layer crystals via CVD-type deposition on Si/SiO_2 substrates.[186]

The recent access to macroscopic atomically-thin films has boosted the invention of new technologies for the transfer of several square centimetre wide bi-dimensional crystals to a variety of functional surfaces. On the one hand, the 'roll-to-roll' technique attempts to transfer extended graphene films produced by CVD on to flexible substrates for device integration.[187] Alternatively, the growth of multilayer systems and selective chemical etching also allows for the fabrication

181 a) Sutter, P. *Nature Mat.* **2009,** *8,* 171-172. (b) Berger, C.; Song, Z.; Li, T.; Li, X.; Ogbazghi, A. Y.; Feng, R.; Dai, Z.; Marchenkov, A. N.; Conrad, E. H.; First, P. N.; de Heer, W. A. *J. Phys. Chem. B* **2004,** *108,* 19912–19916.

182 a) Sutter, P. W.; Flege, J.-I.; Sutter, E. A. *Nature Mat.* **2008,** *7,* 406 - 411. (b) Pletikosić, I.; Kralj, M.; Pervan, P.; Brako, R.; Coraux, J.; N'Diaye, A.; Busse, C.; Michely, T. *Phys. Rev. Lett.* **2009,** *102,* 056808. (c) Dedkov, Y.; Fonin, M.; Rüdiger, U.; Laubschat, C. *Phys. Rev. Lett.* **2008,** *100,* 107602. (d) Vázquez de Parga, A.; Calleja, F.; Borca, B.; Passeggi, M.; Hinarejos, J.; Guinea, F.; Miranda, R. *Phys. Rev. Lett.* **2008,** *100,* 056807. (e) Li, X.; Cai, W.; An, J.; Kim, S.; Nah, J.; Yang, D.; Piner, R.; Velamakanni, A.; Jung, I.; Tutuc, E.; Banerjee, S. K.; Colombo, L.; Ruoff, R. S. *Science* **2009,** *324,* 1312–1314.

183 Jobst, J.; Waldmann, D.; Speck, F.; Hirner, R. How Graphene-like is Epitaxial Graphene, **arXiv:0908.1900**.

184 Shen, T.; Gu, J. J.; Xu, M.; Wu, Y. Q.; Bolen, M. L.; Capano, M. A.; Engel, L. W.; Ye, P. D. *Appl. Phys. Lett.* **2009,** *95,* 172105.

185 Helveg, S.; Lauritsen, J.; Laegsgaard, E.; Stensgaard, I.; Norskov, J.; Clausen, B.; Topsoe, H.; Besenbacher, F. *Phys. Rev. Lett* **2000,** *84,* 951–954.

186 a) Lee, Y. H.; Zhang, X.-Q.; Zhang, W.; Chang, M. T.; Lin, C. T.; Chang, K. D.; Yu, Y. C.; Wang, J. T. W.; Chang, C. S.; Li, L. J. *Adv Mater.* **2012,** *24 (17),* 2320–5 (b) Zhan, Y.; Liu, Z.; Najmaei, S.; Ajayan, P. M.; Lou, J. *Small* **2012,** *8 (7),* 966–971.

187 Bae, S.; Kim, H.; Lee, Y.; Xu, X.; Park, J.-S.; Zheng, Y.; Balakrishnan, J.; Lei, T.; Kim, H. R.; Song, Y. I.; Kim, Y.-J.; Kim, K. S.; Özyilmaz, B.; Ahn, J. H.; Hong, B. H.; Iijima, S. *Nature Nanotechnology* **2010,** *5,* 574–578.

of large surface area free-standing graphene films.[188] Also worthwhile mentioning is the hot press method which allows for the transfer of CVD prepared films on to rigid large substrates, minimizing film stress and damage.[189]

Finally, it important to acknowledge some other more exotic methods of preparing atomically thin crystalline films. For instance, it has been suggested that ultra-short laser pulses may achieve the detachment of graphene flakes from a graphite surface.[190] Related to this technique is the laser thinning of TMDC flakes by the use of the laser source used for Raman spectrocopy reported by Castellanos-Gómez *et al.*[191] Furthermore, there is another technique that reports the growth of single layer or few-layer graphene films from a molten metal-carbon phase.[192] This process involves dissolving carbon inside molten copper or nickel and then lowering the temperature to allow the carbon atoms to nucleate and grow on the surface of the melt. Another interesting route to access graphene is starting from carbon nanotubes (CNTs). On that note it has been reported how it is possible to produce graphene ribbons by cutting open single- or multi-wall CNTs. The "unzipping" of CNTs has so far been achieved by treatment with strongly acidic and oxidizing conditions or with an Ar plasma.[193, 194] Other methods for the synthesis of sub-nanometer thin carbon films include the pyrolysis and sonication of sodium ethoxide or even the reduction of carbon dioxide.[195, 196]

Yet, most of the herein described exfoliation or thin film fabrication methods require specific instrumentation or were difficult to implement in a conventionally equipped laboratory. The great simplicity together with the relatively high efficiency of the micro-mechanical exfoliation method inspired the development

188 Kim, K. S.; Zhao, Y.; Jang, H.; Lee, S. Y.; Kim, J. M.; Kim, K. S.; Ahn, J.-H.; Kim, P.; Choi, J.-Y.; Hong, B. H. *Nature* **2008,** *457,* 706–710.

189 Kang, J.; Hwang, S.; Kim, J. H.; Kim, M. H.; Ryu, J.; Seo, S. J.; Hong, B. H.; Kim, M. K.; Choi, J.-B. *ACS Nano* **2012,** *6,* 5360–5365.

190 Miyamoto, Y.; Zhang, H.; Tománek, D. *Phys. Rev. Lett* **2010,** *104,* 208302.

191 Castellanos-Gomez, A.; Barkelid, M.; Goossens, A. M.; Calado, V. E.; van der Zant, H. S. J.; Steele, G. A. *Nano Lett.* **2012,** *12,* 3187–3192.

192 Amini, S.; Garay, J.; Liu, G.; Balandin, A. A.; Abbaschian, R. *J. Appl. Phys.* **2010,** *108,* 094321.

193 Kosynkin, D. V.; Higginbotham, A. L.; Sinitskii, A.; Lomeda, J. R.; Dimiev, A.; Price, B. K.; Tour, J. M. *Nature* **2009,** *458,* 872–876.

194 Jiao, L.; Zhang, L.; Wang, X.; Diankov, G.; Dai, H. *Nature* **2009,** *458,* 877–880.

195 Choucair, M.; Thordarson, P.; Stride, J. A. *Nature Nanotech.* **2009,** *4,* 30-33.

196 Chakrabarti, A.; Lu, J.; Skrabutenas, J. C.; Xu, T.; Xiao, Z.; Maguire, J. A.; Hosmane, N. S. *J. Mater. Chem.* **2011,** *21,* 9491.

of a modification of the original procedure to adapt it to the challenging exfoliation of other TMDC crystals which appear to be not so easy to exfoliate. The new approach relies in the same fundamentals: direct contact physisorbption of the two-dimensional crystals. However, a few technical upgrades have been incorporated in order to improve the control of the experimental conditions that rule TMDC flake deposition. TMDCs, and more specifically TaS_2, appeared to be less easily exfoliated by conventional Scotch tape deposition procedures than graphene, fact which has been holding back the in-depth physical study of such systems. All in all, the deposition of good quality flakes turned out to be a sheer question of ameliorating the control over the "drawing by chalk on a blackboard" procedure.[172]

Profiting from the expertise acquired in the synthesis of TMDCs required by the solid-state chemistry described in previous chapters, large single crystals were grown to attempt their dry exfoliation (review section 2 on page 100, Chapter 4). While the exfoliation of many TMDC members has been extensively studied, little has been reported on the controlled isolation of atomically thin TaS_2 flakes. Very recent findings report the exfoliation of single and few layer WSe2, $TaSe_2$ and TaS_2, however, surprisingly no direct evidence of the successful deposition of TaS_2 or $TaSe_2$ single layer flakes is provided in the manuscript.[197] In the latter report the thinnest flakes obtained were 2.1 nm high corresponding to 3 layers as claimed by the authors. Therefore, the TaS_2 system appears as a challenging layered material in that which concerns the deposition of single layer flakes. So besides the logical interest in continuing the case study that has been discussed throughout the dissertation, TaS_2 was an ideal benchmark to evaluate the performance of the introduced exfoliation technique.

2 'Press and shear' exfoliation

With the objective of establishing a precise control over the exfoliation process, a whole new mechanical set-up was designed and assembled.[198] A perspective view of the instrumental layout may be viewed in Figure 7.2.The aim of this instrumental

197 Li, H.; Lu, G.; Wang, Y.; Yin, Z.; Cong, C.; He, Q.; Wang, L.; Ding, F.; Yu, T.; Zhang, H. *Small* **2012,** *DOI: 10.1002/smll.201202919*

198 Patent pending: P201300252, "*Método y sistema de exfoliación micromecánica por vía seca de materiales laminares bidimensionales.*"

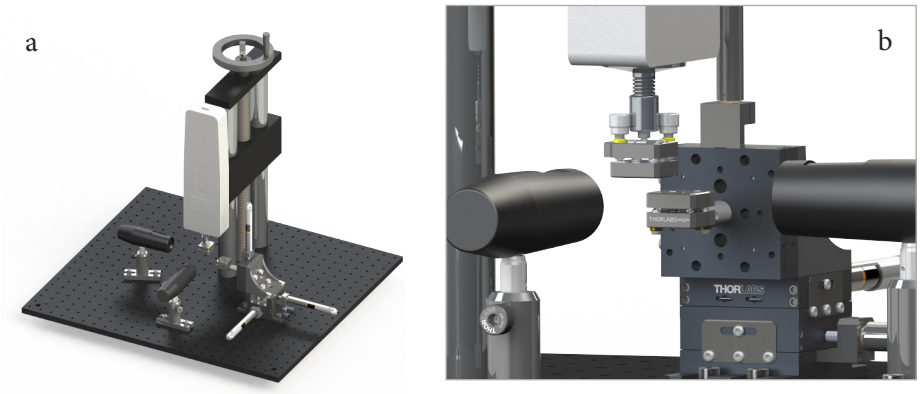

Figure 7.2 Trimetric perspective render of the set-up used for the 'press and shear' exfoliation of TMDC single crystals. **a**. General view; **b**. close-up of contact gauges where substrate and sample crystals are mounted.

assembly was twofold. Firstly, in order to control the physisorbtion of the flakes on a surface, it was desirable to monitor precisely the uniaxial *pressure* that the surface of the single crystal was exerting over the sample substrate. Secondly, it is proposed that a controlled movement of the substrate in a normal direction with respect to the crystallographic stacking *c*-axis of the TMDC crystal (*shear* movement) may increase the density of flakes deposited in a substrate surface and hence improve the thickness distribution statistics. Hence the set-up was optimized in order to maintain a constant applied mechanical pressure over a moving substrate. It is suggested that as the substrate slides across past the crystal, an inter-layer shear stress is induced so that exfoliation occurs.

Curiously, a similar invention at the micro-scale had already been reported. Herein HOPG patches were successfully stamped on Si/SiO_2 surfaces by the use of a μ-cantilever.[199] However, in that case no shearing component was implemented.

2.1 Setup design

In order to control the pressure at which the two surfaces were contacted, a force dinamometer was included in the set-up. The device consists in a spring gauge with a maximum load of 2 N and a maximum resolution of 0.001 N. It was so

199 Zhang, Y.; Small, J. P.; Pontius, W. V.; Kim, P. *Appl. Phys. Lett.* **2005,** *86,* 073104.

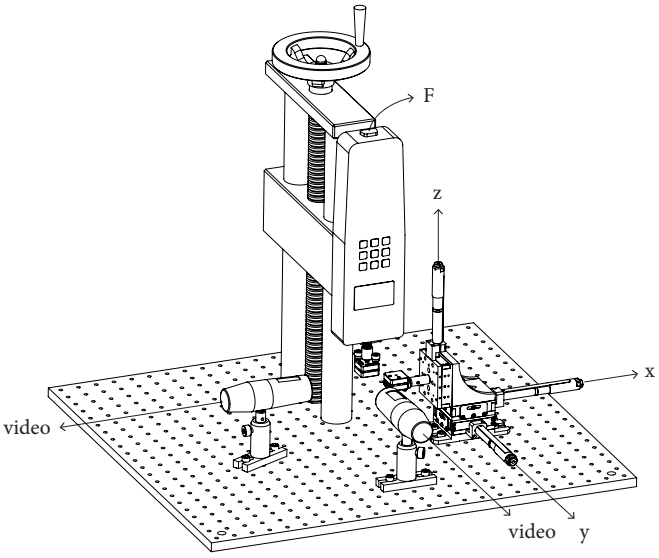

Figure 7.3 Technical drawing scheme of the 'press and shear' set-up highlighting the data output ports: exerted force (*F*) data out of the RS-232 socket; distance translations (*x*, *y*, *z*) out of the actuators (via a USB connected DC cube); video signal out of the USB digital microscopes.

chosen for working at relatively low applied pressures as it was expected that working in the mild applied pressure regime would preserve the integrity of the crystal surface and hence the deposited flakes. The instrument was mounted on a test stand with a handwheel-operated worm guide for coarse approximation of the samples. Figure 7.3 shows a schematic representation of the different components of the micro-mechanical exfoliation device. As may be seen in the cartoon, the different components of the setup were conveniently mounted on an optical table, which conferred stability to the system.

Regarding the sliding exfoliation movement, it was performed by an XYZ motorized stage. The stage was driven by three independent uniaxial step-motor actuators with sub-micron resolution and a wide range of operating speeds (up to 3 mm/s). This allowed for the testing of a wide range of shear conditions in combination with the force range delivered by the dinamometer. A relevant point to rise at this stage is the importance of a good co-planarity between the two contacting surfaces and also a co-lineality between the shear movement axis and

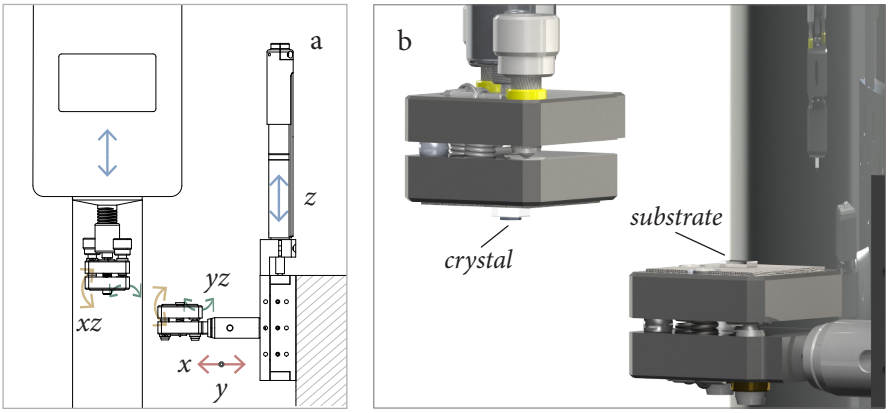

Figure 7.4 TMDC crystal and substrate tilted holders at the core of the exfoliation set-up. **a**. Front view outline of the tow kinematic tilting units, stressing the different movement degrees of freedom of that may be achieved by moving the distinct stages of the setup; **b**. 3-D rendered view of the two tilting units, holding the TMDC crystal and the substrate. Note that between the TMDC crystal and the tilt base, a thin PDMS block was always placed.

the surface of the TMDC crystal *ab*-crystallographic facet. If one wants to achieve an extended surface contact between the donor crystal and the accepting surface, both need to sit on top of each other in a co-planar manner. This is achieved by introducing two kinematic tilting units: one acting as substrate holder and the second one controlling the orientation of the TMDC crystal. Figure 7.4 shows two different representations of the tilt adjusting mechanism. The tilting unit attached to the XYZ stage was used as the substrate holder and hence employed for the correct alignment of the substrate surface with the sliding direction with the help of two orthogonally placed optical microscopes. Secondly, the TMDC crystal was approached with the handwheel and its surface adjusted so that the *ab*-crystallographic plane lied parallel to the substrate underneath. Once again the tilt was corrected according to the two perpendicular side views provided by both microscopes.

2.2 Experimental results: exfoliation of TaS_2 crystals

It may be appreciated how methodology required, in principle, the use of large single crystals that could be conveniently manipulated. Here, a large crystal

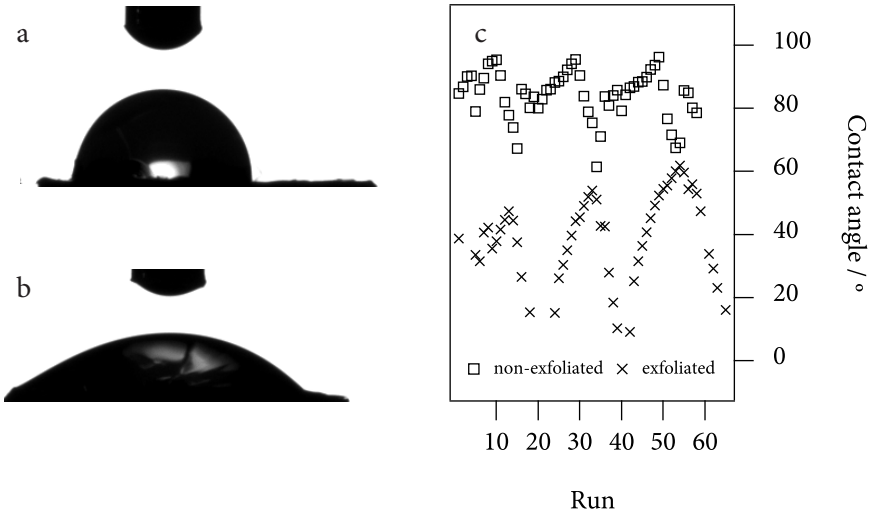

Figure 7.5 Silhouettes of ultrapure 1.5 μL H_2O drops laid on the surface of a non-exfoliated (**a**) and a freshly exfoliated (**b**) large single crystal of TaS_2. **c**. Advancing/receding contact angle cycles performed on non-cleaved and on exfoliated TaS_2 surfaces..

surface area also meant a greater chance of depositing large surface area exfoliated flakes. Single TaS_2 crystals were therefore grown by the CVT technique following the methods described in Chapter 4.

It is also important to emphasize how it is crucial to carry out a cleansing and activation protocol of the surface of the substrates prior to performing the deposition itself. In this way, immersion and sonication in basic 'piranha' solution guaranteed a through cleaning of the surface of a variety of substrates, namely Si and SiO_2. The use of freshly base-activated surfaces guaranteed a clean and successful deposition of large surface area atomically thin flakes.

Moreover, a fresh cleavage of the surface of the TMDC crystal was always carried out before deposition. The exfoliation of the few outermost layers of a single crystal yielded clean surfaces with a remarkable hydrophilicity as opposed to the non-exfoliated facets of air exposed single-crystals. Figure 7.5 illustrates how the contact angle of freshly cleaved TaS_2 surfaces is much smaller than when the crystal had been exposed to ambient conditions for long periods of time. It is

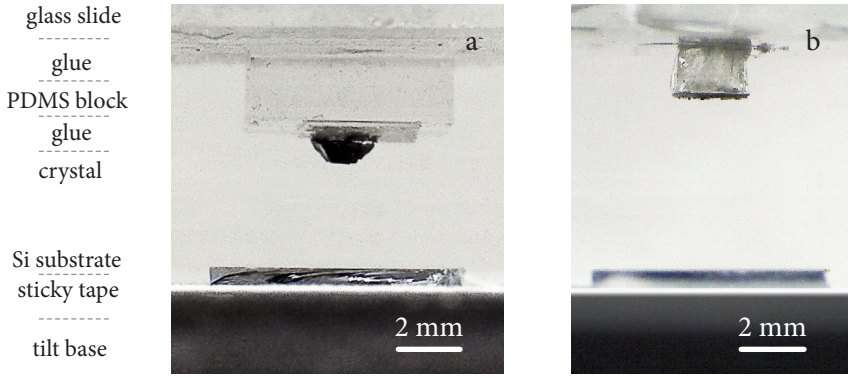

Figure 7.6 USB digital microscope view of the *top* and the *bottom* gauges before contact was made. Two TMDC 'stamps' with a thicker (**a**, ~ 700 μm thick) and a thinner (**b**, ~ 125 μm thick) donor TaS_2 crystals (**5**) are shown. An indication of the different interfaces is provided on the *right* hand side.

suggested that an enhanced hydrophilicity facilitates the adsorption process over a freshly activated substrate surface.

Following, the substrate and the crystal were placed on the bottom and stuck to the top tilt stages respectively. In between the bottom tilt base and the substrate was a double-sided piece of sticky tape to immobilize the substrate. Moreover, in between the top gauge and the TaS_2 crystal a few millimetre thick PDMS cushion mounted on a glass slide was placed (see Figure 7.6). This viscoelastic layer was introduced in order to compensate for small deviations from strict co-planarity between the crystal surface and the substrate, allowing for some accommodation as the pressure was exerted. The crystal was stuck to the PDMS block across the basal face, in such a way that the (001) plane laid co-planar to the base of the tilting unit above.

Finally, the substrate surface was driven by the XYZ stage and centred beneath the crystal, the relative tilt was reduced as accurately as possible by the use of the digital microscopes and the crystal was approached by using the hand-wheel until slight contact was made (F ~ 0.002 N). Once conveniently aligned and brought into contact, both surfaces were pressed against each other. Next, the exfoliation test was carried out by controlling the applied force and the shear movements. The pressure was monitored at a frequency of 1 Hz throughout the process. Figure

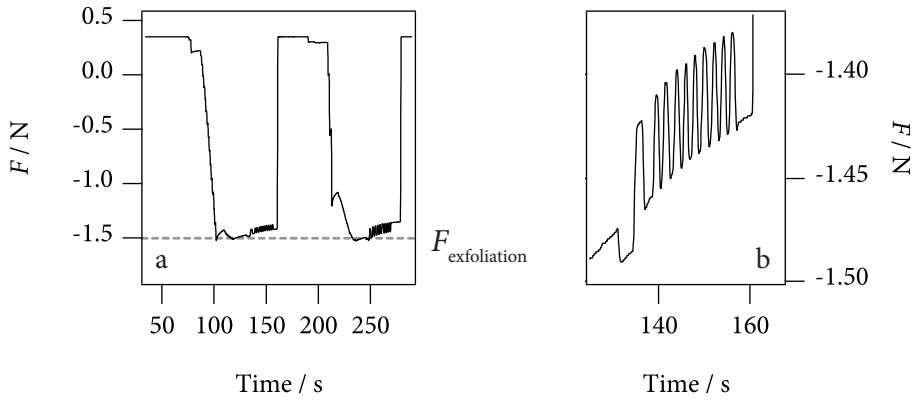

Figure 7.7 Force versus time plot (**a**) of two exfoliation processes carried out in the dynamic non-sliding mode (*vide infra*). Negative values of F denote a pushing force. Note the subtle force fluctuations around the set exfoliation applied force ($F_{exfoliation}$) corresponding to the back and forth shearing jogs. Graph (**b**) shows a zoon-in of the first exfoliation event in (**a**).

7.7 shows a force versus time plot of two consecutive exfoliation events. Finally, the surfaces were drawn apart at the maximum actuator speed (v = 3 mm·s^{-1}, a = 4 mm·s^{-2}). The result of each exfoliation test was evaluated by the preliminary examination of the substrates by bright-field episcopy to ascertain the presence of patches at the surface. The specimens where a high density of low-contrast flakes could be observed were selected for a more in depth study by AFM.

Following, a collection of experimental parameters that were found to influence the exfoliation process are discussed separately and in detail. The optimisation of the deposition parameters was monitored via optical microscopy. Only when a certain deposition quality was achieved in terms of the flake density, the average surface area of the deposited patches and the homogeneity and nature of their optical contrast, was the sample inspected by other techniques (AFM, SEM, etc.).

a. Thickness of donor crystal

It is important to highlight that the experimental results observed suggested that no thinning down of the crystal was required to achieve a relatively clean crystal exfoliation (Figure 7.8). As opposed to that established for most micromechanical

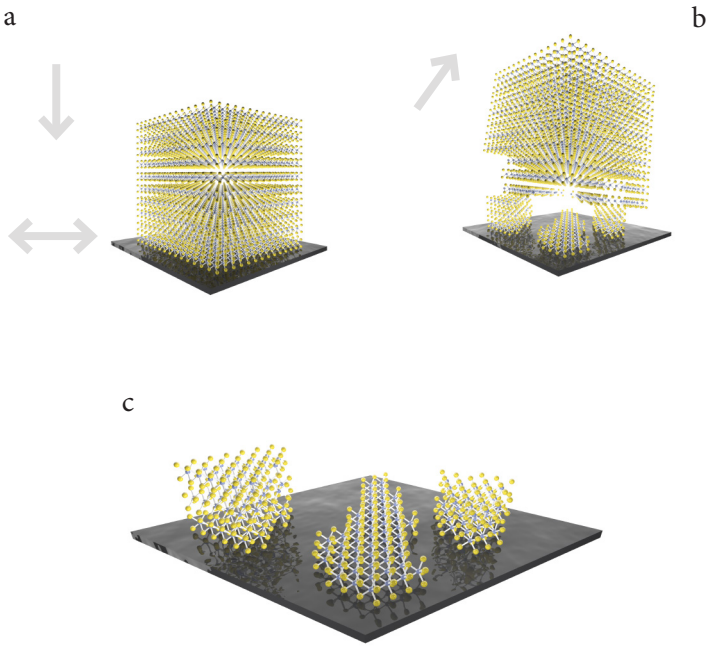

Figure 7.8 Cartoon demonstrating the physical adsorption of thin TaS_2 flakes on a substrate following compression and shearing of the bulk crystal against the surface (**a**) and controlled lift-off (**b**). **c**. The figure emphasizes the fact that a distribution of different thickness (single, bi- and trilayer) and surface area layers are transferred on to the substrate.

exfoliation techniques the approach here introduced makes use of the surface of a bulk crystals as the donor surface.[173] Indeed, it was confirmed that the flakes that were left on the surface of the accepting substrate after rubbing the surface of a bulk crystal rarely exceeded a few hundred nanometres in thickness as measured by AFM. By contrast, the majority of the TaS_2 layers left behind were in the range of the tens of nanomenters. This also introduces a major improvement as compared to the classical micromechanical techniques, such as the Scotch-tape or the silicone stamps methods, since no additional materials other than the desired compound contacts the accepting surface. This implies that no glue or other sticky residues are left behind in the surface of the target substrate.

Typical crystal thicknesses (along the crystallographic *c* axis) ranged from a few hundred of microns to one hundred or even less microns. Figure 7.9 shows

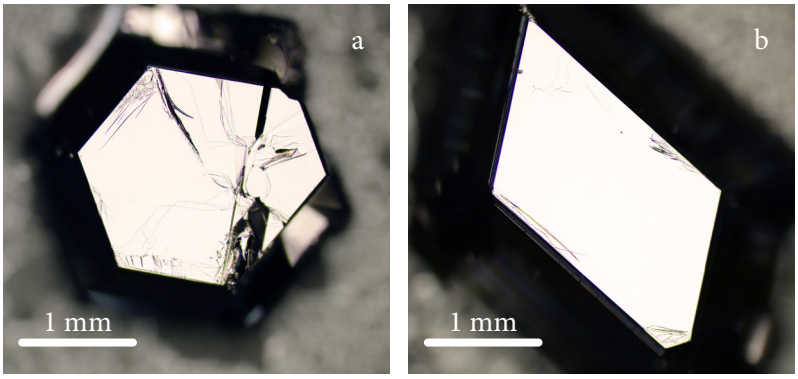

Figure 7.9 Episcopy micrographs of TaS_2 donor crystals (**5**) with falt and clean deposition surfaces of: **a**. 2.7 mm^2; **b**. 2.8 mm^2

optical micrographs of two specimens of TaS_2 donor crystal 'stamps'.[200] Note how the PDMS block had to cut to adjust it to the crystal perimeter in order to avoid contact with the substrate surface as the pressure was applied. It was thought that a thinner crystal profile could lead to a better matching of the crystal and substrate surface and hence improve the contact area. However, though the last hypothesis may indeed be true, the results of the deposition carried out with TaS_2 crystals of different thickness permitted concluding that thicker ones gave rise to a higher yield of transference. The inspection by optical microscopy confirmed a higher density of flakes in the samples prepared with thicker crystals, thus from now on all the results dicussed refer to thicker crystal stamps.

b. Crystal surface

The crystal surface was found to be one of the most determining experimental factors. The flatness of the donor TaS_2 crystal was of great importance in order to achieve a high transference yield and also to transfer high-surface-area layers. The examination of the as-synthesized crystal surfaces by optical microscopy permitted identifying a great number of crevasses and defects. In this context, the crystals had to be previously cleaved along a deeper basal plane. This was performed by driving the tip of a sharp razor blade into the edge of a crystal and

200 By 'stamp' one refers to the crystal glued to the PDMS and the glass slide as a single transferring entity.

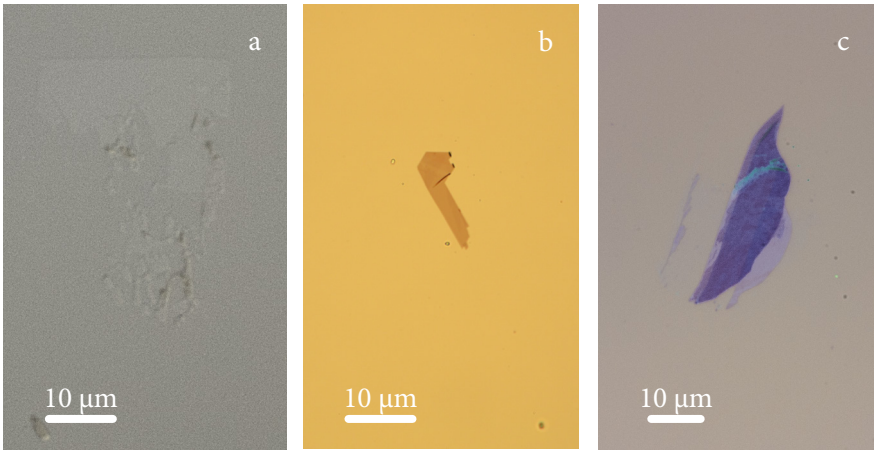

Figure 7.10 Visibility as seen by optical episcopy of approximately 10 nm thick TaS_2 flakes deposited by the press and shear method on different surfaces: **a**. HF-etched Si substrate; **b**. Au/Ta coated (40 nm + 4 nm) Si substrate; **c**. Si / 285 nm SiO2 substrate.

then performing a lever-like sudden movement. Once a flat facet was achieved, the crystal could be used for a large number of depositions by simply peeling-off the outermost layers with a sticky tape as previously indicated. Figure 7.9 shows two examples of TaS_2 freshly cleaved and peeled crystals ready for depositing.

c. Nature of the receiving substrate

It has already been reported in the literature how the substrate influences the roughness of deposited flakes.[201] As a matter of fact, it allows for larger mobilities and the absence of 'electron and hole puddles', giving access to Dirac point physics in suspended graphene.[202] In this line, hexagonal boron nitride (h-BN) is very flat (root mean squared roughness: RMS ~ 10 nm) and graphene is found to adapt to its roughness.[203] Working in such a surface provides enhanced mobility

201 Lui, C. H.; Liu, L.; Mak, K. F.; Flynn, G. W.; Heinz, T. F. *Nature* **2009,** *462,* 339–341.

202 Bolotin, K. I.; Sikes, K. J.; Jiang, Z.; Klima, M.; Fudenberg, G.; Hone, J.; Kim, P.; Stormer, H. L. *Sol. State Comm.* **2008,** *146,* 351–355.

203 a) Dean, C. R. ; Young, A. F.; Meric, I.; Lee, C.; Wang, L.; Sorgenfrei, S.; Watanabe, K.; Taniguchi, T.; Kim, P.; Shepard, K. L.; Hone, J. *Nature Nanotech.* **2010,** *5,* 722–726. (b) Xue, J.; Sanchez-Yamagishi, J.; Bulmash, D.; Jacquod, P.; Deshpande, A.; Watanabe, K.; Taniguchi, T.; Jarillo-Herrero, P.; LeRoy, B. J. *Nature Mat.* **2011,** *10,* 282–285.

with diminished carrier inhomogeneity and also lower intrinsic doping of the graphene layers.

From an experimental deposition point of view, the choice of an appropriate accepting surface conditions the success of the deposition process. Atomically-flat surfaces with negligible roughness are best for larger contact surface areas, hence attaining a better adsorption and maximizing flake sizes. In this respect, among the more standard substrates, Si 100 excels both in terms of its flatness and hardness is. Silicon can be anisotropically grown in large flat wafers along the 001 crystallographic plane. Moreover, it can also be conveniently synthesized in a doped state (p-B is typical) in order to enhance its conductivity. It is also worthwhile to mention that upon exposure to air Si develops a very thin SiO_2 patina coating of a few nanometres thick, the so-called native oxide layer (*nat.*). This means that the deposition process effectively occurs over a SiO_2 surface unless special care was taken to maintain an oxygen-free atmosphere.

In some cases, this oxide layer may even be beneficial. Indeed, it may be profited from for gating purposes in device fabrication or it may also be useful for detection purposes (*vide infra*).[170] In this context, an oxide layer can also be grown in a controlled manner by thermal oxidation.[204] This technique allows for the growth of given thickness of SiO_2 to produce Si / SiO_2 substrates which are equally suitable for deposition purposes.

Concerning the detection of flakes at the surface of the substrate, the thinnest flakes deposited on Si/SiO_2 (*nat.*) exhibited only a very weak optical contrast (see Figure 7.10a). Whilst thin layers of over 10 nm of thickness can be easily spotted out using the microscope, thinner flakes are best searched for when assisted by Nomarski DIC interferometry.[205] It is therefore a difficult task to detect the atomically thin flakes by the naked eye. On the other hand, if one deposits the TaS_2 flakes on Si / SiO_2 (> 200 nm) the same thickness layers exhibit an enhanced optical contrast and are now easily detected (Figure 7.10c).

---

204 Jaeger, R. C. *Thermal Oxidation of Silicon. Introduction to Microelectronic Fabrication*, Upper Saddle River: Prentice Hall, **2001**.

205 Murphy, D., *Differential interference contrast (DIC) microscopy and modulation contrast microscopy, in Fundamentals of Light Microscopy and Digital Imaging*, Wiley-Liss, New York, **2001**, pp. 153–168.

The press and shear method permits depositing on virtually any surface. For instance, it was confirmed that the deposition TaS_2 flakes could also be performed on gold coated surfaces. However, it is important to note that in order to achieve the deposition of flat and relatively large flakes, a low-roughness surface was mandatory. Low-RMS gold coated surfaces could only be accessed via sputtering techniques.

In conclusion, the evaluation tests of the press and shear technique were generally performed over Si/SiO_2 substrates since they allowed to judge the result of the deposition process in a fast and reliable way. The same surface was employed for ultrathin-flake device fabrication. By contrast, if a conducting specimen was required, namely for STM probing or for local oxidation manipulation of flakes (view Chapter 7), flat gold or Si/SiO_2 (*nat.*) surfaces respectively were used.

d. Static pressing mode vs. shearing mode

One of the novelties introduced by the press and shear strategy is the dynamic cleavage of the surface of the donor crystal. This is in contrast to the currently established micromechanical methods. In the latter, a static uniaxial pressure is applied during a given time and then the transferring stamp is eventually simply removed. In this way, experiments were conducted in order to elucidate the effect of the shear movement. As expected, the experiments confirm that the simultaneous pressing and shearing increases the density of flakes that were left on the surface of the substrate. A comparison of both deposition modes is shown in Figure 7.11.

e. Shearing movement

Initial tests were carried out by sliding the crystal all along the full length of the accepting substrate. In this case, a good co-planarity of the crystal with respect to the substrate surface was required in order to maintain a constant forces throughout the deposition. Both the shearing speed (v_s) and the acceleration (a_s) at which the substrate is slid across the crystal also appeared to have a big importance in the morphology of the of the deposited flakes. Indeed it was confirmed that higher speed and higher acceleration brisk shear movements (such as the ones used for

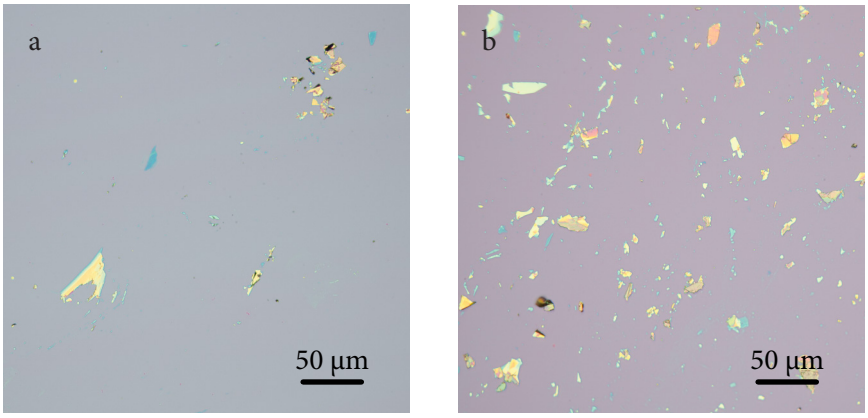

Figure 7.11 Optical micrographs (50×) of a Si / 285 nm SiO2 substrate deposited with TaS_2 flakes in a static (**a**, F = 1.5 N, t = 20 min) and a sliding mode (**b**, v_s = 3 mm·s^{-1}, a_s = 4 mm·s^{-1}, Δl = 2 mm).

the specimen showed in Figure 7.11b) afforded equally higher aspect ratio flakes in comparison to slow ones.

Alternatively, the crystal could also be rubbed against the surface of the substrate in a *non-sliding* mode. In this mode, optimum exfoliation was achieved by performing a shear movement in periodic back and forth short and brisk jogs. As a matter of fact, the step length (Δl) and speed and acceleration (v_s, a_s) of each jog could be tuned and the number of jogs modified in such a way that very large surface area flakes with very faint optical contrasts could be obtained. In this context, a slightly lower deposition density than in the sliding mode was achieved, yet it paid off for the high quality and large size of the exfoliated flakes achieved.

In addition, the number of jogs could be increased in order to rise de flake density but it also resulted in some wearing off and consequent flake size reduction. Figure 7.12 illustrates these findings by showing examples of TaS_2 flakes obtained by the non-sliding deposition mode in different conditions. Note the homogeneous optical contrast exhibited in large areas of some patches. The blue/lilac patches that may be observed in the high magnification images were typically thinner than 50 nm as measured by AFM. Due to the big quality of the flakes accessed by the non-sliding mode, the rest of the exfoliation parameters were optimised for that case.

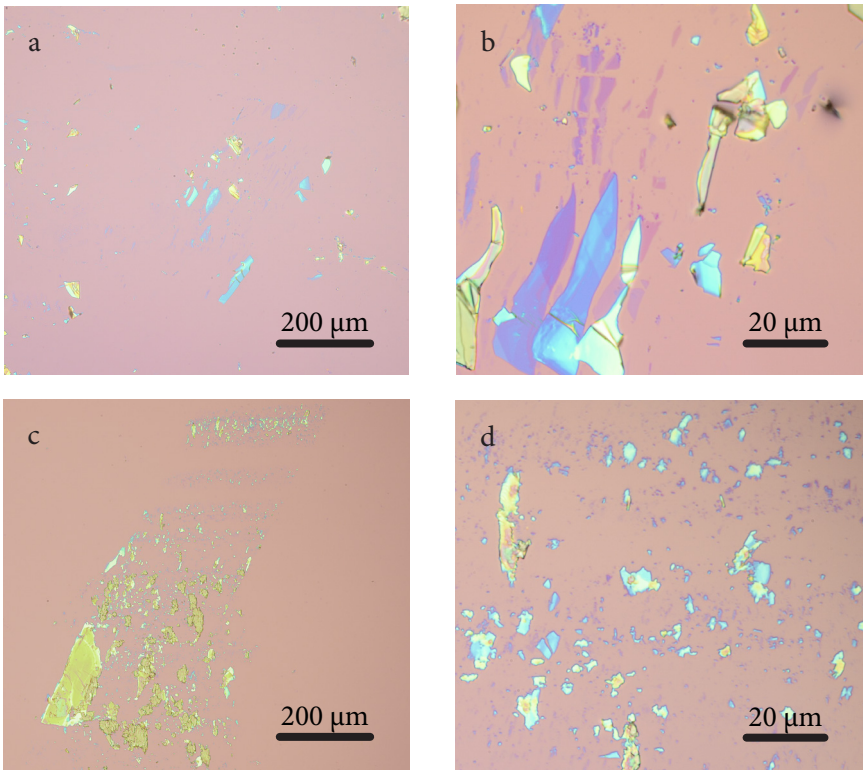

Figure 7.12 TaS_2 flakes deposited by the *non-sliding* mode on a Si / 285 nm SiO_2 substrate at $F_{exfoliation}$ = 1 N and with the following jog parameters: **a**. 20 jogs of Δl = 0.1 mm, v_s = 3 mm·s^{-1}and a_s = 4 mm·s^{-1}; **b**. 40 jogs of Δl = 0.15 mm, v_s = 3 mm·s^{-1}and a_s = 4 mm·s^{-1}. The images on the *right* hand side **b** and **d** show high-magnification micrographs (100×) of selected flakes at **a** and **c** respectively.

f. Pressure

The maximum pressure exerted with the surface of the crystal over the substrate ($P_{exfoliation}$) may be estimated by dividing the crystal surface area extracted from episcopy images by the force exerted given by the dinamometer gauge ($F_{exfoliation}$). A wide range of pressures were surveyed by using the same crystal at different applied forces. In general, an average pressure of 0.5 MPa ($F_{exfoliation}$ = 1.5 N in average crystal surfaces of 3 mm^2) was found out to yield highest flake densities and thinner flake profiles in the non-sliding mode. However, it is important to note that due to inhomogeneities and deviations from a perfectly flat surface,

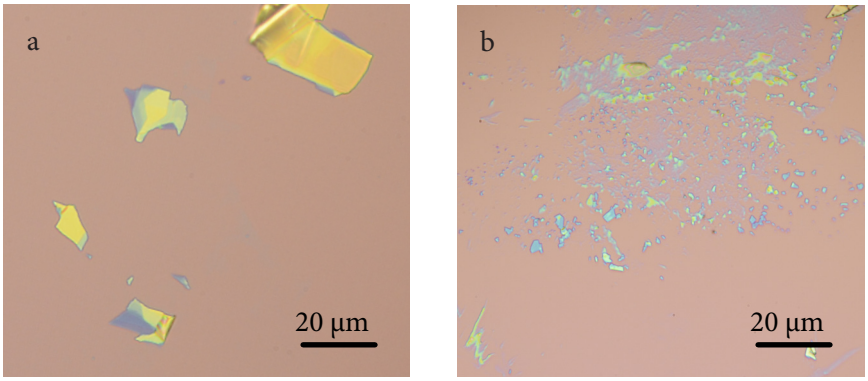

Figure 7.13 High pressure exfoliation tests of TaS_2 crystals : **a**. $P_{exfoliation}$ = 0.9 MPa, v_s = 3 mm·s^{-1}, a_s = 4 mm·s^{-1}, Δl = 0.2 cm; **b**. $P_{exfoliation}$ = 1.7 MPa, v_s = 3 mm·s^{-1}, a_s = 4 mm·s^{-1}, Δl = 0.5 mm

the contact surface was smaller than that observed by optical microscopy, hence pressure values could be easily underestimated. Pressures over 0.5 MPa normally caused thicker chunks of crystal to exfoliate on the substrate as illustrated in Figure 7.13a.

In addition it was important to adjust Δl to the applied pressure in order to control the sliding movement of the crystal along the substrate. In other words, if a non-sliding mode test was to be performed, the applied pressure needed to be high enough to fix the crystal firmly to the surface. Typically, it was observed that pressure of around 0.5 MPa was sufficient to prevent the TaS_2 crystal form sliding with jog step sizes of up to $\Delta l \sim 0.2$ mm. Longer Δl required higher applied pressures or otherwise the back and forth sliding movement generally caused the thinner layers to break and roll up into amorphous dust. An example of this scenario is shown in Figure 7.13 where 1.7 MPa was not a sufficiently high pressure to keep the crystal in place upon setting a step size of Δl = 0.5 mm.

g. Crystal orientation

The two orthogonal displacement shearing directions provided by the XYZ motorized stage inspired the exploration of the crystallographic-direction-dependent exfoliation of a TaS_2 crystal. In this way, two consecutive press and shear exfoliation tests were performed in the same conditions and with same

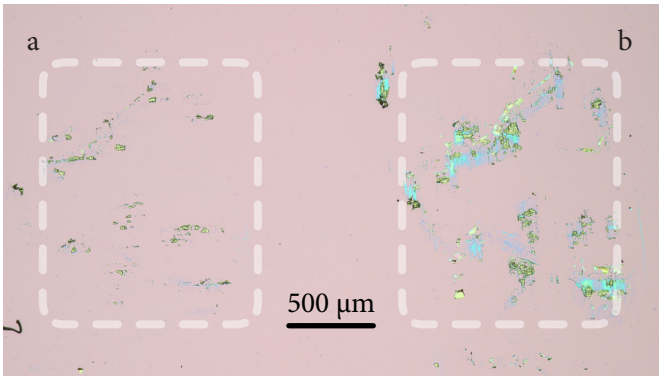

Figure 7.14 Low magnification optical microscopy image illustrating the dependence of the exfoliation result with respect to the shearing direction. While the *x* actuaator was used for the deposition **a**, **b** was performed by operatin the *y* actuator.

crystal and substrate surfaces. Figure 7.14 shows a preliminary result that confirms that exfoliation is indeed dependent on the shearing direction. Whilst deposition was enhanced in one of the orthogonal directions tested, almost no deposition occurred in the other. Nevertheless, further experiments need to be conducted in order to cover a wider range of orientations and, more importantly in order to identify the exfoliation directions with the crystallographic lattice vectors. Future single crystal X-Ray diffraction studies will be performed in order to ascertain the optimum exfoliation shearing direction.

2.3 Press and shear *vs.* PDMS exfoliation

Overall, the press and shear methodology allowed for an efficient surface contact, an extended layer adsorption on the substrate and the deposition of homogeneous large surface area TaS_2 layers. However, most importantly, the shear movement herein introduced appeared to enhance the cleavage of very thin flakes. This could be confirmed by scanning selected flakes with an AFM. Patches as thin as ~ 1.2 nm could be found in this way. Figure 7.15 shows an example of a large area of a Si/SiO_2 (285 nm) substrate with a high density of flakes of thickness < 4 nm. At this stage it is risky to establish a direct comparison between flake thickness and number of layers. After the first claim made by Novoselov *et al.* of the existence of a 'dead layer',[170] many have reported a disagreement between the thickness of

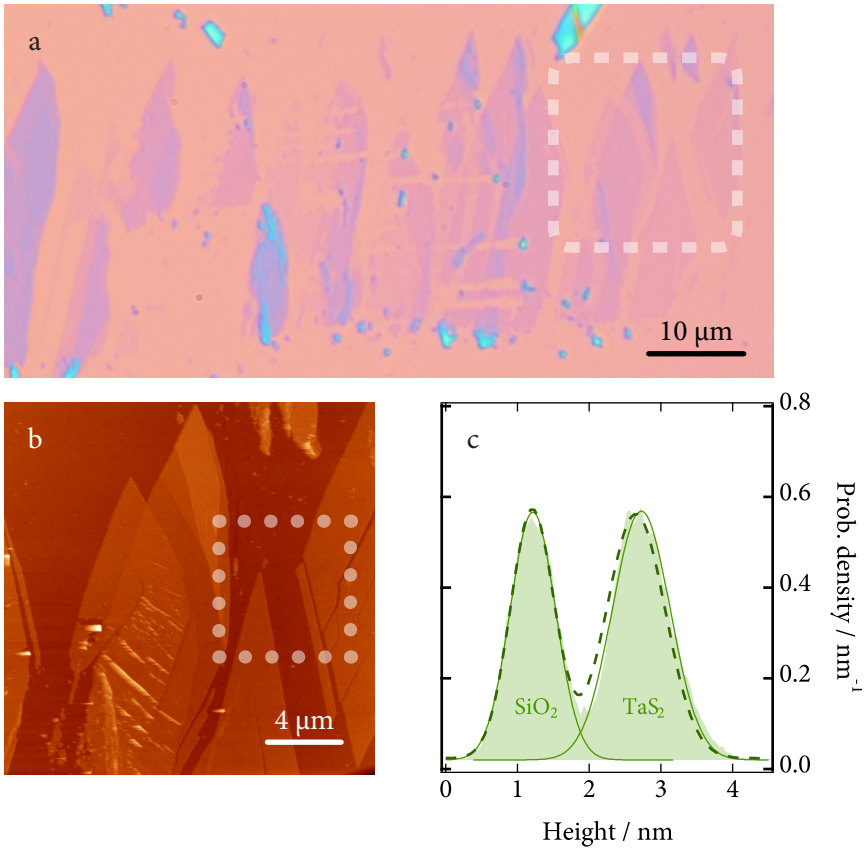

Figure 7.15 Atomically thin TaS_2 flakes deposited on Si/285 nmSiO2 by the press and shear method ($P_{exfoliation}$ = 0.5 MPa, v_s = 3 mm·s^{-1}, a_s = 4 mm·s^{-1}, Δl = 0.2 cm). **a**. Optical microscopy image of a region of the substrate displaying a high density of atomically thin flakes. **b**. AFM image of the region highlighted in **a** by the dashed box. **c**. Probability density distribution of heights inside the dotted box in **b** . In this particular image a flake thickness of 1.5 ± 0.5 nm may be estimated.

a monolayer and the lattice parameters of specific bi-dimensional crystals due to surface adsorbate effects.[174] However, being completely accurate, in our case there was no direct evidence of the presence of a solvent layer captured between the flakes and the SiO_2. In this way a safe hypothesis would be to state that 1.2 - 1.5 nm thick flakes correspond to a bilayer TaS_2 taking into consideration that a single layer packs with an inter-layer distance of approximately 0.6 nm.[96] Further studies to evaluate the exact correspondence between the AFM-measured thickness and

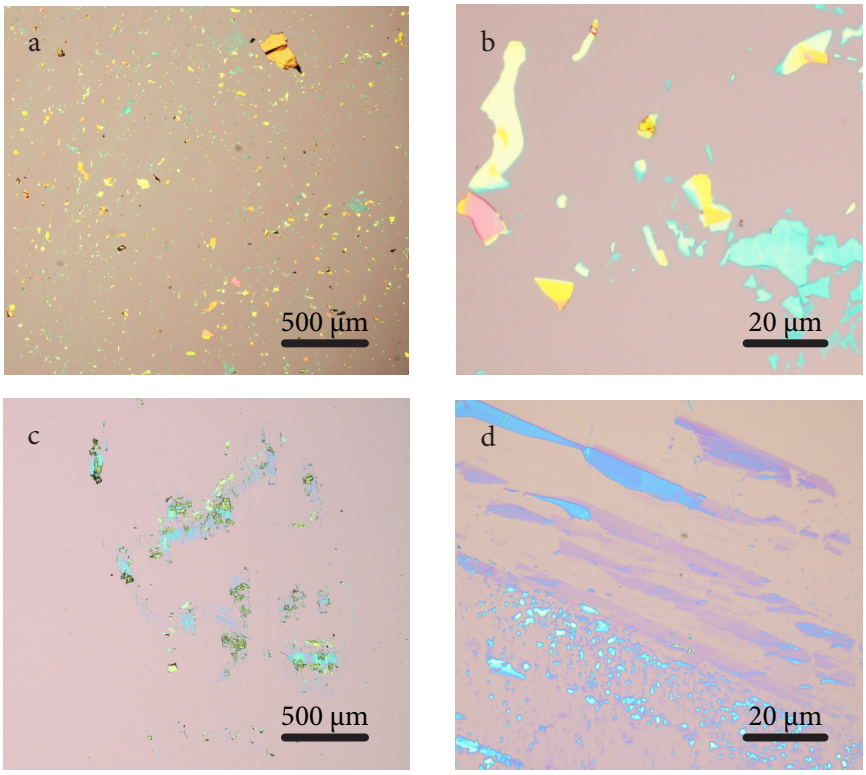

Figure 7.16 High and low magnification images comparing the PDMS-stamp micromechanical (**a**, **c**) and the press and shear (**b**, **d**) exfoliation methods..

the number of layers are currently being conducted by the use of direct high resolution imaging techniques such as HR-TEM.

The truth is that owing to the press and shear exfoliation method, this is the first time that such a low profile has been measured in exfoliated TaS_2 flakes. The direct comparison with the results yielded by the established PDMS method suggested that whilst a greater coverage and slightly higher flakes densities were obtained by the reference method, thinner layers were afforded by the method herein introduced. As a matter of fact, exfoliation experiments carried out by the micromechanical method using PDMS stamps permitted obtaining flakes, which were 4 nm in height at thinnest. Figure 7.16 shows optical images of representative flakes deposited by the two methods. Note that the optical contrast corresponding to the higher flakes in panel **d** corresponds to the thinner part in panel **b**.

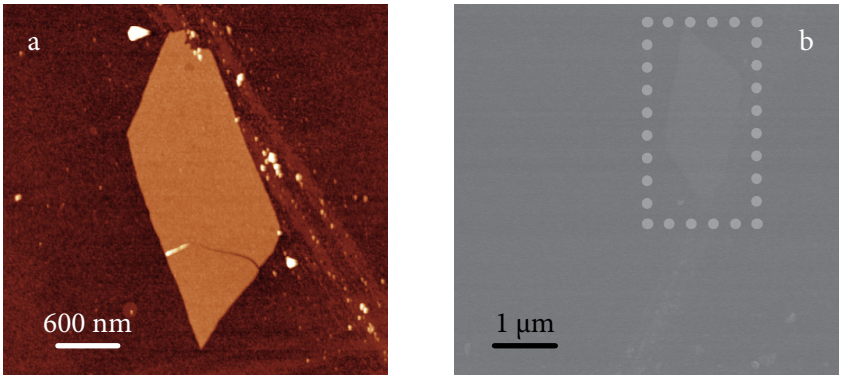

Figure 7.17 Comparison of the visibility of the same TaS_2 flake deposited by the press and shear technique on Si B p-doped as seen by AFM (**a**) and SEM (**b**, inside the dotted box).

3 Detection and characterization techniques

Hitherto, it has been demonstrated that the press and shear technique is a powerful technique for the clean deposition on substrates of large surface area atomically thin TaS_2 flakes. However, if one intends to make any use of these two-dimensional ultrathin crystals a fast, reliable and non-destructive way to identify the atomically thin layers is required. Though matching the accuracy of the AFM technique in the determination of flake thickness is obviously something pretentious, it should be easy to find an alternative in terms of a fast flake detection. SEM being a very fast scanning technique, it lacks sensitivity for comfortable flake recognition (see Figure 7.17)

Optical microscopy on the contrary turns out to be a very useful technique for this purpose. In particular, it has already been mentioned that the TaS_2 flakes exhibit particularly high optical contrast when deposited over a Si surface coated with a hundreds of nanometres thick SiO_2 layer. In addition, the presence of this thick silicon dioxide layer between the pure silicon and the deposited material yields a apparent colour that depends on the flake thickness due to a light interference effect.[206] This effect reveals the presence of the thinner crystals by conferring them a very faint yet detectable optical contrast.

206 Kvavle, J.; Bell, C.; Henrie, J.; Schultz, S.; Hawkins, A. *Optics Express* **2004,** *12,* 5789.

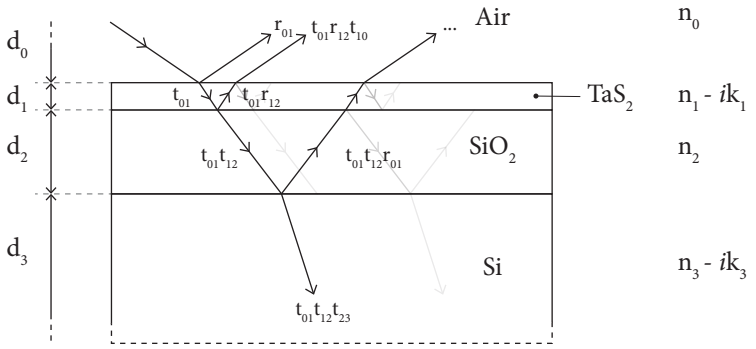

Figure 7.18 Scheme illustrating possible light ray transmission (*t*) and reflection (*r*) pathways across a multilayer structure consisting ins a TaS_2 layer deposited on *top* of a Si/SiO_2 substrate. Nomenclature is consistent with Equation 7.2.

In order to quantitatively study the light interference, the thickness (*d*) dependent optical contrast (*C*) between the flake and the SiO_2 substrate was calculated for different illumination wavelengths (λ) as previously reported.[174, 176, 207] Equation 7.1 shows how the optical contrast may be calculated from the reflected intensities coming from the flake (I_{flake}) and the substrate ($I_{substrate}$).

$$C(d,\lambda) = \frac{I_{flake} - I_{substrate}}{I_{flake} + I_{substrate}}$$

Equation 7.1 Optical contrast

The experimental value of *C* may be compared to the contrast calculated using the model proposed by Blake and co-workers based on Fresnel's laws.[208] This theoretical model accounts for the light intensity reflected either from the substrate or from the flake (Figure 7.18 illustrates possible light ray pathways in the presence of a TaS_2 layer on top of a Si/SiO_2 substrate) as described by Equation 7.1.

---

207 a) Benameur, M. M.; Radisavljevic, B.; Héron, J. S.; Sahoo, S.; Berger, H.; Kis, A. *Nanotechnology* **2011,** *22,* 125706. (b) Castellanos-Gomez, A.; Navarro-Moratalla, E.; Mokry, G.; Quereda, J.; Pinilla-Cienfuegos, E.; Agraït, N.; van der Zant, H. S.; Coronado, E.; Steele, G. A.; Rubio-Bollinger, G. *Nano Res.* **2013,** *6 (3),* 191–199. (c) Li, H; Lu, G.; Yin, Z.; He, Q.;Li, H.; Zhang, Q.; Zhang, H. *Small* **2012,** *8(5),* 682–686.

208 Blake, P.; Hill, E. W.; Neto, A. H. C.; Novoselov, K. S.; Jiang, D.; Yang, R.; Booth, T. J.; Geim, A. K. *App. Phys. Lett.* **2007, 91, 063124.**

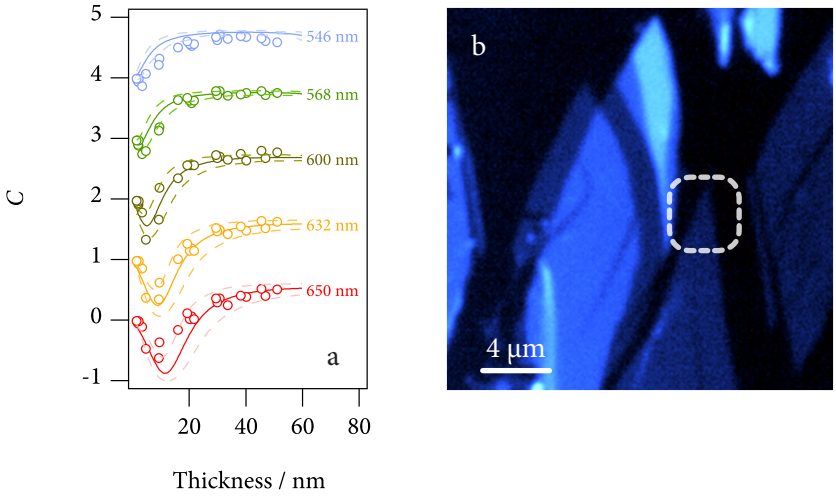

Figure 7.19 a. *C* (*markers*) measured on 2H-TaS_2 flakes as a function of their thickness for illumination at 546 nm < λ < 650 nm. The solid lines correspond to the Fresnel-law-model calculation using the refractive index reported in the literature.209 The different λ sets have been shifted vertically by 1, 2, 3 and 4 units for clarity. The uncertainty in *C* due to a ± 10% variation in the real and imaginary parts of the refractive index is indicated by the dashed lines. **b**. Optical contrast image at λ = 600 nm TaS_2 flakes. The flake region marked by the dashed box is 1.4 nm thick, measured by AFM in contact mode, and shows a negative optical contrast of -0.03.

Here the subscript labels 0, 1, 2 and 3 refer to the different media (air, TaS_2, SiO_2 and Si respectively), $\Phi_j = 2\pi\tilde{n}_j d_j/\lambda$ is the phase shift introduced by medium j, $\tilde{n}_j(\lambda) = n_j - i\kappa_j$ is the complex refractive index of the medium j, d_j is the thickness of medium j, and $r_{jk} = (\tilde{n}_j - \tilde{n}_k)/(\tilde{n}_j + \tilde{n}_k)$ is the amplitude of the reflected path in the interface between the media j and k.

$$I_{substrate}(\lambda) = \left| \frac{r_{02} + r_{23} e^{-2i\Phi_2}}{1 + r_{02} r_{23} e^{-2i\Phi_2}} \right|^2$$

$$I_{flake}(\lambda) = \left| \frac{r_{02} e^{i(\Phi_1+\Phi_2)} + r_{12} e^{-i(\Phi_1-\Phi_2)} + r_{23} e^{-i(\Phi_1+\Phi_2)} + r_{01} r_{12} r_{23} e^{i(\Phi_1-\Phi_2)}}{e^{i(\Phi_1+\Phi_2)} + r_{01} r_{12} e^{-i(\Phi_1-\Phi_2)} + r_{01} r_{23} e^{-i(\Phi_1+\Phi_2)} + r_{12} r_{23} e^{i(\Phi_1-\Phi_2)}} \right|^2$$

Equation 7.2 Flake and substrate intensities calculated by the model in ref. 208.

In order to perform this quantification, 24 2H-TaS_2 flakes prepared by the pres and shear exfoliation of bulk crystals **6** were firstly scanned with an AFM and then analysed under selected illumination wavelengths. The thickness of the flakes measured was in the range of 1.4 to 51 nm (which roughly corresponds to 2 to 85 layers) A narrow illumination band was obtained by the use of passband optical filters spanning the visible spectrum (546, 568, 600, 632 and 650 nm). The measured optical contrast shown in Figure 7.19a, was found to accurately follow the model described by Equation 7.2 using a λ-dependent complex refractive index extracted from permittivity data reported in the literature for bulk 2H-TaS_2 crystals.[209] Notice that for crystals thinner than 20 nm the optical contrast changes sign depending on the illumination wavelength, making it easy to discriminate them from thicker ones especially at the longer wavelengths ($\lambda \geq 600$ nm). It is therefore remarkable that the optical contrast is strongly dependent on the illumination wavelength. Figure 7.19b shows an optical contrast image at $\lambda = 600$ nm of the atomically thin TaS_2 flakes. The darker regions correspond to the SiO_2 substrate, whereas the lighter ones depict the presence of TaS_2 crystals. In this image, the blue colour indicates a negative value of *C*, and the intensity is quantitatively dependent on the thickness of the crystal. In this way, the quantitative analysis of the optical contrast of the flakes under different illumination wavelengths provides a fast and reliable way not only to discriminate atomically thin flakes (< 20 nm) from thicker flakes (> 20 nm) but also to provide an estimation of the thickness.

Alternatively to optical microscopy, Raman spectroscopy has been successfully employed to characterize the thickness of several atomically thin materials such as graphene and MoS_2.[210, 211] However, the technique has also proved unfruitful in other selected case studies such as mica or $NbSe_2$ since they are damaged during the Raman spectroscopy measurements.[176, 212] Nevertheless, Raman experiments were conducted to attempt both the identification of 2H-TaS_2 flakes and for the determination of their thickness. Figure 7.20a shows the Raman spectra measured of selected 2H-TaS_2 flakes with varying thickness. The spectra show

209 Beal, A.R.; Hughes, H. P.; Liang, W. Y. *J. Phys. C: Sol. Stat. Phys.* **1975,** *8 (24),* 4236-4234.

210 Ferrari, A.; Meyer, J.; Scardaci, V.; Casiraghi, C.; Lazzeri, M.; Mauri, F.; Piscanec, S.; Jiang, D.; Novoselov, K.; Roth, S. *Phys. Rev. Lett.* **2006,** *97,* 187401.

211 a) Korn, T. ; Heydrich, S.; Hirmer, M.; Schmutzler, J.; Schüller, C. *Appl. Phys. Lett.* **2011,** *99,* 102109. (b) Mak, K. F.; Lee; Hone, J.; Shan, J.; Heinz, T. F. *Phys. Rev. Lett.* **2010,** *105,* 136805.

212 Staley, N.; Wu, J.; Eklund, P.; Liu, Y.; Li, L.; Xu, Z. *Phys. Rev. B* **2009,** *80,* 184505.

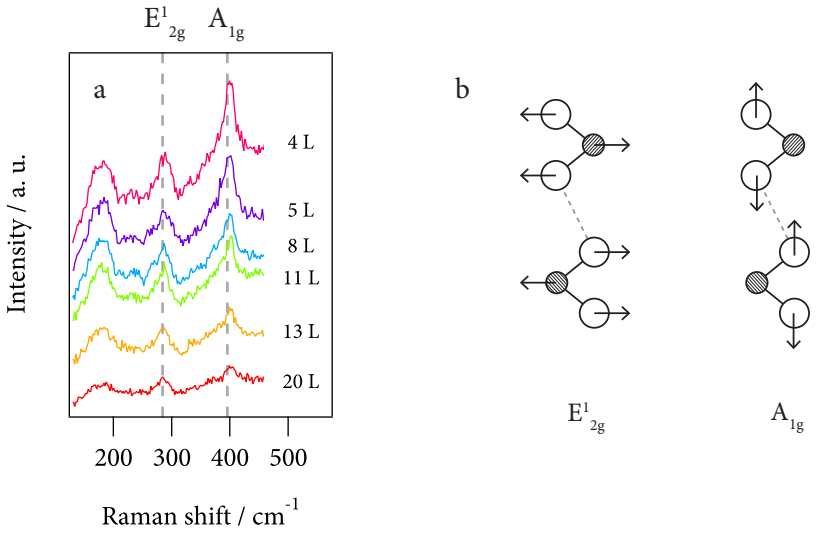

Figure 7.20 a. Raman spectra measured for 2H-TaS_2 flakes with thickness ranging from four layers to 20 layers. **b**. Schematic representation of the vibration modes that correspond to the most prominent peaks at **a**.

three prominent peaks around 180 cm^{-1}, 280 cm^{-1} (E^1_{2g} mode) and 400 cm^{-1} (A_{1g} mode), which are characteristic of 2H-TaS_2.[213] An explicative scheme illustrating the lattice vibrations of the different modes is included in Figure 7.20b. The peak around 280 cm^{-1} corresponds to the excitation of a vibrational mode in which the S and Ta atoms oscillate in anti-phase, parallel to the crystal surface. On the other hand, the peak around 400 cm^{-1} corresponds to the vibration of the S atoms, in anti-phase, perpendicularly to the crystal surface while the Ta atoms are fixed. The Raman peak near 180 cm^{-1} is due to a two-phonon scattering process. The full-range (100 - 580 cm^{-1}) Raman spectra exhibits another prominent peak at 519 cm^{-1} due to the vibration of the lattice of the silicon substrate underneath. This peak has been left out of the range shown in the figure for clarity.

Following, the potential relationship between the flake thickness and the Raman scattering intensity was explored. For this reason a μ-Raman probe was used to explore different thickness flakes. Figure 7.21 shows the thickness

213 Hangyo, M.; Nakashima, S.-I.; Mitsuishi, A. *GFER* **1983,** *52,* 151–159.

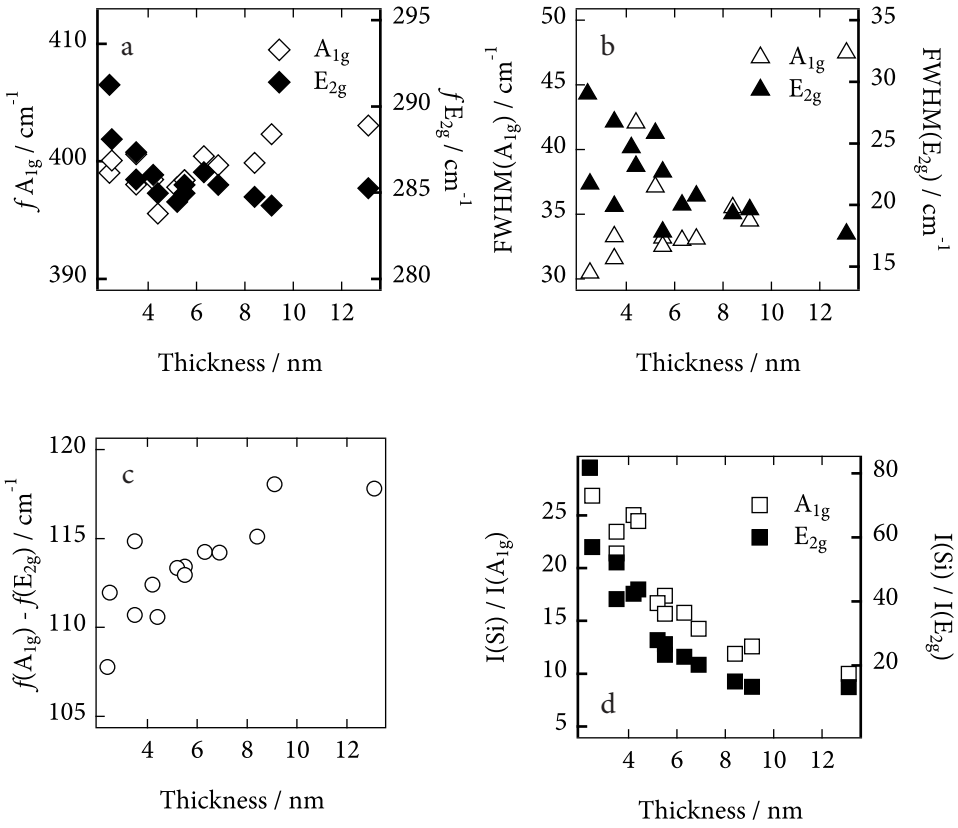

Figure 7.21 Thickness dependence of the Raman frequency shift (**a**) and FWHM (**b**) of the A_{1g} and E^1_{2g} Raman modes. **c**. Frequency difference between the A_{1g} and E_{2g} Raman modes. **d**. Raman intensity ratio between the Si peak (at 521 cm^{-1}) and the A_{1g} and E_{2g} peaks.

dependence of a selection of Raman features. Whereas the frequency shift and the full-width-at-half-maximum (FWHM) of the A_{1g} and E_{2g} Raman modes do not seem to be at all related to the number of layers, it may be clearly appreciated how the ratio between the intensity of the Si peak (at 521 cm^{-1}) and the A_{1g} and E_{2g} peaks both increase upon decreasing the number of layers of the probed flake. The frequency difference between the A_{1g} and E_{2g} Raman modes also exhibit a linear proportionality with the number of layers present if the flakes. It is important to highlight that as for other TMDCs, some sensitivity to the Raman laser beam was also exhibited by the TaS_2 flakes. In this way, upon performing

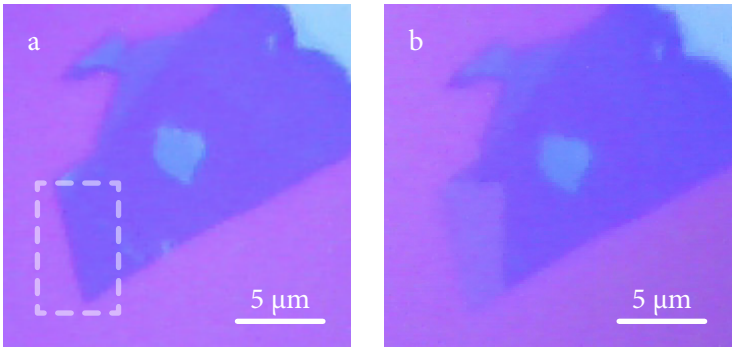

Figure 7.22 Laser oxidation of a 2H-TaS_2 flake by performing a Raman scanning (incident power on the sample 10 mW) experiment on the flake shown in **a** in the region marked by the dashed rectangle. The result of the exposure to the laser is shown in **b**.

experiments with long exposure times or high irradiation powers, the flakes were irreversibly damaged as seen by a change in the optical contrast in the focus spot of the laser beam (Figure 7.22). Yet, no apparent change in the height profile as measured by AFM could be detected. By contrast, the appearance of a strong photoluminescence emission band around 555 nm suggested that some oxidation to Ta_2O_5 had occurred.[214]

On a final note, it has been previously observed in other transition metal dichalcogenides how the intensity of the distinct Raman modes may vary as the angle between the linearly polarized incident beam and the scattered signal is modified.[215] This can be used to confirm the origin of the Raman peaks. In the TaS_2 case, it could be observed that while the intensity of the E_{2g} mode does not depend on the angle between the excitation and detection, the A_{1g} mode presents its maximum intensity for parallel excitation and detection and it vanishes for cross polarized excitation and detection in agreement with that reported for other TMDC flakes,[216] confirming that the Raman signal comes from an analogous crystal (see Figure 7.23).

214 Zhu, M.; Zhang, Z.; Miao, W. *Appl. Phys. Lett.* **2006,** *89,* 021915.

215 Wu, Y.; An, M.; Xiong, R.; Shi, J.; Zhang, Q. M. *J. Phys. D: Appl.Phys.* **2008,** *41,* 175408.

216 a) Plechinger, G.; Heydrich, S.; Eroms, J.; Weiss, D.; Schuller, C.; Korn, T. *Appl. Phys. Lett* **2012,** *101,* 101906–101906–3. (b) Plechinger, G.; Heydrich, S.; Hirmer, M.; Schrettenbrunner, F. X.; Weiss, D.; Eroms, J.; Schuller, C.; Korn, T. *Proc. SPIE 8463, Nanoengineering: Fabrication, Properties, Optics, and Devices IX* **2012,** *DOI:10.1117/12.928068.*

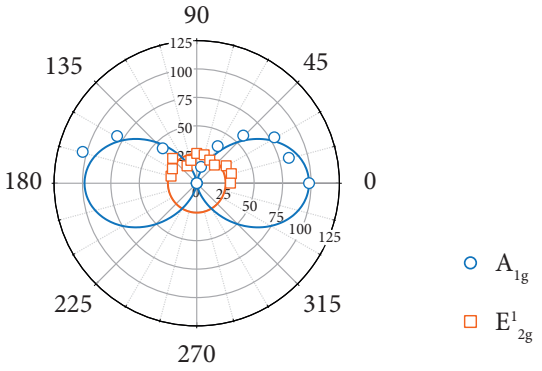

Figure 7.23 Intensity of the A_{1g} and E_{2g} Raman peaks as a function of the angle (°) between linearly polarized excitation and detection.

4 Physical properties of thin TMDC flakes

The isolation of TMDC flakes has important technological implications due to their idiosyncratic properties that may not be found in the bulk materials. Already back in the 60s, the synthesis of crystals of MoS_2 made out of only several layers by micromechanical cleavage was reported,[217] and optical absorption and photoconductivity of these films were studied.[218] More recently, field-effect transistor devices have been fabricated with MoS_2 flakes as thin as 8 or 0.8 nm.[219, 220] Interestingly, their use in integrated circuits for logic operations and also for gas sensing applications has been postulated.[221, 222] Furthermore, exfoliated flakes of the same material have also been used in the fabrication of phototransistors which the authors claim to have an improved photo-responsivity with respect to graphene-based devices.[223]

217 Frindt, R. F. *J. Appl. Phys.* **1966,** *37,* 1928–1929.

218 Frindt, R. F.; Yoffe, A. D. *P. Roy. Soc. A- Math. Phy.* **1963,** *273,* 69–83.

219 Ayari, A.; Cobas, E.; Ogundadegbe, O.; Fuhrer, M. S. *J. Appl. Phys* **2007,** *101,* 014507.

220 a) Radisavljevic, B.; Radenovic, A.; Brivio, J.; Giacometti, V.; Kis, A. *Nature Nanotech.* **2011,** *6,* 147–150. (b) Radisavljevic, B.; Whitwick, M. B.; Kis, A. *ACS Nano* **2011,** *5,* 9934–9938.

221 Radisavljevic, B.; Whitwick, M. B.; Kis, A. *ACS Nano* **2011,** *5,* 9934–9938.

222 Li, H.; Yin, Z.; He, Q.; Li, H.; Huang, X.; Lu, G.; Fam, D. W. H.; Tok, A. I. Y.; Zhang, Q.; Zhang, H. *Small* **2012,** *8,* 63–67.

223 Yin, Z.; Li, H.; Li, H.; Jiang, L.; Shi, Y.; Sun, Y.; Lu, G.; Zhang, Q.; Chen, X.; Zhang, H. *ACS Nano* **2012,** *6,* 74–80.

However, atomically thin MoS_2 flakes have also inspired science at a more fundamental level. For instance, the elastic properties measured for MoS_2 nanosheets suggest and extraordinarily high Young modulus (E = 0.33 ± 0.07 TPa).[224] In addition, it has also been observed that photoluminescence arises from the atomically thinning of MoS_2, which has been explained as a transition from an indirect bandgap to a direct one in going from multilayer to monolayer.[225] However, much has also been already reported on the effect that dimensionality reduction has on the properties of other atomically thin crystals.[226]

A particularly interesting property that has been drawing attention recently in this field is superconductivity. Much of this attention may have triggered by recent studies that have suggested that it may be possible to induce superconductivity in graphene by garnishing the surface of graphene with the right species of dopant atoms or, alternatively, by using ionic liquid gating.[227, 228] However, reported experiments have failed to show direct evidence of superconducting behaviour in exfoliated graphene. Generally speaking, only via the bottom-up approach have some signs of the existence of superconductivity at the two-dimensional limit been observed. Initial experiments were devoted to the study of pure metal layers fabricated by evaporation. In this way *in-situ* grown single layer films have delivered evidence of superconductivity in bi-dimensional systems.[229] More recently, the bottom-up tactic has also been utilized for the epitaxial growth of higher T_{SC} superconducting thin films and even single layers.[230]

224 Castellanos-Gomez, A.; Poot, M.; Steele, G. A.; Van Der Zant, H. S. J.; Agraït, N.; Rubio-Bollinger, G. *Adv Mater.* **2012,** *24,* 772–775.

225 a) Splendiani, A.; Sun, L.; Zhang, Y.; Li, T.; Kim, J.; Chim, C.-Y.; Galli, G.; Wang, F. *Nano Lett.* **2010,** *10,* 1271–1275. (b) Eda, G.; Yamaguchi, H.; Voiry, D.; Fujita, T.; Chen, M.; Chhowalla, M. *Nano Lett.* **2011,** *11,* 5111–5116.

226 a) Lee, C.; Li, Q.; Kalb, W.; Liu, X. Z.; Berger, H.; Carpick, R. W.; Hone, J. *Science* **2010,** *328,* 76–80. (b) Mak, K.; Lee, C.; Hone, J.; Shan, J.; Heinz, T. *Phys. Rev. Lett.* **2010,** *105,* 136805. (c) Ramakrishna Matte, H. S. S.; Gomathi, A.; Manna, A. K.; Late, D. J.; Datta, R.; Pati, S. K.; Rao, C. N. R. *Angew. Chem. Int. Ed.* **2010,** *49,* 4059–4062. (d) Chiritescu, C.; Cahill, D. G.; Nguyen, N.; Johnson, D.; Bodapati, A.; Keblinski, P.; Zschack, P. *Science* **2007,** *315,* 351–353.

227 Profeta, G.; Calandra, M.; Mauri, F. *Nat. Phys.* **2012,** *8,* 131–134.

228 Nandkishore, R.; Levitov, L. S.; Chubukov, A. V. *Nat. Phys.* **2012,** *8,* 158–163.

229 a) Qin, S.; Kim, J.; Niu, Q.; Shih, C.-K. *Science* **2009,** *324,* 1314. (b) Zhang, T.; Cheng, P.; Li, W.-J.; Sun, Y.-J.; Wang, G.; Zhu, X.-G.; He, K.; Wang, L.; Ma, X.; Chen, X.; Wang, Y.; Liu, Y; Lin, H.-Q.; Jia, J.-F.; Xue, Q.-K. *Nat. Phys.* **2010,** *6,* 104.

230 a) Li, Q.; Si, W.; Dimitrov, I. K. *Rep. Prog. Phys.* **2011,** *74,* 124510. (b) Liu, D.; Zhang, W.; Mou, D.; He, J.; Ou, Y.-B.; Wang, Q.-Y.; Li, Z.; Wang, L.; Zhao, L.; He, S.; Yingying Peng, Xu Liu, Chaoyu Chen, Li Yu, Guodong Liu, Xiaoli Dong, Jun Zhang, Chuangtian Chen, Zuyan Xu, Jiangping Hu, Xi Chen, Xucun Ma, Qikun Xue, and X J Zhou. *Nat. Comm.* **2012,** *3,* 931–6.

Given the intrinsic quasi-bidimensional superconductivity exhibited by some TMDCs, one may envision a favourable scenario for the study of such properties at the atomic thickness. In this line, a theoretical study performed by first principles claimed that NbS_2 is supposed to retain metallic conductivity in its atomically thin confined state.[231] Yet, once again, in spite of the exhaustive searches for unconventional superconductivity in single layer exfoliated TMDC sheets, no strong evidence of single layer or bi-layer superconductivity has been provided. Previous studies based on $NbSe_2$ flakes have failed to prove the existence of superconductivity in freshly cleaved specimens of 3 nm in thickness.[164]

TaS_2 has traditionally also been of relevance in the study of quasi-two-dimensional superconductivity. For example, the 2H polytype has been a matter of controversy concerning the coexistence of superconductivity with a charge density wave (CDW).[232] In this context, it has been proposed that superconductivity at 2H-TaS_2 is somehow modulated by a charge density wave with chiral electronic order.[233] Regarding the superconducting behaviour of few layer TaS_2 flakes, transport experiments have been conducted in flakes as thin as 2 nm. Yet superconductivity in TaS_2 layers thinner than 8 nm could not be directly evidenced.[234]

4.1 Low-temperature electrical properties of TaS_2 flakes

Taken the previous experience obtained in the dry exfoliation of TaS_2, 2H-TaS_2 atomically thin flakes were deposited on Si/SiO_2 substrates with the objective of fabricating devices to probe their superconductivity. Besides the natural challenge of obtaining a still non-reported superconducting atomically thin TMDC flake, the realization of ultrathin superconducting layers would enable one to employ the electric field effect to control physical properties such as the superconducting transition temperature or to study the interplay between the superconductivity and the sample dimensionality. The fabrication of ultrathin flake devices was performed in collaboration with the research team Prof. Herre van der Zant from

231 Kuc, A.; Zibouche, N.; Heine, T. *Phys. Rev. B* **2011,** *83,* 245213.

232 Castro Neto, A. H. *Phys. Rev. Lett.* **2001,** *86,* 4382–4385.

233 Guillamón, I.; Suderow, H.; Rodrigo, J. G.; Vieira, S.; Rodière, P.; Cario, L.; Navarro-Moratalla, E.; Martí-Gastaldo, C.; Coronado, E. *New J. Phys.* **2011,** *13,* 103020.

234 Ayari, A.; Cobas, E.; Ogundadegbe, O.; Fuhrer, M. S. *J. Appl. Phys.* **2007,** *101,* 014507.

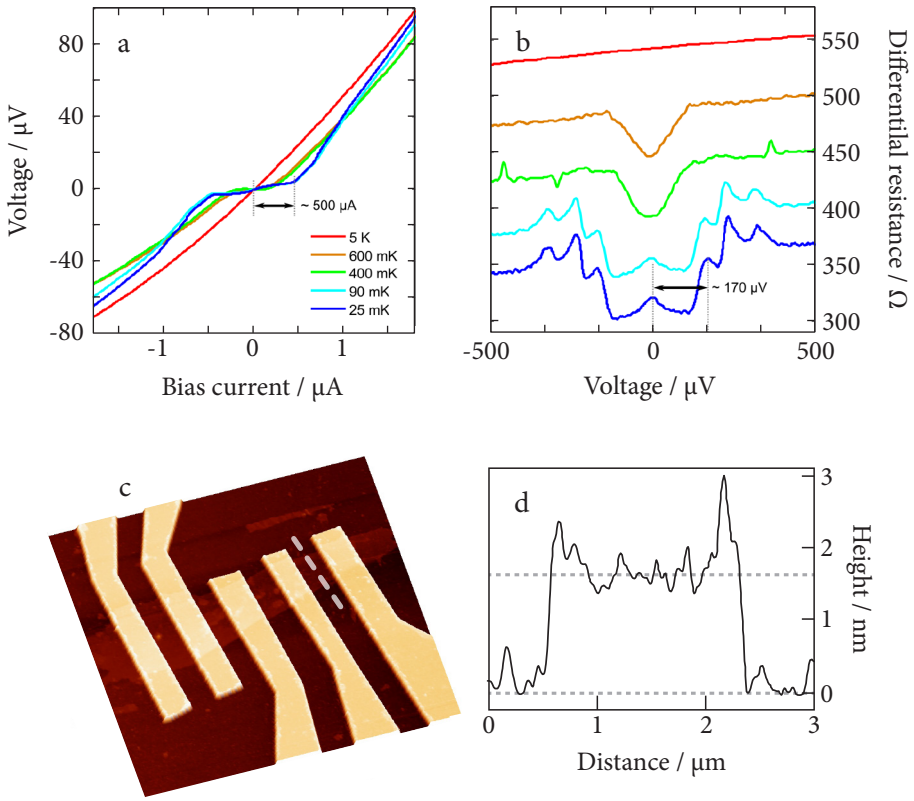

Figure 7.24 a. *I-V* curve of the device measured in four-terminal configuration at different temperatures across the superconducting phase transition. A residual resistance of 300 Ω have been subtracted to facilitate the estimation of the critical current value. **b**. Differential resistance as a function of the voltage. The superconducting gap can be estimated as ~ 170 μV. **c**. AFM image of the TaS_2 device with multiple Ti/Au electrodes. **d**. Thickness profile measured along the dashed line.

the Molecular Electronics and Devices group at the Kavli Institute of Nanoscience Delft (TU Delft, The Netherlands).

Several homogeneous flakes of thickness < 2 nm were selected by optical microscopy for device fabrication. Following, multiple electrode contacts were evaporated on to the thinner flakes by employing PMMA masking/E-beam techniques. Figure 7.24c shows an AFM image of a single-flake device made out of a 1.8 nm thick 2H-TaS_2 layer and five evaporated Ti/Au electrodes. The current-

voltage (*I-V*) curve displayed by this device is shown in Figure 7.24a. In the plot, a residual resistance of 300 Ω has been subtracted to facilitate the estimation of the critical current value. The *I-V* profiles exhibited by the device measured in the four-terminal configuration are approximately linear down to 5 K. However, at lower temperatures, they display a remarkable deviation from linearity around the zero bias current. The evaluation of the differential resistance as a function of the voltage provided with clear signs of a superconducting phase transition with a V-shape gap that starts to open at 600 mK. This permitted estimating a superconducting gap of ~ 170 μV measured at 25 mK. This gap corresponds to a T_{SC} of approximately 2 K according to the BCS theory. This contrasts with T_{SC} ~ 0.8 K of the bulk material. Though it is tempting to ascribe this enhancement to the dimensionality effect, further experiments in different thickness flakes still need to be conducted in order confirm this hypothesis.

However, a non-negligible residual resistance even for temperatures well below the critical temperature could also be observed. This may be attributed to two different causes. On the one hand, the ultrathin TaS_2 devices may behave electrically as a very disordered superconductor consisting of superconducting patches connected by regions of the material in the normal state. From the drop in resistance below T_{SC}, one can estimate that about a 20% of the material would then be in the superconducting state. The scenario reminds of that reported by Ayari *et al.* Having tested devices made out of TaS_2 nanolayers with a thickness down to 3 layers, Ayari and his co-workers concluded that layers thinner than 13 layers exhibited an insulating behaviour. [234] And even more, for sheets 13 layers thick the superconducting transition observed was not abrupt, showing several onsets, which indicated a mixed composition of patches with different critical temperatures. In the same line, this could also indicate a partial oxidation of some regions of the flake to insulating Ta_2O_5, which would give rise to the same phenomenon. On the other hand, an alternative explanation for the large residual resistance could be the invasive role of the contact electrodes. The fabrication of Ti/Au electrodes on the material could have damaged the TaS_2 flake, consequently suppressing the superconducting transition underneath the contacts. Further experiments by modifying the contact lay-out will help to rule out the latter hypothesis. Nevertheless, the conclusion that there are superconducting correlations in the atomically thin sheets holds in both cases.

5 Conclusions

In this chapter, a new and effective route for the exfoliation of challenging layered materials such as TaS_2 has been introduced. The so-called *press and shear* exfoliation has proved as a very useful tool to delaminate bulk TaS_2 crystals down to the atomically thin level. Though the question as to if real single layers are obtained still remains open, thickness values well below 2 nm are achieved. To the best of our knowledge this are the thinnest values of TaS_2 flakes reported so far. Upcoming experiment will be dedicated to the study single flakes by high resolution TEM imaging techniques as to ascertain the correspondance between AFM-measured thickness and number of layers.

Characterization has been conducted in order to ascertain the chemical nature and dimensionality of the isolated ultrathin flakes. In this way, the optical microscopy identification technique proves useful for flake detection and thickness estimation. Raman may also be used to confirm the presence the 2H-TaS_2 structure and the number of layers in selected patches, though it happens to be somehow destructive imposing a big limitation to its use.

Since the developed all-dry technique allows for the deposition of large surface area atomically thin patches, single-flake electrical devices were successfully fabricated. As a result, for the first time ever, traces of superconducting behaviour in an exfoliated material have been witnessed. The wide band gap suggests an unseen increase in the critical temperature according to the BCS theory. Future experiments will be devoted to the study of the variation of the superconducting properties with the flake thickness and also to the investigation of the potential field-effect in the superconducting transition.

The findings delivered in this chapter foretell the arrival of new low-dimensionality physical phenomena, confirming the idea that graphene is indeed not alone.[235]

235 Editorial, *Nat. Nanotec.* **2012**, *7*, 683.

6 Experimental details

Technical specifications of the 'press and shear' setup components

The dinamomter employed was a commercial Sauter FH2 digital force gauge with a maximum load of 2 N and a nominal resolution of 0.001 N. It could be operated in either push or pull modes with a maximum precision of 0.2 % of the load. The maximum frecuency data sampling was of 2 Hz.

An MT3-Z8 XYZ motorized stage supplied by Thorlabs was used as the active substrate holder. The triple uniaxial assembly had a maximum horizontal load of 9 kg and a 4.5 kg vertical one. It included three 12 VDC Z812B servo actuators with sub-micron resolution (0.10 μm minimum achievable incremental movement and 0.4 μm minimum repeatable incremental movement, high accuracy (95 μm absolute on-axis accuracy, 0.52% maximum percentage accuracy) and 12 mm maximum travel. In addition, the micrometer head-steppers feature a maximum speed of 3 mm/sec with a maximum acceleration of 4 mm/sec^2 (± 0.125 mm/sec velocity stability, 1.5 μm bidirectional repeatability). Each actuator is operated by its own single-channel TDC001 DC servo motor controller with +15 V & -15 V drive outputs.

Mounted on the Z stage axis was a KMS kinematic mount from Thorlabs. Samples were mounted at the tip of the force gauge spindle on top of another kinematic mount (Thorlabs KMM/S) for tilt control.

Two orthogonally mounted PCE-MM 200 digital microscopes (1280 x 1024 pixels resolution and 10x to 200x magnification range) were employed for sample adjuSTMent.

General purpose and quantitative optical episcopy

General optical microscopy images were taken using a Nikon D-600 SLR camera mounted on the trinocular stage of a Nikon LV-100 optical microscope. The microscope was equipped with a Nomarski prism for DIC contrast imaging and with 5 Nikon PLAN FLUOR EPI objectives: 5× (numerical aperture, NA =

0.15), 10× (NA = 0.3), 20× (NA = 0.45), 50× (NA = 0.8), 100× (*air*, NA = 0.9). The calibration of the SLR camera with the 5× and the 10× objective lenses was performed with a reference millimetre reticle, resulting in a lateral space calibration value of 95.3 μm·px^{-1} and 47.8 μm·px$^{-1.}$ The higher power lenses were calibrated using an AFM calibration grid with a period of 10 μm, resulting in the following values: 238.0 μm·px^{-1}, 95.2 μm·px^{-1} and 47.4 μm·px^{-1} for the 20×, the 50× and the 100× objectives respectively.

Micrographs for quantitative optical contrast evaluation were taken with a Nikon Eclipse LV100 optical microscope under normal incidence with a 50× objective (NA = 0.55) equipped with a digital camera Edmund Optics EO-1918C 1/1.8" (CMOS 2560 × 1920 px, 8-bit).[236] The illumination wavelength was selected by means of nine narrow band-pass filters (10 nm full width at half maximum FWHM) with central wavelengths 450 nm, 500 nm, 520 nm, 546 nm, 568 nm, 600 nm, 632 nm, 650 nm y 694 nm from Edmund Optics.

Raman spectroscopy

A micro-Raman spectrometer (Renishaw in via RM 2000) was used in a backscattering configuration excited with a visible laser light (λ = 514 nm) to characterize the ultrathin layers. The spectra were collected through a 100× objective and recorded with 1800 lines/mm grating providing the spectral resolution of ~ 1 cm^{-1}. To avoid laser-induced modification of the samples, all spectra were recorded with a power level P = 0.5 – 1 mW and an accumulation time of one second.

Substrate cleaning and activation protocol

Si and Si/SiO_2 substrates were cleaned and simultaneously activated by three 10 min sonication cycles in diluted basic piranha solution: NH_4OH (*conc.*) : H_2O_2 : H_2O, 1 : 1 : 2 (v/v/v). Between each sonication cycle the substrates were rinsed in water and immersed in a fresh aliquot of piranha solution. The substrates were

236 *Truecolor*: 256×256×256

finally washed by sonication in ultrapure milli-Q water during 10 min. Finally the substrate were thoroughly blow dried before used.

Other substrates with metal coatings, such as Au-coated Si, were more prone to be damaged by the ultrasound treatment. In these cases the substrates were typically cleaned by rinsing thoroughly in iPrOH or EtOH and finally blow dried.

Contact angle experiments

Advancing and receding water contact angle measurements were performed by the "add and remove volume" method in a Ramé-hart Model 200 Standard Goniometer with Dropimage Standard v2.3, equipped with an automated dispensing system. This device includes software as well as a fiber optic illuminator, 3-axis leveling stage, high-speed F4 Series digital camera, micro-syringe fixture and assembly for manual dispensing. The system is improved with an automated dispensing system and manual tilting base.

Device fabrication

The fabrication of ultrathin flake devices was entirely accomplished in the facilities of the Kavli Nanolab (part of the Van Leeuwenhoek Laboratory at TU Delft, The Netherlands).

In order to allow for the fabrication of devices out of the TaS_2 atomically thin flakes, the deposition was carried out in special binary-code-marked substrates with a peripheral set of gold pads. The samples were inspected by optical microscopy and a collection of flakes with the desired optical contrast were selected. Optical micrographs of these flakes were taken, making sure that four of the binary code markers were visible in the picture for later pattern alignment. Four additional low-magnification reference pictures were taken. Following, the electrode pattern was designed by making use of the optical high and low magnification reference pictures taken in advance. Four terminal devices were designed by drawing paths out of the periphery gold pads and on to each individual flake. The electrodes were designed so tha they were evenly spread across the surface of the flake. More-terminal devices could designed in the larger flakes.

Next, the substrate is spin coated with a double layer resist: 1) 495K A6 PMMA spin coated at 4500 rpm and baked at 140 ºC for 4 min; 2) 950K A2 PMMA spin coated at 4500 rpm and annealed at 140ºC for 4 min. Once cooled down, the electrode pattern was 'drawn' on the photoresist by electron-beam lithography (in an electron beam pattern generator EBPG 5000+ with a dose of 1300 $C \cdot m^{-2}$). The resist development was performed in two steps: 1) immersion in hot methyl isobutyl ketone : iPrOH, 1 : 3 for 90 sec.; 2) immersion in iPrOH.

Finally, the metallic electrodes were deposited by the use of an e-gun evaporator at a pressure of 10^{-7} mbar. A initial sticking layer of 5 nm of Ti was covered with a 50 nm Au electrode layer. The remaining unsensitized photoresist was eliminated in a lift-off satge performed by immersion in hot (55 ºC) acetone during 15 min. A pipette is employed to clean the surface of the substrate from waste debry and the substrate was thoroughly rinsed in iPrOH and blown dry.

The devices were tested to perform an estimation of the contact resistance. The test was performed in a beeper box at room temperature. In this way, a residual contact resistance of 60 Ω could be calculated by fitting the resistance measured across increaingly distant electrodes.

Illustrative images of each stage of the fabrication process have been included in Appendix 4.4.

8 Local oxidation nano-lithography on TaS_2 flakes

So far, the successful exfoliation of bulk 2H-TaS_2 crystals to atomically thin layers has been analysed in Chapter 7. Furthermore, in the final part of that section a glimpse into the fabrication of devices out of atomically thin layers has also been provided. However, In order to profit from these atomically thin layers for potential applications it is mandatory to be able to control their morphology and chemical characteristics at the nanoscale. A direct approach consists in the manipulation via Scanning Probe Microscopies (SPMs). In this chapter continues to explore the possibilities of TaS_2 exfoliated layers by the manipulation of atomically thin layers via the atomic force microscopy - local oxidation nanolithography (AFM-LON) technique.

1 Introduction

It was established over two decades ago that SPM tips could be used for surface modification.[237, 238] More recently, both STM and AFM have been proposed as a tool for mechanically processing the surface of bulk crystals.[239, 240, 241] In this line, SPM based oxidation experiments were carried out giving rise to the so-called local oxidation nano-lithographies (LONs).[242, 243] Again, despite the fact that some

237 Shedd, G. M.; Russell, P. *Nanotechnology* **1990,** *1,* 67–80.

238 Marrian, C.R.K. *Technology of Proximal Probe Lithography*, SPIE, Vol. IS 10, SPIE Optical Engineering Press, Bellingham, WA, **1993**.

239 Park, J. B.; Jaeckel, B.; Parkinson, B. A. *Langmuir* **2006,** *22,* 5334–5340.

240 Wang, C.; Shang, G.; Qiu, X.; Bai, C. *Appl. Phys. A* **1999,** *68,* 181–185.

241 Hong, S. S.; Kundhikanjana, W.; Cha, J. J.; Lai, K.; Kong, D.; Meister, S.; Kelly, M. A.; Shen, Z.-X.; Cui, Y. *Nano Lett.* **2010,** *10,* 3118–3122.

242 a) Dagata, J.; Schneir, J.; Harary, H. H.; Evans, C. J.; Postek, M. T.; Bennett, *J. Appl. Phys. Lett.* **1990,** *56,* 2001. (b) Snow, E.S.; Campbell, P.M. *Appl. Phys. Lett.* **1994,** *64,* 1932. (c) Campbell, P.M.; Snow, E.S.; McMarr, P.J. *Appl. Phys. Lett.* **1995,** *66,* 1388. (d) Sugimura, H.; Uchida, T.; Kitamura, N.; Masuhara, H. *Appl. Phys. Lett.* **1993,** *63,* 1288. (e) Song, H.J.; Rack, M.J.; Abugharbieh, K.; Lee, S.Y.; Khan, V.; Ferry, D.K.; Allee, D.R. J. *Vac. Sci. Technol. B* **1994,** *12,* 3720. (f) Wang, W.; Tsau, T.; Wang, K.L.; Chow, P. *Appl. Phys. Lett.* **1995,** *67,* 1295. (g) Snow, E.S.; Park, D.; Campbell, P.M. *Appl. Phys. Lett.* **1996,** *69,* 269.

243 *For a summary of the historical accounts in the field, see*: Quate, C. F. *Surf. Sci.* **1997,** *386,* 259–264. *A more recent summary may be viewed in*: Garcia, R.; Martinez, R. V.; Martinez, *J. Chem. Soc. Rev.* **2006,** *35,* 29–38.

of these techniques have been applied for processing graphene or graphene oxide flakes, little has been reported regarding ultrathin flakes of other bi-dimensional materials which are nowadays on the spotlight.[244, 245]

In the past, the oxidation of the surface of TMDC bulk crystals could be done in a very precise manner by applying electric field pulses with the tip of an STM.[239, 240] This chapter describes the manipulation of TaS_2 layers via the AFM-LON technique. The oxidation of TaS_2 affords the corresponding metal oxide, Ta_2O_5, which is a high band gap (3.7 eV) insulator widely extended in circuitry and thin-film electronic components.[246] Therefore, the exfoliation of TaS_2 crystals provided us with a source of room temperature conducting layers, which could be potentially modified at the nanoscale and with a high level of precision by the AFM-LON technique.

2 Surface oxidation performed with the tip of an AFM

LON (*aka.* anodic oxidation) is a lithography method based on the use of a conductive AFM probe for the fabrication of localized oxide nanostructures.

In order to perform the oxidation of the surface, a voltage pulse is applied through the tip. The latter induces a water meniscus to be formed by capillary condensation at the tip-surface interface. This confinement area forms an electrochemical cell where an oxidation reaction takes place. The tip is the anode, the surface is the cathode and the water acts as the electrolyte. A cartoon representation of the LON system is shown in Figure 8.1.

---

244 a) Masubuchi, S.; Arai, M.; Machida, T. *Nano Lett.* **2011,** *11,* 4542–4546. (b) Byun, I.-S.; Yoon, D.; Choi, J. S.; Hwang, I.; Lee, D. H.; Lee, M. J.; Kawai, T.; Son, Y.-W.; Jia, Q.; Cheong, H.; Park, B. H. *ACS Nano* **2011,** *5,* 6417–6424. (c) Alaboson, J. M. P.; Wang, Q. H.; Kellar, J. A.; Park, J.; Elam, J. W.; Pellin, M. J.; Hersam, M. C. *Adv. Mater.* **2011,** *23,* 2181–2184. (d) Biró, L. P.; Lambin, P. *Carbon* **2010,** *48,* 2677–2689. (e) Masubuchi, S.; Ono, M.; Yoshida, K.; Hirakawa, K.; Machida, T. *Appl. Phys. Lett.* **2009,** *94 (8),* 082107 - 082107-3. (f) Giesbers, A.; Zeitler, U.; Neubeck, S.; Freitag, F.; Novoselov, K. S.; Maan, J. C. *Sol. State Comm.* **2008,** *147,* 366–369. (g) Weng, L.; Zhang, L.; Chen, Y. P.; Rokhinson, L. P. *Appl. Phys. Lett.* **2008,** *93,* 093107.

245 a) Wei, Z.; Wang, D.; Kim, S.; Kim, S. Y.; Hu, Y.; Yakes, M. K.; Laracuente, A. R.; Dai, Z.; Marder, S. R.; Berger, C.; King, W. P.;De Heer, W. A.; Sheehan, P. E.; Riedo, E. *Science* **2010,** *328,* 1373–1376. (b) Mativetsky, J. M.; Treossi, E.; Orgiu, E.; Melucci, M.; Veronese, G. P.; Samorì, P.; Palermo, V. *J. Am. Chem. Soc.* **2010,** *132,* 14130–14136. (c) Lu, G.; Zhou, X.; Li, H.; Yin, Z.; Li, B.; Huang, L.; Boey, F.; Zhang, H. *Langmuir* **2010,** *26,* 6164–6166.

246 Nashed, R.; Hassan, W. M. I.; Ismail, Y.; Allam, N. K. *Phys. Chem. Chem. Phys.* **2013,** *15,* 1352-1357.

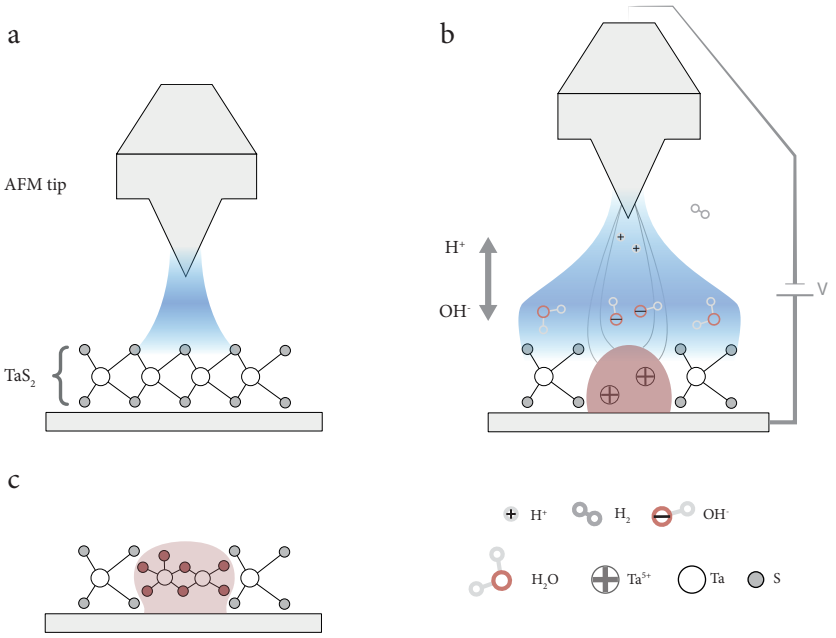

Figure 8.1 Schematic representation of the electrochemical processes by which LON is ruled: tip approach and meniscus formation on a flake (*top left*); voltage pulse represented by electric field lines and H^+/OH^- chemical species gradient established along the tip vertical axis (*top right*). The resulting oxide structure included within the target flake is highlighted in the *bottom* figure. Notice that the cartoon has been adapted to represent LON on a dichalcogenide TaS_2 single-layer flake..

An overall oxidation of the substrate surface occurs after applying a high voltage pulse (see Equation 8.1).The electrochemical reactions that occur on a metallic generic surface (M) and at the AFM tip can be expressed as shown in Equation 8.2. Whilst oxidation takes place at the metallic surface, the reduction reaction formed at the AFM tip releases hydrogen gas.

$$M + nH_2O \rightarrow MO_n + nH_2 \qquad \Delta G^0 < 0$$

Equation 8.1 Generic overall electrochemical equation occurring in the LON cell.

The nano-pattern formed by LON mainly depends on the relative humidity, the size of the water meniscus and the time and voltage pulse and is nowadays easy

$$M + nH_2O \rightarrow MO_n + 2nH^+ + 2ne^-$$
$$M^{n+} + 2nH_2O + 2ne^- \rightarrow nH_2 + 2nOH^- + M$$
$$2H^+ + 2e^- \rightarrow nH_2$$

Equation 8.2 Semi-equations of the reactions occurring at the anode (*top*) and at the cathode (*bottom*) of a generic LON electrochemical process.

to control. In this context, LON is a well-known technique in nanofabrication by means of AFM. Day *et al.* first implemented the anodic oxidation with AFM on a silicon sample.[247] Snow *et al.* later fabricated oxide structures with width less than 10 nm.[248] By modulating the voltage, Dagata and co-workers fabricated oxide motives with higher aspect ratio.[249]

But LON may be carried out on a variety of surfaces. The aim of this study was to perform LON on the surface of a TaS_2 nano-flake such as represented in Figure 8.1 where the water meniscus forms straight on top of a mono or few layer patch deposited on a substrate.

3 LON on TaS_2 flakes

On a first step, both thick and ultrathin TaS_2 flakes were conveniently transferred to freshly base-activated Si p-doped (B) substrates. The deposition of a relatively high density of very flat (RMS = 0.106 nm) ultrathin patches was achieved by the shear and press technique (see Chapter 7). Sample preparation was always performed just before performing the AFM experiment to guarantee a clean and hydrophilic surface of the TaS_2 flakes.

Note that despite the fact that the detection of ultrathin flake is favoured by the existence of a SiO_2 layer on top of the bare Si, the AFM-LON technique is best performed on a slightly conducting substrate in order to allow for efficient discharging after the electric pulse had been applied. As pointed out in the previous chapter, though single layer crystals on top of native oxide coated Si

247 Day, H. C.; Allee, D. R. *Appl. Phys. Lett.* **1993,** *62,* 2691.

248 Snow, E. S.; Juan, W. H.;Pang, S. W.; Campbell, P. M. *Appl. Phys. Lett.* **1995,** *66,* 1729.

249 Dagata, J. A. *Science* **1995,** *270,* 1625–1626.

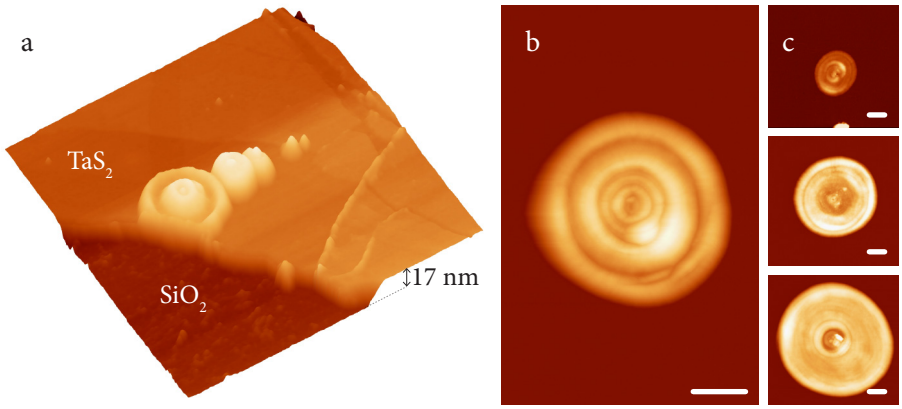

Figure 8.2 Dynamic-tip AFM-LON performed on the surface of TaS_2 flakes. **a**. 2.5 µm x 2.5 µm 3D representation of an array of 5 dots oxidized at 20 V and 35 ms on a 17nm thick flake. **b**. AFM topography image of a rippled mound performed on a thick layer of TaS_2. **c**. From *top* to *bottom*, set of 3 topography images of 3 µm x 3 µm oxidized at 21V with an increasing pulse time of 100 ms, 200 ms and 300ms, respectively. The length of the scale bars in (**b**) and (**c**) is 500 nm.

cannot be detected by the naked eye, flakes as thin as 5 nm may be spotted out by bright-field optical microscope equipped with a DIC prism. The scanning of nearby regions via AFM revealed the presence of multitude of ultrathin few layer TaS_2 patches. The flattest and more homogeneous flakes were selected for carrying out the AFM-LON experiment.

3.1 LON on thick flakes

Next, the AFM-LON experiment was carried out on selected TaS_2 patches in ambient conditions. To the date, the modification of TaS_2 surfaces via an electrical field has been done with an STM under high vacuum.[240] So to our knowledge, AFM-LON on the surface of a TaS_2 crystal remains unexplored. For this reason, preliminary AFM-LON studies were conducted on thick flakes (> 5 nm) using the classical oxidation procedure in which the tip is oscillating during the process (*dynamic-tip* LON). In these samples LON produced massive oxide formations with rippled topographies as shown in Figure 8.2. It is worthwhile noting that these features are unprecedented for an SPM-oxidized material. In fact, they have

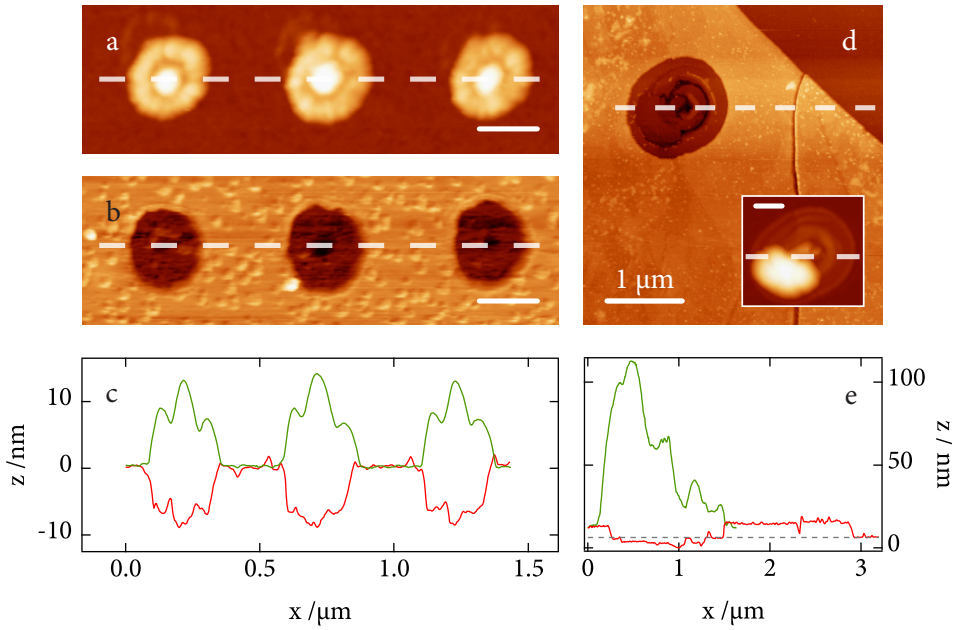

Figure 8.3 AFM topography image of an array of three oxide motifs created at 22.5 V and 45 ms (**a**) and the same three HF etched oxide motifs (**b**). **c**. Profiles of images the pristine (*green*) and etched (*red*) oxide mounds shown above. **d**. AFM topography image of an etched oxide rippled mound on a TaS_2 layer of 8 nm thick. *Inset*: AFM topography image of the oxidized mound fabricated at 27 V and 100 ms. **e**. Height profiles for the oxidized (*green*) and etched (*red*) motifs above. Non-tagged scale bars are 200 nm long.

never before been observed on classical semiconducting surfaces such as silicon, whose oxidation mechanism has been exhaustively studied.[250, 251, 252] Interestingly, this wave-like features resemble that modelled for an acoustic surface plasmon (ASP). Thus, it is suggested that they could be connected to surface Friedel

250 a) Dagata, J. A.; Inoue, T.; Itoh, J.; Matsumoto, K.; Yokoyama, H. *J. Appl. Phys.* **1998,** *84,* 6891. (b) Calleja, M.; Anguita, J.; García, R.; Birkelund, K.; Pérez-Murano, F.; Dagata, J. *Nanotechnology* **1999,** *1,* 10. (c) Avouris, P.; Hertel, T.; Martel, R. *Appl. Phys. Lett.* **1997,** *71,* 285. (d) Stievenard, D.; Fontaine, P. A.; Dubois, E. *Appl. Phys. Lett.* **1997,** *70,* 3272. (d) García, R.; Calleja, M.; Pérez-Murano, F. *Appl. Phys. Lett.* **1998,** *72,* 2295. (e) Tello, M.; García, R. *Appl. Phys. Lett.* **2001,** *79,* 424.

251 Matsumoto, K.; Gotoh, Y.; Maeda, T.; Dagata, J. A.; Harris, J. S. *Appl. Phys. Lett.* **2000,** *76,* 239.

252 a) Teuschler, T.; Mahr, K.; Miyazaki, S.; Hundhausen, M.; Ley, L. *Appl. Phys. Lett.* **1995,** *67,* 3144 (a) Calleja, M.; Anguita, J.; García, R.; Birkelund, K.; Pérez-Murano, F.; Dagata, J. A. *Nanotechnology* **1999,** *10,* 34–38.

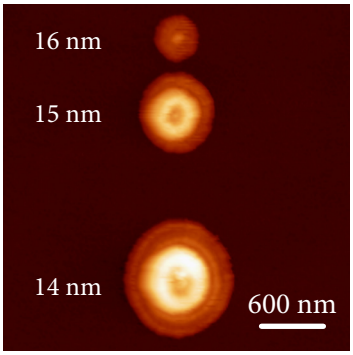

Figure 8.4 AFM topography image of 3 oxide rippled mounds fabricated in *dynamic-tip* LON at the indicated tip-to-sample distances (26 V and 40 ms). From top to down, the figure shows the increasing size of the oxide motives due to the decrease of the tip-sample distance.

oscillations of a bi-dimensional metallic system.[253] Furthermore, the oxide growth does not only occur on the surface but also propagates towards the underlying layers, creating a 3D pattern that even reaches the silicon substrate in the case of the thinner patches. Direct evidence of the bulk characteristics of the oxide motifs created on silicon could be observed by immersing the samples in a HF solution to selectively etch the oxidized motifs. These experiments confirmed that the wave-like nature of the oxidation mechanism on TaS_2 seems to be transferred on the silicon substrate. Figure 8.3 illustrates the rippled morphology of the oxide mounds and the underlying substrate.

Unfortunately, we observed that the size of these motifs was extremely sensitive to the experimental conditions such as the threshold potential, the voltage pulse, the time pulse or the tip to sample distance (see Figure 8.4) and therefore, little reproducible.

In order to overcome this limitation, we propose to use a static oxidation method in which the oscillation amplitude is set to zero just prior and during the application of the voltage pulse (*static-tip* LON). It is noteworthy to emphasize that in contrast with contact mode AFM (also performed at zero oscillation amplitude),[244a, 244f] the tip is here always freely suspended at a certain distance

253 Diaconescu, B.; Pohl, K.; Vattuone, L.; Savio, L.; Hofmann, P.; Silkin, V. M.; Pitarke, J. M.; Chulkov, E. V.; Echenique, P. M.; Farías, D.; Rocca, M. *Nature* **2007,** *448,* 57–59.

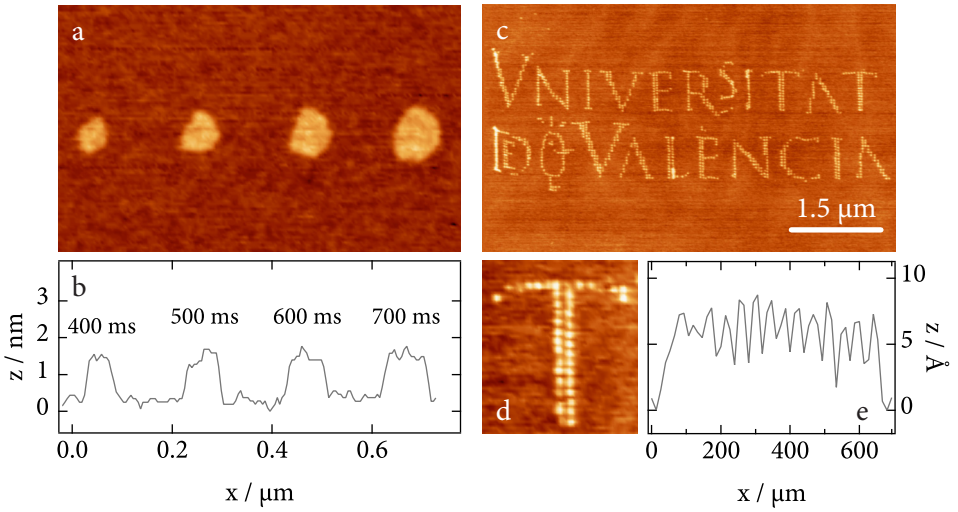

Figure 8.5 AFM topography image of an array of three oxide motifs created at 22.5 V and 45 ms (**a**) and the same three HF etched oxide motifs (**b**). **c**. Profiles of images the pristine (*green*) and etched (*red*) oxide mounds shown above. **d**. AFM topography image of an etched oxide rippled mound on a TaS_2 layer of 8 nm thick. *Inset*: AFM topography image of the oxidized mound fabricated at 27 V and 100 ms. **e**. Height profiles for the oxidized (*green*) and etched (*red*) motifs above. Non-tagged scale bars are 200 nm long.

over the target surface. Indeed, it was found that this second oxidation method yielded drastically different results in comparison to the dynamic one. Firstly, the morphology and profiles of the patterned structures can be controlled in a much more precise manner by fine-tuning the oxidation conditions on the surface of the TaS_2 thick layers. As in the previous *dynamic-tip* mode, the threshold potentials were found to be very sensitive to experimental instant conditions. However, in the present case, once the threshold voltage was established, the resulting oxide sizes can be precisely controlled by adjusting the pulse duration. In this way, sub-nanometric oxide dots (as shallow as 0.5 nm high) may be grown by keeping pulse times within the tens of millisecond (see Figure 8.5). Oppositely, longer pulse durations give rise to oxide motifs that exhibit the characteristic rippled structure already observed in dynamic-tip LON. To sum up, *static-tip* LON allowed for the uniform and reproducible patterning of extremely homogeneous oxide motifs on large surface areas of TaS_2 thick flakes. This illustrates the high reproducibility

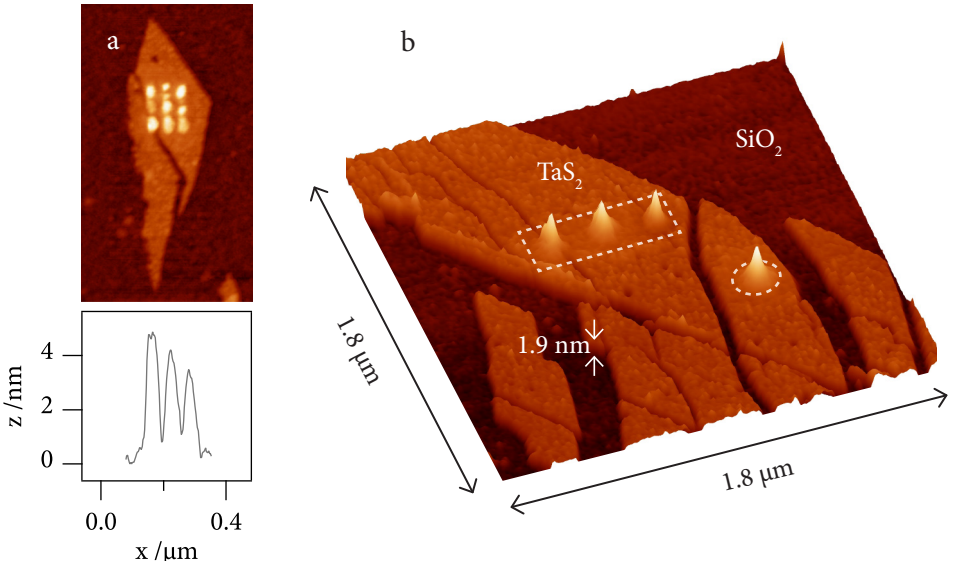

Figure 8.6 Oxidation motifs on ultrathin TaS_2 flakes. (**a**) AFM *topo*graphy image of a 3 x 3 array of oxide nano-dots patterned on a 1.9 nm thick flake. Image size: 690 nm x 1.2 µm. (**b**) AFM *topo*graphy image of a collection of ultrathin TaS_2 flakes. Two flakes have been selectively patterned with oxide motifs: an array of 3 nano-dots (marked with a dashed rectangle) and an isolated nano-dot (highlighted by the dashed circle).

reached with the static-tip mode. To illustrate the uniformity reached, the 1040 oxide nanodots shown in this figure could be fitted to a Gaussian distribution with a standard deviation as small as 0.15 nm. This result is comparable with the precision reached with conventional *dynamic-tip* LON experiments performed on silicon.

3.2 LON on ultrathin flakes

The improved control over the patterning technique achieved via static-tip LON opened the door to the oxidation of ultrathin few layer TaS_2 samples (< 5 nm, see Figure 8.6). Once again, a high reproducibility of low-profile feature fabrication was reached independently on the flake thickness. This is in sharp contrast with previous reports of LON on graphene flakes where the size of the oxide features was dependent on the layer thickness.[244e]

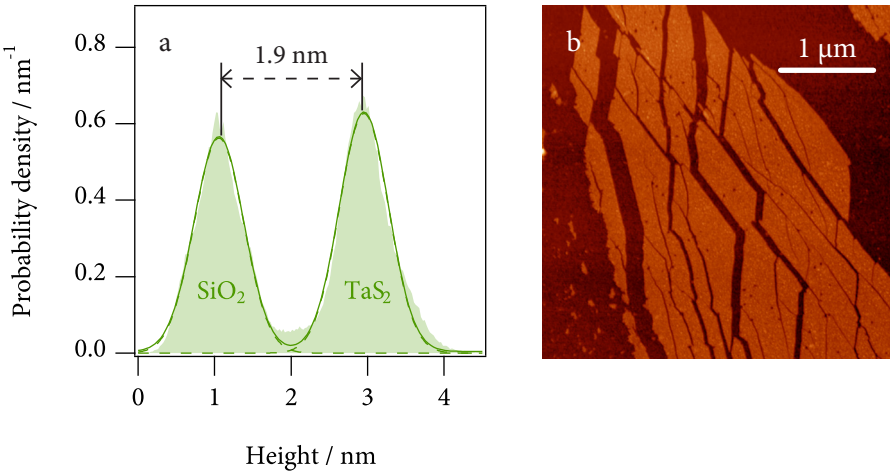

Figure 8.7 a. Height histogram of an AFM *topo*graphy image of a region with a high density of ultrathin TaS_2 flakes of homogenous thickness (**b**). The data could be fitted to two Gaussian distributions corresponding to the SiO_2 (1.06 ± 0.46 nm) and the TaS_2 (2.95 ± 0.46 nm) surfaces. Thus, the calculated flake thickness is around 1.89 ± 0.46 nm.

In an attempt to optimize the response of the TaS_2 few layer flakes to varying voltage and pulse lengths, a series of oxidation conditions were explored on ultrathin layers. As shown in Figure 8.6, very precise oxide dots could be created on TaS_2 layers of less than 1.9 nm in thickness (the thickness was calculated from the Gaussian fit of AFM topography data as is illustrated in Figure 8.7). This was achieved by using voltages lower than 30 V. Higher voltage pulses resulted in the uncontrolled piercing of the flakes down to the silicon substrate.

3.3 Chemical nature of the nanofabricated tantalum oxide

In order to ascertain the actual nature of the oxide motifs produced on the TaS_2 surface, local probe spectroscopies such as EPMA or photoluminiscence (PL) were employed.

A chemical mapping analysis of the surface performed by EPMA clearly showed a high signal of O K_α secondary electrons coming from the oxidized regions (see Figure 8.8).

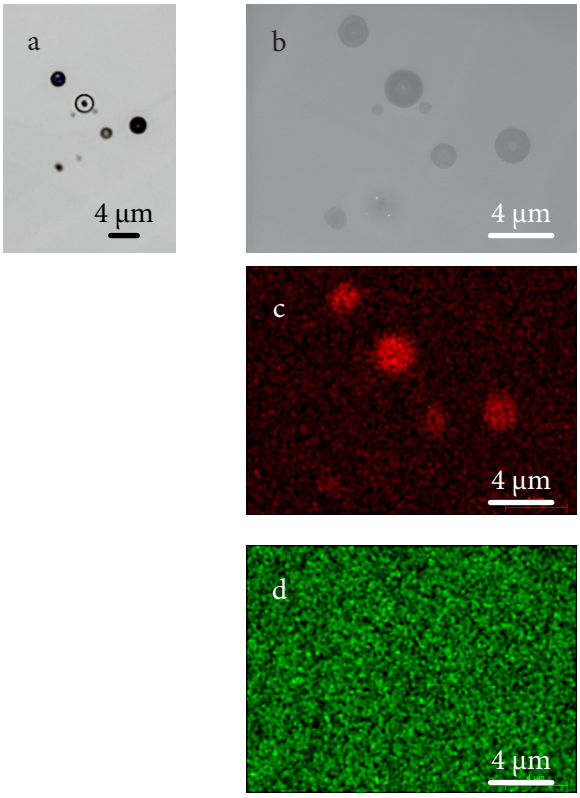

Figure 8.8 SEM-EPMA mapping studies performed on a group of oxide rippled mounds patterned on a thick TaS_2 flake. **a**. Optical microscopy image of the group of rippled mounds. **b**. Secondary electrons (SE) SEM image of the same region. **c**. O K-shell SE channel. **d**. Ta L-shell SE channel.

Figure 8.9 shows PL data collected from a TaS_2 flake decorated by AFM-LON with a large (2.6 μm in diameter) oxide motif. The results show that before LON, the TaS_2 flakes present a strong featureless background signal in their photoluminescence spectra between 520 nm and 700 nm. The oxide microstructure produced by AFM-LON exhibits a much lower background signal indicating a reduction of the optical absorption. In addition, it displays two narrow peaks at 585 nm and 635 nm and a wider one at 615 nm. While the peaks at 585 nm and 635 nm are due to the silicon substrate (probably due to excitation of high order phonons), the peak at 615 nm may be associated to the oxide motif. More precisely, this strong broad peak is characteristic of the presence of amorphous Ta_2O_5 during the oxidization process.[214] Noting the chemical

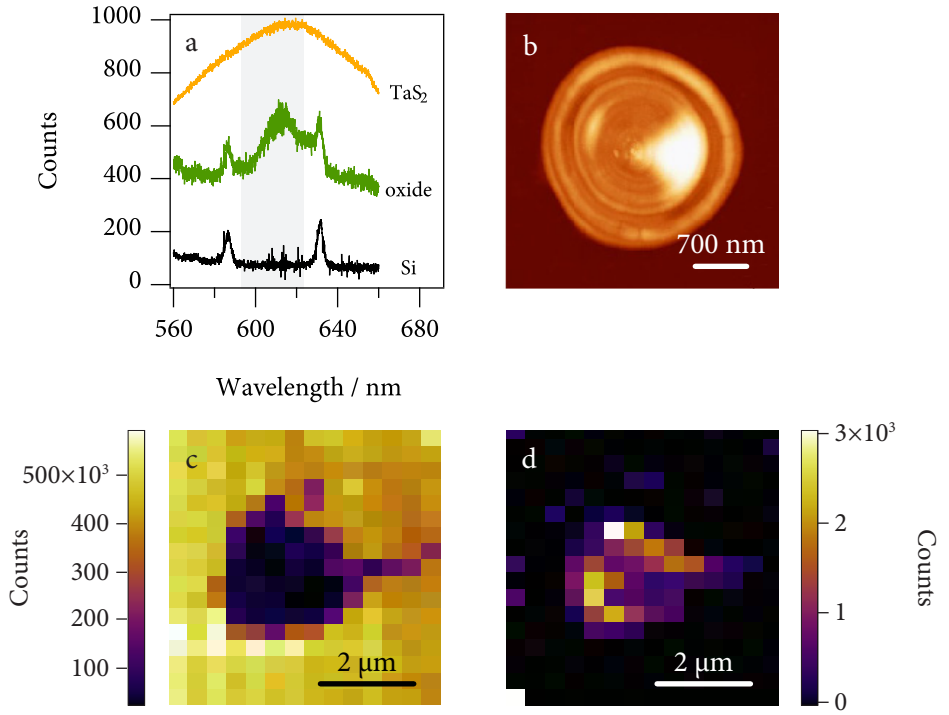

Figure 8.9 Photoluminescence spectra measured on a TaS_2 flake patterned with a large oxide motif by *dynamic-tip* LON. A comparison between the spectra measured on the pristine flake, the oxidized part and the bare Si substrate is shown in (**a**). the profile shown for bare TaS_2 has been re-scaled to 1/10 of the raw intensity for comparison. The optical (**b**) and AFM (**c**) topography images of the oxide motif are also inluded. **b**. Photoluminescence intensity integrated from 600 nm to 625 nm (grey shaded region in (**a**)) before subtracting the baseline.

transformations involved, it is easy to conceive how the properties of TaS_2 flakes are dramatically altered by means of LON. In this way, AFM provides us with a tool of nanometric precision for the patterning of insulating Ta_2O_5 regions within a metallic conducting TaS_2 flake. A similar scenario has been already described for the local oxidation of graphene or the reduction of graphene oxide flakes.[244]

3.4 Electrical properties of the ultrathin layers

Conducting tip AFM (CT-AFM) was used in order to probe the conducting behaviour of the deposited flakes. First, the resistance map of a flake with different

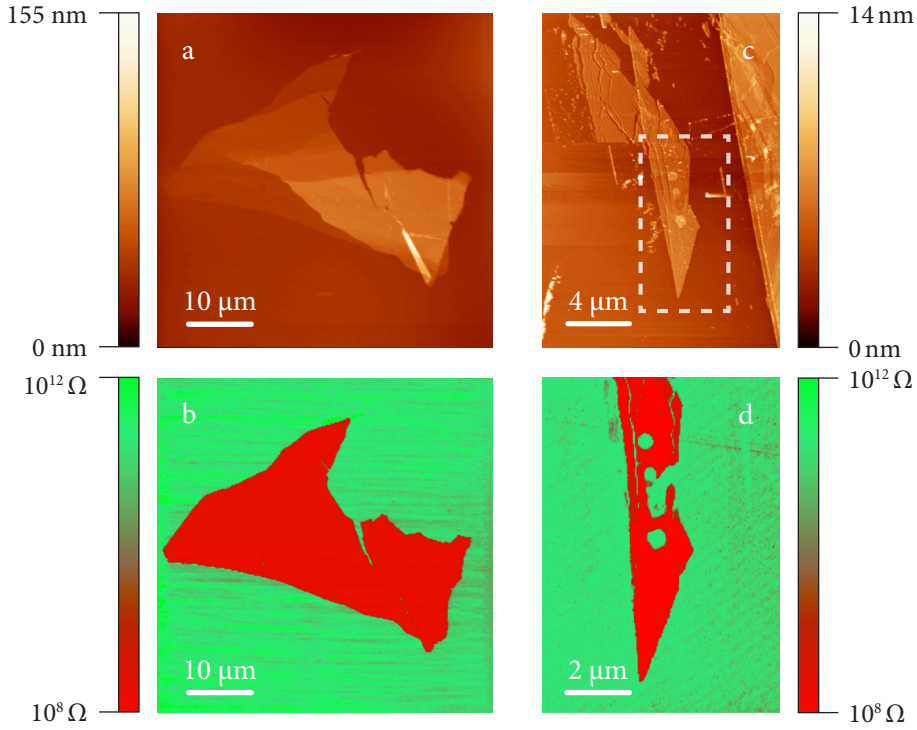

Figure 8.10 a. AFM topography image measured in contact mode of a TaS_2 flake. **b**. CT-AFM resistance mapping of the same flake. **c**. AFM topography image of TaS_2 thin flakes. The flake inside the dashed box has been patterned with three round oxidized regions. **d**. CT-AFM resistance mapping of the patterned flake highlighted in (**c**).

thicknesses deposited on doped silicon was measured. When a 2 V bias was applied between the tip and the surface during contact scanning, a clear contrast in the conductance between TaS_2 flakes and the surface was observed (see Figure 8.10). The entire TaS_2 surface appears to have the same conducting behaviour and therefore, no effect of the flake thickness was observed (Figure 8.10b). The electrical properties of the oxide motifs patterned via AFM-LON on top of TaS_2 layers were also probed. As expected, a clear contrast was observed between conductive pristine and insulating oxidized regions (Figure 8.10d).

The big difference in conductivity makes these TaS_2 / Ta_2O_5 surfaces excellent candidates for the fabrication of circuitry at the nanoscale. Some preliminary results on device fabrication confirm that is it possible to control the oxidation of

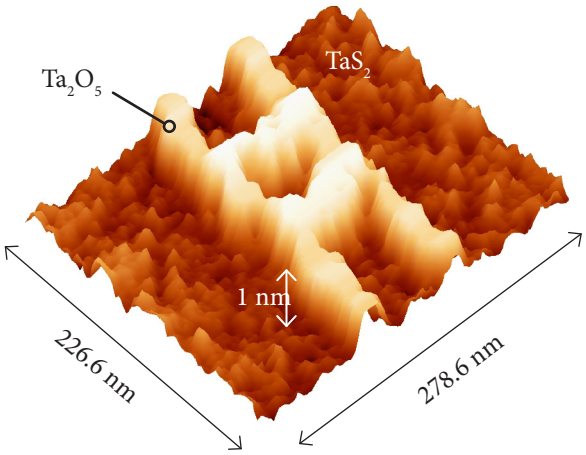

Figure 8.11 Fabrication of the active part of a single electron transistor (SET) out of a TaS_2/Ta_2O_5 structure generated by AFM-LON. **a**. 3D AFM image of the SET design patterned on the surface of a TaS_2 flake. The island on the centre of the pattern is isolated by lines of 1 nm high of Ta_2O_5 that could act as tunnel junctions.

a TaS_2 surface to fabricate completely isolated islands of approximately 20 nm in length. Figure 8.11 displays an example of the design of a potential single-electron transistor (SET) patterned on the surface of a TaS_2 surface. At a more fundamental level AFM-LON could also open the door for the study at low temperature of the physical consequences derived from the confinement at the nanoscale of this layered superconductor.

4 Conclusions

To sum up, we have performed an exhaustive exploration of AFM-LON on TaS_2 surfaces using both thick samples and ultrathin layers. These layered materials have been oxidized using both the conventional *dynamic-tip* mode and the new *static-tip* mode developed in this work. The most spectacular result in this context has been the demonstration that a static-tip LON affords a reproducible oxidation of very low-profile motifs not only on thick TaS_2 flakes (> 5 nm), but also on ultrathin ones (< 5 nm). For the first time, we have shown that these TaS_2 layers may be conveniently oxidized with an unprecedented precision and reproducibility

similar to that achieved on silicon, or more recently on graphene surfaces.[244] In fact, the oxide motifs can be conveniently patterned across several square micron areas of TaS_2 conducting flakes, opening the door for the nanofabrication of extended designs with very low profiles (down to 0.58 nm). As these oxide motifs are insulating, one can envision the controlled printing of nano-circuitry on single TaS_2 conducting layers, which behave as bi-dimensional systems. On the other hand, as TaS_2 exhibits superconducting properties at low temperatures, this methodology could be employed for studying the physical consequences derived from the confinement of this layered superconductor in a nanometric region.

Though the level of precision reached is similar to the one achieved for the oxidation of graphene, the controlled oxidation of TaS_2 opens the door for performing AFM-LON on other TMDC analogues. This offers the possibility of finely tuning the properties of the TMDC/oxide heterostructure depending on the functionality pursued.

Finally, we have found that the mechanism of the oxidation on TaS_2 surfaces clearly differs from the mechanism of oxidation on most surfaces. In fact, characteristic rippled mounds have been obtained in the oxidation of TaS_2 flakes. This unusual behaviour may be inferred from the peculiar Fermi surfaces of these quasi-bidimensional systems. A theoretical study into the charge propagation mechanism along the TaS_2 conducting layers is under way.

5 Experimental section.

AFM and LON

Two different AFMs were used for the local oxidation nanolithography on TMDCs. One is a Nanoscope IIIa (Bruker) interfaced with a home-made voltage amplifier. The other one is a Cervantes Fullmode AFM (Nanotec Electrónica) that provides a powerful nanolithography software (WSxM) that permits to plot customised pre-loaded patterns. All experiments were carried out at room temperature and the ambient relative humidity was maintained as constant as possible (around 75%) by employing a commercial bench-top humidifier.

In both AFMs, a vertical optical microscope is used to visualize the tip over the surface, being able to position the tip on top of the selected flake. The first part of the experiment consists on the topographic characterization of the surface in tapping mode, which is a non- invasive mode of operation. The same Silicon probes of $\nu r \approx 30$ KHz and $K \approx 40$ $N \cdot m^{-1}$ (PPP-NCH Nanosensors) were used for the morphological characterization as well as for performing the LON. The spring constant and resonance frequency of the conducting Si cantilever were 42 $N \cdot m^{-1}$ and 300 kHz, respectively. A positive DC bias voltage (35 V) was applied to the sam- ple during the LAO lithography. The AFM cantilever was scanned with scanning speeds ranging from 10 to 160 $nm \cdot s^{-1}$.

Once the surface is scanned and the target area chosen, a set of pulses of increasing voltage and duration is carried out. This patterns a set of consecutive oxidation features of different characteristics on the flake, allowing for the identification of voltage and time thresholds. To achieve a controlled and reproducible method to oxidise nano-structures it is also very important to control the tip-sample distance. The latter is checked by recording the so called force-distance curve. This distance can be tuned by adjusting the set point in tapping mode.

In general, a cantilever frecuency set point of 1V was initially tuned in order to achieve a reasonable surface proximity for LON purposes. Fine adjusting of the

tip-to-surface distance was performed prior to each LON event in order to control de oxidation outcome.

HF selective etching

The etching of oxidized TaS_2 flakes deposited on Si subtrates was performed by fast dipping (typically < 1 s inside the etching solution) in an concentrated HF (aq.) solution. The samples were then thoroughly rinsed with milli-Q water and blow dried.

EPMA mapping

EPMA spectra were collected with a field emission gun (FEG) Hitachi S-4800 SEM operated at 20 kV and equipped with a Bruker XR detector. The sample was placed at a working distance of 15 mm and scanned at an approximate count rate of 10 kcps for approximately 15 min. The mapping data was collected with Quantax 400 software.

Photoluminesce measurements

PL measurements have been carried out with a homemade setup that consists of a confocal microscope with a NA = 0.8 objective illuminated by a λ = 532 nm laser beam.[254] Typical light intensities of $9.5 \cdot 10^{-5}$ $\mu W/nm^2$ (75 μW incident power and 500 nm diameter spot) are used. For the scanning PL measurement the diffraction limited spot is scanned using a combination of two galvomirrors and a telecentric lens system while a PL spectrum is acquired in each pixel.

254 Buchs, G.; Barkelid, M.; Bagiante, S.; Steele, G. A.; Zwiller, V. *J. Appl. Phys.* **2011,** *110,* 074308.

3

Resumen

A lo largo de la historia, los compuestos laminares han ocupado un lugar destacado en el desarrollo de nuevos materiales, muchos de ellos llegando a tener verdadero impacto tecnológico.[1] El trabajo descrito en esta tesis se encuadra en el ámbito de los materiales laminares con propiedades magnéticas de interés empleados como sistemas químicamente versátiles. En cuanto a su versatilidad química, los materiales laminares constituyen un ejemplo clásico de lo que se denomina una estructura anfitrión, capaz de albergar por intercalación otras especies químicas en su interior de forma mas o menos ordenada. Además, dada la alta anisotropía en la propagación de enlaces a lo largo de su estructura laminada (enlaces fuertes dentro de las capas y mas débiles entre capas) los sólidos laminares presentan la capacidad de ser exfoliados tanto por la vía seca como por la vía húmeda hasta llegar al limite de la separación de capas individuales. En lo que respecta a las propiedades físicas, la categoría de materiales laminares engloba a distintas familias de compuestos con propiedades muy diversas. Dos son las familias de compuestos estudiadas en este trabajo: los hidróxidos dobles laminares (layered double hydroxides, LDHs) que exhiben un comportamiento magnético químicamente modulable y los dicalcogenuros de los metales de transición (transition metals dichalcogenides, TMDCs) de interés en superconductividad de bajas temperaturas. El propósito de esta tesis doctoral es el de estudiar los materiales bidimensionales tanto a nivel químico como a un nivel físico. En el ámbito químico se estudiaron los materiales laminares como componentes estructurales de nuevos compuestos híbridos con multifuncionalidad novedosa. En lo que respecta al enfoque mas físico, se prentendió ahondar en las propiedades bidimensionales intrínsecas de los sólidos laminares a través del estudio y manipulación de monocapas segregadas de espesor atómico.

La primera parte de la tesis versa a cerca de los materiales tipo LDH. Estos hidróxidos metálicos presentan una estructura romboédrica de brucita, con la diferencia de que en los LDHs la combinación de metales trivalentes y divalentes origina capas de naturaleza catiónica: $[M_{3-x}M'_x(OH)_6]^+$ (donde M es un metal trivalente, M' es un metal divalente y $0.1 \leq x \leq 1.0$). La consecuencia directa es que intercaladas entre capas, se hallen de forma natural una serie de aniones que ademas con intercambiables. Esto hace de estos materiales tipo-arcilla, unos auténticos

1 Nótese por ejemplo la aplicación de materiales arcillosos tipo caolín en la fabricación de barbotinas

intercambiadores ionicos. Esta propiedad se puede aprovechar para la inserción de una multitud de especies químicas de interés. Asimismo, la composición metálica de las capas de hidróxido también se puede controlar, de modo que en función de los elementos introducidos, las propiedades físicas del material varían. De particular interés resultan los LDHs de metales de transición que muestran comportamiento magnético y que se ordenan ferro o antiferromagnéticamente a temperaturas bajas. La combinación de las propiedades magnéticas junto con su fácil intercalación definen un contexto único para el diseño de materiales híbridos magnéticos. En este sentido se planteó la posibilidad de sintetizar multicapas magnéticas por inserción de imanes de base molecular. Empleando complejos metálicos precusores, se postuló la posibilidad de aprovechar el espacio interlaminar que ofrecen los LDHs como un reactor a escala nano para el crecimiento de polimeros de coordinación con comportamiento magnético. En esta linea consta ya en la literatura un estudio de crecimiento de redes bidimensionales basadas en el ligando oxalato.[2] Sin embargo, el calculo de densidad de carga de las subredes catiónica (LDH) y aniónica (oxalato bimetálico) reflejan una falta de compensación electrostática en el material final. Sin embargo, al realizar el mismo cálculo sobre una hipotética red cianurada bidimensional, tomando parámetros estructurales de las redes de análogos de azules de Prusia existentes, se constata que la densidad de carga es muy similar y de signo opuesto a la de las capas de LDH. Por consiguiente la subred de cianuros debería de poder crecer en el seno de un hidróxido laminar para dar lugar a un material neutro. No obstante, es bien sabido que los cianuros de metales de transición polimerizan con gran facilidad, dando lugar a redes cubicas tridimensionales en la que los centros metálicos se hallan bien conectados por vías de supercanje magnético. De modo que al interés de obtener una heteroestructura compuesta de redes magnéticas bi-dimensionales, se le añade la posibilidad de poder confinar el crecimiento de un análogo azul de Prusia en dos dimensiones.

Como primer paso en esta investigación, se partió de un LDH diamagnetico, con animo de controlar el crecimiento la subred de base molecular y constatar el efecto que el confinamiento pudiese tener sobre la misma. De este modo se procedió a ensayar el crecimiento de la red cianurada de Cr^{III}-Ni^{II} (con una

2 Coronado, E.; Martí-Gastaldo, C.; Navarro-Moratalla, E.; Ribera, A.; Galán-Mascarós, J. *J. Mater.. Chem.* **2010,** *20,* 9476–9483.

temperatura critica de 90 K en el compuesto obtenido por precipitación directa) en el seno de una LDH ZnAl. A tal efecto se diseñó una síntesis en dos etapas de intercalación sucesivas, la primera de ellas para introducir el hexacianocomplejo de metal trivalente y la segunda para introducir el divalente y así concatenar los centros de metal trivalente. Este método sintético en efecto permitió aislar una multicapa magnética por alternancia de hojas de cinauro bimetálico ferromagnetico con otras de hidróxido diamagnético. Estructuralmente el proceso se puede monitorizar por Rayos-X de polvo, viendo como al partir de una LDH con cationes CO_3^{2-} en su espacio interlaminar se produce un ensanchamiento de las galerías al sustituir por un hexcianomentalato, y como sin embargo no hay apenas cambio en el ultimo paso de polimerización de la red de cianuro. El análisis químico por técnicas de microscopia y de infrarrojo también apunta en el mismo sentido a la existencia de una fase híbrida pura con la siguiente formula empírica: $[Zn_2Al_1(OH)_6][NiCr(CN)_6](NO_3)$. En cuanto a las propiedades físicas del material, se observa una clara reducción de la temperatura a la que el material se ordena magnéticamente. Esta observación una vez mas se ajusta a lo esperado para una reducción de la dimensionalidad de la red de cianuros.

Una vez constatado el efecto de confinamiento del espacio interlaminar de las LDHs y de comprobar que debido a tal confinamiento, la red cianurada ve reducida su T_C a ⅔ del valor obtenido para el compuesto original, se procedió al inspeccionar el crecimiento de una red cianurada magnética de una LDH magnética a base de metales de transición. Desafortunadamente se comprueba que por seguimiento de la estrategia propuesta para el LDH diamagnético no se obtiene el mismo resultado para el caso del LDH CoAl. En esta linea, al intentar polimerizar el cianuro por inserción del metal divalente, todo indica que se produce un colapso de la estructura laminar de la LDH, muy probablemente por el crecimiento descontrolado del cianuro en su seno en las tres direcciones del espacio. En este caso pues la LDH no ofrece la robustez necesaria para confinar el crecimiento de la red cianurada. Futuros experimentos se enfocarán a elucidar la diferencia observada entre los huéspedes ZnAl y CoAl y también al ensayo de nuevas condiciones sintéticas para intentar controlar el proceso de polimerización.

La segunda parte del trabajo de esta tesis se dedicó a los dicalcogenuros de los metales de transición. El principal interés que suscitan estos materiales es que en

función de la naturaleza del metal y el calcogenuro combinado, las propiedades eléctricas y magnéticas varían en gran medida. De este modo existen desde TMDCs con comportamiento aislante o semiconductor hasta otros metálicos e incluso superconductores a baja temperatura. Estos últimos están formados en esencia por el grupo de los dicalcogenuros de metales del grupo V y es donde se centró la mayor parte dela atención. En general, los TMDCS son materiales laminares que presentan una estructura cristalina hexagonal muy similar a la de los LDHs. Sin embargo, en este caso el material se compone de planos que en principio son eléctricamente neutros según una composición tipo MX_2 (M = metal de transición de los grupos III al VI, X = S, Se, Te). Además, los TMDCs presentan una variedad muy rica de politipos. Los politipos (o polimorfos) surgen de la combinación de un tipo de coordinación (octaédrica o trigonal prismática) con un tipo de periodicidad en el apilamiento en el eje *c* de los planos de MX_2. A pesar de que tan solo uno de lo politipos suele ser termodinámicamente estable a temperatura ambiente, la dificultad de interconversión en el estado solido hace que en condiciones normales se pueda dar toda una gama de polimorfos. En el primer capitulo dedicado a este tipo de materiales se investiga en profundidad la síntesis cerámica de estos sistemas, haciendo especial hincapié en el aislamiento de politipo de gran pureza cristalográfica. En esta sección se aborda tanto la síntesis de materiales policristalinos como también las técnicas especiales de síntesis de monocristales de gran tamaño. Además, se estudia la llamada reducción topotáctica de los TMDCs. A través de esta reacción se logra inyectar carga en los planos de dicalcogenuro, induciendo a la vez un cambio estructural de la distancia entre planos causada por la intercalación de especies catiónicas que compensan dicha carga negativa. Esta reacción da acceso a la combinación de los planos de dicalcogenuro con otras especies químicas cargadas positivamente, de forma análoga a como se hacia con las LDHs. Asimismo, la naturaleza cargada de los planos favorece su solvatación con disolventes polares o próticos, facilitando su delaminación por la vía húmeda.

La delaminación de estos compuestos de intercalación da lugar a coloides estables tipo sol de nanolaminas catiónicas. Se constata por técnicas de TEM de alta resolución que estas laminas retienen la estructura hexagonal original. Por reapilamiento electrostático directo de las nano-láminas en suspensión con otra especie catiónica de interés presente en el medio se puede llegar a constituir

una nueva estructura laminar híbrida que combine las propiedades de los compuestos de origen. Es la técnica es conocida con nombre de delaminación/floculacion. De este modo, se investigan los soles de nano-láminas de TaS_2 como fuente de materiales híbridos en los que la superconductividad intrínseca del sistema Na_xTaS_2 (T_{SC}~ 4.5 K) pueda coexistir con alguna propiedad de origen molecular. Empleando la floculacion de las nano-láminas de $[TaS_2]^{x-}$ en presencia de complejos metálicos polinucleares con relajación magnética lenta se logró aislar el primer material en el que coexisten las propiedades superconductoras con la bis-estabilidad de los imanes unimoleculares. A través de estudios detallados de magnetometría de SQUID y de micro-Hall se demuestra que las propiedades superconductoras coexisten en la nueva estructura laminar. No obstante, mientras que la superconductividad exhibida por el componente de estado solido para no variar, la inclusión de las moléculas imán Mn_4 en el entorno laminar el TaS_2 parece alterar las propiedades magnéticas del primero. Un estudio detallado de magnetometría en presencia de campo permite concluir que esta modificación se debe exclusivamente a la formación de la estructura híbrida y no a efecto de la exclusión de campo del superconductor que conduciría al hipotético apantallamiento de las moléculas imán. Próximos estudios por combinación de distintos imanes unimoleculares con otros TMDCs debería proporcionar mas información a cerca de la posible interacción entre la exclusión de campo y la relajación lenta superparamagnética. En concreto se propone la intercalación en monocristales cristales de gran dimensión con ánimo de proveer con superficies planas lo suficiente amplias y perfectas para es estudio de dicho efectos de forma local con la punta de un STM.

La misma técnica de delaminación/floculación de las laminas de TaS_2 pero esta vez partiendo del complejo $[Fe(PyimH)_3]^{2+}$ permitió aislar el primer material que combina la transición de espín con las propiedades superconductoras. Una vez mas a través de las medidas de susceptibilidad magnética, se pudo constatar la coexistencia de ambos fenómenos: la transición de espín claramente visible desde unos 4 K a unos 400 K en las medidas DC y la transición a la fase superconductora patente en las medidas de susceptibilidad AC y en las imanaciones. Ademas los datos concuerdan con otros experimentos de espectroscopia de Mössbauer que permite cuantificar el porcentaje de transición de espín. Futuros experimentos se llevaran a cabo para intentar controlar la transición de espín de los complejos

insertados con estímulos lumínicos a través de un láser, el fenómeno al que se le conoce con el nombre de LIESST. La manipulación de la transición de espín a baja temperatura con estímulos de este tipo podría ayudar a provocar modificaciones en el estado superconductor de los planos del huésped de estado solido.

Un punto importante a resaltar en la síntesis de estos compuestos híbridos basados en laminas de TaS_2 superconductoras, es su aislamiento en forma de copos autosustentables y altamente orientados. Esto es, por medio de técnicas de sedimentación y filtración del material floculado, se logro acceder a copos de gran relación de aspecto en los que la laminas constituyentes se hallaban en disposición aproximadamente coplanar y con los planos basales 001 paralelos a la cara del copo. La imágenes de SEM confirman que al filtrar el material floculado sobre una membrana de teflón sustentada sobre una frita plana, los cristalitos quedan bien orientados. Esto permite manejar los materiales híbridos cono entidades microscópicas con propiedades anisótropas que recuerdan a los cristales laminados del TaS_2 de partida. En concreto este tipo de muestras han permitido caracterizar la anisotropía de las propiedades superconductoras de los materiales híbridos confirmando la naturaleza cuasi-bidimensional de las mismas, a imagen y semejanza de los TDMCs originales. Ademas realizar medidas de transporte contactos eléctricos directos al material, sin necesidad de realizar un prensado en pastilla,[3] es ahora una tarea asequible. Con la síntesis y caracterización de estos dos materiales, se demuestra la gran robustez y a la vez versatilidad de la técnica híbrida basada en combinación de materiales del estado solido con otros de base molecular. En particular la nanolaminas de TaS_2 se erigen como un componente básico para la introducción de propiedades superconductoras en compuesto mixtos. A pesar de que hasta el momento la mutua influencia de las propiedades de los componentes combinados ha sido esquiva, las posibilidades que quedan abiertas aun son numerosas. La elección de la dupla TMDC-material molecular adecuada en cuanto a robustez y rangos térmicos de bi-estabilidad conducirá al aislamiento de un material multifuncional inteligente.

Llegados a este punto ya se había adquirido una gran experiencia en la delaminación de los TMDC. Inspirados por la reciente expansión de la ciencia

3 Ha quedado demostrado en experimentos anteriores que el prensado (a una presión alta, por lo general de varias Ton) en pastillas destruye las propiedades superconductoras.

del grafeno, se procedió al estudio de los cristales bidimensionales de espesor atómico a un nivel mas físico. En efecto, en la actualidad la era del grafeno esta comenzando a dejar paso a una multitud de materiales laminares igualmente interesantes pero un tanto ensombrecidos por la explosión mediática del primero. De hecho ya no pocos estudios a cerca del estudio de laminas ultra-finas de TMDCs han sido publicados. Y sin embargo muy poco figura en la literatura en lo que concierne al sistema TaS_2 y en las a pocas referencias existentes las capas mas finas no presentan traza alguna de superconductividad. Por consiguiente la exfoliación de este material se presentaba como un reto. Inicialmente se ensayó el aislamiento de capas de espesor atómico por la vía húmeda. Sin embargo, esta vía se abandona con premura dado el reducido tamaño de las capas mas finas. Asimismo se constata que por medio de la exfoliacion con disolventes, las estructura cristalina de las capas se degradaba con gran rapidez una vez expuestas al aire. Mucho mas robustas y de mayor extensión se mostraban las capas obtenidas por exfoliación seca de los cristales neutros de TaS_2. En este contexto, la experiencia previa obtenida en la síntesis de monocristales de gran tamaño fue de gran ayuda, proveyendo extensas superficies de gran perfección para ensayar la deposición. Sin embargo los métodos de deposición por vía seca ya establecidos no proporcionaron los resultados esperados en la exfoliación del sistema TaS_2. En general, los métodos de exfoliación micro-mecánica adolecen de falta de control de las condiciones de deposición. Esto motivó la invención de un nuevo sistema de exfoliación seca basado en el principio de la exfoliación micromecánica. El método propuesto se basó en la deposición de capas en la superficie de un sustrato por simple adsorción en presencia de una presión unixial y ortogonal y en la exfoliación de las capas adsorbidas por efecto de un movimiento cizalla en dirección normal a la aplicación de la fuerza uniaxial. Asimismo, la nueva técnica de exfoliación culminó en el diseño de un sistema motorizado que permitiera controlar los distintos pasos del proceso de exfoliación: presión con fuerza controlada y cizalla con una velocidad y aceleración determinadas. La optimización de las condiciones de exfoliación gracias al mecanismo ideado se materializó en el aislamiento de capas de menos dos nanómetros de espesor que por primera vez presentan propiedades superconductoras. La superconductividad fue medida en capas individuales previa fabricación de nano-dispositivos de modo que se pudo estimar la temperatura critica en unos 2 K según la teoría BCS. Asimismo se puso a punto la detección de las capas mas finas por medio de microscopia

óptica y de espectroscopia Raman con objeto de agilizar la manipulación de las mismas. En este mismo sentido, un paso adelante en el campo de las capas finas por exfoliación es su manipulación química. Gracias a las técnicas de oxidación local a escala nano (local oxidation nanolithographies, LON) con microscopias de sonda próxima (scanning probe microcopies, SPM) se puede lograr modificar la naturaleza química de las superficies a voluntad. La aplicación de esta técnica acoplada a un AFM (AFM-LON) y llevada a las láminas de espesor atómico previamente aisladas ha permitido transformar regiones controladas de TaS_2 en su correspondiente óxido. El profundo contraste de propiedades eléctricas de uno y otro material (el TaS_2 es conductor y el Ta_2O_5 es un aislante prototipo) y el exquisito control espacial de la técnica permite prever la fabricación de nano-circuitería sobre laminas ultra-finas de TaS_2. A un nivel mas fundamenta, y dado que las propiedades superconductoras son retenidas tras la exfoliación, también se planea el estudio del confinamiento de regiones superconductoras por medio de barreras aislantes o incluso la fabricación de uniones tipo Josephson.

El estudio desde distintos puntos de vista de los diferentes tipos de materiales laminares llevado a cabo en este trabajo ha permitido ilustrar el gran potencial de estos materiales desde el ámbito de los materiales multinacionales hasta el ámbito de la física mas fundamental. No en vano y a pesar de ser materiales harto conocidos, el numero de publicaciones relacionadas con este tipo de sistemas crece cada día mas. Sin embargo el resurgir de los materiales laminares toma hoy día un cariz multidisciplinar, desde puntos de vista químicos y físicos simultáneamente tal y como se ha intentado demostrar a lo largo de esta disertación. Es gracias a este nuevo concepto de investigación que el campo de las LDHs o de los TMDCs sigue a la orden del día.

4

Appendices

4.1—Superconductivity viewed from magnetism

From a phenomenological point of view, a superconductor is a material that exhibits two characteristic properties once it is cooled below a particular critical temperature (T_{SC}): zero electrical resistance and perfect diamagnetism.

Out of the second premise one may consequently infer that below T_{SC}, $\chi = -1$. Taking note of the general relationship [1] between the magnetic field strength (H)[1] and the magnetic induction or flux (B)[2] that applies when the generated fields pass through magnetic materials— which themselves contribute internal magnetic fields (M)[3]— and combining it with the general definition [2] of magnetic susceptibility (χ), one may easily infer the general expression [3].

$$B = \mu_0 (H + M) \quad [1]$$

$$\chi = \frac{M}{H} \quad [2]$$

$$B = \mu_0 H (1 + \chi) \quad [3]$$

Since a field B may not exist inside a perfect diamagnet, hence the magnetization M points in the opposite direction of the H field as shown by expression [4]

$$M = -H \quad [4]$$

In this way, both cancel out and when a superconductor is placed between the poles of a magnet the lines of field of B go around it. As a result, the internal field at the superconducting material remains zero. This situation is illustrated by the typical *Meissner effect* scheme that may be seen in Figure A.1.1. Here, it may be appreciated how B accounts both for the external uniform applied field and the superconducting sample dipole field reversely magnetized in relation to the former.

1 The *magnetic field strength* (H) designates the driving magnetic influence from an external field in a material. It is independent of the magnetic response characteristic of the material which experiences the H field. It may also be defined as the magnetic flux density (B) divided by the magnetic permeability (μ).

2 The *magnetic flux* (B) is defined from the Lorentz force law: $\overline{F} = q\overline{v} \times \overline{B}$, where F stands for the magnetic force operating on a charge (q) moving at a certain speed (v).

3 The *magnetization* vector field M represents how strongly a region of material is magnetized and it is defined as the net magnetic dipole moment.

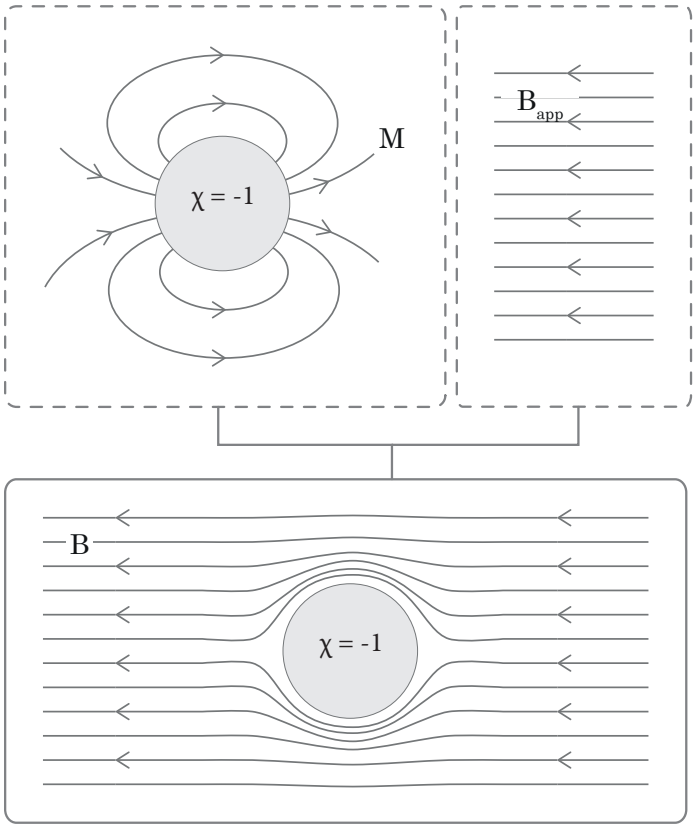

Figure A.1.1 Scheme illustrating the curvature of magnetic field lines around a superconducting sphere (**c**) in a constant applied field as a superimposition of constant the applied magnetic field (**a**) and the superconductor internal dipole field (**b**).

Finally, two additional important aspects of the behaviour of a superconductor are the field exclusion and the field expulsion effects. *Field exclusion* occurs when a material in its normal state (namely at high temperatures) is cooled below T_{SC} past. In that situation, if it is placed in a magnetic field, this filed will be excluded from the space occupied by the superconductor. If by contrast the material is field cooled from its normal state,[4] th field will be gradually expelled form the material. This *field expulsion* in also known as *Meissner effect*.

4 In the normal state and in the presence of field, this field will penetrate through the material since the permeability in this case is so similar to the permeability of free space.

With these basic concepts in mind, it is easy to appreciate how conventional magnetometry techniques are a particularly convenient approach for the detailed study of the supercondcuting behaviour of materials. In particular the two characteristic features of a type II superconductor (H_{c1} and H_{c2}) may be conveniently described by performing magnetization field exclusion studies and the superconducting transion may be easily pictured by perfoming exclusison and expulsion thermal runs.

4.2—Auger electron spectroscopy

Auger electron spectroscopy (AES) is a surface analytical technique based in the Auger effect by which energetic electrons are emitted from an atom that has been previously excited. In this way, when an atom is probed by a photon or an electron with an energy in the range of several eV to 50 eV, an electron may be ripped from a core state leaving a hole behind. A possible pathway to relax from this excited state is for an outer shell electron to fill the vacancy. As the electron moves to a lower lying level, it loses an amount of energy equal to the difference in orbital energies. At this stage the process may be coupled with the emission of a second outer shell electron whenever the energy involved is greater than the orbital binding energy of the second electron (see Figure A.2.1).

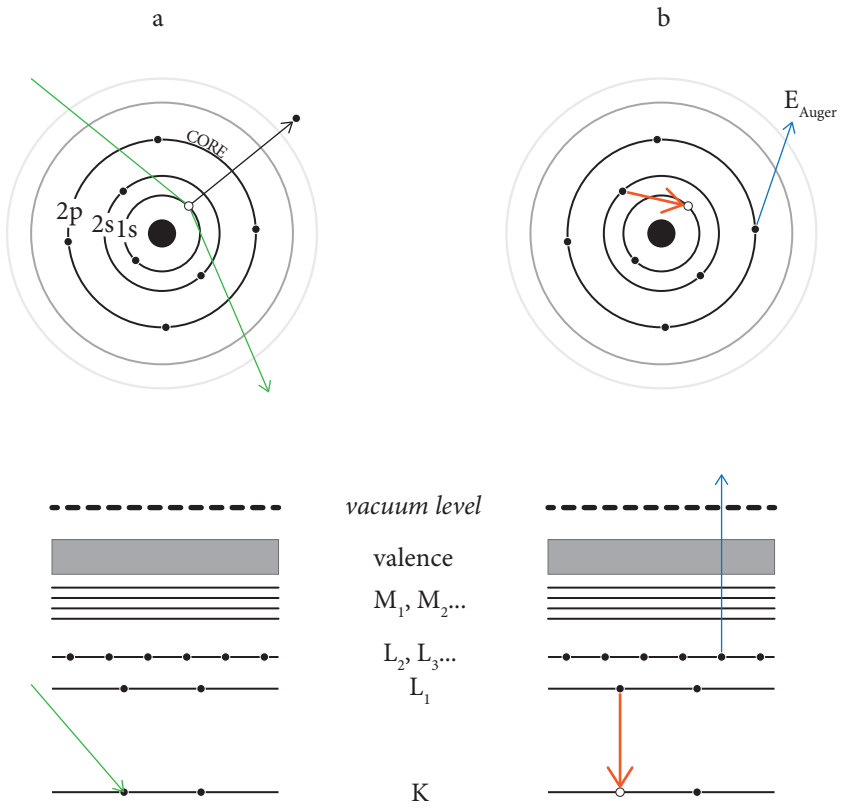

Figure A.2.1 The two fundamental steps of the Auger effect: **a**. Electron ionization; **b**. Hole refilling and Auger electron emission. Both steps are schematised in the using an orbital cartoon (*top*) and a level diagram (labels in spectroscopic notation, *bottom*).

The state-to-state transitions which are characteristic of the core electrons during an Auger event dependent on a range of factors including the spin-orbit coupling,[5] the concomitant energy level splitting for the different shells in an atom, the initial excitation energy or the relative interaction rates. However, a few characteristic transitions often dominate the AES experiment. For instance, in the case of the ionization of a single energy level such as a K level, from the different transition pathways available for filling a core hole, the KLL events dominate the Auger spectrum. An example of a possible KLL process is illustrated in Figure A.2.1

The analytical method profits from the fact that orbital energies are unique to an atom of a specific element, thus the evaluation of the emitted electron provides information about the chemical composition and chemical state of a surface.[6]

A characteristic feature of AES is its big surface sensitivity. This property arises from the short mean free path of the emitted electrons in a solid, since emitted electrons usually have energies in the range of 3 - 50 keV.[7] In this way, the *escape depth* of electrons is restricted to just a few nanometres below the target surface. Electrons coming from deeper in the solid will therefore never reach the detector.

Due to the low energy of Auger electrons, most AES experiments are performed under ultra-high vacuum (UHV). These conditions prevent the Auger electrons from scattering off atmospheric gas atoms. In addition, UHV avoids the formation of a gas adsorbate layer on the surface of the specimen, which generally hinders the analytical process, especially for quantitative purposes.[7]

A final experimental remark is that since the intensity of the Auger peaks is generally low in comparison to the noise level of the background, AES is often run in a derivative mode. This allows to enhance the Auger peaks by modulating the electron collection current by means of a small AC applied voltage.

5 The interaction between the spin of the electron and the orbital angular momentum.

6 a) Chung, M. F.; Jenkins, L. H. *Surf. Sci.* **1970,** *22 (2),* 479-485. (b) Somorjai, G. A.; Szalkowski, F. J. *Auger Electron Spectroscopy* on *Surfaces* in *Advances in High Temperature Chemistry*, Ed. Eyring, L., Elsevier, **1971**, Vol. 4, pp. 137-160.

7 a) Feldman, L. C.; Mayer, J. W. *Fundamentals of Surface and Thin Film Analysis*. Prentice Hall, Upper Saddle River, **1986**. (b) Oura, K.; Lifshits, V. G.; Saranin, A. A.; Zotov, A. V.; Katayama, M. *Surface Science: An Introduction*. Springer, Berlin, **2003**.

4.3—Field-dependent ac susceptibility of compounds **16** and **17**

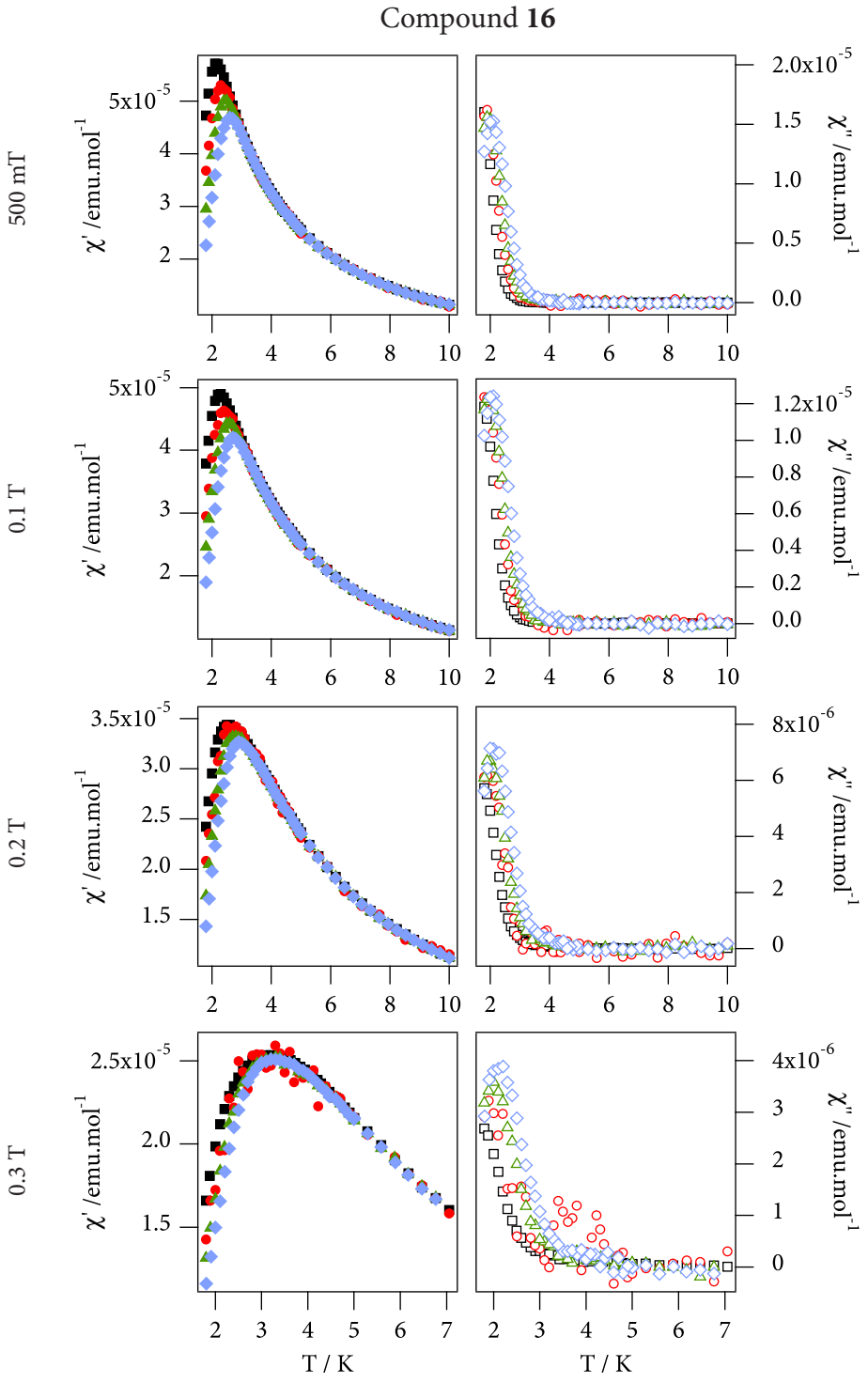
Compound 16
500 mT
0.1 T
0.2 T
0.3 T
χ' /emu.mol-1
χ'' /emu.mol-1
T / K

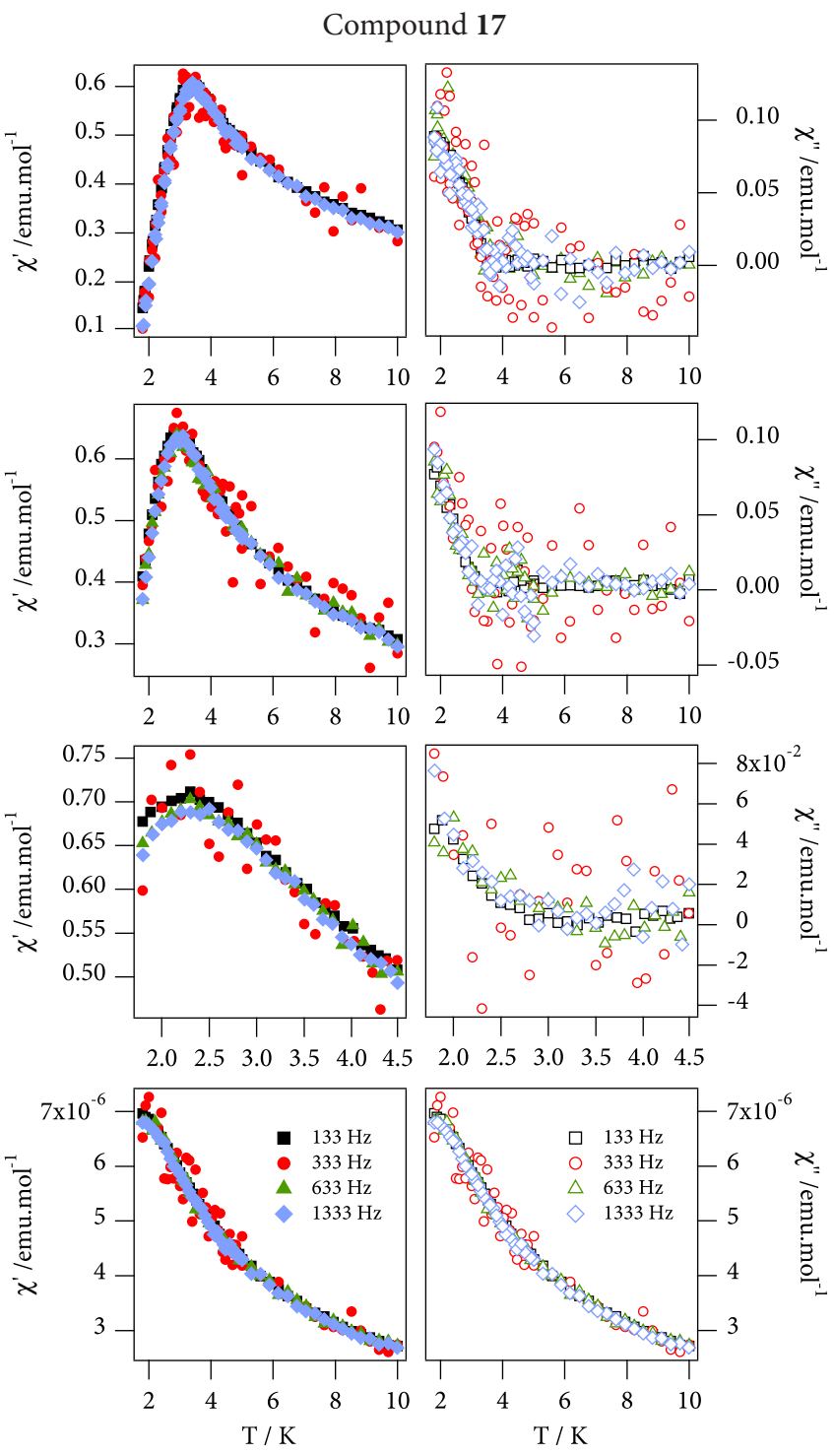
Compound 17
χ' /emu.mol-1
χ'' /emu.mol-1
500 mT
0.1 T
0.2 T
0.3 T
133 Hz
333 Hz
633 Hz
1333 Hz
T / K

4.4—Single-flake device fabrication steps

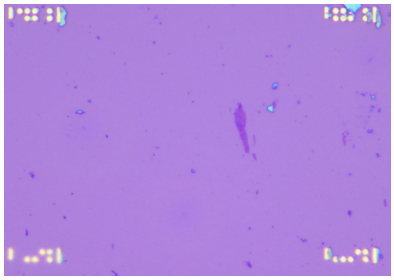

Step 1: Flake selection and reference picture taking

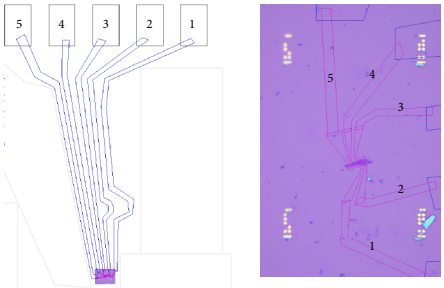

Step 2: Electrode design

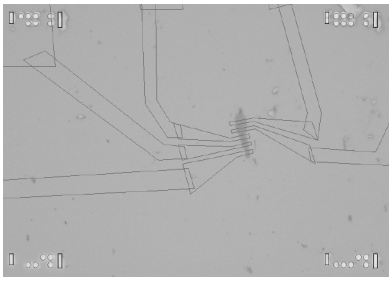

Step 3: E-beam lithography

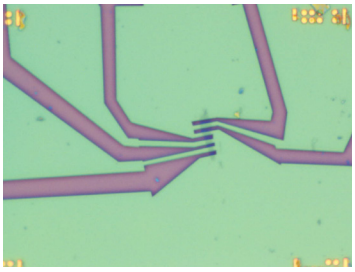

Step 4: Photoresist etching

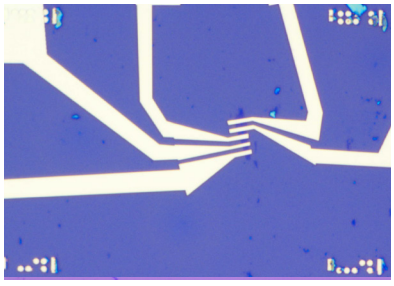

Step 5: Electrode evaporation and resist lift-off

4.5—Experimental equipment and materials

1 General Instruments and Materials

1.1 Starting materials

Unless otherwise stated, all starting materials were used directly as received from the different suppliers.

1.2 Glassware

In general all glassware and especially the one used in the manipulation of air and moisture sensitive chemicals was dried for at least 1hr in a furnace at 120ºC before its use.

1.3 Scales and analytical balances

A Mettler Toledo PB503-S/FACT with a low range readability of 1mg was used for large-scale quantities and general quantification of non-air sensitive materials.

Once weighing air or moisture sensitive chemicals and smaller quantities of products, a Mettler Toledo AB104-S scientific analytical balance with a readability of up to 0.1mg precision and set inside the dry box was used.

1.4 pH Measurements

Acid-base determinations were performed in a Metrohm Titrino Plus pH meter.

1.5 General air sensitive techniques

Experimentation on air or moisture-sensitive chemicals (namely FeII systems) was performed manipulating and reacting them in Schlenk flasks designed to work under a nitrogen inert atmosphere by using standard vacuum/nitrogen manifold techniques (i.e. glass vacuum/nitrogen line) 1. The Ar flow delivered in to the line was provided by an in-house supply.

The line, glassware and other pieces of equipment were evacuated and solvents removed from flasks by *in vacuo* evaporation using an Edwards RV3 vacuum pump. Installed between the pump and the line was a liquid nitrogen-cooled

vapour trap that condensed evacuated solvents keeping the pumping system in optimum state and a good and constant vacuum throughout.

1.6 Solvothermal reaction equipment

Hydrothermal syntheses were carried out on 20 mL teflon-lined steel autoclaves (Parr 4745 General Purpose Bomb) under autogenous pressure. Parr Model 4748 preparation bomb vessels were used for larger-scale preparations.

1.7 The dry box

For the general manipulation of air and moisture sensitive reagents out of reaction vessels a MBraun Unilab ($^{1950}/_{780}$) MB 150 B-G was used. An internal atmosphere of dry nitrogen gas with a typical residual water vapour content of less than 0.1ppm assured inert conditions for dealing with sensitive materials. Inner atmosphere drying and oxygen removal was performed by a recycling unit with molecular sieve for the elimination of oxygen and copper catalyst to do likewise with moisture.

1.8 The O_2/CO_2-free box

For the manipulation of CO2-absorbing materials a VAC glove box with an internal atmosphere of dry nitrogen gas was used. Inner atmosphere CO2 removal was performed by direct absorption over solid NaOH pellets. A relatively dry atmosphere (10% rel. humidity) was kept by use of solid P4O10.

1.9 Ultrasound treatment

General purpose ultrasonication was performed in a small bath Branson sonicator. 70 W 42 Hz (±6%)

For higher ultrasound power requirements a probe sonicator was employed. The set-up includes a Branson Sonifier® S-450A analogical ultrasonic processor that operates a disruptor titanium horn at a maximum output power of 400 W. It allows for either continuous or timed (0-15 minutes) operation and may be operated in pulsed mode to minimize heat generation in thermally-sensitive samples.

1.10 The orbital shaker

Orbital shaking was performed with a Stuart Labscale Orbital Shaker System SSL1 with a speed range of 30 to 300 rpm and an orbit amplitude of 16 mm.

1.11 The membrane filtration apparatus

Some preparations, namely the fabrication of highly-oriented free-standing flakes of TMDC-molecular hybrid materials, were based in the controlled filtration through a membrane in a flat layout as shown in Figure A.5.1.

First, a selected filtration membrane (b) was placed on top of the frit (c) and the system is clamped tightly. The suspension was then poured inside the receptacle (a) and left to filter by connecting the outlet to a vacuum line.

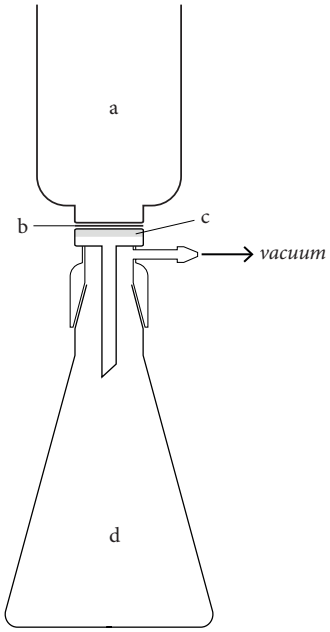

Figure A.5.1 Membrane filtration apparatus: **a**. Suspension receptacle; **b**. Filtration membrane; **c**. Glass frit; **d**: Receiving conical vessel.

2 Ovens, muffles and tube furnaces

2.1 Drying and general purpose ovens

Laboratory drying ovens were used for lower-temperature regime processes.

2.2 The high-temperature muffle

Solid-state reaction processes were carried out inside evacuated quartz ampoules placed in a high-temperature muffle with ceramic heating elements. The muffle operates at a maximum temperature of 1000 °C and is equipped with a precision temperature controller that provides 30 segments heating and cooling steps with ± 1 °C accuracy. The muffle operated at a maximum power output of 24 KWatt.

2.3 The rotatory oven

A general purpose fan oven was modified by fitting a crankshaft turned by an external motor. The oven could be operated in the r.t. - 300 °C range whilst turning the crankshaft at speeds ranging from to.

The oven was designed to perform solvothermal reactions inside general purpose bombs (Parr 4745) that could be fixed to specially designed fittings that were attached to the crankshaft.

2.4 The multi-zone split tube furnace

CVT reactions were performed in an MTI Corporation EQ-OTF-1200L3-III split-tube furnace with Fe-Cr-Al alloy heating elements. The set-up includes stainless steel vacuum flanges with valve and a vacuum gauge.

Sealed quartz ampoules loaded with reagents are placed inside a 1400 mm fused quartz tube (OD: 80 mm × ID: 74 mm). 3 independent 708P precision temperature controllers provide 30 segments heating and cooling steps with +/- 1 °C accuracy. The three sets of heating elements split the tube in three zones of 220 mm + 440 mm + 220 mm. Temperature gradients of up to 270 °C may be achieved under these reaction conditions.

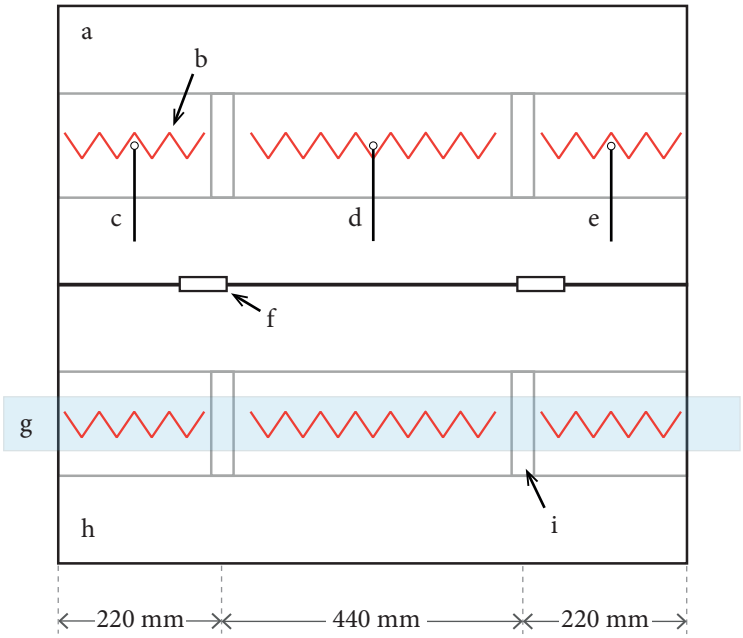

Figure A.5.2 Top view scheme of the principal parts of the EQ-OTF-1200L3-III split-tube furnace: top lid (**a**); heating elements (**b**); independent zone thermocouples (**c** - **e**); folding hinges (**f**); main quartz tube for supporting the reaction vessels (**g**); main bottom chassis (**h**); inter-zone insulating elements.

3 General characterisation instruments and techniques

3.1 FT-Infra-red spectroscopy

Infra-red spectra were recorded on a Nicolet 5700 FT-IR spectrometer. Unless otherwise specified, spectra were recorded from solid products prepared in the form of KBr compressed pellets. Once noting spectra, the letters in the parentheses refer to relative transmittance intensity of the different peaks, being weak (w) less than 40% of the most intensely absorbing peak, medium (m) a 41-74% of the reference peak and strong (s) greater than 75% of this same peak. The code broad (br) and sharp (sh) was also used.

3.2 Elemental analysis

Carbon, nitrogen and hydrogen contents were determined by micro-analytical procedures using an EA 1110 CHNS-O Elemental Analyzer from CE Instruments.

3.3 Thermogravimetric analysis

TG/ATD curves were registered on a thermogravimetric and differential thermal analyzer model Mettler Toledo TGA/SDTA 851e that operates in the range 25 - 1100 ºC with a sensibility of 0.1 μg. A typical load of 3 mg of neat material was employed.

Standard runs were performed at a 10 $^{o}C \cdot min^{-1}$ scan rate and with an air flow of 30 $mL \cdot min^{-1}$.

3.4 Scanning electron microscopy

Metallic ratio composition analysis were performed on a SEM Philips XL-30 coupled to a EDAX column accessory. Neat samples were prepared on copper sample holders, placed under general 10^{-6}mBar pressures and analysed with a 20 kV electron beam at a working height of 10cm.

High resolution SEM images were taken with a field-gun emission (FEG) Hitachi S-4800 scanning electron microscope. Maximum resolution was 1.4 nm at 1 kV.

3.5 Transmission electron microscopy

General purpose TEM microscopy images were taken with a JEM-1010 (JEOL) at 100 kV equipped with a digital camera MegaView III.

High-resolution TEM (HR-TEM) imaging was performed with a TECNAI G^2 F20 (FEI) EFG TEM equipped with a GATAN CCD. Maximum (point) resolution was 0.24 nm. The instrument was employed for performing selected-area electron diffraction (SAED) experiments and for collecting EDS spatially resolved data (mapping).

3.6 Characterisation of magnetic properties

General magnetic data was collected in a SQUID magnetometer model Quantum Design MPMS-XL-5 in the 2-300K range.

Alternate current (AC) measurements were carried out in the 1-10000 Hz frequency range. Higher frequencies were probed in a 'Physical Properties Measurement System' Quantum Design PPMS-9 model.

3.7 X-Ray powder diffraction experiments

X-Ray powder diffraction (XRPD) patterns were collected with a Bruker D8 Advance X-Ray diffractometer (Cu-$K_{\alpha1}/K_{\alpha2}$ radiation; $\lambda_{\alpha1}$ = 1.54060 Å, $\lambda_{\alpha2}$ = 1.54434 Å) operating at 80 mA and 45 kV equipped with a LYNXEYE XE 1-D detector. Samples were mounted on a corrugated PMMA specimen holder ring in a θ-θ reflection geometry. Profiles were generally collected in the 5° < 2θ < 90° range with a typical step size of 0.02°.

Transmission measurements were performed on a Empyrean PANalytical powder diffractometer, using Cu K_{α} radiation (λ = 1.54177 Å). Polycrystalline samples of 1–3 were lightly ground in an agate mortar and pestle and filled into 0.5 mm borosilicate capillaries. Data were collected at room temperature in the 2θ ranges 5 – 90 ° (1), 2 – 60 ° (2) and 3 – 70 ° (3).

Pawley refinements were performed using the TOPAS computer program.[8, 9] Le Bail refinements were performed using the PANAlytical X'Pert HighScore Plus software.

3.8 Atomic Force Microscopy (AFM)

Atomic force microscopy images were performed with a Nanoscope IVa atomic force microscope (AFM) from Veeco. The images were obtained using Tapping-mode in air at room temperature with Si tips (freq. and K of *ca.* 300 kHz and 40 $N{\cdot}m^{-1}$, respectively). Images were recorded with 512 × 512 pixels and 0.5 –

8 Pawley, G. S. J. *Appl. Cryst.* **1981,** *14,* 357

9 Coelho, A. A. TOPAS-Academic, Version 4.1, 2007, see: http:// www.topas-academic.net

1 Hz scan rate. Processing and analysis of the images were carried out using the Nanotec WSXM software.[10]

10 Horcas, I.; Fernéndez, R.; Gómez-Rodríguez, J. M.; Colchero, J.; Gómez-Herrero, J.; Baro, A. M. *Rev. Sci. Instrum.* **2007,** *78,* 013705 (1).

Compound reference

Part 1:

1 $ZnAl\text{-}NO_3$
2 $MgAl\text{-}CO_3$
3 $CoAl\text{-}CO_3$
4 $MgAl\text{-}NO_3$
5 $CoAl\text{-}NO_3$
6 $ZnAl\text{-}[Cr^{III}(CN)_6]$
7 $CoAl\text{-}[Cr^{III}(CN)_6]$
8 $ZnAl\text{-}[Cr^{III}Ni^{II}(CN)_6Cl_2]$
9 $ZnAl\text{-}[Cr^{III}Ni^{II}(CN)_6(NO_3)_2]$
10 $CoAl\text{-}[Cr^{III}Ni^{II}(CN)_6(NO_3)_2]$
11 $CoAl\text{-}[Cr^{III}Ni^{II}(CN)_6(NO_3)_2]$ + NaCl

Part 2:

1 $2H\text{-}TaS_2$ } *polycrystalline*
2 $2H\text{-}TaSe_2$ } *polycrystalline*
3 $2H\text{-}NbSe_2$ } *polycrystalline*
4 $2H\text{-}NbS_2$ } *CVT*
5 $4Hb\text{-}TaS_2$ } *CVT*
6 $2H\text{-}TaS_2$ } *CVT*
7 $2H\text{-}NbSe_2$
8 $2H\text{-}TaSe_2$
9 $2H\text{-}NbS_2$
10 $2H\text{-}Na_{0.33}TaS_2$ *stirring bit*
11 $\delta\text{-}2H\text{-}Na_{0.33}TaS_2$ *orbital*
12 $\alpha\text{-}2H\text{-}Na_{0.33}TaS_2$ *HT*
13 $\delta\text{-}2H\text{-}Na_{0.33}TaS_2$ *single* crystal *HT*
14 $2H\text{-}Na_{0.015}TaS_2$ *polycrystalline*
15 $4Hb\text{-}Na_xTaS_2$ *CVT*
16 $[Mn_4](ClO_4)_2$
17 $[Mn_4]_{0.15}TaS_2$ *polycrystalline*
18 $[Mn4]_{0.15}TaS_2$ *oriented scales*
19 $[Fe(PyimH)_3](ClO_4)_2$
20 $[Fe(PyimH)_3]_{0.1}TaS_2$ *polycrystalline*
21 $[Fe(PyimH)_3]_{0.1}TaS_2$ *oriented scales*